

Signal Processing for Compressed Sensing Multiuser Detection

Dissertation

zur Erlangung des akademischen Grades

Doktor der Ingenieurwissenschaften (Dr.-Ing.)

vorgelegt dem Fachbereich 1 (Physik/Elektrotechnik)

der Universität Bremen

von

Fabian Monsees M.Sc. B.Sc.

Tag des öffentlichen Kolloquiums: 20. Oktober 2017

Gutachter der Dissertation: Prof. Dr.-Ing. Armin Dekorsy

Univ. Prof. Dipl.-Ing. Dr.-Ing. Norbert Görtz

Weitere Prüfer: Prof. Dr.-Ing. Karl-Dirk Kammeyer

Prof. Dr.-Ing. Anna Förster



Universität
Bremen

Bremen, November 8, 2017

Vorwort

Die vorliegende Dissertation entstand während meiner Tätigkeit als wissenschaftlicher Mitarbeiter im Arbeitsbereich Nachrichtentechnik an der Universität Bremen.

Mein besonderer Dank gilt Herrn Prof. Dr.-Ing. Armin Dekorsy, der mir die Promotion in einem überaus interessantem Thema ermöglichte. Zweifelsohne boten mir die durch ihn anvertrauten Forschungsvorhaben viel Potential innovative Ideen umzusetzen. Ich bedanke mich dafür, dass mir bei der Umsetzung dieser Ideen stets große Eigenverantwortung übertragen wurde. Ganz besonders hervorzuheben sind die zahlreichen Diskussionen sowie die wertvollen Anregungen, die mir dabei halfen, meine eigenen Forschung voranzutreiben. Auch für die Unterstützung, meine Forschungsergebnisse in renommierten internationalen Konferenzen zu präsentieren, bedanke ich mich. Es freut mich ganz besonders, dass Prof. Dr.-Ing. Armin Dekorsy in den richtigen Momenten die Initiative ergriff, Teile dieser Arbeit zum Patent anzumelden.

Besonderer Dank gilt auch Herrn Univ. Prof. Dipl.-Ing. Dr.-Ing. Norbert Görtz von der Technischen Universität Wien für das rege Interesse an meiner Arbeit und für die Übernahme des Zweitgutachtens. Herrn Prof. Dr.-Ing. Karl-Dirk Kammeyer und Frau Prof. Dr.-Ing. Anna Förster bin ich für ihre Tätigkeit als Prüfer verbunden.

Für das überaus freundschaftliche und konstruktive Arbeitsumfeld am Arbeitsbereich Nachrichtentechnik bedanke ich mich bei meinen ehemaligen Kollegen. Ganz besonders hervorzuheben ist dabei die Verbindung zu Dr.-Ing. Carsten Bockelmann, der mein Arbeit fachlich begleitete. Er war es, der mir in zahlreichen Diskussionen immer wieder neue Impulse und Richtungen zeigte. Darüberhinaus nahm er sich bei allen Fragen stets die nötige Zeit, diese präzise und umfänglich zu beantworten. Den Herren Matthias Woltering und Herrn Dr.-Ing. Florian Lenkeit gilt mein ganz besonderer Dank für die zahlreichen fachlichen Diskussionen, die meine Arbeit zweifelsohne bereicherten. Ganz besonders hervorzuheben ist dabei

die freundschaftliche Zusammenarbeit mit Herrn Matthias Woltering, auf der ein wesentlicher Teil dieser Arbeit aufbaut. Ihm sowie Herrn Yalei Ji, Herrn Ban-Sok Shin sowie Herrn Tobias Schnier verdanke ich die sorgsame Durchsicht dieser Arbeit. Darüberhinaus bedanke ich mich bei der Deutschen Forschungsgemeinschaft für die Finanzierung meiner Forschungstätigkeit.

Ohne den Rückhalt, den ich durch meine Familie und Freunde erfahren habe, wäre ich nicht dort, wo ich nun stehe. Ihnen verdanke ich zu einem großen Teil das Gelingen meiner Dissertation. Großer Dank gilt dabei meiner Frau Julia, die mich gerade zum Ende meiner Dissertation unverzichtbar unterstützte.

Bremen, November 2017

Fabian Monsees

Contents

1	Introduction	1
1.1	State of the Art and Open Challenges	3
1.2	Objectives of this Thesis	5
1.3	Contribution and Structure of this Thesis	6
1.4	Notation	9
2	M2M Communication and Compressed Sensing Multiuser Detection	11
2.1	Overview	11
2.2	Sporadic Machine to Machine Uplink Communication	12
2.2.1	Augmented Modulation alphabet and Traffic Model	12
2.2.2	Channel and Wireless Transmission Model	14
2.3	Compressed Sensing Multiuser Detection	16
2.3.1	Direct Random Access	16
2.3.2	Resource Efficiency	17
2.3.3	Compressed Sensing Basics	19
2.3.4	Compressed Sensing for Communications	22
2.4	Activity Errors in CS-MUD	23
2.4.1	Definition of Error Measures	23
2.4.2	Definition of Bit and Frame Error Rate	25
2.4.3	Impact of Activity Errors	25
2.4.4	The False Alarm SNR Loss	27
2.5	Chapter Summary	28
3	Optimal Activity Error Rate Control	31
3.1	Overview	31
3.2	Relevant Publications and Scientific Classification	33
3.3	The Activity Log-Likelihood Ratio	34
3.3.1	Setup	34
3.3.2	Symbol-By-Symbol Activity Log Likelihood Ratio	34

3.3.3	Frame-Based activity Log-Likelihood Ratio	37
3.4	Activity LLR based Decision Rules	39
3.4.1	The Maximum-a-Posteriori Decision Rule	39
3.4.2	The Bayes-Risk Decision Rule	42
3.4.3	Impact on Subsequent Data Detection	47
3.4.4	The Neyman-Pearson Decision Rule	49
3.5	Tree Search Algorithms for Finite Alphabet Compressed Sensing	57
3.5.1	Tree Search for Under-Determined Systems	61
3.5.2	Performance Evaluation	63
3.5.3	Complexity Analysis	65
3.6	Chapter Summary	69
4	Graphical Models for CS-MUD	71
4.1	Overview	71
4.2	Relevant Publications and State of the Art	73
4.3	Message Passing	75
4.3.1	Transmission and Node Model	75
4.3.2	The Multiuser Detector	75
4.3.3	The Approximative Multiuser Detector	80
4.3.4	The Frame Belief Propagation	83
4.3.5	Repetition Code Decoder and Data Detection	90
4.3.6	Data Detection and Activity Estimation	91
4.3.7	Sparsity Pattern Equalization and Channel Code	92
4.4	Performance Evaluation	96
4.4.1	Pareto Optimality of the Activity LLRs	99
4.4.2	Random Sequence vs. Direct Sequence Spreading	100
4.5	Chapter Summary	101
5	Multiuser Energy Detection	103
5.1	Overview	103
5.2	Problem Statement and State of the Art	105
5.2.1	Energy Detection	106
5.2.2	Multiple Measurement Vector Compressed Sensing	107
5.3	Multiuser Energy Detection	108
5.4	Concepts for Multiuser Energy Estimation	110
5.4.1	Matrix Matching Pursuit	110
5.4.2	Multiple Signal Classification (MUSIC)	111
5.4.3	Approximate MAP Energy Estimation	114
5.5	Performance Evaluation	121
5.5.1	Performance in AWGN Channels	122
5.5.2	Performance in Fading Channels	126

5.6	Chapter Summary	132
6	Multi-Carrier Compressed Sensing Multiuser Detection	133
6.1	Overview	133
6.2	Relevant Publications and State of the Art	134
6.3	Problem Statement	135
6.4	The MCSM System Concept	136
6.4.1	Key Technology Components	137
6.4.2	Specification of MCSM Node Processing	139
6.4.3	Resource Efficient Time-Frequency Mapping	141
6.4.4	Base-Station Processing	142
6.4.5	Robustness to Asynchronous Transmissions	144
6.4.6	MCSM Parametrization	146
6.5	Simulative Performance Verification	148
6.5.1	Phase Transition Diagrams	150
6.5.2	Performance over the SNR	150
6.5.3	Time-Frequency Diversity	154
6.5.4	The Data-Rate Bandwidth Trade-Off	157
6.5.5	Asynchronous Transmissions	158
6.6	Verification via Lyrtech Hardware Platform	160
6.6.1	Lyrtech Hardware Demonstration Platform	160
6.6.2	Description of the Testbed	161
6.6.3	Measurement Setup	163
6.6.4	Results and Discussion	164
6.7	Chapter Summary	170
7	Summary	171
A	Appendix	177
A.1	Proof of the Bayes-Risk	177
A.2	Proof of the Neyman Pearson Problem	179
A.2.1	Convergence	180
A.3	Mean and Variance of Θ	181
	Acronyms	185
	List of Symbols	189
	Bibliography	193

Chapter 1

Introduction

Human interaction was the main application in mind driving the evolution of mobile communication systems in the past decades. Starting from voice calls, targeted in the GSM era in the early nineties, mobile communication systems evolved from supporting voice calls only to data packets transmitted from and to the Internet. The introduction of the smart phone as a mobile access point to the Internet can be seen as the main driver towards this direction. This change has been supported by succeeding generations of mobile communication systems simultaneously supporting an increased number of subscribers with an ever-increasing demand of data-rate and coverage. To this end, the current communication standard 3GPP Long Term Evolution (LTE) has been developed to exactly target the requirements of human-based communication. Therefore, increasing the data-rate was longly believed to be one of the main drivers in the area of mobile communication systems. However, already today we observe that the amount of human driven communication is superseded by communication between autonomous entities without human communication in mind, known as Machine-to-Machine Communication (M2M). The strongly growing field of M2M covers various applications such as factory automation, smart grid, environmental monitoring and smart cities just to name a few [LCL11]. The rise of M2M applications is tremendous and it is believed that the share of M2M devices grows from 8% of overall mobile devices in 2015 to 26% by 2020 [Cis16]. Surprisingly, it is also believed that the traffic caused by these M2M devices will only represent 7% of the total traffic.

The characteristics of M2M fundamentally differs from what nowadays communication systems were designed for. Human based communication is often characterized by large packets with a demand for high data-rate.

In contrast to that many M2M applications summarize sporadic status messages being transmitted with very small packets with low data-rate and loose delay constraints. On the other hand, M2M applications may also compromise high data-rate services, e.g., for video surveillance, which are critical and therefore less delay tolerant than aforementioned use-cases. Further, M2M traffic is mainly characterized by uplink traffic between a device and a base-station, whereas human based communication is mainly driven by large downlink packages. Due to the tremendous growth of M2M traffic it is believed that cells in future mobile communication system will have to support a *massive* number of M2M devices ranging up to 300,000 devices per cell [TS313].

From the above statements it easily becomes clear that M2M leads to a paradigm shift in the evolution of communication systems. From only targeting higher and higher data-rates, upcoming generations of communication systems have to cope with diverse traffic originating from different sources. To this end, the ongoing discussions regarding the standardization of the 5th generation of mobile communication system (5G) were, among others, also driven by the challenge of aggregating M2M. Especially the European project METIS being part of the 7th framework program of the European Commission established itself as a global reference point towards 5G. METIS thereby differentiates between *massive* M2M and *ultra reliable* M2M traffic [OMM16]. Massive M2M summarizes applications such as smart cities, home automation or road and environmental monitoring. Here the requirements are driven by massive uplink transmissions with small and sporadic packets being transmitted. Ultra reliable M2M, on the other hand, summarizes critical applications with strict requirements on latency and packet error rates. Applications targeted are autonomous vehicle control, factory cell automation and smart grid.

METIS identifies the aggregation of M2M as one of the key requirements for 5G mobile communication systems. Besides the discussions along the lines of 5G other research projects have also identified M2M as an emerging technology. One driver in this direction is the discussion about the fourth industrial revolution summarized by the German initiative "Industrie 4.0". Here different projects specifically address the use-case of factory cell automation as a driver for M2M. The main emphasis within this direction is to enable ultra reliable aggregation of short packages with very low latency requirements. The projects summarizing recent advances in this direction are under the umbrella of the initiative IKT 2020 funded by the Federal Ministry of Education and Research.

1.1 State of the Art and Open Challenges

Aggregating M2M into communication systems is not fundamentally new. Already the second generation of mobile communication systems GSM made first advances towards aggregating M2M in Extended Coverage GSM for IoT (EC-GSM-IoT) [MSP13]. Additionally, recent advances towards aggregating M2M into LTE have been made by the 3GPP consortium. These consider a narrow frequency band scheduled separately to aggregate M2M devices. The key challenges into this direction have been summarized in TS 36.888 in the corresponding LTE standardization embodiments [TS313]. Additionally, a new narrowband air interface to aggregate M2M has been proposed by 3GPP under the name Narrowband Internet of Things (NB-IoT) as a LTE compliant extension [3GP16]. Extending LTE towards M2M is clearly a viable approach. However, it can be expected that the improvements made by the ongoing standardization of the 5th mobile communication system will surpass these advances.

The key challenges for aggregating M2M traffic lies in the aggregation of a *massive* number of nodes only sporadically transmitting small data packets to the base-station. One of the major challenge lies in the design of the medium access. State-of-the-art systems such as LTE rely on orthogonal medium access with access reservation meaning that the base-station allocates time and frequency resources prior to any transmission of payload data. As shown in Fig. 1.1 nodes in a LTE system perform access reservation on a dedicated random access channel called Physical Random Access Channel (PRACH) by sending a unique preamble to the base-station (in LTE evolved Node B (eNB)). If the eNB successfully detects this preamble it sends an acknowledge message in form of a so-called random access response to the node. Here the node also gets information which time frequency resource it should use for further communication. This resource is used by the node to request radio resources for uplink transmissions by a scheduling request. After reception, the eNB grants the uplink to the node which then can perform uplink transmissions on the so-called Physical Uplink Shared Channel (PUSCH). As indicated in Fig. 1.1 (a) the access reservation procedure in LTE consists of four messages being transmitted between node and eNB prior to any payload data transmission.

Such random access procedure is a viable approach for large data-packets. A straightforward approach for scaling this access reservation would be to extend the number of orthogonal preambles used in LTE. However, it can be easily visualized that this impairs with the concept of reduced signaling, targeted for small packets. Therefore, for massive M2M with up to 300,000 nodes per cell, sporadically transmitting only small and short packets, access

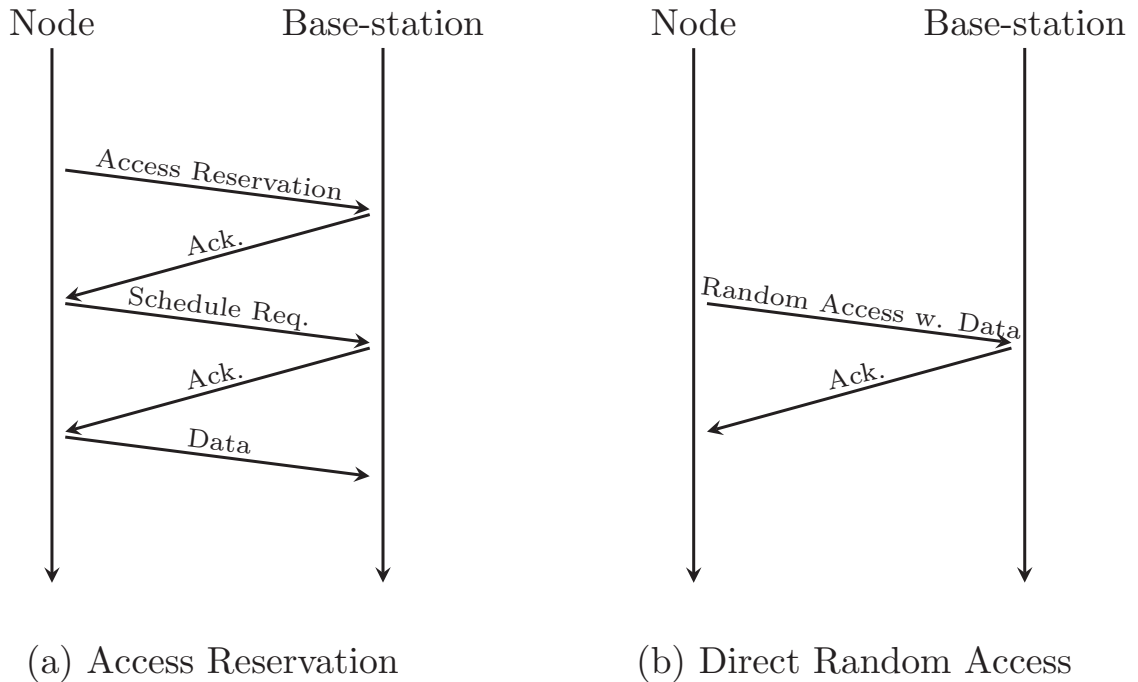


Figure 1.1: Comparison of medium access schemes. Access Reservation as employed in LTE (left) and Direct Random Access as candidate technology for M2M (right).

reservation is unprofitable and technically even impossible.

To cope with *massive* M2M recent discussions about non-orthogonal access with reduced signaling were made [OMM16]. One promising approach addressing the signaling aspect is called direct random access (also one shot transmission). Direct random access is an uplink medium access procedure tailored for sporadic M2M. Here nodes *simply* transmit their data package to the base-station without prior signaling. Fig. 1.1 exemplary shows the data-transmission for direct random access compared to access reservation as used in LTE. As nodes simply transmit, the base-station may receive packets from multiple nodes at the same time and has to resolve the multiuser interference caused. Further, the base-station has no knowledge which node was active at a given time instance such that the PHY layer task is to jointly estimate the activity and the data of the nodes. Comparing direct random access with access reservation carried out in LTE Fig. 1.1 (a) shows that direct random access already saves any 'ping-pong' like message exchange between base-station and node.

Further, it has been shown that the physical layer aspects of direct random access can be optimized. Here resource allocation comes into play and the question arises how physical resources such as time, frequency or code should be assigned to nodes that are known to be only sporadically active. It is

almost self evident that orthogonal resource allocation leads to a waste as most of the resources remain unused most of the time. As a consequence, recent research has focused on optimized non-orthogonal resource allocation as a physical layer method for direct random access [BSD13]. In turn, non-orthogonal resource allocation causes multi-user interference that has to be resolved at the base-station.

The enabler for still coping with this multi-user interference is the sporadic M2M traffic. This even allows to overload the systems in terms of the ratio of nodes per resource. This ratio corresponds to the load of the system and it could be shown that reliable communication is still feasible if the underlying system is highly overloaded [SD11, SD12] and many nodes share few resources only. As being said, the main performance driver is to exploit the knowledge about the sporadic structure of M2M at the base-station. This is facilitated by algorithms taken from the field of Compressed Sensing to solve the underlying estimation problems. This combination is known as Compressed Sensing Multiuser Detection (CS-MUD) and summarizes the joint activity and data detection in non-orthogonal M2M systems based on direct random access. The framework of CS-MUD has been developed in the DFG funded research projects DE 1858/1-1 and DE 759/3-1 and as a part of the contributions to the European project METIS.

1.2 Objectives of this Thesis

The objectives of this thesis address the theoretical and practical aspects of CS-MUD. At its core, CS-MUD involves the joint activity and data detection of nodes in overloaded systems. Consequently, besides having data-errors only CS-MUD may also suffer from activity errors known as false alarm and missed detection. Comparing data errors with activity errors shows that activity errors have a fundamentally different impact on the underlying communication. While false alarm errors may be identified by higher layers, missed detection errors lead to a loss of data that can not be recovered. To address the task of proper activity and data detection, this thesis focuses at three main goals.

First we have to thoroughly identify the particular impact of false alarm and missed detection errors on the data-detection. More specifically, the impact of activity errors on the data detection has to be investigated.

Based on these investigations, this thesis presents several novel concepts and algorithms for the activity and data detection task. While considering separate activity and data detection, this thesis also presents algorithms based on the joint activity and data detection.

Beyond that, and as a third goal the practical aspect of this thesis, is to

demonstrate that CS-MUD is a possible candidate technology for M2M in 5G and beyond. We, therefore, address the key challenges identified by recent research in M2M to formulate a possible system design. This design uses the results achieved in this thesis as a basis for a system concept. Beyond only showing simulative results, we also address the aspect of a possible implementation by showing results obtained by over-the-air transmissions carried out with a hardware demonstrator using the algorithms developed within this thesis.

1.3 Contribution and Structure of this Thesis

The result of this thesis have been achieved by the author's contribution to the two DFG funded projects DE 759/3-1 and DE 1858/1-1. The main contribution of this thesis is to addresses two previously mentioned central questions from different viewpoints. While starting with concepts asking for carrying out activity and data detection optimally, the second part of this thesis addresses practical aspects and formulates a practical system based on CS-MUD.

- Chapter 2 lays the basis for this thesis by introducing the system model and the probabilistic traffic model for M2M uplink communication. We also review the main parts of CS-MUD to formulate a corresponding uplink system model. More specifically we review the direct random access and its combination with sporadic M2M. Further, the impact of activity errors on the underlying communication system is addressed. Here it is shown that an increased false alarm rate yields a SNR loss at the data detection. Further, the definition of activity error rates and the definition of the SNR is given.
- Chapter 3 addresses the sole activity detection and considers the estimation problem from a communications engineering point of view. Based on the definition of the activity Log-Likelihood ratio (LLR), different decision rules for deciding in favor of activity and inactivity are introduced. Here we see that the conventionally optimal and often used Maximum-a-Posteriori (MAP) approach is sub-optimal as the missed detection rate is very high, showcasing that MAP is the wrong criterion for the activity detection task. Therefore minimization of the weighted false alarm and missed detection rates, the Bayes-Risk decision rule is introduced. Indeed, it can be shown that Bayes-Risk detection allows for controlling the activity error rates in a system. However, the particular activity error rate a Bayes-Risk detector achieves is hard to predict, complicating the practical implementation. Therefore,

another concept based on Neyman-Pearson detection is considered. The Neyman-Pearson detector takes the activity LLRs as input statistic and estimates the optimal threshold such that a constant activity error rate is achieved. Here, we consider the case of a constant missed detection rate detector. The results show that constant missed detection rates can be achieved with Neyman-Pearson detection. Beyond that, the algorithms behind the calculation of the activity LLRs are investigated. Here, we adapt tree search algorithms based on Sphere Decoding to work in under-determined systems. We investigate the performance and the complexity of the algorithms. While Sphere Decoding exhibits high complexity, sub-optimal approaches such as K-Best detection are investigated. The results show that K-Best detection is a good trade-off between optimality and complexity. The results of this chapter have been published in [MBWD12, MBD13c, MBWD13, MBD13a, MBD13d, KMB⁺13, KMB⁺14, MBD15].

- Chapter 4 goes one step forward and considers the task of activity and data detection jointly. Beyond only estimating symbols, also a channel code is applied to increase the performance of the data-detection. The approach is based on describing the underlying estimation problem on a graph consisting of factor and variable nodes. Exchanging messages between factors and variables corresponds to the so-called sum-product algorithms which is applied in this chapter. The corresponding graph for CS-MUD is composed of three different parts. First, a multiuser detector resolves multiuser interference given by the superposition of multiple transmit signals on the wireless channel. A second stage estimates the node activity state by combining the information from a bank of multiuser detectors. Additionally, a bank of channel decoders estimates the information bits by combining soft information from the multiuser detectors. The corresponding algorithm is iterative while messages between these three entities are exchanged. This estimator performs a joint activity and data detection by delivering soft information for the information bits for all nodes in a system. As a consequence inactive nodes can be identified by Cyclic Redundancy Check (CRC) carried out. Beyond that, we can show that the stages involved *help* each other. More specifically, the application of a channel code can improve the soft information for the activity estimation while, on the other hand, the activity estimator can improve the soft information delivered to the channel code. The resulting algorithm is clearly superior to a separate activity and data detection, however, the complexity is a non negligible factor. The results of this chapter are in the stage of being published while this thesis is written.

- Chapter 5 considers the well known concept of energy detection for the activity detection task. Here concepts from energy detection are adopted to perform activity detection in CS-MUD. More specifically, the multiuser energy detection problem based on the receive covariance matrix is introduced. It is shown that this approach allows for reliable activity detection even if the channel gains are unknown to the base-station. This is a powerful approach towards a practical application. Further, it can be shown that the energy detection concept applied to CS-MUD yields an SNR gain compared to state-of-the-art Compressed Sensing concepts such as the Group Orthogonal Matching Pursuit (GOMP). To estimate the individual node energies from the superimposed covariance matrix a subsequent estimator is required. Formulating algorithms for this so-called multiuser energy estimator is the heart of this chapter. Here we introduce three algorithms ranging from simple matching pursuits over the well known Multiple Signal Classification (MUSIC) algorithm to a MAP formulation of this problem. In the simulations we show that these algorithms allow for very reliable activity detection even in fading environments. The result of this chapter have been published in [MBD14].
- Chapter 6 takes the results of the previous chapters to formulate a practical system concept based on CS-MUD. This chapter addresses the key challenges for aggregating massive M2M and thereby closes the gap between theory and practice by identifying three key technology components required. The resulting Multicarrier Compressed Sensing Multiuser Detection (MCSM) system aggregates M2M traffic in narrowband systems being part of a multi-carrier scheme being the first technology component. These narrowband systems allow for non-coherent receiver concepts driven by differential modulation that is the second technology component. Finally, on top of the multi-carrier scheme we employ CS-MUD techniques by spreading the information to chips which are then multiplexed to the sub-carriers. For the activity and data detection the multiuser energy estimators from Chapter 5 are used followed by a least squares data detector. Beyond only simulative evaluation of MCSM, the practical verification via two hardware demonstrators from Lyrtech is shown. Here we are able to show that simulations and practical over-the-air transmissions match. The results of this chapter haven been published in [MWBD15b, MWBD15a, BMW15, WMBD16]. The MCSM system concept is filed as a patent under the Patent Cooperation Treaty (PCT) [MWBD16].

1.4 Notation

In the following the the most important nomenclature is given. If not stated otherwise this nomenclature is valid throughout all parts of this thesis. The extended list of this nomenclature can be found in the list of symbols at the end of this work.

- Small italic characters denote scalars x and bold italic lowercase characters denote a column vector \mathbf{x} . Upper case bold italic characters denote a matrix \mathbf{X}
- Sets are indicated by calligraphic characters \mathcal{A}
- Columns of a matrix are denoted in MATLAB notation and $\mathbf{X}_{(:,n)}$ denotes the n th column vector of while $\mathbf{X}_{(n,:)}$ denote the n th row vector of the matrix \mathbf{X} , respectively.
- The $\mathbf{dg}(\mathbf{X})$ operator returns the diagonal elements of the matrix \mathbf{X} . Applying the $\mathbf{dg}(\mathbf{x})$ operator to a vector sets up the diagonal matrix with the vector \mathbf{x} on the main diagonals. The $\mathbf{vec}(\mathbf{X})$ operator stacks the columns of the matrix as a row-vector.
- The transpose of a matrix is denoted as \mathbf{X}^T and \mathbf{X}^H denotes the hermitian of the matrix. \mathbf{X}^{-1} denotes the matrix inverse and \mathbf{X}^\dagger denotes the left side Moore Penrose inverse of the matrix.
- The $N \times N$ identity matrix is denoted as \mathbf{I}_N . The $N \times L$ all zero matrix is denoted as $\mathbf{0}^{N \times L}$ and $\mathbf{0}^N$ denotes the N dimensional all zero vector.
- $|x|$ denotes the absolute value of a variable whereas $\|x\|_p$ denotes the p -norm of a vector. Within this thesis we use the $\|\mathbf{x}\|_0$ zero-”norm” to measure the number of non-zero elements in a vector. $\|\mathbf{X}\|_F$ denotes the Frobenious norm of a matrix.
- A Probability Density Function (PDF) of the random variable y is written as $p_y(y)$, a likelihood function of the variable x based on the observation y is written as $p_y(y|x)$. A Probability Mass Function (PMF) is written as $\Pr(x)$. The notation used in this thesis does not differentiate between realizations of random variables and their processes.
- The natural logarithm is denoted as \log , whereas \log_{10} is the logarithm w.r.t. the basis 10.

Chapter 2

M2M Communication and Compressed Sensing Multiuser Detection

2.1 Overview

Within this chapter we lay the basis for subsequent chapters by introducing the system model for the M2M uplink communication considered. Therefore, Section 2.2 starts with a formal description of the respective uplink scenario and introduces the system model for sporadic M2M uplink communication. This includes the formal description of the nodes and the traffic model causing sporadic M2M. Further, the aspect of sporadic direct random access is reviewed in Section 2.3. Here, we show that resource efficient direct random access leads to a joint activity and data detection problem that can be cast as an underdetermined set of equations. This draws the connection to Compressed Sensing, whose application to multiuser detection, known as CS-MUD is also reviewed in Section 2.3. There it is shown that the application of Compressed Sensing to communications requires a refined look at the particular error events that occur. Especially the activity error events, known as false alarm and missed detection are of major importance and are defined in Section 2.4. It is shown that the impact of both errors on a system is fundamentally different. While missed detection errors lead to a loss of data, false alarm errors lead to a SNR loss for the data detection.

2.2 Sporadic Machine to Machine Uplink Communication

The M2M scenario considered within this work is depicted in Fig. 2.1, where in total N nodes sporadically transmit data to a central base-station. The

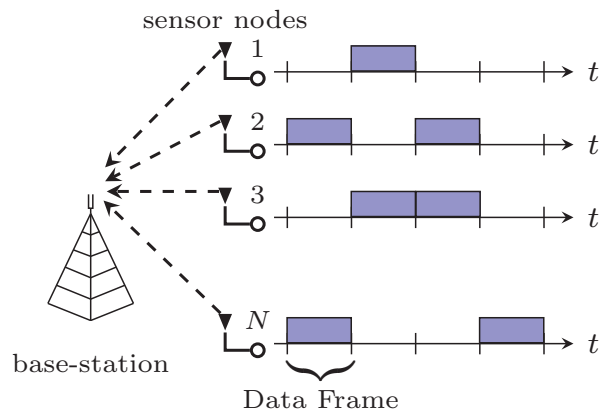


Figure 2.1: Machine to Machine uplink system with N nodes that sporadically transmit data to a central base-station

nodes are only sporadically active to transmit a data-frame to the base-station. More specifically, the time is assumed to be divided into slots. Active nodes wait for the beginning of a slot to transmit a data-frame to the base station. Further, nodes are assumed to be simple devices with limited processing capabilities. In contrast to that, the base-station is equipped with proper processing capabilities to carry out complex estimation tasks.

2.2.1 Augmented Modulation alphabet and Traffic Model

With Fig. 2.1 we now consider one particular slot and describe the processing of one node within this slot. Since nodes can be active or inactive, we require a node model reflecting this activity state. We therefore employ a detection model, which summarizes active and inactive nodes. To describe the processing, we consider any active node denoted as node n . As shown in Fig. 2.2 active nodes encode a stream of L_u information bits u_n with a known channel code of rate R_c to L_c code bits. These code bits are mapped to code symbols by a modulator that are denoted as c_n . The symbols are part of a finite modulation alphabet denoted as \mathcal{A} . The length of the stream of symbols corresponds to a frame with length L_F . For medium access the symbols are spread via a known and node specific spreading sequence to a sequence of chips summarized by the vector $\mathbf{a}_n \in \mathbb{C}^M$ of length M . At

this point we distinguish between active and inactive nodes. While active nodes spread their symbols to chips by weighting the chip sequence with the symbol according to $c_n \underline{\mathbf{a}}_n$, inactive nodes are *modeled* as transmitting a zero symbol. This allows us to summarize active and inactive nodes by augmenting the modulation alphabet via $\mathcal{A}_0 = \mathcal{A} \cup \{0\}$. In turn, both active and inactive nodes can be *modeled* as transmitting a symbol $x_n \in \mathcal{A}_0$ which is part of the augmented modulation alphabet. Later we will see that this eases the formulation of a joint activity and data detection by performing detection w.r.t. \mathcal{A}_0 . As indicated in Fig. 2.2, the node activity

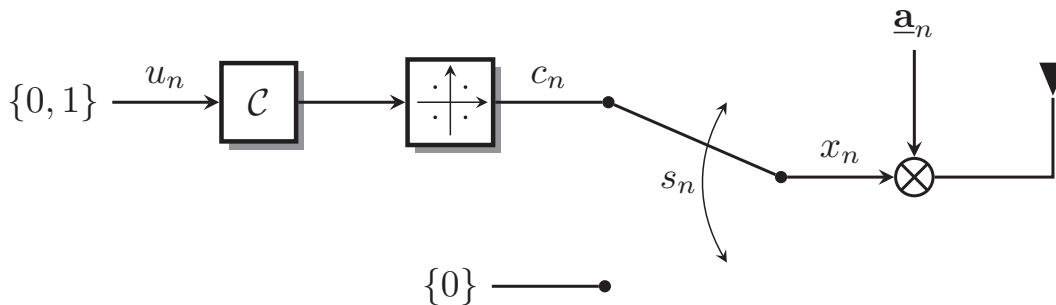


Figure 2.2: Detection Model assumed at the base-station to model the n th node.

state is determined by the random variable s_n . It should be noted that the realization of s_n is unknown to the base-station. However, in some cases probabilistic information about the node activity may be available. E.g. it may be known that nodes transmit periodic status messages leading to a rather deterministic activity state. Further, for sporadic status messages it may be known that these messages occur with a certain probability, leading to probabilistic activity states. Also, a commonly known traffic model such as the well known Poisson arrival model may be employed to capture the behavior of s_n [JBD15]. To address sporadic M2M, we employ a Bernoulli traffic model, such that s_n is a realization of a Bernoulli process with success probability p_a . Consequently, we have

$$\begin{aligned} \Pr(s_n = 1) &= p_a \\ \Pr(s_n = 0) &= 1 - p_a. \end{aligned} \tag{2.1}$$

With (2.1), each node is active at a given slot with probability p_a . The number of active nodes per frame is denoted as $N_{\text{act}} \leq N$. Further, individual activity probabilities are possible in general, however, we assume that the node activity is identically independently distributed (i.i.d.) for all nodes in the system. Extensions to individual p_a are possible for all subsequent algorithms but are avoided to preserve clarity.

2.2.2 Channel and Wireless Transmission Model

Subsequently, we formulate a mathematical description for the system depicted in Fig. 2.1. To facilitate joint activity and data detection at the base-station we set up a vector input-output model for the transmissions from the nodes to the central base-station. We thereby restrict ourself to a time discrete description of the underlying model summarized by the chip-clock. Thus, continuous-time descriptions are avoided. We assume that each node transmits a frame of L_F spreaded symbols to the base-station. To derive the mathematical model we start with a symbol-by-symbol description which is extended to a frame-based description later on.

To start we introduce the symbol clock $1 \leq l \leq L_F$ and the l th symbol from the n th node reads $x_{n,l}$. As stated previously all nodes are modeled to transmit symbols $x_{n,l}$ from the augmented alphabet \mathcal{A}_0 including zero for inactivity. Active nodes send their symbols weighted with a node specific spreading sequence $\mathbf{a}_{n,l} \in \mathbb{C}^M$ of length M to the base-station. After sending, the spreading sequences of the active nodes are convolved with the underlying wireless channels with chip-clock impulse response $\mathbf{h}_n = [h_{n,1}, h_{n,2}, \dots, h_{n,L_h}]^T$ of length L_h . Without loss of generality, L_h is assumed to be the same for all nodes. Throughout the chapters 3-5 we focus on Inter-Symbol-Interference (ISI) free transmissions such that we have $L_h = 1$ for all nodes. This strong assumption is relaxed in Chapter 6 where transmissions over ISI channels are considered. Further we assume block fading such that \mathbf{h}_n does not change over the duration of a frame.

To model the fading coefficient for the single-tap channel, we assume a Rician model with variable K_{rice} to include non line-of-sight and line-of-sight channels. In this case, the channel tap between the n th node and the base-station is modeled via

$$h_n = \frac{K_{\text{rice}}}{1 + K_{\text{rice}}} \sqrt{\bar{\rho}_n} + \frac{1}{1 + K_{\text{rice}}} \mathcal{N}(0, \bar{\rho}_n), \quad (2.2)$$

where $\bar{\rho}_n$ is the mean transmit power of the n th (active) node and K_{rice} determines the power ratio between the direct path to the indirect paths. With (2.2) we have the flexibility to consider AWGN channels $K_{\text{rice}} \rightarrow \infty$ and full Rayleigh fading channels with only indirect components $K_{\text{rice}} = 0$. Additionally, we assume that the base-station has knowledge about the mean transmit powers of the nodes, therefore we can w.l.o.g. assume $\bar{\rho}_n = 1$ for all nodes.

Including spreading and one tap channel, the l th received symbol at the base-station can be modeled as the superposition of the transmit signals of

all N , yielding the symbol-by-symbol model.

$$\mathbf{y}_l = \sum_{n=1}^N h_n \mathbf{a}_{n,l} x_{n,l} + \mathbf{w}_l \quad 1 \leq l \leq L_F. \quad (2.3)$$

Here, $\mathbf{w}_l \in \mathbb{C}^M$ denotes i.i.d. zero-mean white Gaussian noise and any element has a variance σ_w^2 . With the single tap channels, we formulate the diagonal matrix $\mathbf{H} \in \mathbb{C}^{N \times N}$ with h_n on its main diagonals. With \mathbf{H} we can write (2.3) as matrix input-output equation via

$$\mathbf{y}_l = \underline{\mathbf{A}}_l \mathbf{H} \mathbf{x}_l + \mathbf{w}_l \quad 1 \leq l \leq L_F. \quad (2.4)$$

The spreading and channel coefficient can be summarized via the composite signature matrix $\mathbf{A}_l = \underline{\mathbf{A}}_l \mathbf{H} \in \mathbb{C}^{M \times N}$, where each composite signature vector is the weighting of the spreading sequence with the respective node specific channel tap. If the spreading sequence remains unchanged throughout the entire frame, $\mathbf{A}_l = \mathbf{A}$ holds. We term this as direct sequence spreading. If \mathbf{A}_l randomly changes each transmit symbol, random sequence spreading is applied. In random sequence spreading, the multiuser interference changes from symbol to symbol, whereas direct sequence spreading maintains a constant cross correlation among the nodes. Both have certain advantages and disadvantages. This spreading is similar to long and short sequence spreading applied in Code Division Multiple Access (CDMA). The main difference lies in the design of the spreading sequences. In long sequence CDMA spreading long spreading sequences are designed and applied to different symbols [Ver98]. In contrast to that we randomly chose a new spreading sequence each symbol for random sequence spreading. Except from Chapter 5, direct sequence spreading is applied and $\mathbf{A}_l = \mathbf{A}$ holds. If possible, the symbol-clock index l is dropped to keep notation simple.

In case of ISI free transmission and direct sequence spreading, the model (2.4) can be extended to a frame-based model, where each node transmits a frame of L_F symbols. For the frame-based model it is assumed that nodes are either active or inactive for the duration of a whole frame and do not change this status during a frame. If the n th node is active for a frame, it transmits L_F consecutive symbols from the set \mathcal{A} summarized as the row vector $\mathbf{X}_{(n,:)} = [x_{n,1}, x_{n,2}, \dots, x_{n,L_F}] \in \mathcal{A}^{1 \times L_F}$. If the n th node is inactive, it keeps silent and the base-station models this as the transmission of the all zero vector of length L_F , i.e. $\mathbf{X}_{(n,:)} = \{0\}^{1 \times L_F}$. Extending the symbol-by-symbol model (2.4) to a frame-based detection model yields in combination with the signature matrix \mathbf{A}

$$\mathbf{Y} = \mathbf{A} \mathbf{X} + \mathbf{W}. \quad (2.5)$$

Here $\mathbf{Y} \in \mathbb{C}^{M \times L_F}$ contains one particular frame of observations. The matrix $\mathbf{X} \in \mathcal{A}_0^{N \times L_F}$ contains the previously introduced transmit frames of the nodes and $\mathbf{W} \in \mathbb{C}^{M \times L_F}$ contains zero-mean i.i.d. white Gaussian noise where each element has a variance of σ_w^2 . Depending on the context, we sometimes switch between the symbol-by-symbol model (2.4) and the frame-based model (2.5). Additionally, it should be noted that the input-output models introduced assumes synchronous transmission of the nodes within the network. This strong assumption is maintained throughout the Chapters 3-5 and is relaxed in Chapter 6 where practical aspects are considered.

Definition of the SNR

Throughout this thesis each active node transmits with a mean power of $\bar{\rho}_n = 1$ to the base-station. The instantaneous received power at the base-station may vary due to the impact of an unknown channel gain. The received noise at the base-station is contained in the samples y_m being part of the vector \mathbf{y} with dimension M . Hence, increasing M increases the dimension of the received vector. Each element in \mathbf{y} is assumed to be superimposed by AWGN with variance σ_w^2 . With this definition, the total noise per received symbol reads $M\sigma_w^2$ and scales with the spreading sequence length. It is therefore reasonable to subsume $1/\sigma_w^2$ as SNR, which we do throughout this thesis.

2.3 Compressed Sensing Multiuser Detection

2.3.1 Direct Random Access

One of the most important architectural concepts used in the system described here is the medium access scheme differing from what state-of-the-art systems employ. Here it is important to differentiate between physical layer concepts summarizing the mapping from information to waveforms and from access layer solutions summarizing the timing and contention of the medium access. In literature both concepts sometimes refer to the term medium access.

State of the art systems such as 3GPP-LTE rely on access reservation with 64 orthogonal resources resulting in a "ping-pong" like exchange of messages between node and base-station prior to transmission of payload data. Employing access reservation for M2M is seen as being technically unprofitable due to the large signaling overhead caused [BPN⁺16]. To this end, different concepts are currently under discussion for M2M. Here two major directions can be identified. First, small M2M packets requires low

signaling overhead caused by the medium access. Further, resource efficient medium access facilitated by non-orthogonal resources has been identified as a potential solution [BPN⁺16]. One specific example of non-orthogonal medium access is CDMA with spreading sequence length shorter than the number of nodes in the system. Besides CDMA, Sparse Code Medium Access (SCMA) with well designed spreading codes has also been identified as a possible candidate technology of non-orthogonal medium access [NB13]. The advantage of both is the decreased overhead which comes at the cost of increased multiuser interference at the base-station that has to be resolved by advanced receiver concepts.

Beyond sole physical layer concepts, also access layer concepts have been identified for M2M applications. One possible candidate technology into this direction is known as coded random access, where the time is divided into slots according to a slotted ALOHA scheme. Nodes contend by transmitting replicas of their packages randomly in the slots and the base-station estimates the packets by performing successive interference cancellation over the slots [Liv11]. Also, combinations of direct random access and coded random access are currently under discussion [JBD15].

The need for resource efficient non-orthogonal medium access drove research into the direction of direct random access. Direct random access can be seen as medium access scheme driven by advanced physical layer algorithms [OMM16]. In direct random access nodes perform random access by *simply* transmitting the data packets to the base-station without prior signaling. As several nodes sporadically transmit data, the base-station has to estimate the activity and the data of the nodes. Within this thesis we consider direct random access with spreading as a medium access scheme. The spreading from symbols to chips thereby allows for a certain degree of flexibility in terms of making the spreading sequence length longer or shorter affecting the multiuser interference caused. Clearly, decreasing the spreading sequence length increases the spectral efficiency of the system at the cost of increased multiuser interference. According to Fig. 2.1 direct random access is implemented in a combination of a slotted ALOHA scheme [Rob75] separating the time into slots. If a node has data to transmit, it waits until the next slot starts and performs direct random access by transmitting a data-frame. For the sake of simplicity it is assumed that the length of a payload frame is the same for all nodes.

2.3.2 Resource Efficiency

Combining direct random access with spreading allows to adjust the spreading sequence length M to control the load of the system. Therefore, we

consider the spreading sequence in \mathbf{A} to be part of the medium access. In this context the system model (2.4) involves the medium access of N nodes that are assigned to M resources (chips). With M and N the system load $\beta = N/M$ determines the ratio of nodes and spreading sequence length. In case of orthogonal medium access the number of resources has to be greater or equal to the number of nodes in the system and $\beta \leq 1$ holds. This implies that for a massive number of nodes the resources (spreading sequence length here) has to grow in the same manner if orthogonal medium access should be maintained. If the node activity probability is low and only few nodes are active at the same time it is easy to see that orthogonal medium access leads to a waste of resources. To counteract this effect, research towards non-orthogonal medium access has been made [BSD13]. With non-orthogonal medium access the number of resources is much lower than the number of nodes in the system leading to a load much greater than one $\beta \gg 1$. This *efficiency* comes at the cost of increased multiuser interference that has to be resolved at the base-station to ensure decodability of the payload data. The implication of resource efficiency in direct random access means that we have to estimate both, the node activity and the node data in a overloaded system with non-orthogonal resources or spreading sequences in this case. This means $M \ll N$ holds, implying that the set of equations in the system description given in (2.4) is under-determined and cannot be solved in closed form. Therefore, we have two emerging questions to address. First, we need novel algorithmic concepts to still solve this under-determined set of equations. Second, we have to define how the non-orthogonal spreading sequences have to be designed.

The first point is addressed by utilizing the side-knowledge that many variables $x_{n,l}$ have the value zero, making the multi-user vector \mathbf{x}_l sparse. Recent advances in the field of Compressed Sensing have shown that under-determined systems can still be solved if the system is sparse. The idea is to exploit the sparse structure in the multiuser signal to enable detection in overloaded systems. Combining Compressed Sensing with multiuser detection has drawn a lot of attention in the recent years and is summarized under the name CS-MUD [BSD13].

The second point can be answered after taking a closer look into the field of Compressed Sensing. Here research states that sensing matrices containing i.i.d. Gaussian elements show good reconstruction properties. This result has been confirmed in the CS-MUD context by [Sch15]. However, Gaussian spreading sequences exhibit a high Peak to Average Power Ratio (PAPR) making them hard to implement, especially if nodes are cheap with low-cost RF hardware. In contrast to that, Pseudo Noise (PN) sequences consisting of $\{\pm 1\}$ show good PAPR properties and are also commonly

used in state-of-the-art systems. However, they have higher correlations especially if $M \ll N$ [Sch15]. A good trade-off between correlation and PAPR requirements show the so-called random phase sequences. Random phase sequences are generated by taking random points from the unit circle such that the n th entry \underline{a}_n reads

$$\underline{a}_{m,n} \in \exp [j2\pi U] \quad (2.6)$$

with $U \sim \mathcal{U}(0, 1)$ being uniformly distributed. Due to the constant modulus property, the PAPR is low while the correlation is nearly the same as for Gaussian spreading sequences [Sch15]. Within this work, we consider Gaussian spreading sequences.

2.3.3 Compressed Sensing Basics

Subsequently, we briefly review the main aspects of Compressed Sensing and discuss the implication for the application in CS-MUD later on. Compressed Sensing is a recently developed framework that basically augments the well known Shannon-Nyquist sampling theory for a certain class of signals. The Shannon-Nyquist sampling theorem basing on the works of Shannon, Nyquist, Whittaker and Kotelnikov links continuous-time signals to their sampled version and states that band-limited signals have to be equidistantly sampled with a sampling rate that is greater than the bandwidth¹ of the signal [Sha01, Kot33, Whi15]. Under this condition the sampling process is lossless in terms of information contained in the continuous-time signal. Reconstructing the analog version of the sampled signal can be carried out by interpolating the samples with sinc kernels. To this end it is a common process to first sample signals at Nyquist rate and second compress the sampled signal according to some compression scheme. Here it is a well known fact that many signals that occur in practical systems can be compressed by some type of transformation applied to the sampled signal. This is commonly known as transform coding and one of the prominent examples is image compression via the Discrete Cosine Transform (DCT) applied in JPEG. The DCT in image compression is only one example for a transformation that yields a sparse representation for a practical signal. Beyond that, various practical signals have sparse representation and this is what suggests sampling these signals below their Nyquist rate. This connection is exploited in Compressed Sensing. Instead of sampling signals at high data rate and subsequent compression, Compressed Sensing aims at sampling signals in a compressed form with much lower sampling rate. The breakthrough for Compressed Sensing goes back to the joint work of Candes

¹The bandwidth includes positive and negative frequencies

and Tao in 2005 and Candes, Romberg and Tao in 2006 [CT05, CRT06]. In Compressed Sensing, the sampling is carried out by calculating the inner product between the signal and some pre-defined non-adaptive test functionals. Unlike classical sampling theory, where signals are infinitely long continuous-time functionals, Compressed Sensing focuses on finite dimensional vectors and the reconstruction of the compressed signal is carried out by finding the sparse solution to an under-determined set of equations [EK12]. The standard finite dimensional Compressed Sensing model has the form of

$$\mathbf{y} = \mathbf{A}\Psi\mathbf{x}, \quad (2.7)$$

where a measurement system acquires M linear measurements via the sensing matrix $\mathbf{A} \in \mathbb{R}^{M \times N}$. The representation matrix $\Psi \in \mathbb{R}^{N \times N}$ denotes the dictionary or the basis in which the signal $\mathbf{x} \in \mathbb{R}^N$ is sparse. Sparse means that \mathbf{x} has only s non-zero values at maximum. The sparsity is often described in combination with the zero-”norm”² which counts the number of non-zero elements in a vector. For a s sparse vector we can write $\|\mathbf{x}\|_0 \leq s$. The index set of non-zero elements in \mathbf{x} defined as $S_{\mathbf{x}} = \{n : x_n \neq 0\}$ and is known as the vector support of \mathbf{x} .

The compression is carried out via the matrix \mathbf{A} that maps the signal from N dimensional vector space to M dimensional vector space of lower dimension. The problem of reconstructing \mathbf{x} from \mathbf{y} is dependent on the embedding carried out by the sensing matrix, which gives rise to some properties that the matrix \mathbf{A} has to fulfill in order to guarantee lossless recovery of \mathbf{x} .

Looking at the noiseless case and at the recovery of an s sparse vector denoted as \mathbf{x}_s , bijectivity is a necessary condition for possible recovery. I.e., two different s sparse vectors $\mathbf{x}_{s,1}$ and $\mathbf{x}_{s,2}$ have to result in two different observations $\mathbf{y}_1 = \mathbf{A}\mathbf{x}_{s,1}$ and $\mathbf{y}_2 = \mathbf{A}\mathbf{x}_{s,2}$, i.e.,

$$\begin{aligned} \mathbf{A}\mathbf{x}_{s,1} &\neq \mathbf{A}\mathbf{x}_{s,2} \\ \Rightarrow 0 &\neq \mathbf{A}(\mathbf{x}_{s,1} - \mathbf{x}_{s,2}). \end{aligned} \quad (2.8)$$

The sum of two s sparse vectors is generally $2s$ sparse³ which concludes the following. A necessary condition for the recovery of an s sparse vector is that the corresponding sensing matrix has no $2s$ sparse vector in its right null-space. This condition is well known as the Nullspace Condition and has been formulated by [CDD09].

²The zero-”norm” is neither a norm nor a pseudo norm. However, the term ”norm” is commonly used in the Compressed Sensing context.

³In the worst case both vectors have non-zero elements in non-overlapping support sets.

However, if we consider recovery under noise according to

$$\mathbf{y} = \mathbf{A}\Psi\mathbf{x} + \mathbf{w}, \quad (2.9)$$

where \mathbf{w} summarizes the noise, we see that the Nullspace Condition is too weak to ensure reconstruction. For reconstruction under noise it is not only necessary that two different s sparse vectors lead to different observations. Furthermore, both observations have to be *far* away from each other in the M dimensional column space of the matrix \mathbf{A} . Loosely speaking, the Euclidean distance between \mathbf{y}_1 and \mathbf{y}_2 has to be greater than the instantaneous noise realization. Therefore, the reconstruction can only be probabilistically guaranteed determined by the noise statistics. A more specific description is called the Restricted Isometric Property (RIP). The RIP was already applied by Candes and Tao in 2005 [CT05] and states the following.

The Restricted Isometry Property: 1. *A matrix \mathbf{A} satisfies the RIP of order s , if there exist a constant $\delta_s \in (0, 1)$ such that*

$$(1 - \delta_s) \|\mathbf{x}_s\|_2^2 \leq \|\mathbf{A}\mathbf{x}_s\|_2^2 \leq (1 + \delta_s) \|\mathbf{x}_s\|_2^2 \quad (2.10)$$

The RIP is strongly related to the Johnson Lindenstrauss lemma [BDDW08] that states that a small set of points in a high dimensional space can be embedded into a low dimensional space while nearly preserving the distance between the points. While the Johnson Lindenstrauss lemma holds for general mappings via continuous functions, the RIP is a matrix inequality dealing with vectors. The left side of the RIP inequality is a generalization of the Nullspace Condition, i.e., if the matrix \mathbf{A} fulfills the left hand side of the RIP with constant $\delta_s = 1$, it also fulfills the Nullspace Condition for vectors with sparsity $s/2$ [EK12]. Decreasing δ_s requires the sensing matrix to preserve the norm of \mathbf{x}_s within a certain bound determined by δ_s . Setting $\delta_s = 0$ requires the sensing matrix to be orthonormal which can only be fulfilled by square or tall matrices with more rows than columns. The RIP allows some performance guarantees for recovery under measurement noise, or more specifically it determines the minimum number of measurements required. It can be shown [EK12] that for any sensing matrix that fulfills the RIP of order $2s$ with constants $\delta_{2s} \in [0, \frac{1}{2})$ the minimum numbers of measurements that is required reads

$$M \geq 0.28s \log \frac{N}{s}. \quad (2.11)$$

Having measurement noise in the form of (2.9), perfect recovery (in terms of a bijective mapping) cannot be guaranteed anymore and bounds on the

reconstruction error can only be formulated probabilistically. To this end, various bounds relating RIP constants, number of measurements and sparsity exist. These bounds were formulated with specific recovery algorithm in mind such as ℓ_1 -norm minimization. In nearly all the cases performance measures are bounds on the ℓ_2 -norm of the error vector such as the Mean Square Error (MSE). However, for the specific application in this thesis, of joint activity and data detection the MSE fails as a performance measure as it does not reflect the underlying application properly. We therefore consider communication specific error measures requiring carefully designed algorithms.

2.3.4 Compressed Sensing for Communications

Connecting Compressed Sensing to communications needs more than just an adaptation of the algorithms. Even though the underlying optimization problems appear very similar at first glance, we will see that a closer look reveals significant differences, requiring carefully designed algorithms. Connecting the world of sporadic Communications to Compressed Sensing is not generally new. This idea goes back to the pioneering work of Zhu & Giannakis in 2011 [ZG11]. The main contribution of the authors was to formulate the MAP problem for the symbol-by-symbol detection model with the prior-knowledge of Bernoulli node activity. While the authors mainly considered over or fully determined systems, the connection to Compressed Sensing was not that apparent at that time. Later [SD11] drew the connection to Compressed Sensing by exploiting sparse node activity in under-determined systems by using classical Compressed Sensing algorithms as the Orthogonal Matching Pursuit (OMP) and Orthogonal Least Squares (OLS). The subsequent works of Bockelmann, Schepker and Dekorsy [BSD13] summarized the application of Compressive Sensing to multiuser detection under the term CS-MUD. A good overview of the recent advances in CS-MUD can also be found in [DK17].

The two major differences between the standard Compressed Sensing model and CS-MUD are the lack of a representation basis Φ in the CS-MUD model. While classically, Compressed Sensing aims at estimating a dense vector via its sparse representation, CS-MUD directly aims at estimating the sparse vector itself. More specifically, the sparse vector is represented via the canonical basis. Additionally, in CS-MUD the sparse source vector obeys a finite modulation alphabet \mathcal{A}_0 , which is not continuous like in many Compressed Sensing applications. The very first works connecting Compressed Sensing and finite alphabets was given in [DM09] whose work were mainly information theoretic driven, by formulating bounds on the

reconstruction error. While various works approached this problem theoretically, practical applications of finite alphabet Compressed Sensing exist such as the adaptation of Bayesian Message passing for the estimation of finite alphabet Quadrature Amplitude Modulation (QAM) symbols in a CS-MUD fashion [HMMG16]. There the authors approached the joint activity and data detection problem by formulating a finite alphabet message passing algorithm. Beyond that, the term 'digital' Compressed Sensing as a synonym for finite alphabet problems first showed up in [SF14], where the authors combined a classical OMP with a Sphere Decoder to estimate finite alphabet Compressed Sensing problems. However, the sole application of Compressed Sensing algorithms in the CS-MUD context has to be taken with a grain of salt. As shown in the following, the system specific demands have to be taken into account.

2.4 Activity Errors in CS-MUD

2.4.1 Definition of Error Measures

As stated above, CS-MUD requires a refined look at the implications for an underlying communication system. Compressed Sensing rather employs the MSE as a performance measure. This might be reasonable where measurements of a physical process are taken. However, in the communication's context the variables are part of a data transmission and are thus exactly determined by the transmitter. Therefore, taking the MSE as a performance measure is far too shortsighted for an underlying communication system.

Even though, the standard Compressed Sensing problem (2.9) and the multiuser detection problem (2.4) are very similar at first glance, a detailed look reveals fundamental differences. The multi-user vector \mathbf{x} is composed of symbols for active nodes and zeros for inactive nodes. Hence, estimating \mathbf{x} from \mathbf{y} summarizes an activity and data-detection where the vector support $S_{\mathbf{x}}$ with cardinality $|S_{\mathbf{x}}| = N_{\text{act}}$ summarized the set of active nodes. It is obvious that the estimation of the vector support and the estimation of the symbols may be prone to errors. The possible activity error events are graphically illustrated in Fig. 2.3 on a vector support basis.

If the activity detection is successful the estimated support set $S_{\hat{\mathbf{x}}}$ matches $S_{\mathbf{x}}$ and the element x_n is contained in both sets. For x_n this means that $x_n \in \mathcal{A}$ and $\hat{x}_n \in \mathcal{A}$. We term this event as true active. False alarm errors occur, if the n th source element x_n is not contained in $S_{\mathbf{x}}$ but in $S_{\hat{\mathbf{x}}}$. On an element basis this means $x_n = 0$ while $\hat{x}_n \in \mathcal{A}$ holds. Missed detection errors, on the other hand, occur if x_n is contained in $S_{\mathbf{x}}$ but not in $S_{\hat{\mathbf{x}}}$. this happens if $x_n \in \mathcal{A}$ and $\hat{x}_n = 0$ holds. Throughout this thesis, we use

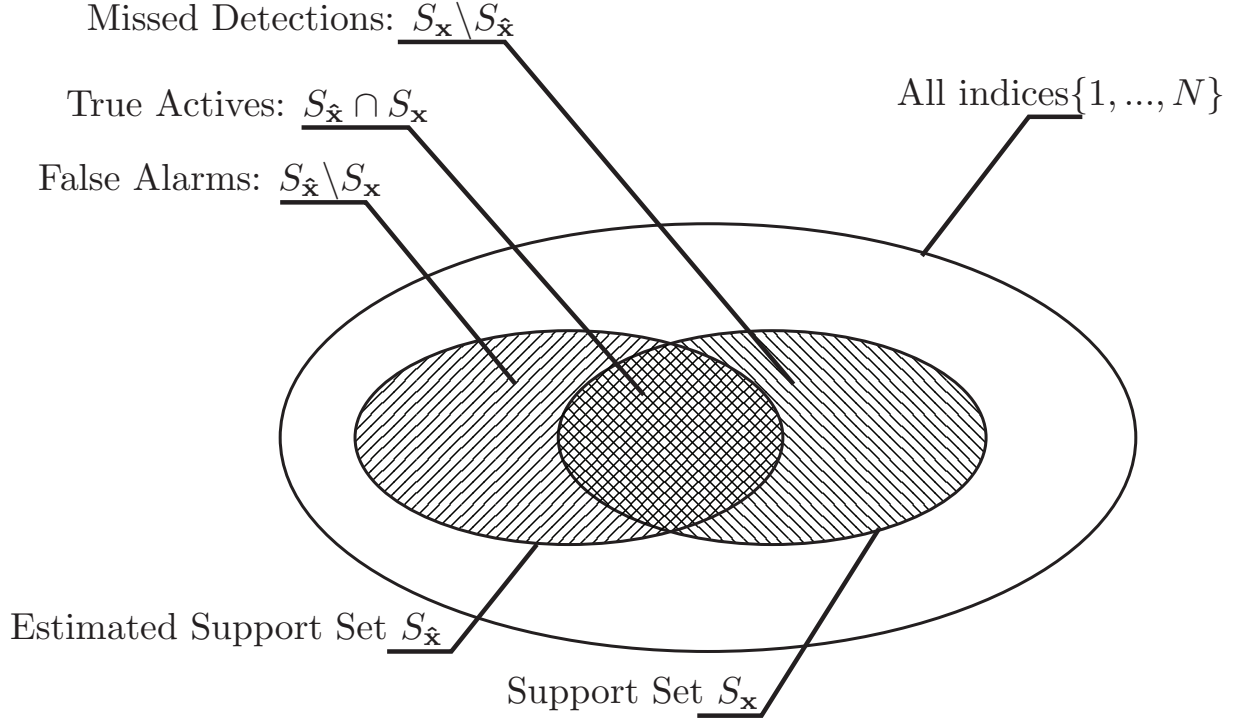


Figure 2.3: Venn Diagram of False Alarm and Missed Detection Errors

a formal definition for measuring the activity errors occurred. These are defined on a vector support basis as follows.

$$\text{False Alarms} := |\{S_{\hat{\mathbf{x}}}\setminus S_{\mathbf{x}}\}| \quad (2.12)$$

$$\text{Missed Detections} := |\{S_{\mathbf{x}}\setminus S_{\hat{\mathbf{x}}}\}| \quad (2.13)$$

$$\text{True Alarms} := |\{S_{\hat{\mathbf{x}}}\cap S_{\mathbf{x}}\}| \quad (2.14)$$

$$\text{Activity Errors} := |\{S_{\hat{\mathbf{x}}}\setminus S_{\mathbf{x}}\}| + |\{S_{\mathbf{x}}\setminus S_{\hat{\mathbf{x}}}\}|. \quad (2.15)$$

The respective set specific averages are defined as

$$\text{False Alarm rate (FAR)} := \frac{\text{False Alarms}}{N - N_{\text{act}}} \quad (2.16)$$

$$\text{Missed Detection rate (MDR)} := \frac{\text{Missed Detection}}{N_{\text{act}}} \quad (2.17)$$

$$\text{True Alarm rate (TAR)} := \frac{\text{True Alarms}}{N_{\text{act}}} \quad (2.18)$$

$$\text{Activity Error rate (AER)} := \frac{\text{Activity Errors}}{N} \quad (2.19)$$

Even though these error events are introduced for vectors \mathbf{x} , the formal definition to frames is straight forward. Since nodes are either active or

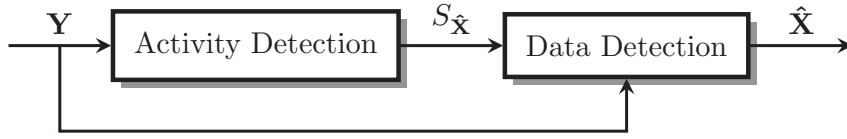


Figure 2.4: Example system with separate activity and data detection.

inactive for an entire frame, the frame support is defined as

$$\mathcal{S}_{\mathbf{X}} := \bigcup_{l=1}^{L_F} \mathcal{S}_{\mathbf{x}_l}. \quad (2.20)$$

2.4.2 Definition of Bit and Frame Error Rate

Besides activity errors, we also consider the Bit Error Rate (BER) or the Frame Error Rate (FER). To really focus on bit errors caused by data transmissions, we condition bit and frame errors on active nodes only. Hence, bit or frame errors do not contain false alarm errors. However, missed detections are included. Hence, bit or frame errors are based on the following two events

1. Active nodes, with correct activity detection, where erroneous data detection leads to errors.
2. Active nodes which have been identified as inactive \rightarrow missed detections.

In the latter case bit errors are counted at being 100% erroneous, since no bits are estimated.

2.4.3 Impact of Activity Errors

To address the impact of activity errors, we consider an example system with separate activity and data detection as depicted in Fig. 2.4. The goal of the activity detector is to yield an estimate for the frame support $\mathcal{S}_{\hat{\mathbf{X}}}$ that is used as the data detection as side information. While having false alarm and missed detection errors, we have to consider the impact on an underlying communication system. The impact of a missed detection error is quite obvious. In this case data packets are lost. If the loss can be identified, these packets have to be retransmitted, which burdens higher layer protocols such as Automatic Repeat Request (ARQ) and may increase the traffic and the

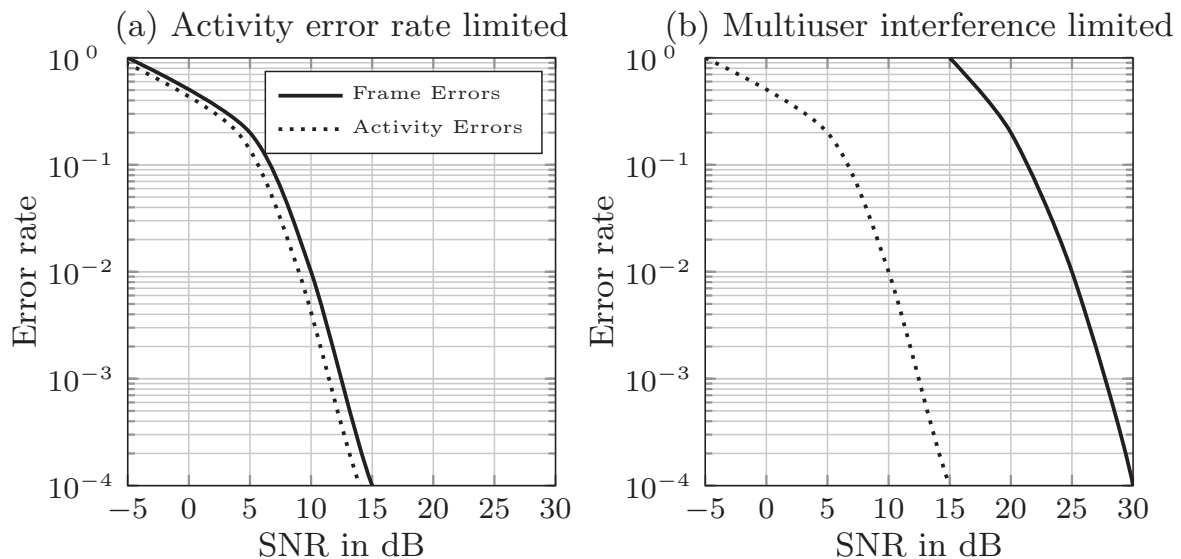


Figure 2.5: Illustration of different systems. System (a) is activity error rate limited, whereas system (b) is multiuser interference limited.

latency in the system. This may lead to congestions if the missed detection rate is very high and nodes have to repeat packages several times. In contrast to that, the impact of false alarm errors is not that apparent. In case of a false alarm error, message integrity checks such as CRC are able to identify this type of pseudo data and discard it, showcasing that false alarm errors are not that demanding for higher layers. The main problem caused by false alarm errors lies in the physical layer multi-user detection being part of the data detection. As shown later false alarm errors increase the multi-user interference and decreases the SNR for active nodes, thereby, decreasing the system performance. It is therefore reasonable to control activity errors on the physical layer. A very crude way to decrease the missed detection rate in a system is to estimate more nodes as active. Since more nodes are estimated as active it is very likely that these estimates contain some correct estimates. Hence the missed detection rate decreases. However, it is also very likely that some estimates will be false alarms. As said, these false alarms yield an SNR loss and affect the data detection.

Thus, controlling the activity error rate has always to be seen in the combination with the data detection and only makes sense if the activity error rate is the limiting factor for a system. To illustrate this, Fig. 2.5 shows the activity error and the frame error rate of two possible systems with separate activity and data detection.

In Fig. 2.5 (a) we have a system where the performance of the activity detection and the data detection are nearly equal. It is self evident that the frame error rate can not be decreased unless the activity error rate is

decreased. In such system, activity error rate control may help to improve the system performance. We consider this case in Chapter 4.

On the other hand, in Fig. 2.5 (b) we consider a system where the performance of the activity detection is better than the data detection. The frame error rate declines at high SNR where the activity error rate is already very low or even perfect. From this we conclude that the frame errors occurring at high SNR are not caused by activity errors. Thus, controlling the activity error rates does not make sense in this setup. This case is considered in Chapter 5.

2.4.4 The False Alarm SNR Loss

To exactly address the loss experienced by false alarms, again consider separate activity and data detection as in Fig. 2.4. More specifically, we assume a genie activity detector that perfectly estimates the vector support such that $S_{\hat{\mathbf{x}}} = S_{\mathbf{x}}$ holds. The data detection can thus be carried out by solving the so-called reduced multi-user problem

$$\mathbf{y} = \mathbf{A}_{(:,S_{\hat{\mathbf{x}}})}\mathbf{x} + \mathbf{w}. \quad (2.21)$$

The dimension of the reduced signature matrix reads $\mathbf{A}_{(:,S_{\hat{\mathbf{x}}})} \in \mathbb{C}^{M \times \hat{N}_{\text{act}}}$ and the task of the multi-user detector is to resolve the multi-user interference of $\hat{N}_{\text{act}} = N_{\text{act}}$ nodes. We see that the performance of the data detection is heavily impacted by the activity detection. Simple linear detectors such as Zero-Forcing or linear MMSE are restricted by the dimension of the system and can only find viable solutions for $M \geq \hat{N}_{\text{act}}$, i.e., (2.21) is of full column rank, which in turn requires the number of false alarms to not violate this restriction. Apart from this condition, we can show that false alarm errors decrease the SNR for the active nodes in the system. This can be shown by looking at a system where $S_{\hat{\mathbf{x}}} = S_{\mathbf{x}}$ and $N_{\text{act}} < M$ holds. The reduced multi-user system has the form of (2.21) and $\mathbf{A}_{(:,S_{\hat{\mathbf{x}}})}$ is of full column rank. We now make a QR decomposition on the system matrix yielding $\mathbf{QR} = \mathbf{A}_{(:,S_{\hat{\mathbf{x}}})}$ with the $M \times M$ matrix \mathbf{Q} and the upper triangular matrix \mathbf{R} of dimension $M \times \hat{N}_{\text{act}}$. The matrix \mathbf{Q} is unitary, and the first \hat{N}_{act} column vectors summarized in $\mathbf{Q}_c \in \mathbb{C}^{M \times \hat{N}_{\text{act}}}$ constitute an orthonormal basis for the column space of $\mathbf{A}_{(:,S_{\hat{\mathbf{x}}})}$, while the remaining $M - \hat{N}_{\text{act}}$ column vectors summarized in $\mathbf{Q}_n \in \mathbb{C}^{M \times M - \hat{N}_{\text{act}}}$ constitute an orthonormal basis for the left null-space. As $\mathbf{Q} = [\mathbf{Q}_c, \mathbf{Q}_n]$ is unitary, we do not change the system by

filtering with \mathbf{Q}^H , yielding

$$\begin{pmatrix} \mathbf{Q}_c^H \mathbf{y} \\ \mathbf{Q}_n^H \mathbf{y} \end{pmatrix} = \begin{pmatrix} \mathbf{Q}_c^H \mathbf{A}_{(:,S_{\hat{x}})} \mathbf{x} + \mathbf{Q}_c^H \mathbf{w} \\ \underbrace{\mathbf{Q}_n^H \mathbf{A}_{(:,S_{\hat{x}})} \mathbf{x} + \mathbf{Q}_n^H \mathbf{w}}_{=0} \end{pmatrix} \quad (2.22)$$

$$\begin{pmatrix} \mathbf{Q}_c^H \mathbf{y} \\ \mathbf{Q}_n^H \mathbf{y} \end{pmatrix} = \begin{pmatrix} \mathbf{Q}_c^H \mathbf{A}_{(:,S_{\hat{x}})} \mathbf{x} + \mathbf{Q}_c^H \mathbf{w} \\ \mathbf{Q}_n^H \mathbf{w} \end{pmatrix} \quad (2.23)$$

Here $\mathbf{Q}_n^H \mathbf{A}_{(:,S_{\hat{x}})} = 0$ holds, as column space and left null-space are orthogonal. This shows, that any signal that is contained in the left nullspace of $\mathbf{A}_{(:,S_{\hat{x}})}$ has to be noise. Thus, we can de-noise the system by deleting the last $M - \hat{N}_{\text{act}}$ rows after filtering with \mathbf{Q}^H . In this case, the noise term $\mathbf{Q}_n^H \mathbf{w}$ is *filtered* out of the system. The mean noise power that remains in the system reads

$$\mathbb{E} (\|\mathbf{Q}_c^H \mathbf{w}\|_2^2) = \hat{N}_{\text{act}} \sigma_w^2, \quad \hat{N}_{\text{act}} \leq M, \quad (2.24)$$

and scales with \hat{N}_{act} . Clearly if $\hat{N}_{\text{act}} < N_{\text{act}}$ missed detection errors occur which is not desired. However, if we estimate more nodes as active by setting $\hat{N}_{\text{act}} = N_{\text{act}} + \Delta$ with $\Delta \in \mathbb{N}^+$ we cause false alarm errors. With (2.24) we see that a system with $\Delta > 0$ suffers an SNR loss as more noise power remains in the system compared to $\Delta = 0$. We summarize this effect subsequently as the false alarm SNR loss.

Claim 1. *The False Alarm SNR loss:*

Systems with separate activity and data detection suffers an SNR loss if the false alarm rate increases.

2.5 Chapter Summary

Within this chapter we have introduced the system model for CS-MUD basing on non-orthogonal medium access paired with direct random access. Here nodes simply transmit their data and the base-station has to estimate the node activity and the payload data. It was shown that the estimation problem for direct random access with non-orthogonal medium access yields a sparse under-determined set of equations, thereby, connecting Compressed Sensing to communications. However, it was shown that activity errors known as false alarms and missed detection are of major importance. While

missed detection errors lead to a loss of data, false alarm errors require special attention. Here we could shown that false alarm errors lead to a SNR loss for other nodes - the so-called false alarm SNR loss.

Chapter 3

Optimal Activity Error Rate Control

3.1 Overview

Within this chapter we mainly focus on the sole task of activity detection and address the question of optimally estimating node activity. Here we formulate the activity detection problem in a Bayesian posteriori fashion. Further, this chapter also addresses the implementation of the derived activity detectors by Sphere Decoding.

The starting point of this chapter is the so-called activity LLR giving us soft information about node activity. The derivation of the symbol-by-symbol activity LLR is given in 3.3. The main part of this Chapter is to answer the question of how to optimally decide in favor of activity or inactivity. To answer this question we consider different decision rules that take the activity LLR as input and estimate the support set $\mathcal{S}_{\hat{\mathbf{x}}}$. These decision rules are derived in Section 3.4 where we start with the well known MAP decision rule. However, as shown MAP estimation is not suitable for performing activity detection with a communication system in mind. Even though, the overall activity error rate for MAP is the lowest we can achieve, a look on the false alarm and missed detection rates show sub-optimality. As we will see, the missed detection rate is very high when pursuing MAP activity detection. As discussed in the previous chapter this is not practical for a M2M system.

Motivated by this observation, two different decision rules are introduced. The first approach is the Bayes-Risk decision rule that aims at minimizing a risk function composed of the pre-defined risk for false alarm and the

risk of missed detection. The results show that Bayes-Risk detection allows for controlling the activity error rates through a single parameter and can be interpreted as a generalized MAP approach. The downside of Bayes-Risk detection is that the connection between pre-defined risk and resulting activity error rates can not be described analytically. A more sophisticated approach is achieved by the so called Neyman-Pearson detection which aims at minimizing one activity error rate while bounding the other below a certain limit. In this section we augment the classical Neyman-Pearson approach towards an adaptive threshold Neyman-Pearson detector that infers the optimal threshold adaptively from the activity LLRs. The result is an activity detector that minimizes the false alarm rate while bounding the missed detection rate to a pre-defined value. Simulations, however, show that the detector leads to an over-fitting, especially in the low and mid SNR region. This over-fit is compensated by augmenting the Neyman-Pearson decision rule into a randomized decision rule. Results show that the randomized decision rule improves the detector such that a constant missed detection rate is achieved over the entire SNR range yielding a precise activity error rate control.

Further, the implementation of the activity decision rules is introduced. Therefore, we address the calculation of the activity LLR in Section 3.5. To obtain the activity LLR we have to solve a regularized and under-determined mixed integer problem. The emphasis in this section is to apply algorithms known from communications to solve this problem. Here the well known framework of tree search for mixed integer problems is employed. It is a well known result that different tree-traversing strategies allow for an optimality complexity trade-off. To reduce the complexity, we consider two common tree traversing strategies. On the one hand Sphere Decoding approached by Schnorr Euchner [SE94] with radius reduction yields an optimal tree traversing strategy which allows for exact solution of the activity LLR at the cost of non-predictable complexity. As a sub-optimal but more practicable tree traversing strategy, K-Best detection [BBW⁺05] is employed. The results show that the complexity of Sphere Decoding increases as the overloading of the system increases. As a major result, we will see that K-Best detection allows for calculating the activity LLRs with much lower complexity than Sphere Decoding at the cost of minor performance losses.

3.2 Relevant Publications and Scientific Classification

Within this chapter we take a perspective motivated by the field of communications by looking at soft information processing such as LLRs to tackle the activity detection task. The idea of identifying the active users in multiuser communications is not generally new. In 1998 [WC98] presented the idea of identifying the set of active users in a CDMA system based on subspace methods applied to the covariance matrix of the received signal. Later this idea has been developed further by using tracking filters to track user activity over the time. The methods used were based on Kalman filters and on random set theory. A good overview of research in this field can be found in [VM13]. Research in this direction rather focuses on multiuser detection in general without any specific application in mind.

In 2011 Zhu and Giannakis came up with the idea to tailor user activity detection specifically to sporadic M2M [ZG11]. The idea was to exploit the sporadic structure of M2M traffic to design novel physical layer concepts for performing joint activity and data detection. This paper can be seen as the birth of a new research direction aiming at exploiting the traffic models of M2M traffic to design novel physical layer concepts. However, a deeper analysis of this work revealed the lack for a detailed view on the activity error rates. The concepts introduced were not designed for controlling the activity error rates in a manner a M2M system would require. The author's contribution [MBWD12] addresses this issue and shows that false alarm and missed detection rates have to be considered separately. Additionally, it was shown that the MAP approach followed by Zhu and Giannakis exhibits a high missed detection rate, when the node activity is low. The author's contributions [MBWD13, MBD13c] address this issue by proposing a Bayes-Risk based activity detector that allows to control false alarm and missed detection rates by a single parameter. The results are shown for a symbol-by-symbol detector and are extended toward frame-based activity detection in [MBD13b] later on. To allow for a precise activity error rate control the author introduced a Neyman-Pearson based activity detector in [MBD15], which allows bounding one activity error rate while minimizing the other. The implementation of these concepts was addressed in [KMB⁺14] where the author showed that K-Best detection is a viable approach to solve the optimization problems for the concepts introduced. It could be shown that the complexity of K-Best detection is much lower than a Sphere Decoder while maintaining the performance.

Own Publications regarding this Chapter: [MBWD12, MBWD13, MBD13c, MBD13b, MBD15, KMB⁺14]

3.3 The Activity Log-Likelihood Ratio

3.3.1 Setup

To focus on the activity detection, we consider a two stage approach according to Fig 3.1. The observation from the channel \mathbf{y}_l is fed into an activity estimator whose task is to estimate $\mathcal{S}_{\hat{\mathbf{x}}}$. This estimate is conveyed to a data detector that takes $\mathcal{S}_{\hat{\mathbf{x}}}$ to estimate the data of the nodes. More specifically, the data detector solves the reduced multiuser problem given in (2.21). Within this chapter we consider Additive White Gaussian Noise (AWGN)

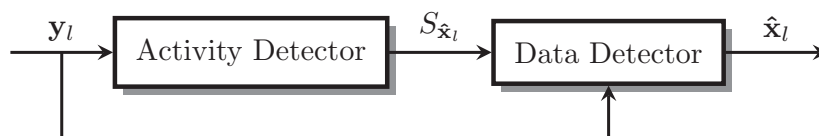


Figure 3.1: Two stage activity and data detection.

channels characterized by $K_{\text{rice}} \rightarrow \infty$ and Binary Phase Shift Keying (BPSK) modulation applied at the nodes.

3.3.2 Symbol-By-Symbol Activity Log Likelihood Ratio

To formulate activity decision rules based on soft information, we start by defining the activity LLR for the symbol-by-symbol multiuser uplink model described by (2.4). The activity LLR is the ratio of the posteriori probability for the n th node being inactive divided by the counter hypothesis and conveys soft information about activity. The activity LLR on a symbol-by-symbol basis for one particular node denoted as node n at the symbol l is defined via

$$L_{n,l} = \log \frac{\Pr(x_{n,l} = 0 | \mathbf{y}_l)}{\sum_{x_{n,l} \in \mathcal{A}} \Pr(x_{n,l} | \mathbf{y}_l)}. \quad (3.1)$$

We see that the hypothesis for node activity in the denominator depends on all possible sub-hypothesis for node activity. Unfortunately, the posteriori Probability Mass Function (PMF) $\Pr(x_{n,l} | \mathbf{y}_l)$ can only be calculated by marginalization of the joint PMF $\Pr(\mathbf{x}_l | \mathbf{y}_l)$ w.r.t. the n th element in the vector \mathbf{x}_l . To do so, we denote the set of all vectors $\mathbf{x}_l \in \mathcal{A}_0^N$ with the n th element set to the value ν as $\mathbb{X}_{n,\nu} := \{\mathbf{x} \in \mathcal{A}_0^N : x_n = \nu\}$. Applying

Bayes-Rule and marginalization allows writing the posteriori PMF via

$$\Pr(x_{n,l} = \nu | \mathbf{y}_l) \propto \sum_{\mathbf{x}_l \in \mathbb{X}_{n,\nu}} p_{\mathbf{y}_l}(\mathbf{y}_l | \mathbf{x}_l) \Pr(\mathbf{x}_l). \quad (3.2)$$

The proportional to sign indicates that normalization via $p_{\mathbf{y}_l}(\mathbf{y}_l)$ has been omitted. Inserting this marginalization into the definition of the activity LLR (3.1) yields,

$$L_{n,l} = \log \frac{\sum_{\mathbf{x}_l \in \mathbb{X}_{n,0}} p_{\mathbf{y}_l}(\mathbf{y}_l | \mathbf{x}_l) \Pr(\mathbf{x}_l)}{\sum_{\mathbf{x}_l \in \mathbb{X}_{n,\mathcal{A}}} p_{\mathbf{y}_l}(\mathbf{y}_l | \mathbf{x}_l) \Pr(\mathbf{x}_l)}, \quad (3.3)$$

where the sum in the denominator and the marginalization can be re-written as a marginalization with respect to all possible elements in \mathcal{A} according to the set $\mathbb{X}_{n,\mathcal{A}} := \{\mathbf{x} \in \mathcal{A}_0^N : x_n \in \mathcal{A}\}$. Solving (3.3) is computationally intractable due to the exponentially growing numbers of terms in the summation. To still calculate the activity LLR, we make use of the fact that the likelihood function is determined by the white Gaussian noise accordingly

$$p_{\mathbf{y}_l}(\mathbf{y}_l | \mathbf{x}_l) = \frac{1}{\sqrt{\pi^M \sigma_w^{2M}}} \exp \left[-\frac{1}{\sigma_w^2} \|\mathbf{y}_l - \mathbf{A}\mathbf{x}_l\|_2^2 \right]. \quad (3.4)$$

With (3.4) the marginalization is carried out over exponential functions. Thus, we make use of the well known max-log approximation [BV07], stating that a sum over exponential functions is mainly dominated by the greatest summand. This converts the two summations into two optimization problems and we obtain

$$L_{n,l} \approx \log \frac{\max_{\mathbf{x}_l \in \mathbb{X}_{n,0}} p_{\mathbf{y}_l}(\mathbf{y}_l | \mathbf{x}_l) \Pr(\mathbf{x}_l)}{\max_{\mathbf{x}_l \in \mathbb{X}_{n,\mathcal{A}}} p_{\mathbf{y}_l}(\mathbf{y}_l | \mathbf{x}_l) \Pr(\mathbf{x}_l)}. \quad (3.5)$$

Applying the max-log approximation is a commonly applied technique in communications. However, it should be noted that the LLR sacrifices optimality due the max-log application. To assess the impact of this approximation extensive numeric simulations are required which is out of the scope of this thesis. Further, some works have analytically investigated this loss in a Bit Interleaved Coded Modulation (BICM) system and showed that the loss is of minor importance [IHB⁺16].

To ease further derivations, we assume that the user data is i.i.d. and that the activity probability p_a is the same for all nodes. This assumption is only made for notational convenience and can be dropped to individual activity probabilities. With these assumptions, the prior $\Pr(\mathbf{x}_l)$ can be

expressed via

$$\begin{aligned}
\Pr(\mathbf{x}_l) &= \prod_{n=1}^N \Pr(x_{n,l}) \\
&= (1 - p_a)^{\# \text{ of inactive nodes}} \left(\frac{p_a}{|\mathcal{A}|} \right)^{\# \text{ of active nodes}} \\
&= (1 - p_a)^{N - \sum_n \mathbf{1}_{\mathcal{A}}(x_{n,l})} \left(\frac{p_a}{|\mathcal{A}|} \right)^{\sum_n \mathbf{1}_{\mathcal{A}}(x_{n,l})} \\
&= (1 - p_a)^{N - \|\mathbf{x}_l\|_0} \left(\frac{p_a}{|\mathcal{A}|} \right)^{\|\mathbf{x}_l\|_0}. \tag{3.6}
\end{aligned}$$

Here, $\mathbf{1}_{\mathcal{A}}(\cdot)$ denotes the indicator function that is one if the argument is part of the set \mathcal{A} and zero otherwise. We use the indicator function to count the number of active and inactive nodes within \mathbf{x}_l . In (3.6) the indicator function is replaced by the zero-”norm” $\|\mathbf{x}\|_0$ to count the number of non-zero elements in \mathbf{x}_l . Further, the probability of the modulation symbols of active nodes are assumed to follow a uniform distribution with probability mass of $\frac{1}{|\mathcal{A}|}$.

In combination with the likelihood function (3.4) and prior (3.6) the calculation of the activity LLR (3.5) can finally be cast as

$$\begin{aligned}
L_{n,l} &\approx \min_{\mathbf{x}_l \in \mathbb{X}_{x_n, \mathcal{A}}} \left[\underbrace{\|\mathbf{y}_l - \mathbf{A}\mathbf{x}_l\|_2^2}_{\textcircled{1}} + \underbrace{\|\mathbf{x}_l\|_0 \sigma_w^2 \log \left(\frac{1 - p_a}{p_a / |\mathcal{A}|} \right)}_{\textcircled{2}} \right] \\
&- \min_{\mathbf{x}_l \in \mathbb{X}_{x_n, 0}} \left[\underbrace{\|\mathbf{y}_l - \mathbf{A}\mathbf{x}_l\|_2^2}_{\textcircled{1}} + \underbrace{\|\mathbf{x}_l\|_0 \sigma_w^2 \log \left(\frac{1 - p_a}{p_a / |\mathcal{A}|} \right)}_{\textcircled{2}} \right]. \tag{3.7}
\end{aligned}$$

To obtain (3.7) we also made use of the fact that the maximum of a functional can be found by minimizing the negative version of the function, i.e., $\max f(x) = \min -f(x)$.

The activity LLR is composed of two parts. One part, denoted by $\textcircled{1}$ summarizes the observation from the channel \mathbf{y}_l and contains the likelihood function. The second part $\textcircled{2}$ summarizes the prior knowledge about the multiuser signal and contains the knowledge about the sparse multiuser activity. Most interestingly, the prior is weighted with the noise variance

σ_w^2 , showcasing that the activity LLR is dominated by the prior knowledge in the low SNR range and by the observation from the channel in the high SNR range, respectively.

3.3.3 Frame-Based activity Log-Likelihood Ratio

Extending the symbol-by-symbol activity LLR towards frame-based transmissions requires calculating the activity LLR for the frame-based model (2.5). This can be done by replacing the observation \mathbf{y}_l and the multiuser vector \mathbf{x}_l in (3.5) with the respective matrices from the frame-based model (2.5). This yields

$$L_n \approx \log \frac{\max_{\mathbf{X} \in \mathbb{X}_{(n,:), \{0\}}^{L_F}} p_{\mathbf{Y}}(\mathbf{Y}|\mathbf{X}) \Pr(\mathbf{X})}{\max_{\mathbf{X} \in \mathbb{X}_{(n,:), \mathcal{A}}^{L_F}} p_{\mathbf{Y}}(\mathbf{Y}|\mathbf{X}) \Pr(\mathbf{X})}. \quad (3.8)$$

Here the notation is slightly extended such that $\mathbb{X}_{(n,:), \mathcal{V}}^{L_F} := \{\mathbf{X} \in \mathcal{A}_0^{N \times L_F} : \mathbf{X}_{(n,:)} \in \mathcal{V}\}$ denotes that the n th row vector of the matrix \mathbf{X} contains elements from the set \mathcal{V}^{L_F} . The assumption of i.i.d. Gaussian noise makes the likelihood function $p_{\mathbf{Y}}(\mathbf{Y}|\mathbf{X})$ factorizable over the symbol clock such that we can write

$$p_{\mathbf{Y}}(\mathbf{Y}|\mathbf{X}) = \prod_{l=1}^{L_F} p_{\mathbf{y}_l}(\mathbf{y}_l|\mathbf{x}_l). \quad (3.9)$$

The prior probability reads

$$\Pr(\mathbf{X}) = \prod_{n=1}^N (1 - p_a)^{\mathbf{1}_0(\mathbf{X}_{(n,:)})} \left(\frac{p_a}{|\mathcal{A}|^{L_F}} \right)^{1 - \mathbf{1}_0(\mathbf{X}_{(n,:)})}, \quad (3.10)$$

with

$$\mathbf{1}_0(\mathbf{X}_{(n,:)}) := \begin{cases} 1 & \text{if } x_{n,l} = 0 \ \forall l \\ 0 & \text{else.} \end{cases} \quad (3.11)$$

Unfortunately, the prior (3.10) can not be decomposed into factors over the symbol-clock. The reason for this is that nodes are either active or inactive for the whole frame. Hence, the calculation of a single activity LLR reads

$$L_n \approx \log \frac{\max_{\mathbf{X} \in \mathbb{X}_{(n,:), \{0\}}^{L_F}} \prod_{l=1}^{L_F} p_{\mathbf{y}_l}(\mathbf{y}_l|\mathbf{x}_l) \Pr(\mathbf{X})}{\max_{\mathbf{X} \in \mathbb{X}_{(n,:), \mathcal{A}}^{L_F}} \prod_{l=1}^{L_F} p_{\mathbf{y}_l}(\mathbf{y}_l|\mathbf{x}_l) \Pr(\mathbf{X})}. \quad (3.12)$$

The fact that the prior is not further decomposable renders the calculation of a single frame activity LLR as a matrix optimization problem with $N \times L_F$

variables, which is clearly infeasible. Here we identify two possible strategies to still find frame activity LLRs. First, we could exclude the prior in (3.12). In this case the activity LLR would solely be determined by the likelihood function and the knowledge about sporadic node activity is not exploited. A more sophisticated approach is to approximate the frame activity LLRs by *assuming* the node activity to be independent within a frame. As shown later this approach leads to correct frame activity LLRs in the high SNR range. For low and mid SNR, the LLRs are biased. Assuming i.i.d node activity within a frame factorizes the frame prior probability into

$$\Pr(\mathbf{X}) = \prod_{l=1}^{L_F} \Pr(\mathbf{x}_l). \quad (3.13)$$

Inserting (3.13) into (3.12) yields after rearranging

$$L_n \approx \sum_{l=1}^{L_F} \min_{\mathbf{x}_l \in \mathbb{X}_{x_n \in \mathcal{A}}} \left[\underbrace{\|\mathbf{y}_l - \mathbf{A}\mathbf{x}_l\|_2^2}_{\textcircled{1}} + \underbrace{\|\mathbf{x}_l\|_0 \sigma_w^2 \log\left(\frac{1-p_a}{p_a/|\mathcal{A}|}\right)}_{\textcircled{2}} \right] - \sum_{l=1}^{L_F} \min_{\mathbf{x}_l \in \mathbb{X}_{x_n=0}} \left[\underbrace{\|\mathbf{y}_l - \mathbf{A}\mathbf{x}_l\|_2^2}_{\textcircled{1}} + \underbrace{\|\mathbf{x}_l\|_0 \sigma_w^2 \log\left(\frac{1-p_a}{p_a/|\mathcal{A}|}\right)}_{\textcircled{2}} \right]. \quad (3.14)$$

Considering (3.14) shows that the prior part denoted via $\textcircled{2}$ is involved in the calculation of each activity LLR. This leads to a higher impact of the prior in the frame LLRs and hence, the frame LLRs are biased. However, due to the weighting of prior with the noise variance this effect diminishes in the high SNR range, also decreasing the bias in this region. One naive approach would be to calculate and subtract the bias from the activity LLR. However, this approach is not feasible as the bias is part of the optimization problem and its impact on the activity LLR can not directly be calculated.

Rearranging (3.14) shows that under the assumption of i.i.d. prior, the frame activity LLR can be written as the sum of the symbol-by-symbol activity LLRs via

$$L_n = \sum_{l=1}^{L_F} L_{n,l}. \quad (3.15)$$

For the following section, we assume that we can perfectly calculate the symbol-by-symbol activity LLR by solving (3.7). If frame activity LLRs

are used, the calculation is done by summing up symbol-by-symbol activity LLRs via (3.15). The tree search algorithms used to calculate the activity LLRs are introduced in Section 3.5.

3.4 Activity LLR based Decision Rules

Based on the activity LLRs a hard activity decision can be facilitated by thresholding $L_{n,l}$ according to a given threshold t . We define the activity estimation such that nodes with an activity LLR greater than t are added to the support set $\mathcal{S}_{\hat{\mathbf{x}}}$ while nodes with lower activity LLR are excluded from the support set. Such a decision rule can formally be written as

$$\phi(L_{n,l}) = \begin{cases} \mathcal{S}_{\hat{\mathbf{x}}_l} \setminus n & \text{if } L_{n,l} \geq t \\ \mathcal{S}_{\hat{\mathbf{x}}_l} \cup n & \text{if } L_{n,l} < t. \end{cases} \quad (3.16)$$

The goal of the following subsections is to address the question for an optimal threshold t and the resulting activity error rates.

3.4.1 The Maximum-a-Posteriori Decision Rule

A well known decision rule which is commonly applied in communications is the MAP decision rule. Here the goal is to decide in favor of the hypothesis with the most probable posteriori probability. Applying the MAP decision rule sets the threshold to $t = 0$ and we have

$$\phi^{\text{MAP}}(L_{n,l}) = \begin{cases} \mathcal{S}_{\hat{\mathbf{x}}_l} \setminus n & \text{if } L_{n,l} \geq 0 \\ \mathcal{S}_{\hat{\mathbf{x}}_l} \cup n & \text{if } L_{n,l} < 0. \end{cases} \quad (3.17)$$

Fig. 3.2 (a) exemplary shows the activity error rates for MAP estimation. The MAP decision rule is known to be the best decision rule in terms of minimizing the overall probability of errors, it is therefore not a surprise that the activity error rates are monotonically decreasing as the SNR increases. In the very low SNR regime the activity error rate converges to the activity probability p_a , which is 0.2 in this setting. Overloading the system by decreasing the spreading sequences to $M < N$ also increases the activity error rates significantly as a fact that the multiuser interference increases.

Decomposing the activity error rate into false alarm and missed detection error rates yields a surprising result. While the missed detection rates are high in the low SNR regime and also monotonically decrease in the high SNR, the false alarm rates, on the other hand, increase over the SNR, reach a peak around 10 – 15 dB and decrease for higher SNR. In contrast to

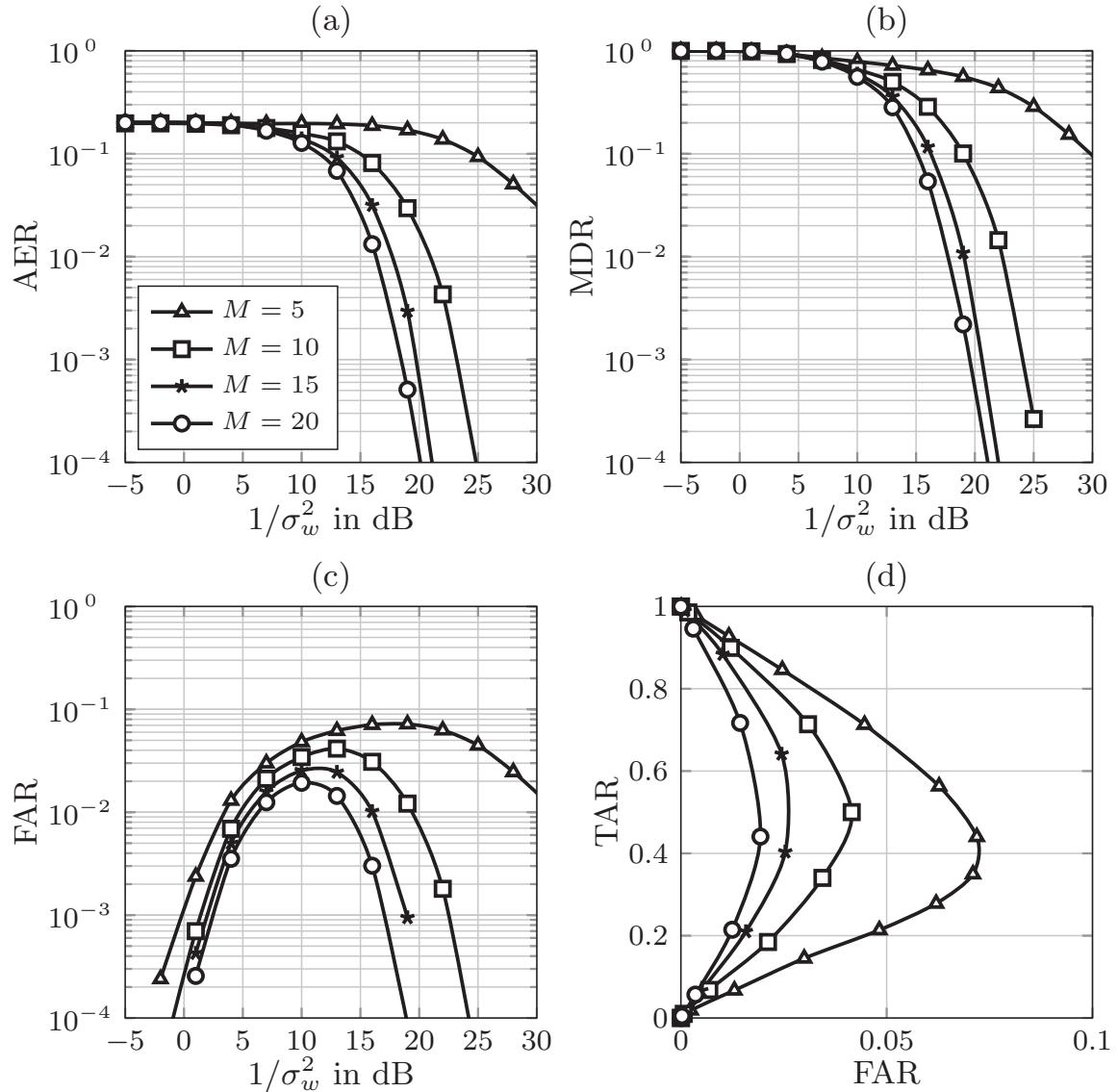


Figure 3.2: Performance of MAP activity detector in systems with different spreading factors M , $N = 20$, $p_a = 0.2$. Activity error rates are shown in (a), missed detection rates in (b), false alarm rates in (c) and Receiver Operating Characteristics (ROC) in (d).

that the missed detection rate exhibits values around 100% for low SNR, whereas the false alarm rate remains always far below 10% yielding a severe imbalance between false alarm and missed detection rates. This imbalance can be visualized in the so called Receiver Operating Characteristics (ROC) as shown in Fig. 3.2 (d). The ROC plots the tuple of true alarm and false alarm rate for each SNR simulated. Connecting the points yields a path that starts at (0,0) and ends at the point (0,1). We see that MAP activity detection starts with 0% true alarm and false alarm rate. While the true alarm rate increases for higher SNR, the false alarm rate always remains

low, and never exceeds 10%. We term such a detector *conservative*, as it only estimates nodes as active if the probability of being active is high. The reason for this unexpected behavior becomes clearer while looking at the definition of the activity LLR in (3.7). Here we see a composition of a likelihood function and a prior. In case of low SNR the prior dominates the activity LLR and as long as p_a is sufficiently low, the resulting activity LLR remains positive. With increasing SNR, the impact of the likelihood function increases and due to the weighting with the inverse noise variance, this part dominates the activity LLR. As a consequence, the MAP decision rule always decides in favor of inactivity in the low SNR range yielding less false alarms. This effect is reversed in the high SNR regime. Here, the likelihood part dominates the activity LLR yielding correct activity decisions with no false alarms and missed detections. The range in between shows the peak shown in Fig. 3.2 (c). The reason for this *conservative* behavior can be found in the prior knowledge about the multiuser signal. Having $p_a \ll 1$ renders inactivity to be an likely event. As a consequence, the MAP detector tends to rather decide in favor of inactivity.

Frame-Based Transmissions

In case of frame-based transmissions the MAP decision rule can be directly applied to the frame LLR defined in (3.15). The frame MAP decision rule reads in this case

$$\phi^{\text{MAP}}(L_n) = \begin{cases} S_{\hat{\mathbf{x}}} \setminus n & \text{if } \sum_l L_{n,l} \geq 0 \\ S_{\hat{\mathbf{x}}} \cup n & \text{if } \sum_l L_{n,l} < 0. \end{cases} \quad (3.18)$$

This approach is clearly superior to any symbol-by-symbol detection since knowledge over multiple time instances is used.

Fig. 3.3 (a) plots the frame activity error rate over the frame length L_F that is achieved with an SNR of 15dB for different spreading sequence lengths M . It can be seen that the activity errors exhibit a step decrease for short frame length of only a few symbols. We also see that this decrease is higher for systems with higher spreading sequence length where the system load is lower. This leads to the conclusion that most of the gains are achieved already with short frames which is suitable for M2M applications.

Fig. 3.3 (b) also plots the missed detection rates over the SNR for different spreading sequence lengths M for a fixed frame length of $L_F = 20$. Only the missed detection rates are plotted as false alarm errors could not be measured. This shows how the bias of the frame activity LLRs affects the activity error rates. The bias contained in each activity LLR makes the detector even more conservative yielding no false alarms.

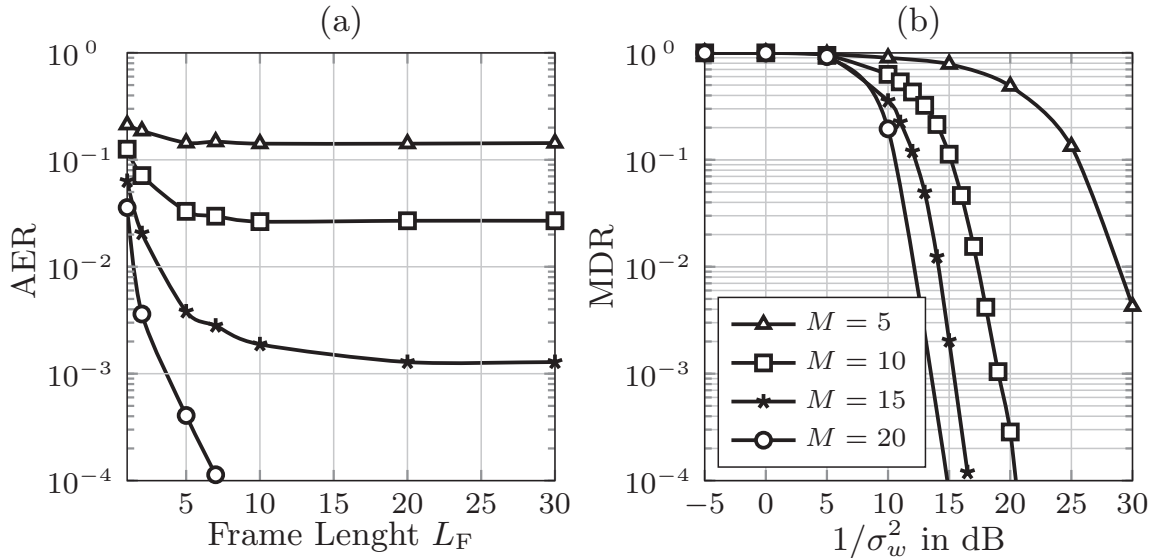


Figure 3.3: Frame activity error rate versus frame length L_F at a fixed SNR of 15dB on (a) and missed detection rate versus SNR for MAP detection at a frame length of $L = 20$ for different spreading sequence length M . The number of nodes is $N = 20$ with $p_a = 0.2$.

3.4.2 The Bayes-Risk Decision Rule

The analysis of the MAP decision rule has shown, that MAP activity estimation tends to be conservative. The prior knowledge of a sparse multiuser signal keeps the false alarm rate low, while the missed detection rate is quite high. Even though the activity error rate is as low as possible, the individual error rates, and especially the high missed detection rate, may be incompatible with the requirements of an underlying system. As stated in Chapter 2 high missed detection rates lead to loss of data and depending whether retransmissions are initiated the system may suffer from delays and congestions. Further, critical applications may be incompatible with delays caused by missed detections.

One possible way to counteract this problem is Bayes-Risk [VT04] based detection, which allows weighting both error events individually by defining cost for false alarm and missed detection probabilities. As shown in this section this approach allows finding an activity LLR threshold that minimizes the weighted false alarm and missed detection probability. For this sake, we define the costs C_{FA} for the false alarm and C_{MD} for missed detection, respectively. The Bayes-Risk for an activity error decomposed in false alarm

and missed detection error reads

$$\begin{aligned} \mathcal{R}_{n,l} = & C_{\text{FA}} \Pr(x_{n,l} = 0) \underbrace{\int_{Z_A} p_{\mathbf{y}_l}(\mathbf{y}_l | x_{n,l} = 0) d\mathbf{y}_l}_{\text{Prob. of false alarm}} + \\ & C_{\text{MD}} \Pr(x_{n,l} \in \mathcal{A}) \underbrace{\int_{Z_I} p_{\mathbf{y}_l}(\mathbf{y}_l | x_{n,l} \in \mathcal{A}) d\mathbf{y}_l}_{\text{Prob. of missed detection}}. \end{aligned} \quad (3.19)$$

Z_I and Z_A are the regions in the observation space where the detector assigns the observation to the hypotheses H_I for inactivity and H_A for activity, respectively [VT04]. As shown in appendix A.1 the minimization of the Bayes-Risk for node n can be cast as a Likelihood Ratio Test (LRT)¹

$$\begin{aligned} \log \frac{p_{\mathbf{y}_l}(\mathbf{y}_l | x_{n,l} = 0) \Pr(x_{n,l} = 0) C_{\text{FA}}}{\sum_{x_{n,l} \in \mathcal{A}} p_{\mathbf{y}_l}(\mathbf{y}_l | x_{n,l}) \Pr(x_{n,l}) C_{\text{MD}}} & \underset{H_A}{\overset{H_I}{\geq}} 0 \\ \log \frac{p_{\mathbf{y}_l}(\mathbf{y}_l | x_{n,l} = 0) \Pr(x_{n,l} = 0)}{\sum_{x_{n,l} \in \mathcal{A}} p_{\mathbf{y}_l}(\mathbf{y}_l | x_{n,l}) \Pr(x_{n,l})} & \underset{H_A}{\overset{H_I}{\geq}} \log \frac{C_{\text{MD}}}{C_{\text{FA}}} \\ L_{n,l} & \underset{H_A}{\overset{H_I}{\geq}} \log \frac{C_{\text{MD}}}{C_{\text{FA}}}. \end{aligned} \quad (3.20)$$

The right hand side of (3.20) clearly defines a threshold for the activity LLR $L_{n,l}$ based on the ratio of costs defined as $\Omega = \frac{C_{\text{FA}}}{C_{\text{MD}}}$. The Bayes-Risk activity decision rule reads

$$\phi^\Omega(L_{n,l}) = \begin{cases} \mathcal{S}_{\hat{\mathbf{x}}_l} \setminus n & \text{if } L_{n,l} \geq \log \frac{1}{\Omega} \\ \mathcal{S}_{\hat{\mathbf{x}}_l} \cup n & \text{if } L_{n,l} < \log \frac{1}{\Omega} \end{cases}. \quad (3.21)$$

Considering (3.21), the estimated support set $\mathcal{S}_{\hat{\mathbf{x}}}$ depends on the particular choice for Ω . Clearly, controlling Ω allows for controlling the activity error rates. Exemplary, decreasing Ω increases the decision threshold, which in turns leads to a higher likelihood that nodes are estimated as active. Conversely, increasing Ω leads to the opposite results, meaning that it is more likely that nodes are estimated as inactive. Setting $\Omega = 1$ turns the decision threshold to 0 corresponding to the MAP decision rule. In terms of *conservative* and *liberal* the parameter Ω allows to seamlessly adjust between both.

¹Likelihood ratio tests are commonly carried out over likelihood functions only. In this case the prior is included inside the test which leads to a slightly different test. However, in this thesis, we stick to the term Likelihood Ratio Test

Pareto Optimality

Even though Bayes-Risk detection allows minimizing one activity error rate to arbitrary low values, one has to keep in mind that the other error rate automatically increases. This is not a surprise, since both error rates are coupled. Such characteristic is known as Pareto Optimality [BV07]. The set of false alarm and missed detection rates that can be achieved by changing Ω forms the so-called Pareto frontier.

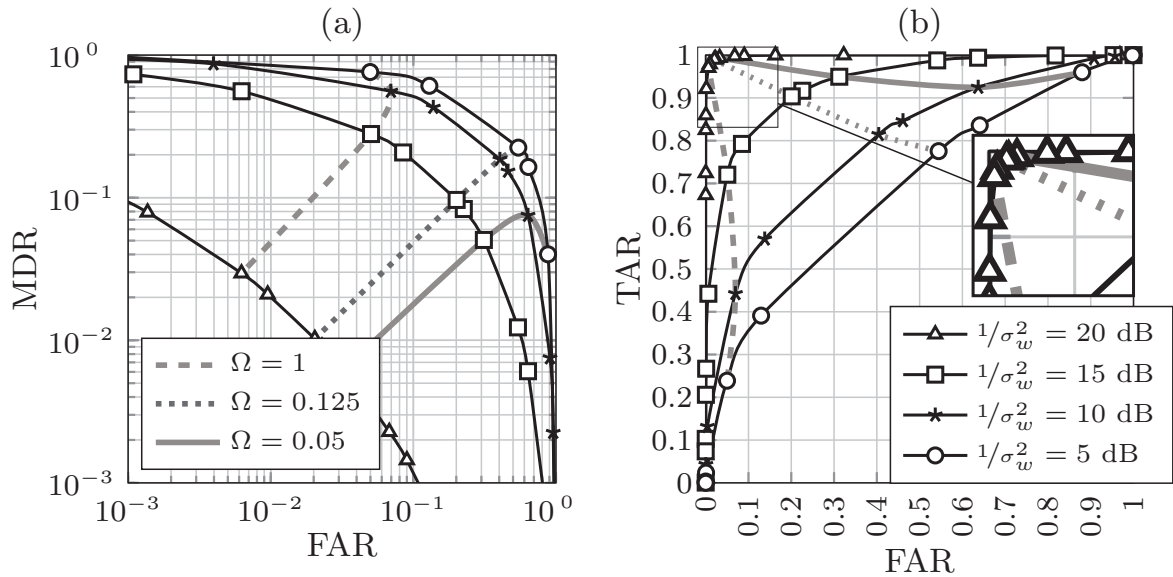


Figure 3.4: Performance of Bayes-Risk activity detection in a system $M = 10, N = 20, p_a = 0.2$. Missed detection rate versus False Alarm rate in (a), and ROC in (b).

Fig. 3.4 (a) exemplarily shows the Pareto frontier for Bayes-Risk activity detection. The solid lines denote the Pareto frontiers for different SNR, where higher SNR generally allows for lower activity error rates. Changing Ω at a given SNR simultaneously changes false alarm and missed detection rates, while the performance follows the Pareto frontier. Here we see that decreasing Ω simultaneously decreases the missed detection rate while the false alarm rate increases. Increasing Ω yields the opposite, an increased missed detection rate and a decreased false alarm rate. In summary we have the following connection between Ω and the activity error rates.

- $\Omega \uparrow \Rightarrow \text{MDR} \uparrow$ and $\text{FAR} \downarrow$
- $\Omega \downarrow \Rightarrow \text{MDR} \downarrow$ and $\text{FAR} \uparrow$

Fig. 3.4 (b) shows the corresponding ROC for different values of Ω and different SNRs. The black solid lines connect points for one particular SNR and different Ω . Following the concept of liberal and conservative

detectors, we see that for each SNR Bayes-Risk detection enables adjusting the detector to be liberal or conservative. Instead of following the path for MAP detection, which was shown to be quite conservative, Bayes-Risk detection allows adjusting the activity error rates. Exemplary, both graphs in Fig.3.4 also plot these paths for different choices of Ω , where $\Omega = 1$ corresponds to MAP detection.

We also observe that for a fixed Ω , activity error rates develop rather uncontrolled with changing SNR, i.e., the particular path for a certain Ω does not follow a predictable path and both activity error rates change with changing SNR. Especially in the low SNR range the path for a fixed Ω is bent.

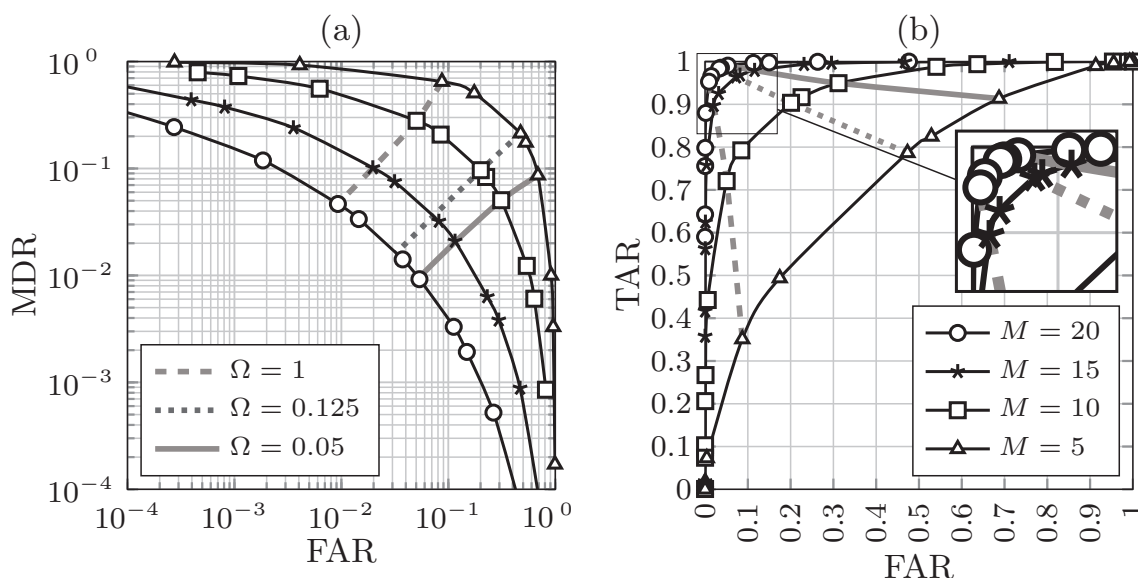


Figure 3.5: Performance of Bayes-Risk activity detection in a system $N = 20, p_a = 0.2$ for varying spreading sequence length M for a fixed SNR = 15dB. Missed detection rate versus False Alarm rate in (a), and ROC in (b).

The impact of overloading on the performance of Bayes-Risk detection is shown in Fig. 3.5 (a) and (b) where the Pareto frontier and the ROC is plotted for different spreading sequence length M with a fixed SNR of 15 dB. Overloading the system decreases the performance and the Pareto frontier shifts towards higher activity error rates in this case. This shift is similar as in Fig. 3.4 (a), suggesting that higher overloading has a similar effect as decreasing the SNR. This effect can also be observed in the ROC in 3.5(b).

Even though Bayes-Risk detection allows controlling the tendency for the activity error rates, it is still far away from a predictable control. The reason for this is twofold. First, the connection between Ω and activity error rate is not known in closed form and one has to simulate all possible rates and

store them in a look-up table. Second, changing the SNR also changes the connection between Ω and the activity error rates.

Frame-Based Transmissions

Extending the Bayes-Risk concept toward frame-based reads

$$\phi^\Omega(L_{n,l}) = \begin{cases} S_{\hat{\mathbf{x}} \setminus n} & \text{if } \sum_l L_{n,l} \geq \log \frac{1}{\Omega} \\ S_{\hat{\mathbf{x}} \cup n} & \text{if } \sum_l L_{n,l} < \log \frac{1}{\Omega} \end{cases}. \quad (3.22)$$

As seen in Section 3.4.1 the bias contained in the frame activity LLRs leads to a high missed detection rate for MAP detection. In the terminology of Bayes-Risk this means we have a conservative detection. However, Bayes-Risk detection allows counteracting this conservative behavior by properly adapting Ω to enable liberal detection. Considering the Pareto frontier in Fig. 3.6 (a) and the ROC in Fig. 3.6 (b) for a frame length of $L_F = 20$ shows the impact of this effect. The Ω required to achieve certain activity error

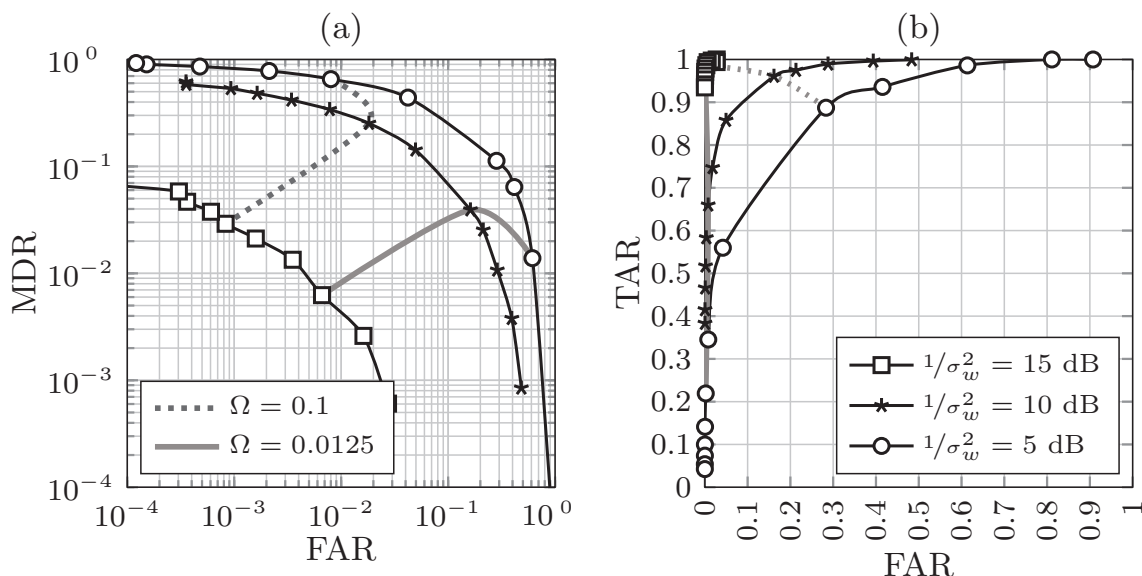


Figure 3.6: Performance of frame-based Bayes-Risk activity detection in a system $M = 10, N = 20, p_a = 0.2, L_F = 20$. Missed detection rate versus false alarm rate in (a), and ROC in (b).

rates has decreased and the point with $\Omega = 1$ is not shown on the Pareto frontier, as the false alarm rate is zero. Comparing the Pareto frontiers for the frame-based detection with symbol-by-symbol detection in Fig. 3.4 (a) shows that the Ω required to control the activity error rates has decreased and much lower values of Ω are required to enable liberal detection. However, even with this conservative impact, we can still trace out the full Pareto

frontier by choosing Ω properly. Comparing the ROC curves in Fig. 3.6 (b) for the frame-based Bayes-Risk to the symbol-by-symbol detection show in Fig. 3.4 (b) shows that we have a SNR gain through the processing of multiple activity LLRs. The ROC curves are shifted to the upper left corner for the frame-based setup. This confirms the results obtained for MAP detection where we have shown that longer frames exhibit SNR gains.

3.4.3 Impact on Subsequent Data Detection

The choice of Ω clearly impacts the subsequent data detection. Choosing Ω too low increases the missed detection errors that can not be compensated at higher layers. On the other hand, increasing Ω decreases the missed detections but also leads to a false alarm SNR loss. However, this SNR loss might be acceptable, especially, if the missed detection rate can be decreased. This depends on the capabilities of the multiuser detector to resolve the multiuser interference of the nodes. We therefore consider a two stage activity and data detector as depicted in Fig. 3.1. Subsequently, we consider two different data-detectors. We compare the performance of a Maximum Likelihood Detection (MLD) that solves the reduced multiuser problem optimally to a least-squares approach, implemented by filtering via the pseudo inverse of the reduced multiuser system (2.21). In contrast to the least-squares data detector, which interprets the reduced multiuser system to be continuous, the MLD approach solves the problem as finite alphabet optimization problem where the modulation symbols are from the set \mathcal{A} . Fig. 3.7 (a) plots the BER over Ω for different SNRs considered for the MLD and 3.7 (b) for the least-squares detector, respectively. As stated in Sub-Section 2.4.2, the BER is defined for active nodes only, such that missed detection errors do not impact the BER. The curves indicate that different data detectors have different demands on Ω . For MLD the optimal value for Ω is slightly below $\Omega = 1$, confirming the result that separate MAP activity detection is not optimal in terms of having the lowest BER with a MLD data detector. To optimize the BER Ω has to be set to values smaller than one, corresponding to rather liberal detection with increased false alarm rate. In this case, MLD gains from the liberal detection even if the SNR is slightly decreased. Subsequently, we observe that for lower SNR the optimal value for Ω further decreases, which is due to the known fact that the MAP activity detection tends to only decide in favor of inactivity. This yields an BER of 100% hence, decreasing Ω automatically decreases the BER.

Almost the same behavior holds true using a least-squares data detector. In this case, the optimal Ω is even lower than for the MLD. However, the general performance is worse as the BER achieved for a particular SNR is

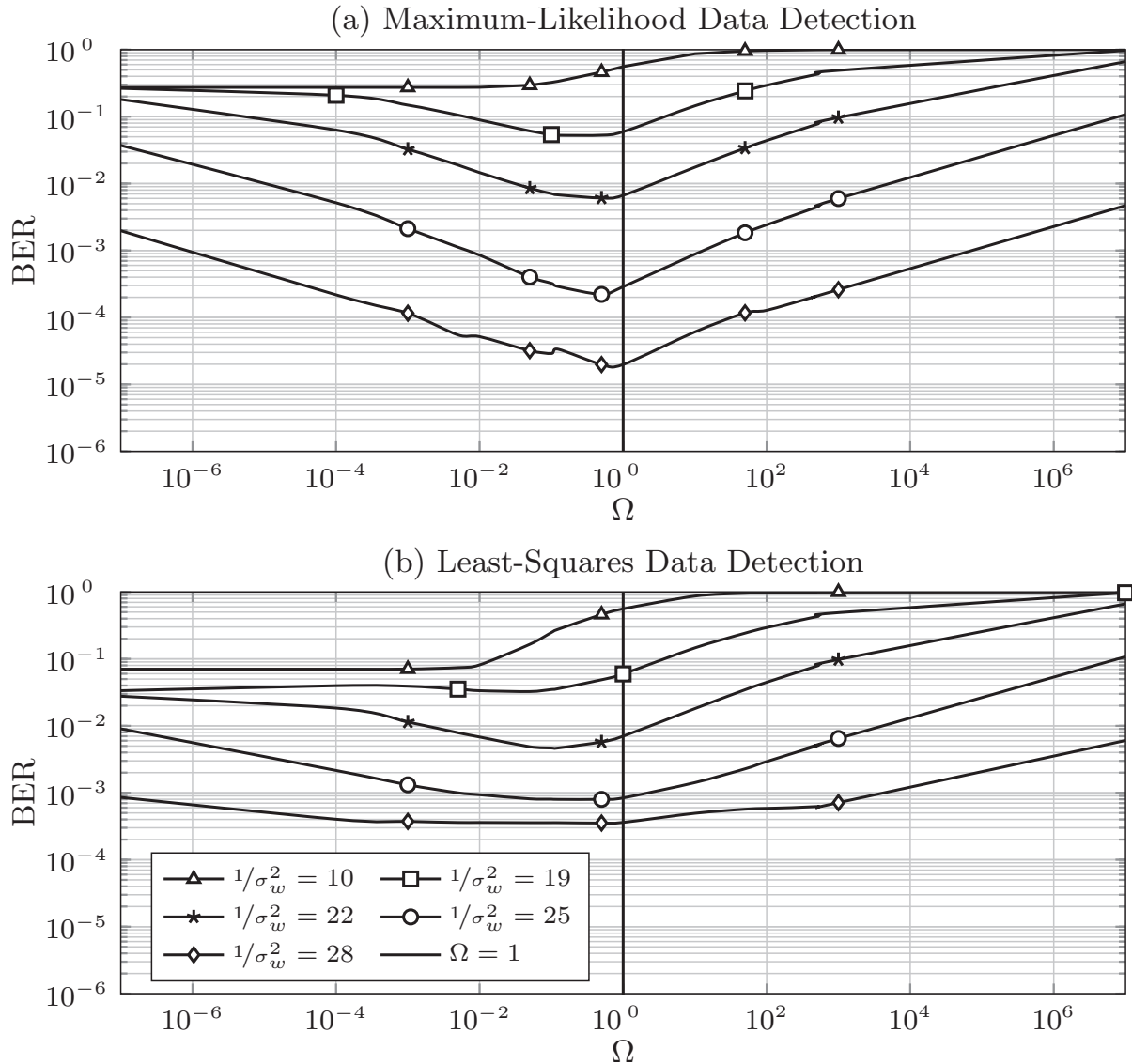


Figure 3.7: BER vs. the choice for Ω for different SNR employing maximum likelihood data detection in (a) and Least-Squares data detection in (b) in a system parametrized by $N = 20$, $M = 10$ and $p_a = 0.2$.

considerably higher. The reason for this is based on the fact the pseudo inverse is a linear detector, whereas MLD is a non-linear detection scheme. In this case, least-squares estimation can better cope with an increased false alarm rate, leading to a lower Ω compared to MLD. Additionally, we observe that the curve flattens out for very high SNR such as $1/\sigma_w^2 = 28$ dB. Changing Ω over a wide range only has moderate impact on the BER. This is based on the fact that a least-squares detector does not restrict to a finite set as the MLD does. The least-squares detector has thereby the capability to estimate the modulation symbol from nodes caused by false alarm to be almost zero. The least-squares detector thereby has the capability to correct

the erroneous activity estimation. If the SNR is very high, the false alarm SNR loss has only a minor impact on the BER for least-squares detection.

3.4.4 The Neyman-Pearson Decision Rule

Even though Bayes-Risk detection allows for a certain activity error rate control, the loose relation between Ω and the resulting activity error rates makes the Bayes-Risk approach hard to fine tune. To overcome these shortcomings, we formulate a new decision rule that a-priori allows controlling the resulting activity error rates. One strategy which is commonly known from literature is the so-called constant false alarm (or constant missed detection) detector. Such a decision rule is strongly related to the so-called Neyman-Pearson decision rule which aims at minimizing one particular error rate, while bounding the other rate to a fixed threshold [NP33, Cho10]. This decision rule depends on the optimal threshold t^* which minimizes one error rate (false alarm or missed detection) while keeping the other rate below a pre-defined threshold η . This threshold is either found in closed form or by optimization.

As an motivating example we consider a scalar binary hypothesis test with the hypotheses H_A and H_I (analog for active and inactive). Further, we assume that it is possible to calculate the posteriori probabilities $\Pr_I(y)$ and $\Pr_A(y)$ for activity and inactivity based on an observation y . Further, we can formulate a likelihood ratio test

$$\frac{\Pr_I(y)}{\Pr_A(y)} \underset{H_A}{\overset{H_I}{\geq}} t, \quad (3.23)$$

with decision threshold $t \geq 0$. The region where (3.23) decides in favor of H_I is parametrized by t and reads $Z_I(t) := \{y : \Pr_I(y) > t\Pr_A(y)\}$. The region, where the test decides in favor of H_A reads $Z_A(t) := \{y : t\Pr_A(y) > \Pr_I(y)\}$. Here we see that the regions in the observation space depend on the choice of t . Consequently, the corresponding false alarm and missed detection probabilities also depend on t .

For our CS-MUD problem we can also express the missed detection and false alarm probability as a function of the regions Z_I and Z_A via

$$\Pr_{\text{MD}}(t) = \Pr(x_{n,l} \in \mathcal{A}) \int_{Z_I(t)} p_{\mathbf{y}_l}(\mathbf{y}_l | x_{n,l} \in \mathcal{A}) d\mathbf{y}_l \quad (3.24a)$$

$$\Pr_{\text{FA}}(t) = \Pr(x_{n,l} = 0) \int_{Z_A(t)} p_{\mathbf{y}_l}(\mathbf{y}_l | x_{n,l} = 0) d\mathbf{y}_l. \quad (3.24b)$$

Note that missed detection and false alarm probabilities now both depend on t , i.e., t is a free parameter to control false alarm and missed detection

probabilities. The optimal threshold t^* minimizes the false alarm or missed detection probability while keeping the counterpart below η . One example of this optimization problem reads

$$\begin{aligned} t^* &= \arg \min_{t \geq 0} \Pr_{\text{FA}}(t) \\ &\text{s.t. } \Pr_{\text{MD}}(t) \leq \eta. \end{aligned} \quad (3.25)$$

In most of the applications, t^* is found by first re-formulating (3.24a) and (3.24b) in closed form which are then used to solve the optimization problem (3.25) yielding t^* . For the multiuser uplink transmission considered here, closed form expressions for missed detection and false alarm probabilities are intractable. Due to the multi-source, multi observation problem each observation y_m contains information about all nodes. To remedy this problem, we now formulate a Neyman-Pearson detector that takes estimates of \Pr_{FA} and \Pr_{MD} based on the activity LLRs instead of the observations \mathbf{y} themselves.

Adaptive Threshold Neyman-Pearson Detection

For the sub-sequent approach we assume that the activity LLRs $L_{n,l}$ are ergodic. More specifically, we assume that the statistical processes generating the activity LLRs have the same moments. If this holds true, we can formulate an adaptive threshold Neyman-Pearson detector as published in [MBD15]. This consists of two steps. First, we take the activity LLRs as samples of false alarm and missed detection probabilities. This turns the integral in the calculation of $\Pr_{\text{MD}}(t)$ and $\Pr_{\text{FA}}(t)$ in (3.24a) into a sum which can numerically be calculated. The second step is to find the proper threshold t^* by solving a discrete version of the optimization problem (3.25). Later it is shown that the discrete approximation is feasible as it converges to the integral if a sufficiently high number of activity LLRs is contained in the calculation.

For the first part the false alarm and missed detection posteriori probabilities are calculated from the activity LLRs via

$$\Pr(x_{n,l} \in \mathcal{A} | L_{n,l}) = \frac{1}{1 + \exp(L_{n,l})} \quad (3.26a)$$

$$\Pr(x_{n,l} = 0 | L_{n,l}) = \frac{1}{1 + \exp(-L_{n,l})}. \quad (3.26b)$$

The idea of adapting the threshold for Neyman-Pearson detection is driven by the idea that multiple activity LLRs describe the same statistical process,

parametrized by p_a . As long as p_a is unchanged, the activity LLRs can be used as samples for the false alarm and missed detection probabilities. These samples can be used for a discrete description of the functionals in (3.25). The idea is to take a set of activity LLRs denoted as \mathcal{L} with cardinality N_L and find the set specific threshold t^* that solves the Neyman-Pearson problem for this set. The size of the set is thereby crucial for the performance. Within this thesis we set $N_L = N$ which means we solve the Neyman-Pearson problem for each received symbol. For frame-based transmissions we sum the activity LLRs up before we process them into the Neyman-Pearson detector. Hence for symbol-by-symbol detection and for frame-based detection $N_L = N$ holds.

To calculate the set specific false alarm and missed detection probabilities, we use a decision rule that is parametrized by the free parameter t

$$\phi^t(L_{n,l}) = \begin{cases} S_{\hat{\mathbf{x}}_l} \setminus n & L_{n,l} \geq t \\ S_{\hat{\mathbf{x}}_l} \cup n & L_{n,l} < t. \end{cases} \quad (3.27)$$

The goal is to find t such that the desired false alarm and missed detection rate is met. The difference to the Bayes-Risk detection rule (3.21) is that we adaptively change t while monitoring false alarm and missed detection probabilities. In contrast to that the Bayes-Risk detection rule pre-defines the threshold without revising it.

Fixing the threshold t to any value separates the set \mathcal{L} of available activity LLRs into two subsets. We define \mathcal{L}_A as the set containing the activity LLRs belonging to active nodes and \mathcal{L}_I as the complementary set containing the LLRs belonging to inactive nodes, respectively. The decision rule $\phi^t(\cdot)$ is used to separate the N_L activity LLRs into the two subsets \mathcal{L}_A and \mathcal{L}_I

Claim 1. *Given the two sets \mathcal{L}_A and \mathcal{L}_I , the false alarm and missed detection probabilities can be estimated via*

$$\tilde{P}_{\text{rMD}}(\mathcal{L}, t) = \frac{\sum_{n \in \mathcal{L}_I} \Pr(x_{n,l} \in \mathcal{A} | L_{n,l})}{|\mathcal{L}_I|} \quad (3.28a)$$

$$\tilde{P}_{\text{rFA}}(\mathcal{L}, t) = \frac{\sum_{n \in \mathcal{L}_A} \Pr(x_{n,l} = 0 | L_{n,l})}{|\mathcal{L}_A|}. \quad (3.28b)$$

With the law of large numbers, the variance of this estimator decreases linearly in the number of elements \mathcal{L}_A and \mathcal{L}_I .

The justification of this approach is given in appendix A.2. Here the subset \mathcal{L}_I contains all activity LLRs above and \mathcal{L}_A contains the all activity LLRs below the current threshold t , respectively. Averaging over the subsets

of activity LLRs \mathcal{L}_A and \mathcal{L}_I yields sample average false alarm and missed detection probabilities. These allow finding the set specific threshold $t_{\mathcal{L}}^*$ such that the sample average false alarm or missed detection probability is minimized while bounding the other one to an upper limit η . As shown in appendix A.2 the sample average false alarm and missed detection probabilities converge to their means (3.24b) (3.24a) if $|\mathcal{L}_A|$ and $|\mathcal{L}_I|$ are sufficiently large. The optimal set specific decision threshold can be found analogous to (3.25) via

$$\begin{aligned} t_{\mathcal{L}}^* &= \arg \min_{t \geq 0} \tilde{\text{Pr}}_{\text{FA}}(\mathcal{L}, t) \\ &\text{s.t. } \tilde{\text{Pr}}_{\text{MD}}(\mathcal{L}, t) \leq \eta, \end{aligned} \quad (3.29)$$

where η is the desired target error rate that must not be exceeded. Note that missed detection and false alarm probabilities can be interchanged in (3.29).

Investigating objective and constraint in (3.29) as functions of t shows that $\tilde{\text{Pr}}_{\text{MD}}(\mathcal{L}, t)$ is strictly decreasing whereas $\tilde{\text{Pr}}_{\text{FA}}(\mathcal{L}, t)$ is strictly increasing. Additionally, $\tilde{\text{Pr}}_{\text{FA}}(\mathcal{L}, t)$ and $\tilde{\text{Pr}}_{\text{MD}}(\mathcal{L}, t)$ are discrete due to the restriction to the set \mathcal{L} . Consequently, t can only take discrete values. Hence t^* is the largest value t that still fulfills the constraint. One possible approach to solve this optimization problem is to try each possible t until the optimal value has been attained. This procedure is illustratively shown in Fig. 3.8. The set specific false alarm and missed detection probabilities change discretely due to the restricted set \mathcal{L} . Consequently, the desired missed detection constraint may not be fulfilled with equality yielding a conservative over fitting.

Additionally, changing t also varies the size of the sets \mathcal{L}_A and \mathcal{L}_I leading to unreliable false alarm and missed detection estimates. In the extreme case at least one of the sets may contain only a few or even none activity LLRs. This effect will be significant, if the activity error rate constraint is very low and makes the detector unreliable.

The Neyman-Pearson detector adaptively changes its threshold based on the activity LLRs. Therefore, it can be interpreted as a Bayes-Risk detector that varies Ω . Thus, this detector traces out the Pareto frontier adaptively.

The false alarm and missed detection rates for two different target missed detection rates are shown in Fig. 3.11. The left plot shows the performance for a target missed detection rate of $\eta = 10^{-1}$. The number of nodes is $N = 20$ and the set of activity LLRs $N_L = N$ is set to the same value such that the threshold is calculated for each symbol. As expected this results in an over-fitting for the missed detection rate which is even more challenging when the missed detection constraint is further decreased as shown in the right plot. The missed detection rate constraint is set to $\eta = 10^{-2}$ resulting in a significant over-fitting in the low and high SNR range. Only in the

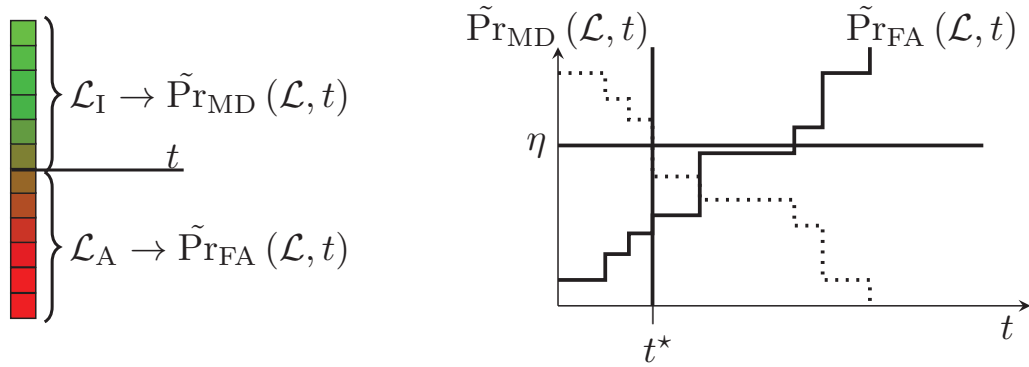


Figure 3.8: Illustration of estimated set specific false alarm and missed detection probabilities with missed detection constraint η and optimal threshold t^* .

mid SNR range, the detector is nearly able to fulfill the missed detection constraint with equality. The reason for this strong over-fitting is based on

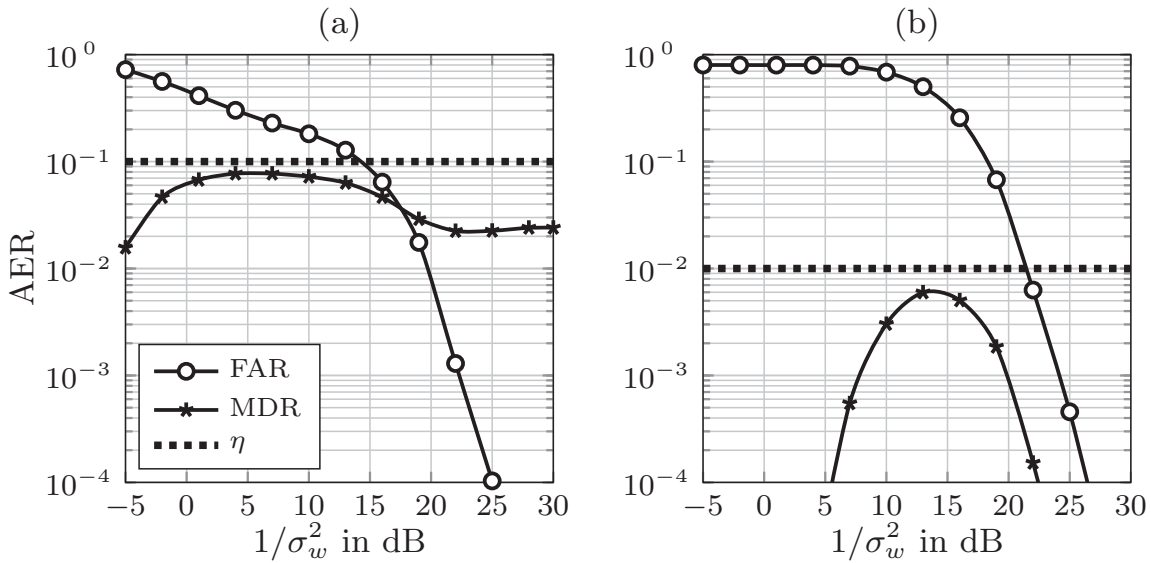


Figure 3.9: Performance of Neyman-Pearson detector in a system with $M = 10$, $N = 20$, $p_a = 0.2$ with missed detection constraint $\eta = 0.1$ (a) and $\eta = 0.01$ (b).

the discrete optimization problem (3.29) being solved.

Test Randomization

As the number of available activity LLRs N_L is limited, test randomization is a powerful approach to boost the performance of Neyman-Person detection. This approach is especially useful in cases where low target error probabilities η are targeted yielding very small sets \mathcal{L}_A or \mathcal{L}_I . For further general infor-

mation about test randomization the reader is referred to [LR05, CK⁺01] and the references therein. Test randomization allows solving the Neyman-Pearson optimization problem even if the constraint is only discrete and cannot be fulfilled with equality. The key is to randomize the mapping rule $\phi^t(\cdot)$ (3.27). To illustrate this idea, we start by considering a set of activity LLRs which we assume to be sorted in ascending order such that $L_1 \leq L_2 \leq \dots \leq L_{N_L}$. To ease notation, we consider the Neyman-Pearson optimization problem in (3.29) where the missed detection probability is constrained to η . Consider two different values for t denoted as t^- and t^+ where t^+ is the threshold yielding an over-fitting of the constraint to $\text{Pr}_{\text{MD}}(t^+) := \eta - \alpha$ and t^- is the first possible threshold yielding a constraint violation by $\text{Pr}_{\text{MD}}(t^-) := \eta + \beta$. Fig. 3.10 shows that the desired sample

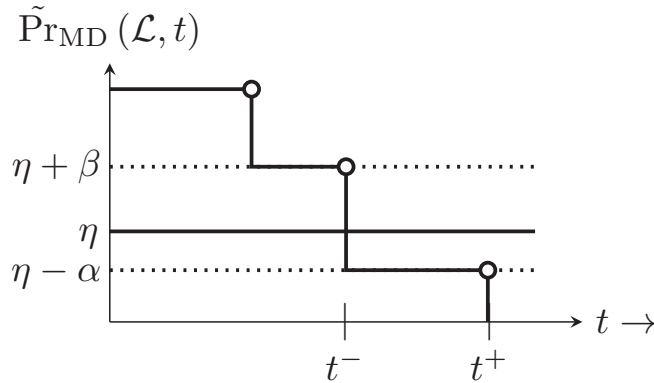


Figure 3.10: Illustration of possible missed detection sample averages

average missed detection probability can not be met by the discrete Neyman-Pearson optimization problem. The goal is to modify the deterministic mapping rule (3.27) into a randomized rule which on average meets the desired missed detection probability [Gal13]. The idea is to introduce a binary random variable κ and form a convex combination of the thresholds t^- and t^+ , which yields the same combination for the probabilities $\text{Pr}_{\text{MD}}(t^-)$ and $\text{Pr}_{\text{MD}}(t^+)$. This *randomized* combination is forced to meet constraint η as

$$\eta \stackrel{!}{=} \kappa \text{Pr}_{\text{MD}}(t^-) + (1 - \kappa) \text{Pr}_{\text{MD}}(t^+) \quad (3.30)$$

$$\Rightarrow \kappa = \frac{\eta - \text{Pr}_{\text{MD}}(t^+)}{\text{Pr}_{\text{MD}}(t^-) - \text{Pr}_{\text{MD}}(t^+)}. \quad (3.31)$$

As a consequence, the constraint can only be met by randomizing the mapping rule such that

$$\phi_{\text{Rand}}^t(L_n) = \begin{cases} S_{\hat{x}} \setminus n & \text{if } L_{n,l} \geq t^+ \\ S_{\hat{x}} \cup n \text{ with Probability } \kappa & \text{if } L_{n,l} = t^- \\ S_{\hat{x}} \cup n & \text{if } L_{n,l} < t^- \end{cases} \quad (3.32)$$

The randomized mapping rule works as follows: the threshold is shifted downwards until t^+ is reached. The next threshold, t^- is only taken with probability κ , i.e., a sample from a Bernoulli process with success probability κ is taken. If the outcome is one, the threshold is set to t^- , if the outcome is zero, the threshold remains unchanged. Eq. (3.30) can now be interpreted as the mean of a Bernoulli process which is set to η . Fig. 3.11 shows the performance of the adaptive threshold Neyman-Pearson detector employing a randomized mapping rule. The impact of test randomization is tremendous,

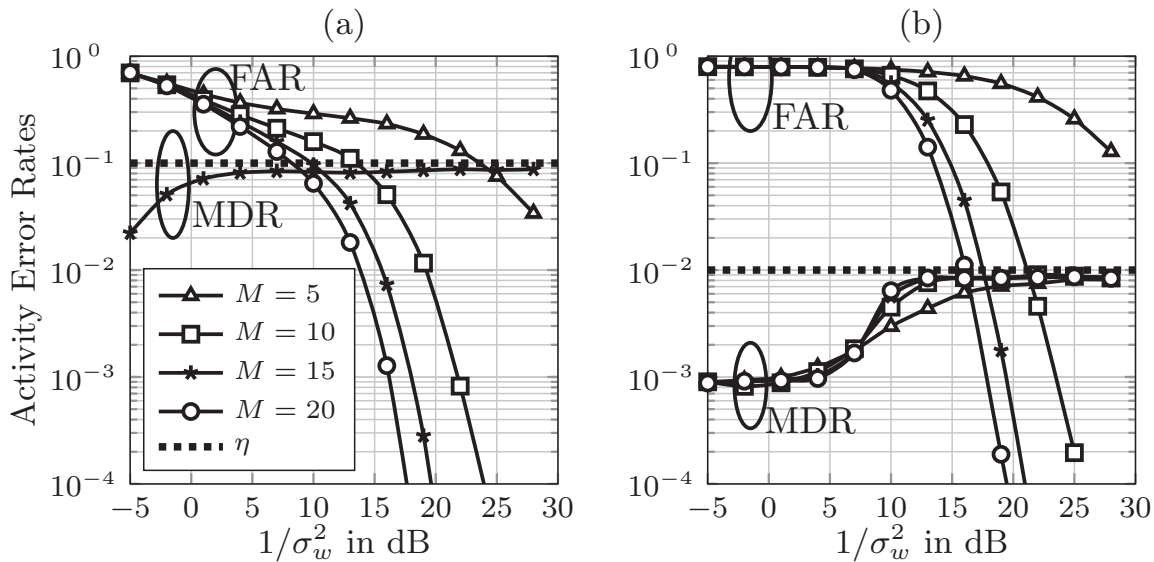


Figure 3.11: Performance of randomized Neyman-Pearson detector in a system with $M = 10$, $N = 20$, $p_a = 0.2$ with missed detection constraint $\eta = 0.1$ (a) and $\eta = 0.01$ (b).

as the missed detection constraint is much tighter fulfilled compared to the detector without randomized mapping rule. For the case with $\eta = 0.1$, the missed detection constraint is slightly over-fitted in the low SNR range and equally fulfilled for the medium and high SNR range. The curves for the missed detection do not differ for varying M . Decreasing the constraint to $\eta = 0.01$ yields an increased over-fitting in the low SNR range which diminishes for medium and high SNRs. Over-fitting in the low SNR range is due to the fact that LLRs are quite unreliable there, making the set specific activity error rate estimates also unreliable.

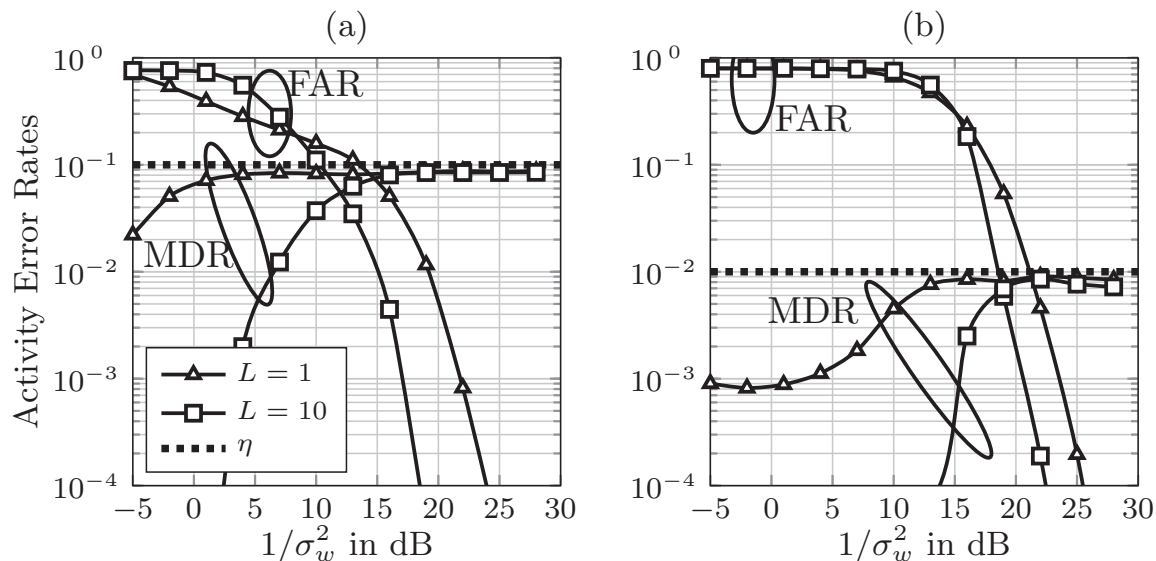


Figure 3.12: Performance of randomized Neyman-Pearson detection in a system with $M = 10$, $N = 20$, $p_a = 0.2$ for different frame length L_F and missed detection constraints $\eta = 0.1$ (a) and $\eta = 0.01$ (b).

Frame-Based Transmissions

Compared to MAP and Bayes-Risk detection Neyman-Pearson exploits the connection between the posteriori probability and the activity LLR. Here the bias of the frame LLRs destroys this connection making Neyman-Pearson detection unreliable for frame-based transmission. Calculating the false alarm and missed detection probabilities from frame activity LLRs is not possible anymore. The bias shifts the activity LLRs towards in-activity yielding a mismatch between the calculated and the true false alarm and missed detection probabilities. More specifically, the missed detection probability is lower than assumed, while the false alarm rate is higher than assumed by the Neyman-Pearson detector. Clearly, this bias could be subsumed into to Neyman-Pearson decision rule to correct the activity LLRs. However, this approach is not considered in this thesis. To show the impact of this bias we apply the randomized Neyman-Pearson decision rule (3.32) to the frame activity LLRs as is. Thus, it is not a surprise that the frame-based Neyman-Pearson detection yields a severe over-fitting in the low and mid SNR range as shown on Fig.3.12(a) and (b). This over-fitting is stronger for the lower missed detection constraint resulting in an increased false alarm rate. This is a consequence of the overfitting and the Pareto optimality of the activity error rates. In the high SNR range the bias diminishes and the activity LLRs are correct. Therefore, the Neyman-Pearson detector achieves a constant missed detection rate in this region. Additionally, the achieved false alarm rate is also lower for the frame-based system compared

to symbol-by-symbol detection shown in Fig. 3.11, showing that gains are achieved by using frame activity LLRs.

3.5 Tree Search Algorithms for Finite Alphabet Compressed Sensing

The core of the previously introduced decision rules was the activity LLR, which turned out to be the result of a penalized integer vector optimization problem stated in (3.7) which has the general form of

$$\min_{\mathbf{x} \in \mathcal{A}_0^N} \|\mathbf{y} - \mathbf{A}\mathbf{x}\|_2^2 + \alpha \|\mathbf{x}\|_0. \quad (3.33)$$

Setting $\alpha = \sigma_w^2 \log \left(\frac{1-p_a}{p_a/|\mathcal{A}|} \right)$ corresponds exactly to the activity LLR optimization problem in (3.7). The constraint for \mathbf{x} obeying to a finite alphabet \mathcal{A}_0^N and the zero-”norm” are casting the problem as a non-convex integer optimization problem which is NP-hard to solve [HV02]. More specifically, the only known complexity bound scales exponential with the size of the input alphabet. A straightforward exponential complexity algorithm is to try each possible \mathcal{A}_0^N candidate vector in a brute force fashion. This approach is clearly not feasible. To still solve (3.33) different approaches exist. A common approach is to relax the non-convex problem to a convex one by replacing the zero-”norm” by its convex hull which is the ℓ_1 -norm. Further, the finite set constraint has to be replaced to be continuous. The resulting optimization problem is commonly known as the Least Absolute Shrinkage and Selection Operator (LASSO) [Tib96] and can be solved in polynomial time. The second approach which is followed in this thesis is to efficiently solve the problem in its non-convex form with sophisticated algorithms commonly known from the field of communications. To this end, tree search algorithms have been identified to be powerful tools that solve (3.7) with a complexity which is often much lower than the exponential bound. Within this work we start with the most prominent example of a tree search algorithm, which is Sphere Decoding.

Sphere Decoding goes back to the works of and Pohst in 1981 [Poh81] and the joint work of Fincke and Pohst in 1985 [FP85]. These first works were rather mathematically motivated and without any practical application in mind. The first application of Sphere Decoding in a practical communication’s context showed up in 1999 in [VB99] where Sphere Decoding was used to decode lattice codes. Later, especially in the Multiple Input Multiple Output (MIMO) era Sphere Decoding was shown to be an efficient way to perform maximum likelihood detection in layered space time codes such as

BLAST [DCB00]. During that time, the Sphere Decoding algorithm was also extended to work hand in hand with a subsequent channel decoder in iterative receiver structures. Instead of calculating the maximum-likelihood estimate, the so-called soft Sphere Decoding algorithm produces soft estimates in the form of LLRs for the underlying transmit bits which can be used as extrinsic information in a channel decoder [VHK04, SBB07, JO05]. Since then, Sphere Decoding has become a standard tool that is widely used in communications.

Sphere Decoding is a tree search approach that restricts the solution to lie within a sphere with a certain radius d around the received vector \mathbf{y} . To start, we first restrict to a non-penalized least-squares problem with full rank system matrix $\mathbf{A} \in \mathbb{R}^{M \times N}$ that is fully or over determined $M \geq N$. In a subsequent step the application to under-determined and regularized problem is shown. To start we consider the full rank least-squares problem, where the solution is restricted to lie within a sphere with radius d . Accordingly, we have

$$\min_{\mathbf{x} \in \mathcal{A}_0^N} \|\mathbf{y} - \mathbf{A}\mathbf{x}\|_2^2 \quad (3.34)$$

$$\text{s.t. } d^2 \leq \|\mathbf{y} - \mathbf{A}\mathbf{x}\|_2^2. \quad (3.35)$$

Introducing the radius d itself does not decrease the complexity for solving (3.35) as checking the constraint is itself exhaustive at first glance. However, methods exist to efficiently check the sphere constraint step-by-step. Moreover, it should be noted that only $d = \infty$ guarantees that the solution to (3.34) corresponds to the solution of the original problem. The key for complexity reduction is to decompose the vector optimization problem and the vector constraint into a set of coupled scalar problems. Therefore, the system matrix is triangularized via the *skinny* QR-decomposition into $\mathbf{Q} \in \mathbb{C}^{M \times N}$ and the upper triangular matrix $\mathbf{R} \in \mathbb{R}^{N \times N}$. Here, \mathbf{Q} contains the basis vectors for the column space of \mathbf{A} . Without changing the optimization problem, we now left multiply the arguments of the ℓ_2 -norms (3.34) and (3.35) with \mathbf{Q}^H and obtain

$$\min_{\mathbf{x} \in \mathcal{A}_0^N} \|\tilde{\mathbf{y}} - \mathbf{R}\mathbf{x}\|_2^2 \quad (3.36)$$

$$\text{s.t. } d^2 \leq \|\tilde{\mathbf{y}} - \mathbf{R}\mathbf{x}\|_2^2, \quad (3.37)$$

with $\tilde{\mathbf{y}} = \mathbf{Q}^H \mathbf{y}$. Thanks to the application of the QR decomposition the calculation of the constraint (3.37) can efficiently be carried out row-by-row also called layer. The calculation of the squared ℓ_2 -norm is thereby decomposed in partial increments also called Partial Euclidian Distance (PED). The main point is that the PED for layer n only depends on the

sub-vector $\mathbf{x}^{(n)} = [x_N, x_{N-1}, \dots, x_n]^T$. To calculate the squared euclidean distance we start at layer N and recursively calculate

$$D_n(\mathbf{x}^{(n)}) = D_{n-1}(\mathbf{x}^{(n-1)}) + \underbrace{\left| y_n - \sum_{i=n}^N r_{n,i} x_i \right|^2}_{\Delta_n(\mathbf{x}^{(n)})}, \quad (3.38)$$

with $D_{N+1}(\mathbf{x}^{(N+1)}) = 0$ and $D_1(\mathbf{x}^{(1)}) = \|\tilde{\mathbf{y}} - \mathbf{R}\mathbf{x}\|_2^2$. The calculation of the squared euclidean distance can thus be geometrically interpreted as a tree with N layers and $|\mathcal{A}_0|^N$ leafs at layer $n = 1$, where each leaf node corresponds to one particular candidate vector. The square in the distance increments $\Delta_n(\mathbf{x}^{(n)})$ makes the PED an increasing sequence. Given any sphere constraint d , it follows immediately, that whenever the PED of any node in the tree violates the sphere constraint, then the PED of all child nodes will violate the sphere constraint as well. Hence, the tree can be pruned above this child node and the PED does not have to be calculated.

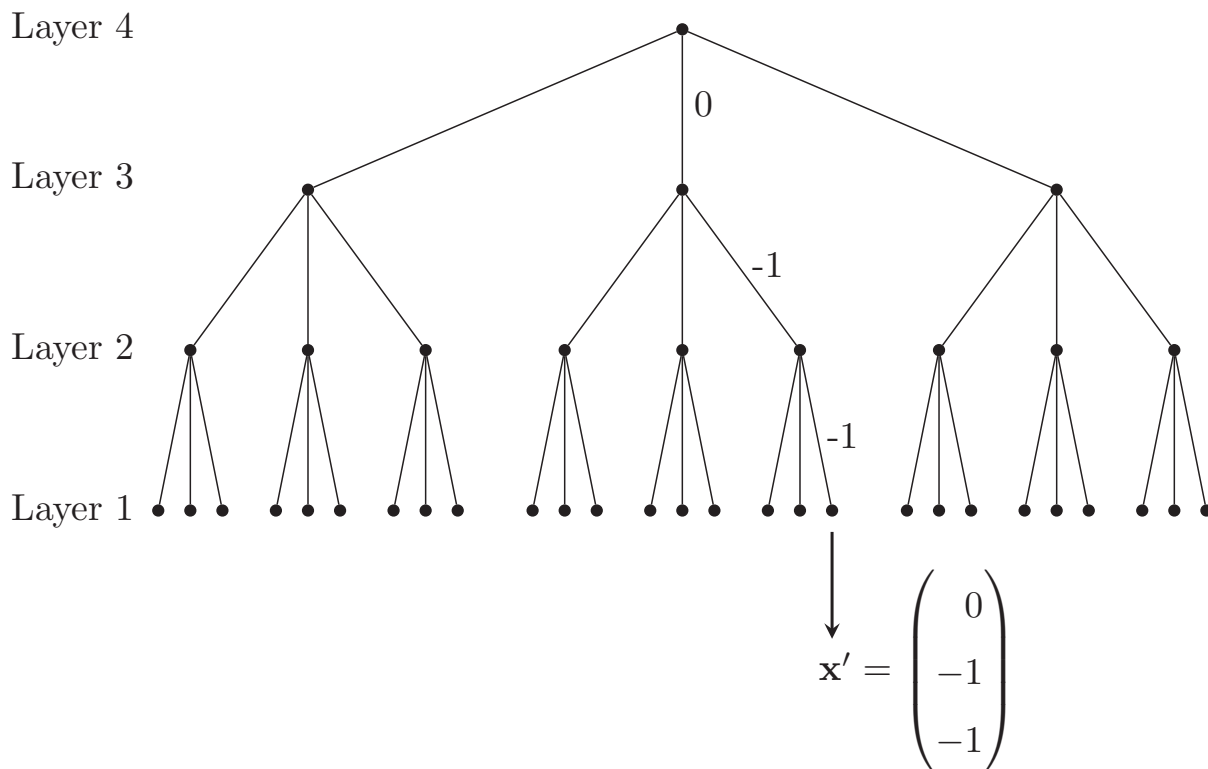


Figure 3.13: Illustration of search tree used for Sphere Decoding.

Schnorr-Euchner Sphere Decoding with Radius Reduction

To obtain the optimal solution for the integer least-squares problem, one has to ensure that the sphere constraint contains this solution. One reasonable

approach for Sphere Decoding is thus, to start with $d = \infty$ and selecting the hypothesis at each layer in ascending order of their PED increments. Once a leaf is reached, the radius is updated to the PED corresponding to this particular path. This so-called *depth first* approach is repeated until only one leaf survives. This leaf will correspond to the optimal solution of the integer least-squares problem. Selecting the hypothesis in ascending order is known as the Schnorr-Euchner method [SE94]. Besides this search strategy, other tree traversing strategies exist. A great overview about tree traversing strategies is given in [Stu09] and the references therein. The Sphere Decoding algorithm with initial radius set to infinity guarantees to find the optimal solution. The downside is, that the complexity can only be bounded via the exponential bound determined by exhaustive search. Even though, Sphere Decoding is much faster in most of the cases, the complexity and the throughput are random without a polynomial bound on complexity.

K-Best Detection

The random runtime and throughput of Sphere Decoding makes this approach hard to implement. To this end, suboptimal but constant throughput tree traversing strategies exist. One of these tree traversing strategy with polynomial complexity and good adaptivity between optimality and speed is the K-Best approach. K-Best detection is a breadth first tree traversing strategy that starts at the highest layer N [BBW⁺05, Stu09] similar to Sphere Decoding. From this point, the K-Best algorithm calculates the PEDs of all paths and retains only K_{best} paths with the K_{best} lowest accumulated PEDs. Once Layer 1 is reached, the algorithm is terminated and the leaf with the lowest accumulated PED corresponds to the estimate of the algorithm. Clearly with any $K_{\text{best}} < |\mathcal{A}_0|^N$ this approach is sub-optimal. However, later simulations show that K-Best detection with reasonable K_{best} is indeed a suitable alternative for Sphere Decoding. Compared to Sphere Decoding, K-Best detection allows for a constant throughput and a polynomial complexity.

Successive Interference Cancellation

In the special case of a K-Best detector with $K_{\text{best}} = 1$ the algorithm is commonly known as Successive Interference Cancellation. In this case only the best hypothesis (in terms of lowest PED) is evaluated. As simulations will show, SIC sacrifices optimality especially in highly overloaded systems, such that its application for CS-MUD is almost not relevant.

Sorting

Sorting the detection order is a powerful tool to decrease the complexity of Sphere Decoding and to enhance the performance of sub-optimal approaches such as K-Best. The core idea is to change the ordering of the layers such that layers with high SNR are detected first. If these layers are detected correctly, the likelihood of errors at lower layers is decreased as errors made at higher layers propagate through the tree. Sorting thereby enhances the performance for sub-optimal algorithms such as K-Best. For Sphere Decoding, sorting does not affect the performance, but greatly improves the runtime of the algorithm. The sorting is carried out via a modified version of the QR decomposition, also known as Sorted QR decomposition (SQRD) [WBR⁺01] which is entirely used for the tree search algorithms used within this thesis.

3.5.1 Tree Search for Under-Determined Systems

Transferring tree search algorithms to penalized under-determined systems is twofold challenging. First, the application of the QR decomposition is problematic as the system matrix cannot be brought into an upper diagonal form. Second, the penalty term in (3.33) has to be taken into regard.

The first problem becomes more obvious by considering the QR decomposition of any $M \times N$ matrix. With $M < N$, the corresponding \mathbf{R} matrix has the following form

$$\mathbf{R} = \begin{pmatrix} r_{1,1} & r_{1,2} & \cdots & \cdots & \cdots & r_{1,N} \\ 0 & r_{2,2} & \cdots & \cdots & \cdots & r_{2,N} \\ 0 & 0 & \ddots & \cdots & \cdots & \vdots \\ 0 & 0 & \cdots & r_{M,M} & \cdots & r_{N,N} \end{pmatrix} \quad (3.39)$$

Equation (3.39) shows that the row-by-row calculations of the PED is not possible anymore since the last row (corresponding to Layer N) already depends on a sub-vector containing $N - M$ elements. One possible approach to overcome this effect is to insert $N - M$ zero-rows in the matrix \mathbf{R} and in the observation vector \mathbf{y} . While doing so, the PEDs for layer N up to layer $N - M$ denoted as $D_{N-M}(\mathbf{x}^{(N-M)}) = 0$ turn zero. In this case, the Sphere Decoding algorithm will still find the optimal solution by brute-forcing these layers yielding increased complexity.

A more elegant approach to fully triangularize the matrix is to exploit the penalty term in (3.33) such that the matrix \mathbf{R} turns to be upper triangular. To do so, we restrict the following analysis to constant modulus source data,

i.e., $|x_k| = c \forall x_k \in \mathcal{A}$. This defines the modulation set to Phase Shift Keying (PSK) which may be an acceptable restriction for low-rate M2M traffic. With this restriction, it is possible to replace the penalty term based on the l_0 -”norm” by any norm $\|\mathbf{x}\|_0 = \|\mathbf{x}\|_1 = \|\mathbf{x}\|_2^2 \Leftrightarrow |s_k| = 1 \forall k$. The penalized least-squares problem can then be transformed as

$$\begin{aligned}
\hat{\mathbf{x}} &= \arg \min_{\mathbf{x} \in \mathcal{A}_0^K} \|\mathbf{y} - \mathbf{A}\mathbf{x}\|_2^2 + \alpha \|\mathbf{x}\|_0 \\
\hat{\mathbf{x}} &= \arg \min_{\mathbf{x} \in \mathcal{A}_0^K} \|\mathbf{y} - \mathbf{A}\mathbf{x}\|_2^2 + \alpha \|\mathbf{x}\|_0 + \delta \|\mathbf{x}\|_0 - \delta \|\mathbf{x}\|_0 \\
\hat{\mathbf{x}} &= \arg \min_{\mathbf{x} \in \mathcal{A}_0^K} \|\mathbf{y} - \mathbf{A}\mathbf{x}\|_2^2 + \delta \|\mathbf{x}\|_0 + [\alpha - \delta] \|\mathbf{x}\|_0 \\
\hat{\mathbf{x}} &= \arg \min_{\mathbf{x} \in \mathcal{A}_0^K} \|\mathbf{y} - \mathbf{A}\mathbf{x}\|_2^2 + \delta \|\mathbf{x}\|_0^2 + \underbrace{[\alpha - \delta]}_{\Sigma} \|\mathbf{x}\|_0 \\
\hat{\mathbf{x}} &= \arg \min_{\mathbf{x} \in \mathcal{A}_0^K} \left\| \begin{bmatrix} \mathbf{y} \\ \mathbf{0}^N \end{bmatrix} - \begin{bmatrix} \mathbf{A} \\ \sqrt{\delta} \mathbf{I}_N \end{bmatrix} \mathbf{x} \right\|_2^2 + \Sigma \|\mathbf{x}\|_0 \quad \delta \geq 0. \tag{3.40a}
\end{aligned}$$

Eq. (3.40a) contains $\delta \geq 0$ as a free parameter that can be used to regularize the augmented system matrix to have full rank. Then QR decomposition leads to an upper triangular matrix \mathbf{R} . For any $\alpha \geq 0$, this parameter can be chosen as $\delta = \alpha$, which is a convenient choice as the penalty term turns to zero and the whole optimization problem is implicitly regularized. For any $\alpha < 0$, however, this is not possible anymore as $\delta \geq 0$ has to hold meaning that the penalty term remains negative which violates the condition of positive PEDs. With possibly negative PEDs, Sphere Decoding is not guaranteed to optimally solve the problem anymore.

In the following we show how (3.40a) still can be re-written such that the penalty term remains positive. To enable Sphere Decoding the penalty term $\Sigma = \alpha - \delta$ has to be greater or equal zero. Without changing the optimization problem, (3.40) is rewritten with an equivalent positive penalty term even if $\Sigma < 0$ holds. The key point is that we subtract the magnitude of Σ and add the constant $|\Sigma|N$ to the problem. This does not change the output of the optimization problem. After re-arranging, $[N - \|\mathbf{x}\|]$ can be written as a sum of indicator functions $\mathbf{1}_0(\cdot)$, which returns a one if the

argument is zero and a zero otherwise. For $\Sigma < 0$ we obtain

$$\begin{aligned}\hat{\mathbf{x}} &= \arg \min_{\mathbf{x} \in \mathcal{A}_0^N} \left\| \begin{bmatrix} \mathbf{y} \\ \mathbf{0}^N \end{bmatrix} - \begin{bmatrix} \mathbf{A} \\ \sqrt{\delta} \mathbf{I}_N \end{bmatrix} \mathbf{x} \right\|_2^2 - |\Sigma| \|\mathbf{x}\|_0 + |\Sigma| N \\ &= \arg \min_{\mathbf{x} \in \mathcal{A}_0^N} \|\mathbf{y}' - \mathbf{A}' \mathbf{x}\|_2^2 + |\Sigma| [N - \|\mathbf{x}\|_0] \\ &= \arg \min_{\mathbf{x} \in \mathcal{A}_0^N} \|\mathbf{y}' - \mathbf{A}' \mathbf{x}\|_2^2 + |\Sigma| \sum_{n=1}^N \mathbf{1}_0(x_n),\end{aligned}\quad (3.41)$$

where the penalty term is always positive and penalizes the zero symbol. Comparing (3.41) and (3.40) shows that the penalty term in both problems can be summarized as

$$f_p(\mathbf{x}, \Sigma) = \begin{cases} \sum_{n=1}^N \Sigma \mathbf{1}_{\mathcal{A}}(x_n), & \text{if } \Sigma \geq 0, \\ \sum_{n=1}^N |\Sigma| \mathbf{1}_0(x_n), & \text{if } \Sigma < 0, \end{cases}\quad (3.42)$$

yielding

$$\hat{\mathbf{x}} = \arg \min_{\mathbf{x} \in \mathcal{A}_0^N} \|\mathbf{y}' - \mathbf{A}' \mathbf{x}\|_2^2 + f_p(\mathbf{x}, \Sigma),\quad (3.43)$$

where $f_p(\cdot, \cdot) \geq 0$ is positive and reflects the penalty term. The PEDs can now be calculated according to (3.38) via

$$D_n(\mathbf{x}^{(n)}) = D_{n-1}(\mathbf{x}^{(n-1)}) + \underbrace{|y_n - \sum_{i=n}^N r_{n,i} x_i|^2 + f_p(\mathbf{x}^{(n)}, \Sigma)}_{\Delta_n(\mathbf{x}^{(n)})},\quad (3.44)$$

where the distance increments $\Delta_n(\mathbf{x}^{(n)})$ remain positive which allows for application via Sphere Decoding or any other tree search approach such as K-Best.

3.5.2 Performance Evaluation

K-Best vs. Sphere Decoding

In the following we analyze the performance and the complexity of Sphere Decoding and K-Best detection. To assess the performance, we consider the activity LLRs that the corresponding algorithm generate and look at the Pareto frontiers. These will show the performance loss of K-Best detection while having Sphere Decoding as benchmark.

Fig. 3.14 shows the Pareto frontiers achieved with K-Best detection in differently overloaded systems with $\Omega \in [10^{-8}, \dots, 10^8]$. Considering Fig. 3.14

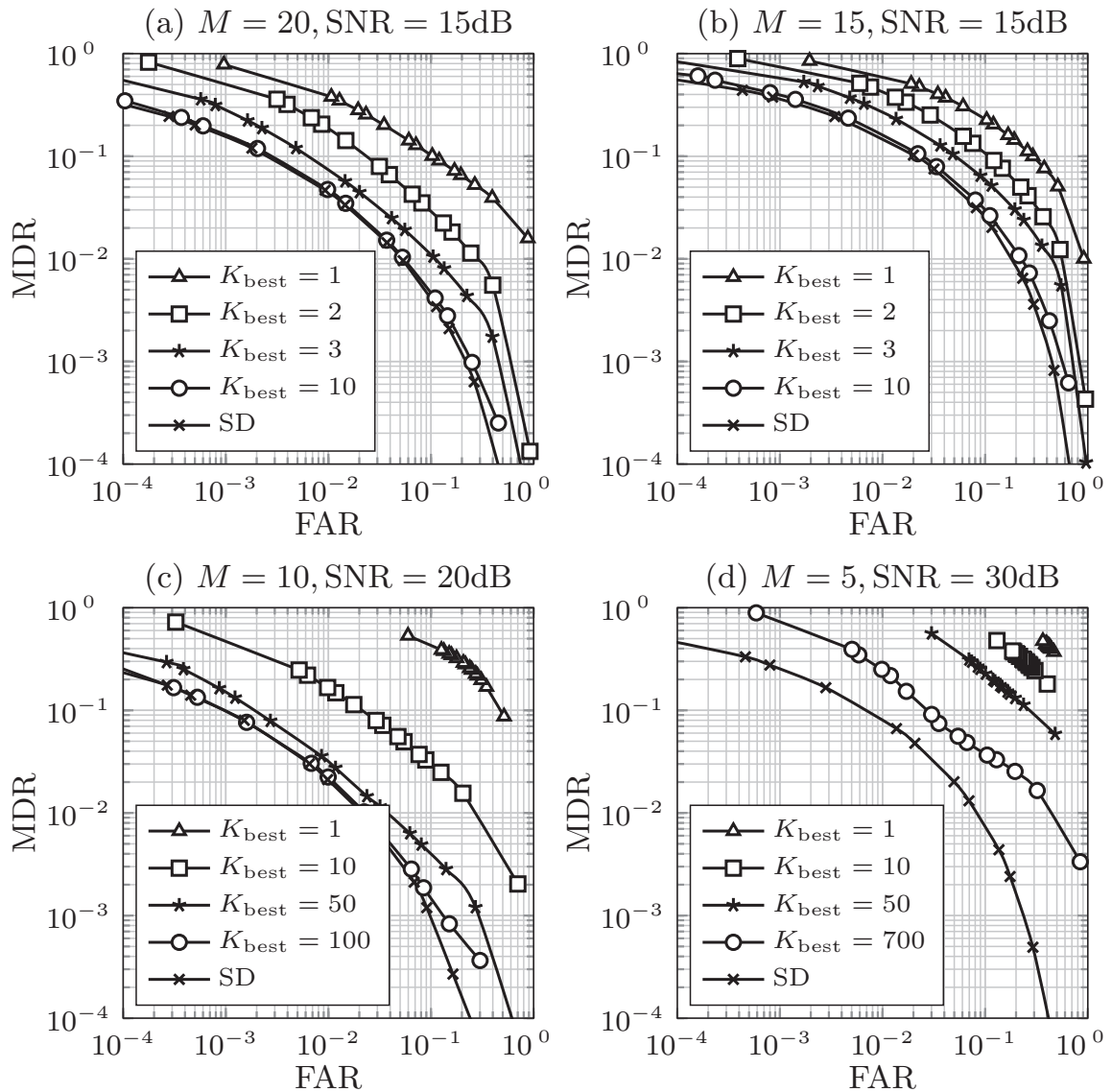


Figure 3.14: Pareto Frontiers for K-Best detection with varying parameter K_{best} compared to Sphere Decoding (Sphere Decoding) in a system with $N = 20, p_a = 0.2$ with different spreading sequence length $M = 20$, $\text{SNR} = 15$ dB in (a), $M = 15$, $\text{SNR} = 15$ dB in (b), $M = 10$, $\text{SNR} = 20$ dB in (c), $M = 5$, $\text{SNR} = 30$ dB in (d).

(a) shows the performance of the fully determined system. Here we see that with low $K_{\text{best}} = 1$ the loss encountered is about one order of magnitude in false alarm and missed detection rates. Increasing K_{best} already decreases this degradation until $K_{\text{best}} = 10$ achieves the same performance as Sphere Decoding with diminishing losses. Investigating systems that have a higher overloading such as shown in Fig. 3.14 (b)-(d), shows that this does not in general apply for under-determined systems. While with $M = 15$ $K_{\text{best}} = 10$ still achieves the performance of Sphere Decoding, decreasing the number of observations down to $M = 10$ as in Fig. 3.14 (c) $K_{\text{best}} = 100$ is required

which is a tremendous increase compared to the fully determined system. Fig. 3.14 (d) shows the extreme case, with only $M = 5$ observations. Here even very high values like $K_{\text{best}} = 700$ do not achieve the performance of Sphere Decoding. Especially in the highly overloaded case the Pareto frontier is quite short, i.e., it does not cover the whole range of false alarm and missed detection rates. It seems that varying Ω does not change false alarm and missed detection rates as it does for the activity LLRs obtained from Sphere Decoding.

The reason for this can be found by considering the calculation of the activity LLRs. While Sphere Decoding calculates the activity LLRs optimally, K-Best detection does this only approximatively. Especially if the system is highly overloaded and K_{best} is set to low values. This effect can be observed when comparing the Probability Density Function (PDF) of the activity LLRs for Sphere Decoding and K-Best detection. The PDF of the activity LLRs calculated by Sphere Decoding and K-Best detection for the system with only $M = 5$ observations are shown in Fig. 3.15. We see that the PDF of the activity LLRs for the Sphere Decoding is bimodal with support between $L \in [-20, 20]$. Comparing the PDFs from K-Best detection with the PDF achieved by Sphere Decoding, shows that only $K_{\text{best}} = 700$ resembles the activity LLR PDF of Sphere Decoding. Decreasing K_{best} broadens the PDF until for $K_{\text{best}} = 10$ the PDF is nearly flat with increased support compared to Sphere Decoding. Clearly, changing the quantization threshold in the activity LLRs has lower impact if the PDF has a wide support. Concluding that K-Best detection is only suitable if the number of observations is not too low.

3.5.3 Complexity Analysis

Analyzing the complexity of Sphere Decoding can only be carried out in terms of statistics. This is due to the fact, that the complexity of Sphere Decoding is a random variable. Henceforth, complexity is often analyzed in terms of average number of nodes the algorithm visits. This analysis is rather of high level as the number of multiplications or flops is not considered. However, visiting a node requires calculating the PEDs of the corresponding \mathcal{A}_0 leafs of that node. Thus, the number of visited nodes scales in the same manner as the number of multiplications required. To demonstrate the complexity of Sphere Decoding, we consider solving (3.7) for a single activity LLR. Calculating this activity LLR requires solving two instances of the under-determined and penalized integer least-squares problem. The penalty term reflecting the prior knowledge is subsumed via α . In the following analysis we restrict the calculation to a single instance of this

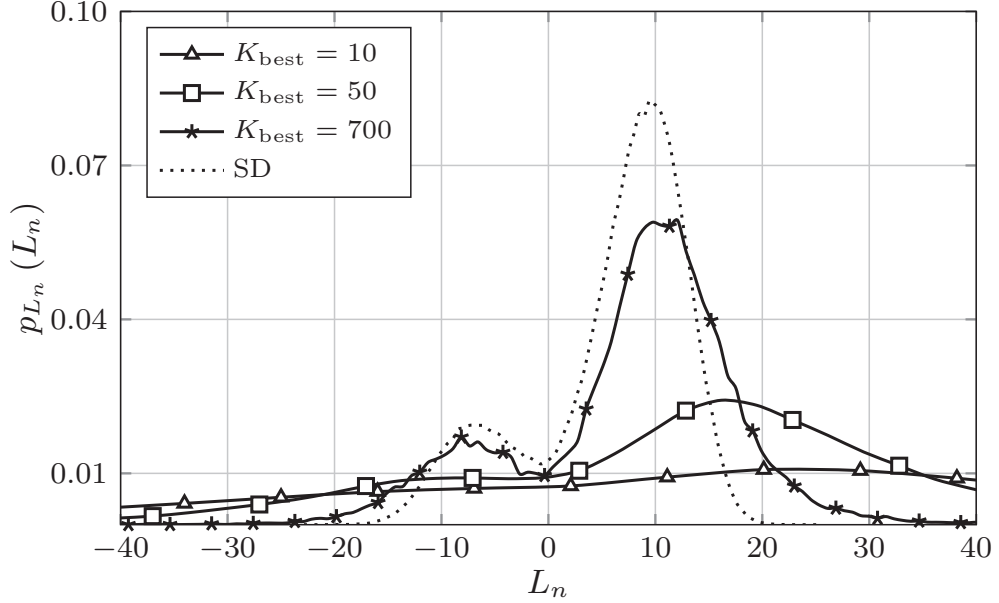


Figure 3.15: PDF of the activity LLRs for K-Best detection in a system with $M = 5$, $N = 20$, $p_a = 0.2$ at a SNR of $1/\sigma_w^2 = 30\text{dB}$

optimization problem. Thus, the following results have to be multiplied by two in order to obtain the complexity for calculating one activity LLR. Fig. 3.16 plots the average number of visited nodes over the SNR for different numbers of observations. In the low SNR range the number of visited nodes is 20 for all cases considered. This is due to the fact that in low SNR α dominates the optimization problem due to the dependency of σ_w^2 . Thus, the all-zero vector is always the optimal solution to the optimization problem and the PEDs are dominated by the impact of α . In this case the Sphere Decoding traverses the tree only once. In higher SNR the number of visited nodes heavily depends on the overloading of the system. For the fully determined system, the number of visited nodes exhibits a peak and decreased again down to 20. This does not hold not true for systems with lower number of observations. Here, the number of visited nodes increases in the same manner in the mid range SNR, but the decrease cannot be observed. The reason for this lies in the prior knowledge that depends on the noise power. In the low and mid SNR range the prior knowledge is exploited to implicitly regularize the under-determined system matrix. With decreasing α , the lower $M - N, \dots, N$ rows in the matrix \mathbf{R} converge to zero. If this happens, the PEDs for the layers $N, \dots, M - N$ converge to zero $D_{N-M} \rightarrow 0$. That means the Sphere Decoder algorithm cannot reasonably estimate the sub-vector $\mathbf{x}^{(N-M)}$. For the first Sphere Decoding iterations the estimate for the sub-vector $\mathbf{x}^{(N-M)}$ is merely a random guess. This guess is most likely incorrect and causes interference at the lower layers and the Sphere Decoding

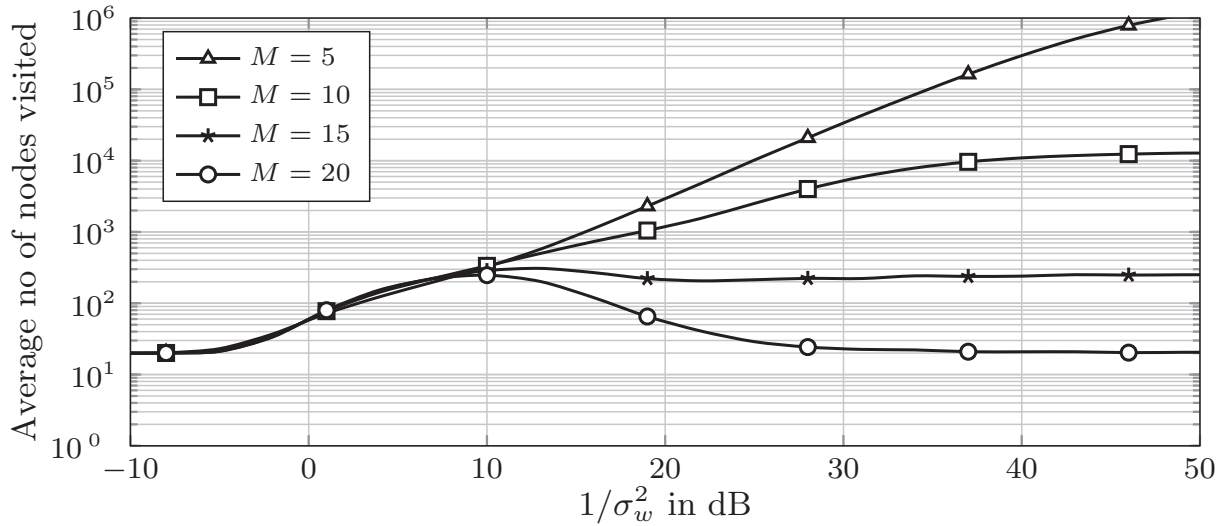


Figure 3.16: Average number of visited nodes for Sphere Decoding in a system with $N = 20$, $p_a = 0.2$ with varying number of observations M , with implicit regularization.

algorithm has to run longer until the interference is canceled. In the extreme case with $\alpha = 0$ the Sphere Decoding still finds the optimal solution but brute forces the layers $N, \dots, M + 1$, leading to increased complexity, especially if the system is highly overloaded such as $M = 5$.

Sphere Decoding vs. K-Best Detection

The K-Best algorithm instead allows for a fixed complexity, which solely depends on the dimensions of the underlying tree. This tree is only determined by the number of layers, corresponding to N and the cardinality of the augmented modulation alphabet $|\mathcal{A}_0|$. At layer n , the K-Best algorithm visits at most K_{best} nodes. If the number of nodes at layer n is lower, the K-Best algorithm only visits $|\mathcal{A}_0|^{N-n}$ nodes, corresponding to the maximum number of nodes at layer n . The number of nodes for K-Best detection thus reads

$$\sum_{n=1}^N \min [K_{\text{best}}, |\mathcal{A}_0|^{N-n}], \quad (3.45)$$

which, is in contrast to Sphere Decoding, a fixed number. With (3.45) and the complexity analysis for Sphere Decoding, a certain break-even point where K-Best detection outperforms Sphere Decoding in terms of complexity exists. We therefore consider the Pareto frontiers given in Fig. 3.14 and consider the value K_{best} where K-Best detection achieves the same performance as Sphere Decoding. Further, we define the K_{best} -SD break even point,

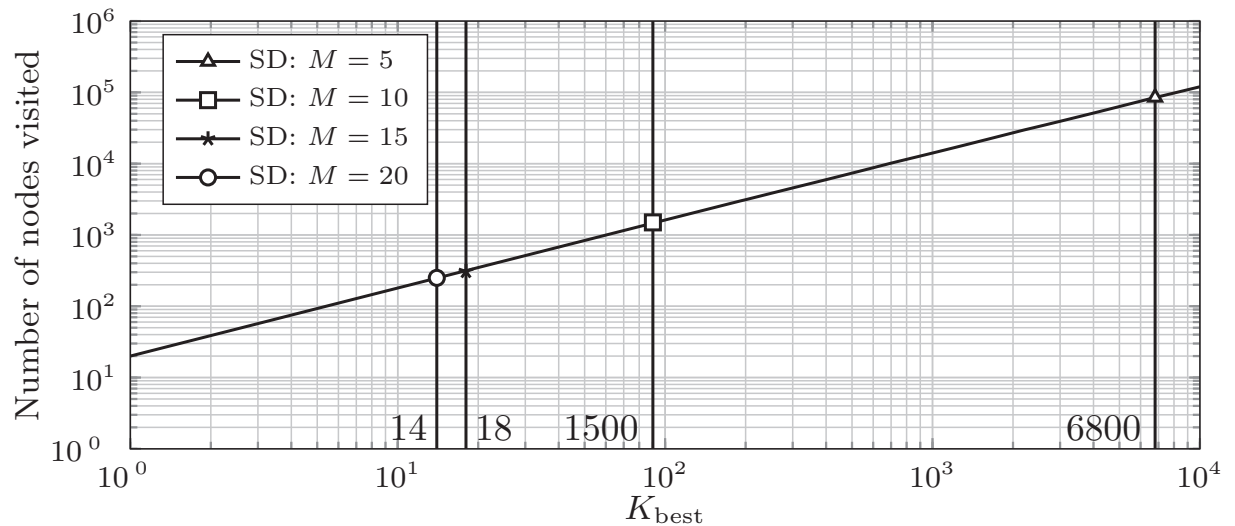


Figure 3.17: Number of visited nodes versus K_{best} for a system with $N = 20$ nodes and a varying number of observations.

denoting the value K_{best} where a K-Best detector has the same complexity as a Sphere Decoder. If the number of nodes a K-Best detector visits is below this point, we assume that K-Best detection is feasible. Fig. 3.17 plots the number of nodes visited versus K_{best} for a system with $N = 20$ nodes according to (3.45), which is a straight line. In contrast to that, the complexity of Sphere Decoding depends on the number of observations M and the particular SNR. Thus, the points on the line in Fig. 3.17 denote the maximum average number of nodes a Sphere Decoder requires for a given M . Hence, the corresponding value on the x-axis denotes the K_{best} -SD break-even point.

These values are summarized in Table 3.1. In all cases considered, the K_{best} that is required to nearly achieve the performance of Sphere Decoding lies below the break-even point, showing that K-Best detection is indeed a viable approach to nearly achieve the performance of Sphere Decoding with lower complexity.

M	K_{best} required according to Fig. 3.14	K_{best} -SD break-even
5	> 700	6800
10	100	1500
15	10	18
20	10	14

Table 3.1: Comparison of K_{best} required and the K-best Sphere Decoding break-even point for different numbers of observations M .

3.6 Chapter Summary

Within this chapter we have focused on the sole activity detection task with a communication's perspective via activity Log-Likelihood ratios. The activity estimation task was carried out by defining a decision rule where activity or inactivity is estimated. Motivated by the fact that the well known MAP decision rule exhibits unacceptable high missed detection rate, this chapter introduces two subsequent activity detection rules. Namely, the Bayes-Risk rule as a generalization of the MAP rule and the Neyman-Pearson decision rule. The Bayes-Risk decision rule represents a generalized MAP decision rule by allowing to weight between false alarm and missed detection errors. The Bayes-Risk detector can be tuned to rather decide in favor of activity or inactivity, thereby, increasing one activity error rate while decreasing the other. Implementing the Bayes-Risk detector is intricate as the dependence between weight and resulting activity error rate is not known in closed form and has to be simulated. The impact of Bayes-Risk detection on the data detection and the BER shows two important results. First, optimizing the activity error rates has to be seen in conjunction with the particular algorithm used for data detection. Slightly increasing the false alarm rate improves the BER despite of the false alarm SNR loss.

Further, the Neyman-Pearson detector is shown to allow for a constant false alarm or constant missed detection rate. For Neyman-Pearson detection one activity error rate is fixed, while the other error rate is minimized. The derivation is done by taking the activity LLRs as an input statistic to the detector. Based on this statistic the Neyman-Pearson detector estimates the threshold such that the desired activity error rates are met. While this decision rule suffers from being too conservative, a randomized Neyman-Pearson detector is introduced. Here the decision rule is augmented by a random variable which allows to better achieve the desired target error rate.

Simulations show that the randomized Neyman-Pearson detector achieves a constant missed detection rate while simultaneously minimizing the false alarm rate.

Additionally, this chapter addresses the calculation of the activity LLR via Sphere Decoding. Here it is shown that the underlying penalized optimization problem is undetermined. Hence, a direct implementation via Sphere Decoding is not possible. Therefore, it is shown that the penalty term can be used to rewrite the problem as an overdetermined set of equations which allow for implementation via Sphere Decoding. Beyond sole Sphere Decoding also K-Best detection is introduced as a means to calculate the activity LLR with lower complexity than Sphere Decoding. While K-Best detection sacrifices optimality by approximating the problem, it is still shown that K-Best detection with reasonable low K_{best} nearly achieves the performance of Sphere Decoding.

Chapter 4

Graphical Models for CS-MUD

4.1 Overview

The previous chapter mainly focused on separate activity and data detection. As the results have shown, this approach is twofold challenging. First, the hard activity detection affects the data detection and the interplay between both entities has to be tuned in order to match system specific requirements. Second, the detection in frame-based systems is sub-optimal due to the bias of the frame activity LLRs. Within this chapter we address both challenges and derive a detector that considers the activity and data detection task jointly in an iterative soft information framework without hard estimates. Moreover, we address the question of how channel coding and knowledge of frame activity can jointly be exploited to enhance the detection performance. The track followed is based on belief propagation (also message passing) and the sum-product algorithm. This allows factorizing the joint activity and data detection problem graphically which allows for a decomposition of the estimation problem into factor nodes and variable nodes. The desired soft information can efficiently be calculated by exchanging messages between factor and variable nodes.

Main Contribution

The novelty of the work presented in this chapter is to apply belief propagation to frame-based CS-MUD including channel coding and frame activity information. As shown in Fig. 4.1, this approach consists of three building

blocks that exchange extrinsic information. The first block is the multiuser detector that estimates the multiuser symbols \mathbf{x} based on the observations given by the channel \mathbf{y} which is presented in Subsection 4.3.2. Here we mainly adapt the recent advances of [Sch10] to resolve multiuser interference. The multiuser detector itself does not exploit information about the channel code and about frame activity.

The main contribution of this chapter is given in given in Subsection 4.3.4 where L_F multiuser detectors are combined with a bank of channel decoders and a bank of activity estimators called Sparsity Pattern Equalizer (SPE). The bank of channel decoders is composed of N individual decoder instances that individually decode the information words for all nodes in the system. The same holds true for the bank of SPE.

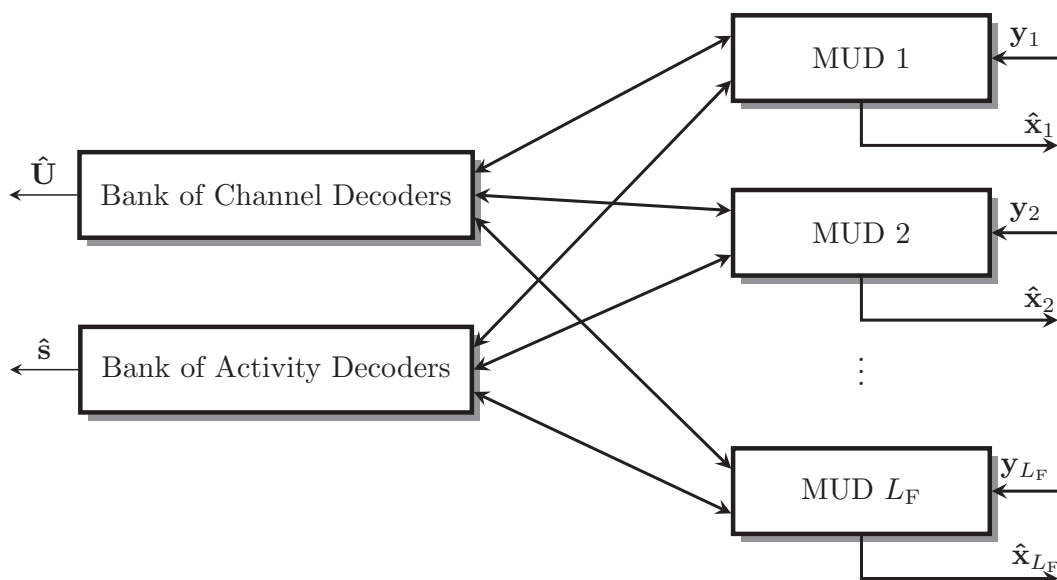


Figure 4.1: Overview about extrinsic information exchange between multiuser detector, channel decoder and activity decoder.

The general setup of the frame Belief Propagation (BP) as depicted in Fig. 4.1 shows that the algorithm consists of L_F multiuser detectors, a bank of channel and activity decoder connecting the L_F multiuser detectors. The main advantage of the frame BP algorithm is that the marginal posteriori densities for all variables involved are calculated. Besides estimating the multiuser vectors $\hat{\mathbf{x}}_l$, the frame BP also yields estimates of the information bits $\hat{\mathbf{U}}$ and of the node activity state (denoted as $\hat{\mathbf{s}}$). The frame BP itself does not perform any hard estimation and outputs soft values for the variables considered. To perform hard estimation, these values have to be estimated from the respective soft values by deciding in favor of the most possible hypothesis. Further, the frame BP yields estimates for the information bits of all nodes, no matter if active or inactive, at the decoder output. Therefore,

the code symbols for active and for inactive nodes are both estimated by the frame BP. Consequently, missed detection errors do not exist anymore. Inactive nodes can only be identified by performing a CRC at the output of the frame BP.

The analysis of how the soft information is combined within the frame BP and how the different entities interact is also one of the major contributions of this thesis and given in Subsection 4.3.6. The results of this chapter have not yet been published. A publication summarizing this chapter is pending.

4.2 Relevant Publications and State of the Art

The whole idea of describing functions on graphs goes back to the pioneering work of Gallager, who described LDPC codes graphically [Gal62]. Later, the term factor graph was firstly introduced by Kschischang and Frey in 1998 [KF98]. Currently, factor graphs are applied in various disciplines, including statistical inference, decoding, image denoising and many more. A good introduction on factor graphs and the sum-product algorithm can be found in [KFL01]. The first application of factor graphs to Compressed Sensing problems goes back to the works of Donoho Maleki and Montanari in 2009 [DMM09, DMM10a, DMM10b] and the works of Rangan and Baron [Ran11, BSB10]. The main difference compared to previous applications is the fact that the sensing matrix is a dense matrix, making the underlying factor graph fully connected. Calculating the messages in fully connected graphs is intricate as the messages themselves are functions. Therefore, messages are approximated by prototype functions that resemble Gaussian density functions which can be described by two parameters only. Thus, message passing boils down to the exchange of the parameters of a function instead of the function itself.

Applying belief propagation to CS-MUD has sporadically been addressed in the literature. In [HMMG16] the authors applied approximate message passing to detect the activity and data in overloaded CDMA systems with QAM modulation symbols and frame-based transmissions. The main focus there is adapting the approximate message passing to finite modulation alphabets composed of complex modulation symbols. Further, in [HMJ⁺15] the application of message passing as a means for channel estimation in has been considered. Here the activity detection is carried out by combining activity detection and channel estimation in overloaded systems. Finally, combining message passing with proper post processing algorithms has been considered in [MG15]. The main focus there is to decrease the false

alarms caused by the application of message passing algorithms. Research for tailoring message passing to CS-MUD differs in two significant points from what is presented here. First, the underlying algorithms are based on approximate message passing, which is an approximation to message passing introduced by [DMM10a]. With approximate message passing, several messages are summarized by one common message to reduce the complexity of the algorithm. Second, the schemes considered do not involve channel coding into the estimation. Applying message passing with channel coding to frame-based transmissions in CS-MUD can be seen as a significant extension to previous works.

Soft information processing is a well known framework from communications. Exemplary, the concept of concatenated turbo codes, the turbo concept [HOP96], is clearly one of the prominent examples. Beyond sole iterative channel decoding, iterative receiver structures such as the soft Successive Interference Cancellation (SIC) or soft RAKE combine iterative channel coding with soft multiuser detection yielding a full soft multiuser detector [Wym07]. These schemes mostly exchange extrinsic information between two entities, namely the multiuser detector and the decoder. The main difference in the work shown in this chapter is that we have a third entity accounting for the activity estimation - the SPE. In the field of CS-MUD iterative receiver structures are rather new and only two concepts haven been introduced in the past. In [Sch15] the authors introduced the Block Correlation Successive Interference Cancellation (bcSIC) algorithm, which combines multiuser detection with channel coding in an iterative framework. The bcSIC consists of a GOMP with a combined data detector and channel decoder. Compared to the GOMP, the bcSIC performs non-linear estimation of the data by decoding it via a channel decoder. Based on the side-knowledge of the channel decoder, the contribution of the nodes is iteratively subtracted from the received signal. However, the bcSIC involves hard estimation of the symbols and does not account for an information exchange in a soft information framework. Within this chapter the bcSIC is used as a state-of-the-art algorithm to assess the performance of the frame BP.

Beyond that, the authors in [Boc15] introduced a soft interference cancellation including a channel code to detect BPSK signals iteratively. This approach contains a bank of linear Minimum Mean Square Error (MMSE) pre-filters to filter out interference. The filtered signal is decoded in a soft information framework and the node activity is estimated. Based on these estimates, the bank of linear MMSE filters is updated. This algorithm runs iteratively until a certain stopping criterion is met.

4.3 Message Passing

4.3.1 Transmission and Node Model

For the derivation of the subsequent frame BP we consider the same uplink scenario as in the previous chapter. In contrast to the previous chapter we include channel coding from information bits u_n to code symbols c_n by a known channel code of rate R_c . The over-the-air transmission is non-frequency selective with an AWGN channel such that we can write for the l th received symbol in matrix form

$$\mathbf{y}_l = \mathbf{A}_l \mathbf{x}_l + \mathbf{w}_l, \quad 1 \leq l \leq L_F. \quad (4.1)$$

Additionally, it is assumed that the spreading sequences of the nodes change randomly each transmit symbol according to random sequence spreading. This is indicated by the composite signature matrix \mathbf{A}_l depending on the symbol-clock index l . With random sequence spreading the multiuser interference caused changes randomly each receive symbol. We will see that this randomness is required for the frame BP in order to perform well. This point is picked up again in Subsection 4.4.2. Further BPSK modulation is applied at the nodes.

With the model (4.1), the task is to derive an iterative algorithm consisting of a multiuser detector, a channel decoder and a SPE block that efficiently calculates the posteriori probabilities of all variables involved by exchanging extrinsic information between these entities. The starting point for the following derivations is the multiuser detector stage, yielding soft estimates for the multiuser vectors \mathbf{x}_l , that is later connected to the channel decoder and the SPE. With (4.1) we see that the task of resolving the multiuser interference can be carried out for each symbol independently of other symbols. Therefore, we start by deriving one particular multiuser detector instance. In a subsequent step we connect L_F multiuser detectors over the temporal domain to exploit the structure carried by the code and by the activity model. This multiuser detector will be the building block for the frame BP algorithm.

4.3.2 The Multiuser Detector

In the following we derive the multiuser detector stage which aims at calculating the marginal posteriori PMFs for all multiuser symbols. The resulting algorithm is computationally intractable and cannot be implemented. Therefore, we introduce certain approximations that result in an approximative multiuser detector.

The starting point is to consider one specific symbol x_n from one particular node. The time instance l is dropped to preserve clarity. Our goal is to estimate its posteriori PMF based on the observations made through the channel \mathbf{y} . We know that the likelihood function connecting both is a function of the whole multiuser vector \mathbf{x} . Additionally, we already know that the multiuser vector \mathbf{x} is composed of the code symbols \mathbf{c} for active nodes and of zeros for inactive nodes modeled by the hidden binary variables \mathbf{s} . Since \mathbf{x} is fully determined by the joint distribution of \mathbf{s} and \mathbf{c} we include these two variables within the derivation but replace them with their prior probability as the channel decoder and SPE are included later on. To this end, we start by defining the marginal posteriori PMF for the symbol x_n for any specific node n which we find by marginalizing the joint posteriori as

$$\Pr(x_n|\mathbf{y}) \propto \sum_{\sim x_n} \sum_{\mathbf{s} \in \{0,1\}^N} \sum_{\mathbf{c} \in \mathcal{A}^N} p_{\mathbf{y}}(\mathbf{y}|\mathbf{x}, \mathbf{c}, \mathbf{s}) \Pr(\mathbf{x}, \mathbf{c}, \mathbf{s}), \quad \forall n. \quad (4.2)$$

Here the "proportional to" sign denotes that normalization to unit area has been omitted to enhance readability. The term $\sim x_n$ is a shorthand notation for the set $\{\mathbf{x} \in \mathcal{A}_0^N \setminus x_n\}$. Clearly, the likelihood function $p_{\mathbf{y}}(\mathbf{y}|\mathbf{x}, \mathbf{c}, \mathbf{s})$ connects the multiuser vector \mathbf{x} to the observation obtained at the output of the channel \mathbf{y} that is solely determined by the Gaussian noise. Hence, the likelihood function $p_{\mathbf{y}}(\mathbf{y}|\mathbf{x}, \mathbf{c}, \mathbf{s})$ is well defined by the multiuser vector \mathbf{x} that subsumes \mathbf{c} and \mathbf{s} . Consequently, the likelihood function can be written as $p_{\mathbf{y}}(\mathbf{y}|\mathbf{x})$. Additionally, we know from the previous chapter that due to the assumption of white noise, the likelihood function can be factorized as a product over the observations y_m via

$$p_{\mathbf{y}}(\mathbf{y}|\mathbf{x}) = \prod_{m=1}^M p_y(y_m|\mathbf{x}). \quad (4.3)$$

Moreover, we can assume that the data transmitted is independent over the nodes. The same applies for the node activity states. Hence, the joint PMF $\Pr(\mathbf{x}, \mathbf{c}, \mathbf{s})$ can also be factorized. Thus, (4.2) can be written as

$$\Pr(x_n|\mathbf{y}) \propto \underbrace{\sum_{\sim x_n} \prod_{m=1}^M p_y(y_m|\mathbf{x})}_{\nu_{g \rightarrow x_n}(x_n)} \underbrace{\sum_{s_n \in \{0,1\}} \sum_{c_n \in \mathcal{A}} \prod_{n=1}^N \Pr(x_n, c_n, s_n)}_{\nu_{f_n \rightarrow x_n}(x_n)}, \quad \forall n. \quad (4.4)$$

In (4.4) we see that the marginal PMF for x_n is composed of two parts, corresponding to the likelihood function summarizing the information given by the channel, one the one hand, and the joint PMF for x_n, c_n, s_n on the

other hand. These two factors can be interpreted as messages coming from two different entities. The message $\nu_{g \rightarrow x_n}(x_n)$ describes the information from the likelihood function about the symbol x_n and $\nu_{f_n \rightarrow x_n}(x_n)$ describes the information from the marginalization of the PMF $\Pr(x_n, u_n, s_n)$ about x_n and the product of the two messages yields the marginal PMF via

$$\Pr(x_n|\mathbf{y}) \propto \nu_{g \rightarrow x_n}(x_n)\nu_{f_n \rightarrow x_n}(x_n). \quad (4.5)$$

Decomposing the marginal posteriori into a graph of different factor and variable nodes is at the heart of the so-called sum-product algorithm. Variable nodes summarize the variables in the equation describing the marginals, and factors describe functionals of the variables. One example of such factorization is the likelihood function that can be factorized according to (4.3). Whenever a variable is contained within one particular function, a connection called edge is drawn between variable and factor node. If the factor graph for a marginalization is free of loops, exact marginalization can be obtained by exchanging the messages on the graph. If the graph has cycles, marginalization can only be obtained approximately by iterating between the factor and variable nodes [KFL01]. The underlying formalism defining the messages between factor and variable nodes is called *sum-product* algorithm.

As depicted in Fig. 4.2 the graph for the particular calculation of the posteriori PMF in (4.2) consists of M factor nodes g_m , accounting for the M factors of the joint likelihood function $p_{\mathbf{y}}(\mathbf{y}|\mathbf{x})$, and of N variable nodes, accounting for the variables x_1, \dots, x_N . The function node g_m is a shorthand notation for

$$g_m = p_{y_m}(y_m|\mathbf{x}). \quad (4.6)$$

Additionally, each variable node x_n is connected to one function node f_n , which connects to the variables c_n and s_n representing code symbols and the activity state, respectively. The function f_n summarizes the connection between the variables $\{x_n, c_n, s_n\}$, accounts for their probabilistic dependencies and can be seen as a check node that is zero for any invalid combination of the variables involved. With the node detection model shown in Fig. 2.2 we can write

$$f_n(x_n, c_n, s_n) = \quad (4.7)$$

$$s_n [c_n \delta(x_n - 1) + (1 - c_n) \delta(x_n + 1)] + (1 - s_n) \delta(x_n). \quad (4.8)$$

At this stage the variable nodes c_n and s_n are stubs representing a-priori knowledge. Therefore, we set s_n and c_n to their respective prior probabilities $s_n \rightarrow p_a$ and $c_n \rightarrow 0.5$, respectively. Thus, we obtain for the processing at

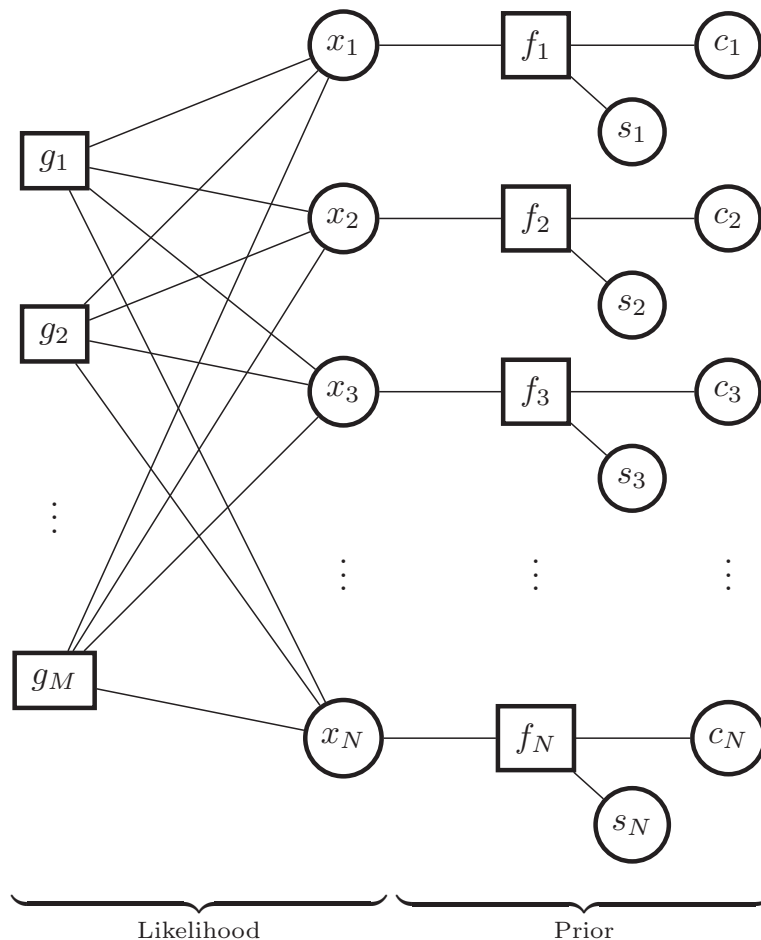


Figure 4.2: Factor graph of multiuser detector Belief Propagation algorithm with variable nodes $\{x_n, s_n, c_n\}$ accounting for the symbol, the node activity state and the code symbol. The factor nodes g_m and f_n account for the likelihood function and for the prior probability, respectively.

the function node

$$f_n(x_n) = p_a \left[\frac{1}{2} \delta(x_n - 1) + \frac{1}{2} \delta(x_n + 1) \right] + (1 - p_a) \delta(x_n), \quad (4.9)$$

which corresponds to the prior probability of x_n only. The sparsity is enforced by having $p_a \ll 1$ yielding high probability mass for the probability of $x_n = 0$. Later in Section 4.3.4 these stubs allow for information exchange over multiple multiuser detector stages by connecting them over the variables $\{s_n, c_n\}$. The composite signature matrix \mathbf{A} determines the connectivity between the factors g_m and the variables x_n and if the m, n th element of \mathbf{A} is nonzero, a connection between factor g_m and variable node x_n exist. As \mathbf{A} contains the spreading sequences of the nodes the matrix is dense and, thus, each variable is connected to each observation making the graph *dense*.

Considering the graph of the factorization of the marginal posteriori density in Fig. 4.2 shows that each variable node x_n is connected to m function nodes g_m and to one factor node f_n . To calculate the posteriori densities within such a graph messages between function and variable nodes have to be exchanged.

The underlying formalism applied for solving this problem is the sum-product algorithm. It is once again stated that the sum-product algorithm can only be used to calculate the exact marginals in graphs without loops. With loopy graphs the sum-product algorithms has shown good performance while running iteratively [KFL01]. However, according to current research, exact marginalization can not be guaranteed anymore. In the following we apply the sum product algorithm to the graphical decomposition shown in Fig.4.2.

The underlying iterative update equations at iteration number i summarize the messages from function to variable nodes

$$\nu_{g_m \rightarrow x_n}^{i+1}(x_n) = \sum_{\sim x_n} g_m(y_m | \mathbf{x}) \prod_{l \neq n} \nu_{x_l \rightarrow g_m}^i(x_n) \quad (4.10)$$

and the messages from variable to factor nodes

$$\nu_{x_n \rightarrow g_m}^{i+1}(x_n) = \underbrace{f_n(x_n)}_{\nu_{f_n \rightarrow x_n}(x_n)} \prod_{l \neq m} \nu_{g_l \rightarrow x_n}^i(x_n). \quad (4.11)$$

The message passing rules may appear bulky at first glance, nevertheless, the calculation of messages is straightforward and formalistic. Most importantly one has to note that messages are not only single values but functionals over the real line. In (4.10) and (4.11), the messages are functionals of the variable x_n . As shown in (4.10), function nodes multiply incoming messages, corresponding to a multiplication of functionals. Subsequently, the function, the function node is associated with, summarizes extrinsic information or a-priori probability is also pointwise multiplied with the incoming messages. Finally, the function node marginalizes this point-wise multiplication with respect to the variable the message is sent to.

Variable nodes instead only point-wise multiply incoming messages and forward them as shown in (4.11). Here the variable node x_n takes all incoming messages and multiplies them point-wise. Further, we see that (4.11) contains the message $\nu_{f_n \rightarrow x_n}(x_n)$ from the function $f_n(x_n)$ to x_n . Since this message only depends on x_n , no marginalization is carried out.

As factor-to-variable-messages depend on the incoming variable-to-factor-messages and vice versa, the BP scheme is iteratively denoted by the iteration number i . After a certain number of iterations, the algorithm is stopped and

the MMSE or the MAP estimate can be calculated by taking the posteriori mean or the posteriori mode from the factor to variable messages according to

$$x_n^{\text{MMSE}} = \text{Mean} \left(\sum_{\sim x_n} g_m(y_m|\mathbf{x}) \prod_{l=1}^N \nu_{x_l \rightarrow g_m}^i(x_n) \right) \quad (4.12)$$

$$x_n^{\text{MAP}} = \arg \max_{\sim x_n} \sum_{\sim x_n} g_m(y_m|\mathbf{x}) \prod_{l=1}^N \nu_{x_l \rightarrow g_m}^i(x_n). \quad (4.13)$$

The pseudo code of the optimal multiuser detector is given in listing 4.1.

Algorithm 4.1 Multiuser Detector

- 1: *#Definitions#*
 - 2: $f_n(x_n) = p_a \left[\frac{1}{2} \delta(x_n - 1) + \frac{1}{2} \delta(x_n + 1) \right] + (1 - p_a) \delta(x_n)$
 - 3: **repeat**
 - 4: *#Messages from likelihood function to augmented symbol#*
 - 5: $\nu_{g_m \rightarrow x_n}^{i+1}(x_n) = \sum_{\sim x_n} g_m(y_m|\mathbf{x}) \prod_{l \neq n} \nu_{x_l \rightarrow g_m}^i(x_n)$
 - 6: *#Messages from symbol to likelihood function#*
 - 7: $\nu_{x_n \rightarrow g_m}^{i+1}(x_n) = f_n(x_n) \prod_{l \neq m} \nu_{g_l \rightarrow x_n}^i(x_n)$
 - 8: **until** Any stopping criterion is met
 - 9: $x_n^{\text{MAP}} = \arg \max_{\sim x_n} \sum_{\sim x_n} g(y_m|\mathbf{x}) \prod_{l=1}^N \nu_{x_l \rightarrow g_m}^i(x_n)$
-

Implementing this type of BP algorithm is algorithmically intractable due to the $N - 1$ summations that have to be calculated for the factor to variable message and due to the fact that messages are functionals along the real line. To still implement this BP algorithm, the authors in [DMM09] introduced some approximations that exploit the structure of the likelihood function resembling a Gaussian PDF. With Gaussian likelihood functions the messages can be approximated via exponential functionals that are similar to Gaussian PDFs that are fully determined by their mean and variance. Instead of exchanging messages along the real line, only mean and variance are exchanged, yielding a feasible implementation.

4.3.3 The Approximative Multiuser Detector

The following section reviews the main steps of said approximation. For a thorough derivation, the reader is referred to [DMM09, Sch10]. To ease notation, we drop the iteration index i . The starting point is the factor of the likelihood function over the vector \mathbf{x} given the observation y_m

$$g_m(y_m|\mathbf{x}) \propto \exp\left(-\frac{1}{2\sigma_w^2}\|y_m - \mathbf{A}_{(m,:)}\mathbf{x}\|_2^2\right). \quad (4.14)$$

Inserting into (4.10) yields

$$\nu_{g_m \rightarrow x_n}(x_n) \propto \sum_{\sim x_n} \exp\left(-\frac{1}{2\sigma_w^2}\|y_m - \underbrace{\mathbf{A}_{(m,:\sim n)}\mathbf{x}_{\sim x_n}}_{Z_{m,n}} - \mathbf{A}_{(m,n)}x_n\|_2^2\right) \prod_{l \neq n} \nu_{x_l \rightarrow g_m}(x_n) \quad (4.15)$$

for the message from the factor node corresponding to the factorization of the likelihood function about the variable x_n . Subsequently, we call these messages the *messages from the likelihood factors*, as they convey the information obtained by the received symbol \mathbf{y} . In (4.15) the notation $\mathbf{A}_{(m,:\sim n)}$ denotes the m th column of the matrix \mathbf{A} reduced by the n th row. Through the multiplication of $N - 1$ variables with the matrix \mathbf{A} , we can assume by the central limit theorem that the resulting product $\mathbf{A}_{(m,:\sim n)}\mathbf{x}_{\sim x_n}$ is Gaussian distributed. More specifically, as shown in [DMM09], if the elements x_n have bounded first and second order moments, the variable $Z_{m,n}$ is Gaussian distributed with mean and variance

$$\begin{aligned} z_{m \rightarrow n} &= y_m - \sum_{q \neq n} \mathbf{A}_{(m,q)} \mu_{q \rightarrow m} \\ \zeta_{m \rightarrow n} &= \sigma_w^2 + \sum_{q \neq n} |\mathbf{A}_{(m,q)}|^2 v_{q \rightarrow m}. \end{aligned} \quad (4.16)$$

We see that the mean $z_{m \rightarrow n}$ depends on the mean $\mu_{q \rightarrow m}$ that denoted the mean of the incoming messages from the nodes $x_q \in \{1 \dots m \setminus n\}$. Likewise, the variance $\zeta_{m \rightarrow n}$ depends on the variance $v_{q \rightarrow m}$ denoting the variance of the incoming messages. Eq. (4.15) can now be seen as a function of the Gaussian variable Z that is distributed according to the product measure $\prod_{l \neq n} \nu_{x_l \rightarrow g_m}(x_n)$. With this Gaussian approximation, the sum in (4.15) can be approximated by a single integral over the real line over a Gaussian distributed random variable Z with mean and variance.

$$\nu_{g_m \rightarrow x_n}(x_n) \propto \int_{-\infty}^{\infty} \underbrace{\exp\left(-\frac{1}{\sigma_w^2}\|Z - \mathbf{A}_{(m,n)}x_n\|_2^2\right)}_{\Xi_{x_n}(Z)} \cdot \mathcal{N}(Z, z_{m \rightarrow n}, \zeta_{m \rightarrow n}) dZ \quad (4.17)$$

We see that (4.17) denotes the mean of the Gaussian variable Z under the transformations via the functional $\Xi_{x_n}(Z)$. Due to the fact that this

transformation involves an exponential function, we end up with a simple expression that reads

$$\begin{aligned} \nu_{g_m \rightarrow x_n}(x_n) &\propto \int_{-\infty}^{\infty} \Xi_{x_n}(Z) \cdot \mathcal{N}(Z, z_{m \rightarrow n}, \zeta_{m \rightarrow n}) dZ \\ &= \mathcal{N}(\mathbf{A}_{(m,n)} x_n, z_{m \rightarrow n}, \zeta_{m \rightarrow n}) \\ &= \mathcal{N}\left(x_n, z_{m \rightarrow n} / \mathbf{A}_{(m,n)}, \zeta_{m \rightarrow n} / \mathbf{A}_{(m,n)}^2\right) \end{aligned} \quad (4.18)$$

At this point one can see that the messages from the likelihood factors $\nu_{g_m \rightarrow x_n}(x_n)$ about x_n are proportional to a Gaussian PDF, which is fully described by the two parameters, mean and variance (4.16). This means instead of having whole functionals, messages were reduced to two parameters given in (4.16). Note that this step exploited the structure of the likelihood function resembling a Gaussian PDF.

The next step is to find simple expressions for the messages from the variable nodes x_n to the likelihood factors g_m . As shown in (4.16) the messages from the likelihood factors to the variable nodes for x_n depend on the mean and the variance of these messages. These messages are composed of the prior information about the variable x_n summarized by the function node f_n and the product of all incoming messages. In the following we call these messages *messages from the symbol*. According to the definitions in (4.11), the product is carried out over all $M - 1$ incoming messages from the likelihood factors, which were approximated by Gaussian PDFs. Thus, we have to calculate the product of $M - 1$ Gaussian PDFs. We use the fact that a product over Gaussian PDFs is itself proportionate to a Gaussian PDF as

$$\prod_q \mathcal{N}(x, \mu_q, v_q) \propto \mathcal{N}\left(x, \frac{\sum_q \mu_q / v_q}{\sum_q v_q^{-1}}, \frac{1}{\sum_q v_q^{-1}}\right). \quad (4.19)$$

Inserting mean and variance from (4.16) into (4.19) yields for the messages from the symbol node x_n to likelihood factors f_n

$$\nu_{x_n \rightarrow g_m}(x_n) \propto f(x_n) \cdot \mathcal{N}\left(x_n, \frac{\sum_{l \neq m} \frac{z_{l \rightarrow n} \mathbf{A}_{(l,n)}}{\zeta_{l \rightarrow n}}}{\sum_{l \neq m} \frac{\mathbf{A}_{(l,n)}^2}{\zeta_{l \rightarrow n}}}, \frac{1}{\sum_{l \neq m} \frac{\mathbf{A}_{(l,n)}}{\zeta_{l \rightarrow n}}}\right). \quad (4.20)$$

In the following we assume that the matrix \mathbf{A} has unit norm columns, such that $\sum_{l \neq m} \mathbf{A}_{(l,n)}^2 \approx \sum_{l=1}^M \mathbf{A}_{(l,n)}^2 = 1$. Additionally, we approximate the variance $\zeta_{l \rightarrow n}^i$ by its mean via

$$\zeta_{l \rightarrow n} \approx \zeta_n := \frac{1}{M} \sum_{m=1}^M \zeta_{m \rightarrow n}. \quad (4.21)$$

This simplifies (4.20) to

$$\nu_{x_n \rightarrow g_m}(x_n) \propto f_n(x_n) \cdot \mathcal{N}\left(x_n, \sum_{l \neq m} \mathbf{A}^{(l,n)} z_{l \rightarrow n}, \zeta_n\right). \quad (4.22)$$

The next step is to calculate the mean $\mu_{n \rightarrow m}$ and the variance $v_{n \rightarrow m}$ of the message (4.22). These are the inputs of the messages from the likelihood factors to the symbol nodes $\nu_{g_m \rightarrow x_n}(x_n)$ being approximated by (4.16). Calculating mean and variance of (4.22) is simple. This is based on the fact that $x_n \in \mathcal{A}_0$ is discrete. Therefore, mean and variance can numerically be calculated via

$$\begin{aligned} \mu_{n \rightarrow m} &= \frac{1}{\gamma} \sum_{x_n \in \mathcal{A}_0} x_n \nu_{x_n \rightarrow g_m}(x_n) \\ v_{n \rightarrow m} &= \frac{1}{\gamma} \sum_{x_n \in \mathcal{A}_0} (x_n - \mu_{n \rightarrow m})^2 \nu_{x_n \rightarrow g_m}(x_n) \end{aligned} \quad (4.23)$$

with $\gamma = \sum_{x_n \in \mathcal{A}_0} \nu_{x_n \rightarrow g_m}(x_n)$ being the normalization constant, to ensure that the PMF describes by (4.22) has unit area. Here, the normalization constant γ is explicitly shown to emphasize that the normalization has to be involved in the numerical calculation of the mean and the variance. Note that the numerical calculation can only be done for discrete variables x_n , for continuous variables mean and variance have to be found in closed form.

Exchanging $\{z_{m \rightarrow n}, \zeta_{m \rightarrow n}\}$ from the likelihood factor and $\{\mu_{n \rightarrow m}, v_{n \rightarrow m}\}$ from the symbol nodes, yields the iterative multiuser detector which is summarized in listing 4.2.

In the following the multiuser detector is extended towards a frame detector including SPE and decoder. The connecting point for this is the function node $f_n(x_n)$ that connects the multiuser detector with the SPE and the decoder.

4.3.4 The Frame Belief Propagation

In the following the multiuser detector acts as a building block for a frame-based BP including decoder and SPE. The resulting frame BP consists of L_F multiuser detectors yielding probabilistic information about the symbols x_n in the vectors \mathbf{x}_l . The information is then processed within a SPE block and a decoder block. Both blocks exchange extrinsic information with L_F multiuser detectors. As stated previously, the function node $f_{n,l}$ with the variables $c_{n,l}$ and $s_{n,l}$ is the connecting point for the channel decoder and the

Algorithm 4.2 Approximative Multiuser Detector

- 1: *#Definitions#*
 - 2: $f_n(x_n) = p_a \left[\frac{1}{2} \delta(x_n - 1) + \frac{1}{2} \delta(x_n + 1) \right] + (1 - p_a) \delta(x_n)$
 - 3: $\mathcal{N}(x, \mu, \sigma^2) = \frac{1}{\sqrt{2\pi\sigma^2}} \exp -\frac{1}{2\sigma^2}(x - \mu)^2$
 - 4: *#Initialize factor to variable messages#*
 - 5: $z_{m \rightarrow n} = y_m, \quad \zeta_{m \rightarrow n} \gg \sigma_w^2$
 - 6: **repeat**
 - 7: *#Symbol to likelihood function#*
 - 8: $\zeta_n = \frac{1}{M} \sum_{m=1}^M \zeta_{m \rightarrow n}^i$
 - 9: *#Calculate Normalization Constant#*
 - 10: $\gamma = \sum_{x_n \in \mathcal{A}_0} f_n(x_n) \cdot \mathcal{N}\left(x_n, \sum_{l \neq m} \mathbf{A}_{(l,n)} z_{l \rightarrow n}, \zeta_n\right)$
 - 11: *#Calculate mean and variance#*
 - 12: $\mu_{n \rightarrow m} = \frac{1}{\gamma} \sum_{x_n \in \mathcal{A}_0} x_n f_n(x_n) \cdot \mathcal{N}\left(x_n, \sum_{l \neq m} \mathbf{A}_{(l,n)} z_{l \rightarrow n}, \zeta_n\right)$
 - 13: $v_{n \rightarrow m} = \frac{1}{\gamma} \sum_{x_n \in \mathcal{A}_0} (x_n - \mu_{n \rightarrow m})^2 f_n(x_n)$
 $\times \mathcal{N}\left(x_n, \sum_{l \neq m} \mathbf{A}_{(l,n)} z_{l \rightarrow n}, \zeta_n\right)$
 - 14: *#Likelihood function to Symbol#*
 - 15: $z_{m \rightarrow n} = y_m - \sum_{q \neq n} \mathbf{A}_{(m,q)} \mu_{q \rightarrow m}$
 - 16: $\zeta_{m \rightarrow n} = \sigma_w^2 + \sum_{q \neq n} |\mathbf{A}_{(m,q)}|^2 v_{q \rightarrow m}$
 - 17: **until** Any stopping criterion is met
 - 18: $x_n^{\text{MAP}} = \arg \max f(x_n) \cdot \mathcal{N}\left(x_n, \sum_{m=1}^M \mathbf{A}_{(l,n)} z_{l \rightarrow n}, \zeta_n\right)$
-

SPE. Therefore, we now use the description of the function node according to (4.7) and have

$$f_{n,l}(x_{n,l}, c_{n,l}, s_{n,l}) = s_{n,l} [c_{n,l} \delta(x_{n,l} - 1) + (1 - c_{n,l}) \delta(x_{n,l} + 1)] + (1 - s_{n,l}) \delta(x_{n,l}). \quad (4.24)$$

To process the code bits $c_{n,l}$ and the hidden activity variable $s_{n,l}$, we require two new function nodes corresponding to the decoder and SPE. These nodes are subsequently denoted as a_n and h_n . As shown in Fig. 4.3 these function nodes are drawn in gray as they lie outside the multiuser detector. Additionally, we know that channel code and activity states are node specific. Therefore, the branch corresponding to one node connects to one function a_n and h_n only. However, for each node several multiuser detectors are connected to a central channel decoder and SPE stage reflecting the temporal dependencies within the transmit frames. According to the general sum-product update rules, the corresponding beliefs have to be

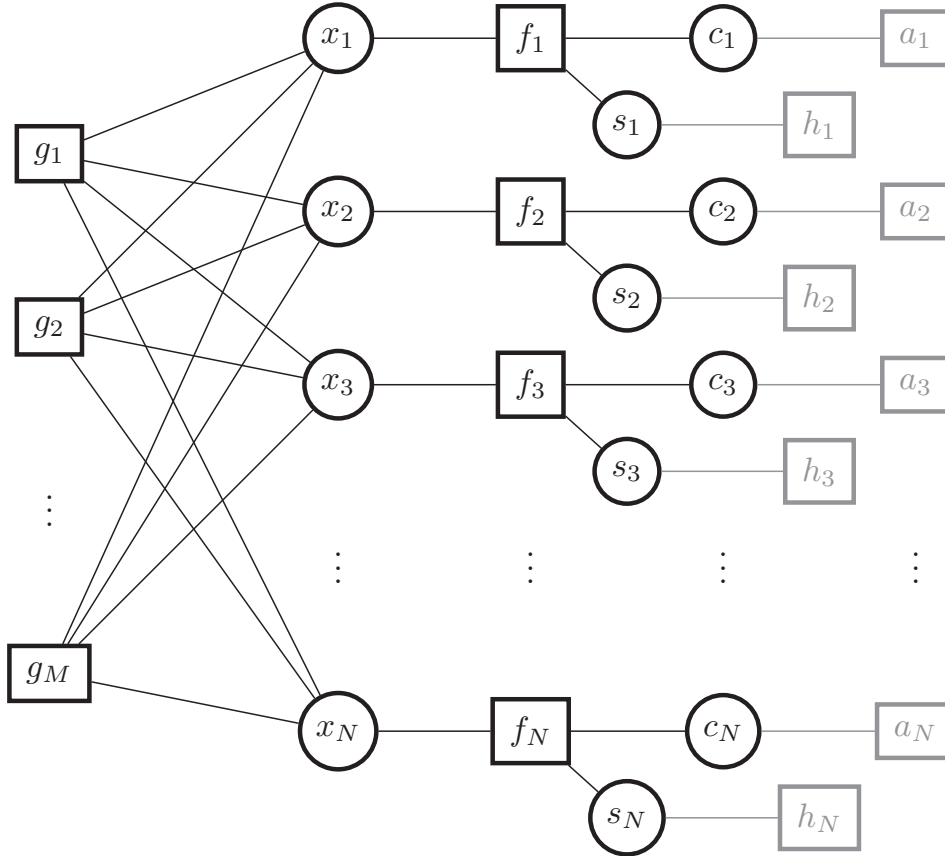


Figure 4.3: Overview of BP algorithm including function nodes a_n for the channel code and h_n for the activity decoder.

multiplied point-wise and marginalized. Further we can directly express the messages from the multiuser detector to the decoder. Formally, we first have to express the message from the multiuser detector to the code symbol $\nu_{f_{n,l} \rightarrow c_{n,l}}(c_{n,l})$ and the message from the code symbol to the decoder function $\nu_{c_{n,l} \rightarrow a_n}(c_{n,l})$. However, as the variable node $c_{n,l}$ has only two connections, the output message equals the input message. Therefore, we can directly give the message from the multiuser detector to the decoder

$$\begin{aligned}
 & \nu_{f_{n,l} \rightarrow a_n}(c_{n,l}) \\
 & \propto \sum_{x_{n,l}, s_{n,l}} f_{n,l}(x_{n,l}, c_{n,l}, s_{n,l}) \nu_{h_n \rightarrow f_{n,l}}(s_{n,l}) \nu_{x_{n,l} \rightarrow f_{n,l}}(x_{n,l}) \\
 & \propto \sum_{x_{n,l}, s_{n,l}} f_{n,l}(x_{n,l}, c_{n,l}, s_{n,l}) \nu_{h_n \rightarrow f_{n,l}}(s_{n,l}) \prod_{m=1}^M \nu_{g_{m,l} \rightarrow x_{n,l}}(x_{n,l}). \quad (4.25)
 \end{aligned}$$

In (4.25) we already see that the message to the decoder already contains information from the SPE and from the likelihood function. We will pick this point up in Subsection 4.3.7 to show how messages influence each other.

Likewise, the message from the multiuser detector to the SPE can also directly be formulated as

$$\begin{aligned}
& \nu_{f_{n,l} \rightarrow h_n}(s_{n,l}) \\
& \propto \sum_{x_{n,l}, c_{n,l}} f_{n,l}(x_{n,l}, c_{n,l}, s_{n,l}) \nu_{a_n \rightarrow f_{n,l}}(c_{n,l}) \nu_{x_{n,l} \rightarrow f_{n,l}}(x_{n,l}) \\
& \propto \sum_{x_{n,l}, c_{n,l}} f_{n,l}(x_{n,l}, c_{n,l}, s_{n,l}) \nu_{a_n \rightarrow f_{n,l}}(c_{n,l}) \prod_{m=1}^M \nu_{g_{m,l} \rightarrow x_{n,l}}(x_{n,l}). \quad (4.26)
\end{aligned}$$

The messages from the function node $f_{n,l}$ to likelihood factor $g_{m,l}$ needs to be extended to capture the extrinsic information from the channel decoder and the SPE. Here we apply the formalism of the sum-product update rules meaning that the messages from the SPE $\nu_{h_n \rightarrow f_{n,l}}(x_{l,n})$ and the message from the channel decoder $\nu_{a_n \rightarrow f_{n,l}}(x_n)$ are point-wise multiplied, yielding

$$\begin{aligned}
& \nu_{f_{n,l} \rightarrow g_{m,l}}(x_{n,l}) \propto \\
& \sum_{c_{n,l}, s_{n,l}} f_{n,l}(x_{n,l}, c_{n,l}, s_{n,l}) \nu_{a_n \rightarrow f_{n,l}}(c_{n,l}) \nu_{h_n \rightarrow f_{n,l}}(s_{n,l}) \prod_{q \neq m} \nu_{g_{q,l} \rightarrow x_{n,l}}(x_{n,l}). \quad (4.27)
\end{aligned}$$

After connecting L_F multiuser detectors to a central decoder and a central SPE, we can formulate the graphical model as depicted in Fig. 4.4. This graphical model consists of L_F multiuser detector instances where the variable nodes for the code symbols of one particular node $c_{n,l}, \forall l$ are connected with a central factor node a_n representing the channel decoder for the n th node and each activity variable $s_{n,l}, \forall l$ is connected to a central factor node h_n representing the SPE for the n th node, respectively. Fig. 4.4 shows that channel and activity decoder factors have *horizontal* connections to all multiuser detector instances. The beliefs from the SPE to the multiuser detector is specified by the knowledge, that a node is either active or inactive for the whole frame. This means, the factor node h_n takes the incoming beliefs, corresponding to L_F soft estimates for the variable s_m being either zero or one. According to the terminology of message passing, h_n is a check node [KFL01] that multiplies the beliefs point wise according to

$$\nu_{h_n \rightarrow s_{n,l}}(s_{n,l}) \propto \begin{cases} \prod_{q \neq l} \nu_{s_{n,q} \rightarrow h_n}(s_{n,q} = 1) & \text{if } s_{n,l} = 1 \\ \prod_{q \neq l} \nu_{s_{n,q} \rightarrow h_n}(s_{n,q} = 0) & \text{if } s_{n,l} = 0 \end{cases} \quad (4.28)$$

which can compactly be written as

$$\nu_{h_n \rightarrow s_{n,l}}(s_{n,l}) \propto \sum_{\sim s_{n,l}} \prod_{q \neq l} \delta(s_{n,l} - s_{n,q}) \cdot \nu_{s_{n,q} \rightarrow h_n}(s_{n,q}), \quad (4.29)$$

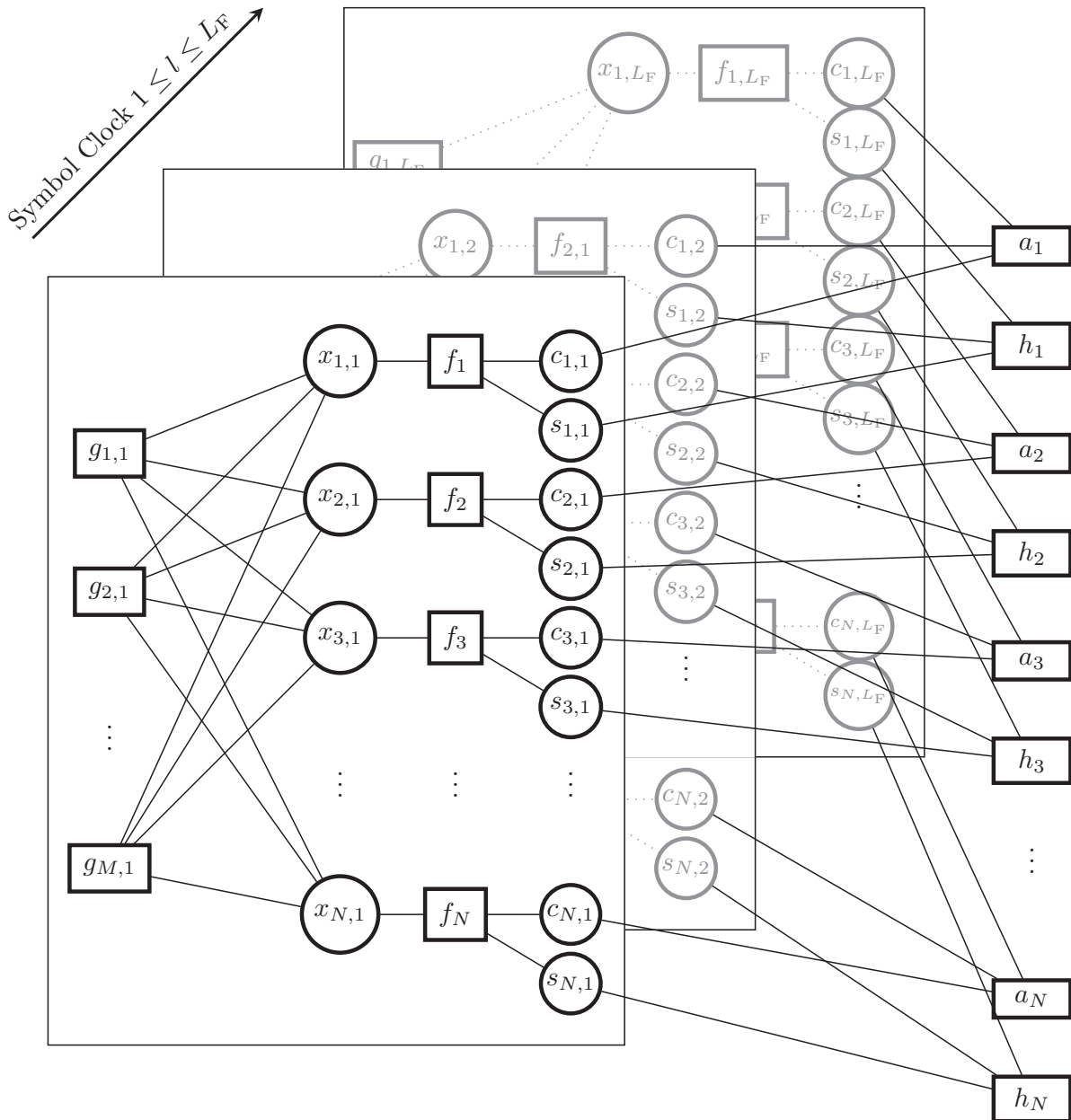


Figure 4.4: Overview of BP algorithm including function nodes for activity and channel decoder for a frame of L_F symbols.

Within this work we do not restrict to a specific channel code. To comply with the frame BP algorithms, the decoder used should allow for a soft-input soft-output decoding (which can itself be iterative). In the following example we demonstrate how the messages look like when a repetition code is applied at the nodes. The beliefs $\nu_{f_{n,l} \rightarrow a_n}(c_{n,l})$ summarize the code symbol beliefs of the frame BP and yield as soft estimates about them. Each decoder should decode the sequence of code symbols and yield beliefs $\nu_{a_n \rightarrow f_{n,l}}(c_{n,l})$ to the multiuser detector instances. The frame BP is an iterative algorithm that has to be stopped after a certain number iterations. After stopping the

frame BP the posteriori PMFs of all code symbols $c_{n,l}$, information symbols $u_{n,l}$ and activity states $s_{n,l}$ are calculated and can further be processed. The frame BP itself does not perform any hard estimation of one of these variables, hence the outputs are probabilities or LLRs for these variables. The BP algorithm with decoding and SPE stage is subsequently summarized via pseudo code in listing 5.2.

The proportional to sign indicates that the corresponding messages have to be normalized to unit area. This can easily be done numerically, as the PMFs are of discrete nature and have in case of BPSK only 2 values. The frame BP is an iterative algorithm consisting of several iterative stages. Therefore, proper scheduling between these stages may greatly decrease the complexity of the algorithm. Additionally, the L_F multiuser stages can either run in parallel or serial one after another. Trading off the complexity and performance via scheduling is not considered within this thesis and left for further research. Within this thesis, we run all multiuser detector stages in parallel and stop the whole algorithm after 10 iterations.

It is not hard to see that the complexity of the frame BP is still tremendous. Even though matrix inversions are avoided by this algorithm, the number of messages that have to be tracked is huge. A single multiuser detector has to track $M \times N$ messages being exchanges between likelihood functions and the symbol nodes. When running the frame BP, this number scales in the frame length L_F . Further, the messages between the multiuser detector stages, decoder and SPE have to be taken into regard. Consequently, approximations have to be made in order to come up with a feasible implementation. Here, previous works have considered the so-called Approximate Message Passing (AMP) [DMM09]. The AMP applies to the fully connected part of the multiuser detector and simplifies the messages such that only N messages have to be tracked. The application of the AMP is a promising extension to the work presented here. However, it is left for further research.

Algorithm 4.3 Belief Propagation with activity and data decoder

- 1: *#Definitions#*
 - 2: $f_{n,l}(x_{n,l}, c_{n,l}, s_{n,l}) = s_{n,l} [c_{n,l} \delta(x_{n,l} - 1) + (1 - c_{n,l}) \delta(x_{n,l} + 1)] + (1 - s_{n,l}) \delta(x_{n,l})$
 - 3: $\mathcal{N}(x, \mu, \sigma^2) = \frac{1}{\sqrt{2\pi\sigma^2}} \exp -\frac{1}{2\sigma^2}(x - \mu)^2$
 - 4: *#Initialize factor to variable messages#*
 - 5: $z_{m \rightarrow n}^{(l)} = y_m, \quad \zeta_{m \rightarrow n}^{(l)} \gg \sigma_w^2 \quad \forall n, l$
 - 6: $\nu_{h_n \rightarrow f_{n,l}}(s_{n,l} = 1) = p_a, \quad \nu_{h_n \rightarrow f_{n,l}}(s_{n,l} = 0) = 1 - p_a \quad \forall n, l$
 - 7: $\nu_{a_n \rightarrow f_{n,l}}(c_{n,l} = 0) = \nu_{a_n \rightarrow f_{n,l}}(c_{n,l} = 1) = 0.5 \quad \forall n, l$
 - 8: **repeat**
 - 9: *#From multiuser detector to decoder and SPE#*
 - 10: **for** $l = 1, l \leq L_F, l = l + 1$ **do**
 - 11: $\zeta_{n,l} = \frac{1}{M} \sum_{m=1}^M \zeta_{m \rightarrow n}^{(l)}$
 - 12: $\nu_{f_{n,l} \rightarrow a_n}(c_{n,l}) = \frac{1}{\gamma} \sum_{x_{n,l}, s_{n,l}} f_{n,l}(x_{n,l}, c_{n,l}, s_{n,l}) \nu_{h_n \rightarrow f_{n,l}}(s_{n,l})$
 $\times \mathcal{N}\left(x_{n,l}, \sum_{m=1}^M \mathbf{A}_{(m,n)}^{(l)} z_{m \rightarrow n}^{(l)}, \zeta_{n,l}\right)$
 - 13: $\nu_{f_n \rightarrow h_n}(s_{n,l}) = \frac{1}{\gamma} \sum_{c_{n,l}, s_{n,l}} f_n(x_{n,l}, c_{n,l}, s_{n,l}) = \nu_{a_n \rightarrow f_n}(c_{n,l})$
 $\times \mathcal{N}\left(x_{n,l}, \sum_{m=1}^M \mathbf{A}_{(m,n)}^{(l)} z_{m \rightarrow n}^{(l)}, \zeta_{n,l}\right)$
 - 14: **end for**
 - 15: *#From Decoder and SPE to multiuser detector#*
 - 16: $\nu_{h_n \rightarrow f_n}(s_{n,l}) \frac{1}{\gamma} \sum_{\sim s_{n,l}} \prod_{q \neq l} \delta(s_{n,l} - s_{n,q}) \cdot \nu_{s_{n,q} \rightarrow h_n}(s_{n,q})$
 - 17: $\nu_{a_n \rightarrow f_n}(c_{n,l}) = \text{Extrinsic Information from Decoder}$
 - 18: *#Symbol node to likelihood function#*
 - 19: **for** $l = 1, l \leq L_F, l = l + 1$ **do**
 - 20: $\mu_{n \rightarrow m}^{(l)} = \frac{1}{\gamma} \sum_{x_{n,l}} x_{n,l} \sum_{s_{n,l}, c_{n,l}} f(x_{n,l}, s_{n,l}, c_{n,l})$
 $\times \mathcal{N}\left(x_{n,l}, \sum_{q \neq m} \mathbf{A}_{(q,n)}^{(l)} z_{q \rightarrow n}^{(l)}, \zeta_{n,l}\right) \nu_{a_n \rightarrow f_n}(c_{n,l}) \nu_{h_n \rightarrow f_n}(s_{n,l})$
 - 21: $v_{n \rightarrow m}^{(l)} = \frac{1}{\gamma} \sum_{x_{n,l}} \left(x_{n,l} - \mu_{n \rightarrow m}^{(l)}\right)^2 \sum_{s_{n,l}, c_{n,l}} f(x_{n,l}, s_{n,l}, c_{n,l})$
 $\times \mathcal{N}\left(x_{n,l}, \sum_{q \neq m} \mathbf{A}_{(q,n)}^{(l)} z_{q \rightarrow n}^{(l)}, \zeta_{n,l}\right) \nu_{a_n \rightarrow f_n}(c_{n,l}) \nu_{h_n \rightarrow f_n}(s_{n,l})$
 - 22: *#Likelihood function to Symbol node#*
 - 23: $z_{m \rightarrow n}^{(l)} = y_{m,l} - \sum_{q \neq n} \mathbf{A}_{(m,q)}^{(l)} \mu_{q \rightarrow m}^{(l)}$
 - 24: $\zeta_{m \rightarrow n}^{(l)} = \sigma_w^2 + \sum_{q \neq n} |\mathbf{A}_{(m,q)}^{(l)}|^2 v_{q \rightarrow m}^{(l)}$
 - 25: **end for**
 - 26: **until** Any stopping criterion is met
 - 27: $\zeta_{n,l} = \frac{1}{M} \sum_{m=1}^M \zeta_{m \rightarrow n}^{(l)}$
 - 28: $\Pr(x_{n,l}) \frac{1}{\gamma} \sum_{c_{n,l}, s_{n,l}} f_n(x_{n,l}, s_{n,l}, c_{n,l}) \mathcal{N}\left(x_{n,l}, \sum_{m=1}^M \mathbf{A}_{(m,n)}^{(l)} z_{l \rightarrow n}^{(l)}, \zeta_{n,l}\right)$
 $\times \nu_{a_n \rightarrow f_n}(c_{n,l}) \nu_{h_n \rightarrow f_n}(s_{n,l})$
 - 29: $\Pr(s_n) \frac{1}{\gamma} \sum_{x_{n,l}, c_{n,l}} f_n(x_{n,l}, s_{n,l}, c_{n,l}) \mathcal{N}\left(x_{n,l}, \sum_{m=1}^M \mathbf{A}_{(m,n)}^{(l)} z_{l \rightarrow n}^{(l)}, \zeta_{n,l}\right)$
 $\times \nu_{a_n \rightarrow f_n}(c_{n,l}) \nu_{h_n \rightarrow f_n}(s_{n,l})$
 - 30: $\Pr(u_{n,l}) \rightarrow$ At the decoder output.
-

4.3.5 Repetition Code Decoder and Data Detection

With full soft information processing, arbitrary channel codes can be applied. However, for the sake of completeness and subsequent analysis, we briefly give the corresponding update equations if a repetition code with repetition factor R is applied. In this particular case, the decoder function a_n consists of L_u sub-functions resembling check nodes. Each sub-function connects one particular information bit to its corresponding R code bits. The messages for a repetition code corresponds to the point-wise multiplication of the probabilities for the information bit. In terms of the sum-product rules, this corresponds to [KFL01].

$$\nu_{a_n \rightarrow c_{n,r}}(c_{n,r}) \propto \sum_{\sim c_{n,r}} \prod_{q \neq r} \delta(c_{n,r} - c_{n,q}) \cdot \nu_{c_{n,q} \rightarrow a_n}(c_{n,q}) \quad (4.30)$$

The block diagram for the decoder function a_n is illustratively shown in Fig. 4.5. The posteriori densities for the information symbols can be calcu-

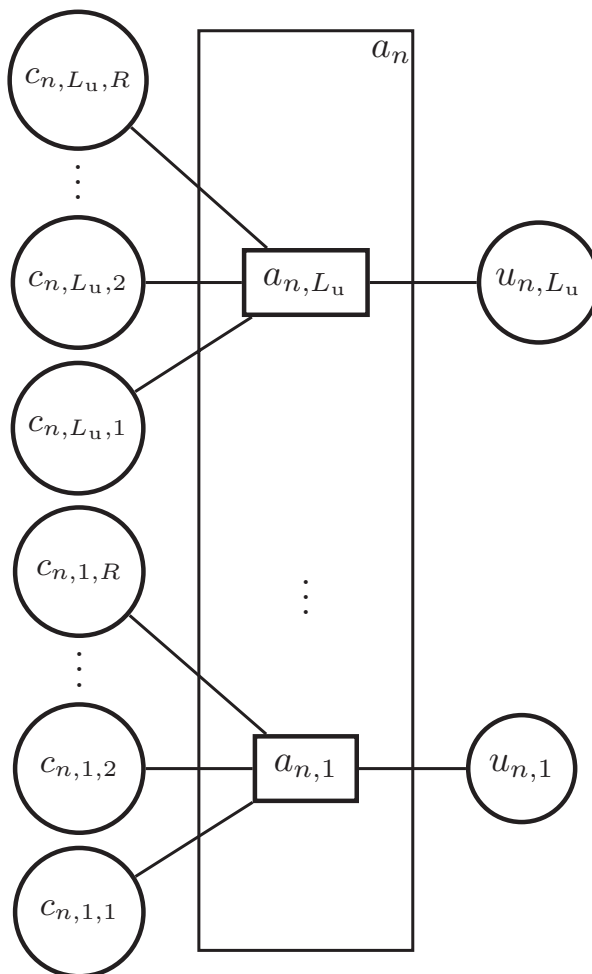


Figure 4.5: Illustration of the decoder function a_n in case of a repetition code.

lated via [KFL01]

$$a_n(u_{n,L_u}) \propto \prod_q \delta(u_n) \cdot \nu_{c_{n,q} \rightarrow a_n}(c_{n,q} = 0) + \quad (4.31)$$

$$\prod_q \delta(u_n - 1) \cdot \nu_{c_{n,q} \rightarrow a_n}(c_{n,q} = 1). \quad (4.32)$$

4.3.6 Data Detection and Activity Estimation

Once the posteriori estimates for the information symbols are calculated, MAP detection can be carried out by taking the estimate that maximizes the posteriori PMF via

$$u_{n,l_u}^{\text{MAP}} = \arg \max a_n(u_{n,l_u}). \quad (4.33)$$

However, one has to keep in mind that the frame BP calculates the posteriori probabilities for *all* code symbols no matter if active or inactive. Since the decoder itself has no knowledge about inactivity, the posteriori probabilities for all $N \times L_u$ information symbols are calculated. As a consequence, the activity has to be decided in order to properly estimate the information symbols of the active nodes. As the frame BP also delivers probabilistic information about the node activity state s_n , one approach would be to employ this and calculate the underlying activity LLR via

$$L_n = \log \frac{\Pr(s_n = 0)}{\Pr(s_n = 1)}. \quad (4.34)$$

However, the question how the activity is decided still has to be addressed. Based on the activity LLR, concepts known from the previous chapter such as Bayes-Risk and Neyman-Pearson detection can be applied by using the corresponding decision rules to decide the node activity.

A more elegant approach is to take the estimates for the information bits and process them via a CRC code to sort out erroneous packages. While doing so, CRC errors are based on the following two events:

1. Active nodes where the decoding leads to an invalid information word summarizing a frame error
2. Inactive nodes, where the information symbols detected are merely random

As a consequence, missed detection errors can not be distinguished from frame errors anymore. However, higher layers still have to judge, whether a node was active or inactive to (possibly) initiate retransmissions. This

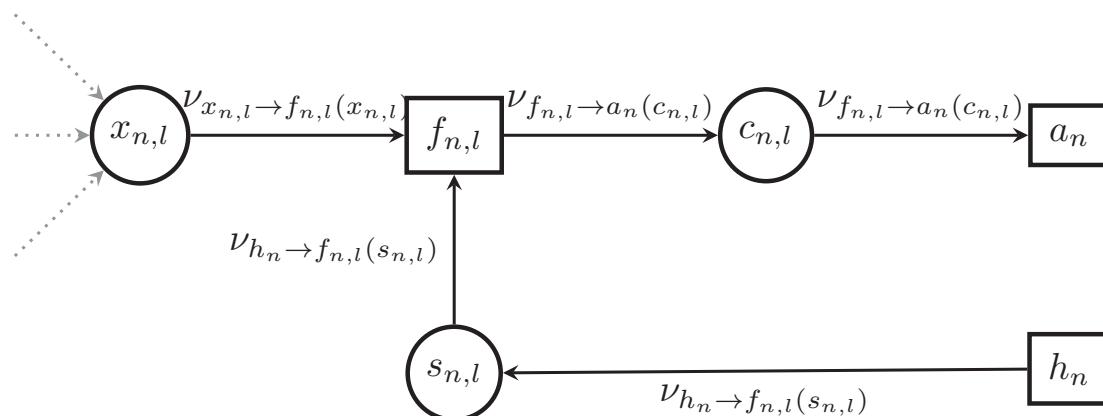


Figure 4.6: Block diagram showing that the beliefs from the multiuser detector to the decoder are composed of the beliefs about the variable $x_{n,l}$ and the beliefs from the SPE about the nodes's activity state.

can be achieved by considering the activity LLRs allowing inferring the probability that a node was active.

$$\Pr(\text{nth node was active} | L_n) = \frac{1}{1 + \exp(-L_n)}. \quad (4.35)$$

If this probability exceeds a certain threshold, a subsequent ARQ stage could initiate a retransmission of that package.

4.3.7 Sparsity Pattern Equalization and Channel Code

The data estimation of inactive nodes is slightly contradictory at first glance, as only active nodes transmit data that can be decoded. Further, the decoder has no knowledge about node (in)activity and assumes each node to be active. As the frame BP does not decide in favor of (in)activity, the question of how inactive nodes are decoded arises.

In the following this question is addressed by showing that the beliefs exchanged between multiuser detector, decoder and SPE are influencing each other. We will see that the beliefs from the multiuser detector to the decoder are of low magnitude if the SPE has a high belief toward inactivity. Additionally, the beliefs from the multiuser detector to the SPE are also influenced by the beliefs from the decoder about the code symbols. We therefore consider the message exchange between multiuser detector, SPE and decoder as depicted on Fig. 4.6.

We start by looking at the message from the multiuser detector to the decoder (4.26) being composed of the message from the SPE to the multiuser detector and from the message from the likelihood factor. In combination

with the definition of the function node $f_{n,l}$ (4.7) we have

$$\begin{aligned}
\nu_{f_{n,l} \rightarrow a_n}(c_{n,l}) &\propto \sum_{x_{n,l}, s_{n,l}} f_{n,l}(x_{n,l}, c_{n,l}, s_{n,l}) \nu_{h_n \rightarrow f_{n,l}}(s_{n,l}) \nu_{x_{n,l} \rightarrow f_{n,l}}(x_{n,l}) \\
&\propto \nu_{h_n \rightarrow f_{n,l}}(s_{n,l} = 0) \nu_{x_{n,l} \rightarrow f_{n,l}}(x_{n,l} = 0) + \\
&(1 - c_{n,l}) \nu_{h_n \rightarrow f_{n,l}}(s_{n,l} = 1) \nu_{x_{n,l} \rightarrow f_{n,l}}(x_{n,l} = -1) + \\
&c_{n,l} \nu_{h_n \rightarrow f_{n,l}}(s_{n,l} = 1) \nu_{x_{n,l} \rightarrow f_{n,l}}(x_{n,l} = 1)
\end{aligned} \tag{4.36}$$

As said, messages are functions reflecting probabilities. In this case, we can summarize the message as code symbol LLR by calculating

$$L_{f_{n,l} \rightarrow a_n}(c_{n,l}) := \log \frac{\nu_{f_{n,l} \rightarrow a_n}(c_{n,l} = 1)}{\nu_{f_{n,l} \rightarrow a_n}(c_{n,l} = -1)}. \tag{4.37}$$

This expresses the belief of the multiuser detector about the n, l th code symbol as a code symbol LLR that reads

$$\begin{aligned}
&\overbrace{L_{f_{n,l} \rightarrow a_n}(c_n)}^{\text{MUD} \rightarrow \text{Dec.}} = \\
&\frac{\underbrace{\nu_{h_n \rightarrow f_{n,l}}(s_{n,l} = 0) \nu_{x_{n,l} \rightarrow f_{n,l}}(x_{n,l} = 0)}_{\text{SPE} \rightarrow \text{MUD}} + \underbrace{\nu_{h_n \rightarrow f_{n,l}}(s_{n,l} = 1) \nu_{x_{n,l} \rightarrow f_{n,l}}(x_{n,l} = 1)}_{\text{Likelihood fct.} \rightarrow \text{MUD}}}{\underbrace{\nu_{h_n \rightarrow f_{n,l}}(s_{n,l} = 0) \nu_{x_{n,l} \rightarrow f_{n,l}}(x_{n,l} = 0)}_{\text{SPE} \rightarrow \text{MUD}} + \underbrace{\nu_{h_n \rightarrow f_{n,l}}(s_{n,l} = 1) \nu_{x_{n,l} \rightarrow f_{n,l}}(x_{n,l} = -1)}_{\text{Likelihood fct.} \rightarrow \text{MUD}}} \tag{4.38} \\
&\underbrace{\hspace{10em}}_{\text{Belief towards inactivity}} \qquad \underbrace{\hspace{10em}}_{\text{Belief towards activity}}
\end{aligned}$$

In (4.38) we observe how the LLR about the code symbol is generated. The multiuser detector takes the information from the SPE and from the likelihood factor. The LLR is composed of two parts, corresponding to the belief of activity and of inactivity. The part corresponding to activity contains the ratio of the likelihood for $x_{n,l}$ being ± 1 which corresponds to a valid code symbol. This belief is weighted with the belief from the SPE towards activity. On the other hand, the LLR also contains the belief from the likelihood factor towards inactivity, which is $x_{n,l} = 0$. This is weighted with the belief from the SPE towards inactivity.

To further highlight the connection between code symbol LLR and SPE, the activity LLR from the SPE to the multiuser detector is defined as the ratio of the beliefs towards inactivity and activity via

$$L_{h_n \rightarrow f_{n,l}}(s_{n,l}) = \log \frac{\nu_{h_n \rightarrow f_{n,l}}(s_{n,l} = 0)}{\nu_{h_n \rightarrow f_{n,l}}(s_{n,l} = 1)}. \tag{4.39}$$

Subsequently, we consider an example where the belief from the likelihood factor towards inactivity is $\nu_{x_{n,l} \rightarrow f_{n,l}}(x_{n,l} = 0) = 0.5$. The beliefs from the

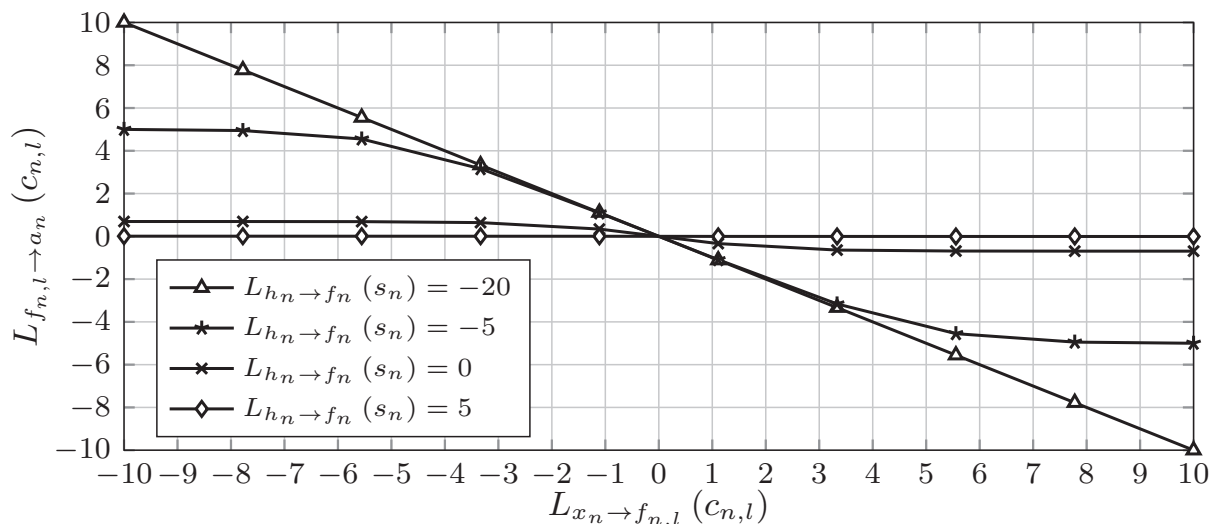


Figure 4.7: LLRs about the code symbols from the multiuser detector to the decoder vs. the LLR from the variable node $x_{l,n}$ parametrized by the activity LLR from the SPE to the multiuser detector.

likelihood factor about the code symbol being $c_{n,l} = \pm 1$ is also expressed via an LLR as

$$L_{x_{n,l} \rightarrow f_{n,l}}(x_{n,l}) := \log \frac{\nu_{x_{n,l} \rightarrow f_{n,l}}(x_{n,l} = 1)}{\nu_{x_{n,l} \rightarrow f_{n,l}}(x_{n,l} = -1)}. \quad (4.40)$$

With this definition, we can see how the SPE affects the code symbol LLR sent to the decoder. Fig. 4.7 plots the LLR about the code symbols transmitted from the multiuser detector to the decoder over the code symbol LLR which corresponds to the belief from the likelihood factor, given in (4.40). The curve is parametrized by the activity LLR from the SPE. Most interestingly, if the SPE has a high belief towards activity (negative activity LLR), the LLR to the decoder $L_{f_{n,l} \rightarrow a_n}(c_{n,l})$ matches the code symbol LLR generated by the likelihood factor. However, if activity becomes more and more unlikely and the activity LLR decreases, the code symbol LLR, in turn, gets clipped at some value. This example shows that the activity LLR can be seen as a moderating variable on the code LLR. Consequently, the decoder works on LLRs with low magnitude. This is a reasonable result by visualizing that in case of inactivity no code symbols exist for that particular node. The likelihood for either one of the code symbols turns to be 0.5 in this case, yielding an LLR of zero. The decoder sees code symbol LLRs that basically were generated by observing only noise.

For the sake of completeness, we also look at the activity LLRs from the multiuser detector to the SPE and consider how the beliefs from the

decoder contribute here. For this, we consider the message from the multiuser detector to the SPE (4.26). As shown in Fig. 4.8 this message is composed

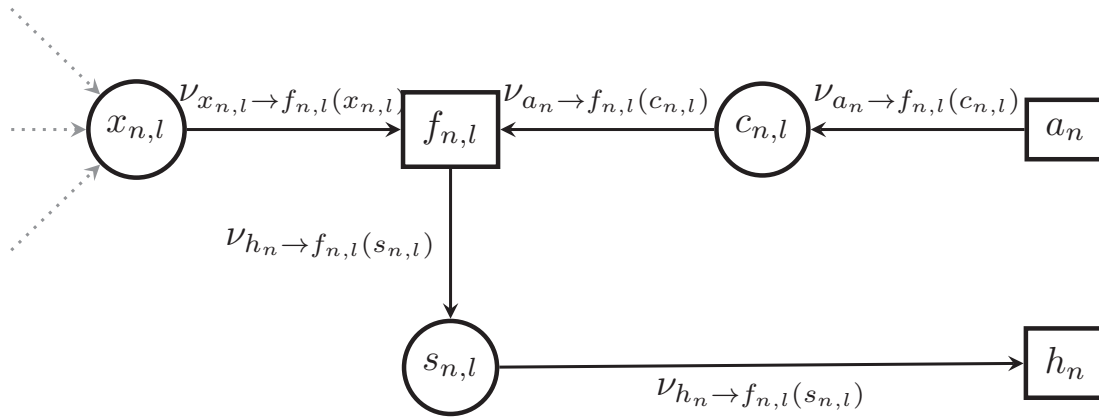


Figure 4.8: Block diagram showing that the beliefs from the multiuser detector to the SPE are composed of the beliefs from the the variable node $x_{n,l}$ and from the decoder.

of the beliefs given by the likelihood factors and the beliefs from the decoder. This message reads

$$\nu_{f_{n,l} \rightarrow h_n}(s_{n,l}) \propto \sum_{x_{n,l}, c_{n,l}} f_{n,l}(x_{n,l}, c_{n,l}, s_{n,l}) \nu_{a_n, l \rightarrow f_{n,l}}(c_{n,l}) \nu_{x_{n,l} \rightarrow f_{n,l}}(x_{n,l}). \quad (4.41)$$

Again, this message can be compactly summarized as a LLR using the definition of the function node $f_{n,l}$ from (4.7)

$$\begin{aligned} \overbrace{L_{f_{n,l} \rightarrow h_n}(s_{n,l})}^{\text{MUD} \rightarrow \text{SPE}} &:= \log \frac{\nu_{f_{n,l} \rightarrow h_n}(s_{n,l} = 0)}{\nu_{f_{n,l} \rightarrow h_n}(s_{n,l} = 1)} \\ &= \log \frac{\overbrace{\nu_{x_{n,l} \rightarrow f_{n,l}}(x_{n,l} = 0)}^{\text{Likelihood fkt.} \rightarrow \text{MUD}}}{\underbrace{\nu_{x_{n,l} \rightarrow f_{n,l}}(x_{n,l} = -1)}_{\text{Likelihood fkt.} \rightarrow \text{MUD}} \underbrace{\nu_{a_n \rightarrow f_{n,l}}(c_{n,l} = 0)}_{\text{Decoder} \rightarrow \text{MUD}} + \underbrace{\nu_{x_{n,l} \rightarrow f_{n,l}}(x_{n,l} = 1)}_{\text{Likelihood fkt.} \rightarrow \text{MUD}} \underbrace{\nu_{a_n \rightarrow f_{n,l}}(c_{n,l} = 1)}_{\text{Decoder} \rightarrow \text{MUD}}}. \end{aligned} \quad (4.42)$$

Most interestingly, in (4.42), only the hypothesis for activity in the denominator depends on the messages from the decoder. The hypothesis for inactivity in the numerator only depends on the messages coming from the channel. Here, we see that the decoder can influence the activity LLR only in one direction, which is activity. The hypothesis towards inactivity is solely determined by the observation given by the channel. This shows that the decoder output is almost irrelevant for the activity LLR, if the observation given by the channel has a strong indication towards inactivity.

4.4 Performance Evaluation

In the following we analyze the performance of the frame BP in different setups. For the subsequent analysis we consider the frame error rate for different parameter settings. As frame errors are considered and different coding parameters are investigated, we subsume the impact of the repetition factor of the repetition code applied into the definition of the SNR. For the remainder of this chapter the SNR is defined as $1/R\sigma_w^2$.

Impact of Code-Rate and Frame Length

Most of the performance is gained due to the fact that whole frames are estimated and that the information symbols are coded to code symbols. The impact of both can be observed in Fig. 4.9 in a system with $N = 60$ nodes using spreading sequence length of $M = 20$ to transmit data. The node activity probability is $p_a = 0.2$. The left figure shows the impact of the code rate. Here a repetition code with different repetition factors R is employed and the frame length is set to $L_F = 60$ code symbols. Most interestingly, choosing R too low, yields an error floor at high SNR. Here we see, how the frame BP exploits the code space as a resource. With the repetition code applied, each node repeats its code symbol R times. In case of a repetition code this can be interpreted as a secondary spreading factor that comes on top of M . With a repetition code of factor R each code symbol is represented by $M \times R$ observations. Therefore, it is not a surprise that the frame BP achieves low FER with $R = 3$, yielding $M \times R = 60$ observations per node, which matches the number of nodes in the system. Increasing R yields a vanishing of the error floor and a slight SNR gain, which might be higher for better coding schemes.

In turn we can conclude that the product of the code rate and spreading sequence length determines whether or not the frame BP is able to reliably detect. This result is commonly known from chip interleaved systems, where the length of the spreading sequence, on the one hand, and the code-rate, on the other hand, determine the resources within the system [PLWL04]. However, it might be the case that stronger codes achieve better results and allow for detection with even fewer observations.

The frame length on the other hand determines the performance of the SPE. Fig. 4.9 (b) plots the influence of the frame length L_F for the same system with a repetition code of $R = 5$, such that the frame BP is able to decode in general as the number of resources $M \cdot R = 100$ is greater than the number of nodes in the system. Surprisingly, the FER degrades in the low SNR regime by increasing L_F while it improves in the high SNR regime. The degradation in the low SNR regime is based on the low decoding capabilities

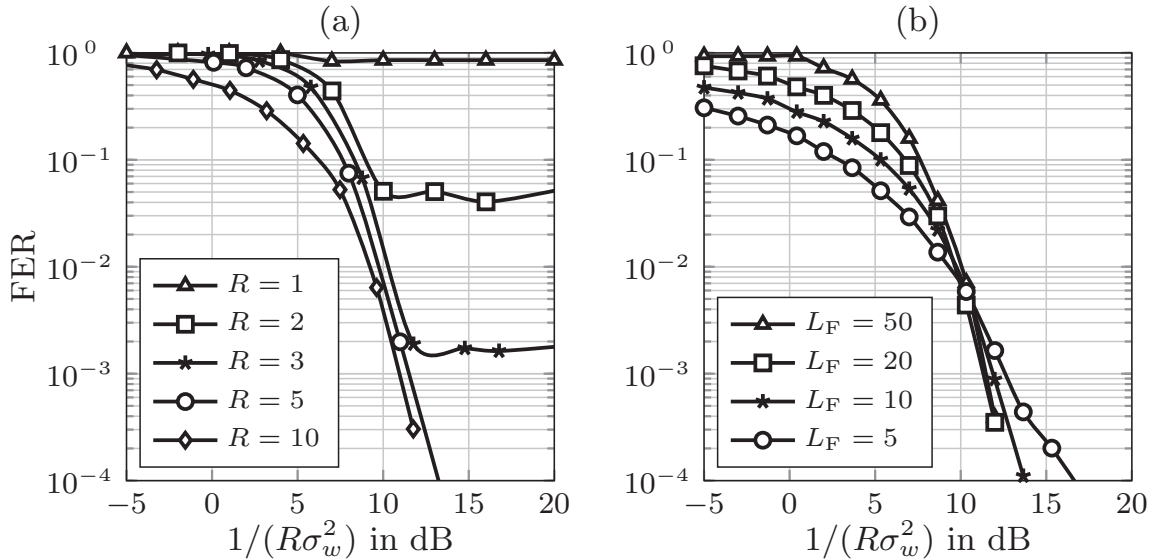


Figure 4.9: Performance of frame BP in a system with $M = 20$, $N = 60$, $p_a = 0.2$ for different repetition factors R with a frame of length $L_F = 60$ in (a) and for different frame lengths L_F over the SNR in a system with a repetition code of $R = 5$ in (b).

in this range. Here the likelihood for decoding errors is relatively high and increasing the frame length (which automatically increases the information symbols) increases the likelihood that at least one information symbol is decoded erroneously causing a frame error. At a certain SNR point this behavior changes. Here the interplay between SPE and decoder changes. Short frames degrade the performance of the SPE which yields activity LLRs of low magnitude. As seen previously in Fig.4.7, these low activity LLRs clip the code symbol LLRs from the multiuser detector to the decoder thereby decreasing the decoder performance. Hence, the decoder can only perform well, if the activity LLRs from the SPE are good enough. However, we see that the performance gain of increasing the frame length is only moderate in the high SNR range, showcasing that short frames already suffice to achieve good activity LLRs at high SNR.

Phase Transition Diagram

In the following we investigate the performance of the frame BP in a wider set of parameters. To this end, we consider the impact of the spreading sequence length and the node activity probability p_a on the FER. This is done by using a modified version of the so-called Donoho-Tanner phase transition diagram [DT09], plotting the tuples of M and p_a , where a FER $< 10^{-3}$ can be achieved. A FER of 10^{-3} would result in a success probability of 99.9% for direct random access, which is a reasonable value for most

applications. However, especially for ultra reliable M2M, different values have to be considered by simulations. The phase transition diagram is plotted for the noise free detection and is thus only states whether detection is possible in general.

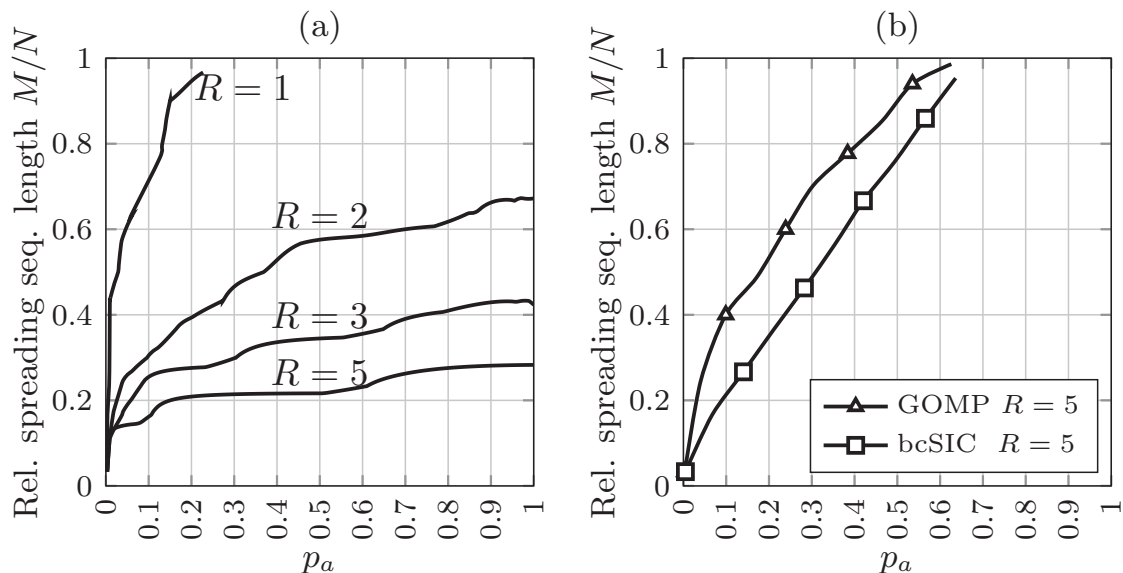


Figure 4.10: Phase transition diagram of frame BP in the noise free case with different code rates in (a) and phase transition diagram for GOMP and bcSIC with a repetition code of $R = 5$ in (b). The number of nodes is $N = 30$ in both cases and the frame length is $L_F = 30$.

Fig. 4.10 (a) plots the phase transition diagram for the frame BP for different repetition factors R . Note that the y -axis shows the relative spreading sequence length M/N , as the results are independent of the particular choice for N and solely depend on the ratio. The curves indicate two significant results. First, decreasing the code-rate by increasing the repetition factor indeed requires lower spreading, thereby confirming the results stated above. Exemplary, with $R = 2$, the spreading sequence length can be much lower than in the previous case. However, one has to keep in mind that the half rate repetition code has to be involved by looking at the number of resources that is required. The same holds true for the lower rate codes with higher repetition factors respectively. Here the spreading required is even lower, showcasing that the frame BP fully exploits the code dimension in order to decrease the spreading sequence length. Fig. 4.10 (b) shows the phase transition diagrams for two state-of-the-art algorithms in the same setup with repetition factor $R = 5$. First, the GOMP with a subsequent decoder stage is used. Second, the bcSIC which is a code exploiting non-linear algorithm from [Sch15] is used. Both algorithms exhibit good detection properties and allow for detection in overloaded systems up to a certain p_a . However, both

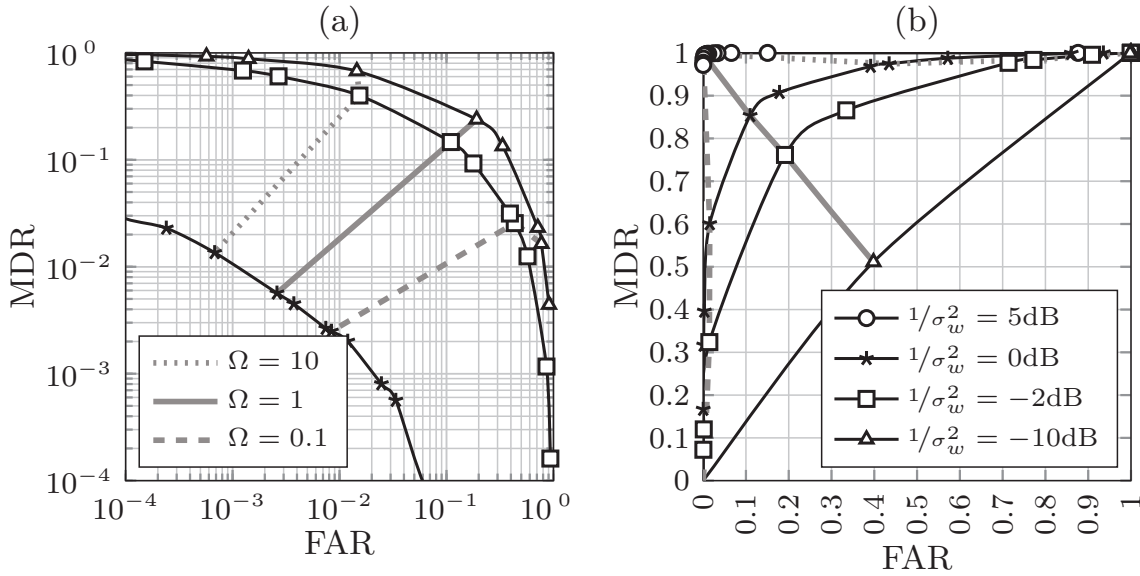


Figure 4.11: Pareto frontiers in (a) and ROC in (b) for a Bayes-Risk activity detector based on activity LLRs taken from an frame BP. In a system with $M = 20$, $N = 15$, $p_a = 0.2$, $R = 1$, $L_F = 30$.

schemes cannot exploit the code-space as a means for resources in the same manner as the frame BP does. This shows that the Frame BP is superior to the GOMP and bcSIC.

4.4.1 Pareto Optimality of the Activity LLRs

Compared to the frame LLRs used at the Bayes-Risk detector from Section 3.4.2, the frame BP yields true frame activity LLRs which capture the statistical process of node (in)activity properly. It is therefore interesting to see, how the activity LLRs of the frame BP perform in terms of being conservative or liberal. We therefore take the frame LLRs at the output of a frame BP and feed them into a Bayes-Risk detector (3.21). The resulting Pareto frontiers and Receiver Operating Characteristics (ROC) are plotted in Fig. 4.11. We see that the activity LLR exhibit a good trade-off between false alarm and missed detection rates. Even with $\Omega = 1$, false alarm and missed detection rates are almost equal. As expected, varying Ω impacts both error rates. However, compared to the frame Bayes-Risk in Section 3.4.2, where a variation on Ω lead to extreme changes in the activity error rates, the impact of Ω is rather moderate. Compared to the Bayes-Risk detector, the calculation of the frame LLRs in the frame BP seems to better capture the underlying probabilistic model of node activity. These results may simplify the application of an ARQ scheme that initiates retransmissions based on the activity LLRs delivered from the frame BP. This question is left for

further research.

4.4.2 Random Sequence vs. Direct Sequence Spreading

Throughout this chapter random sequence spreading was assumed such that the composite signature matrix changes each code symbol. This randomness significantly improves the performance of the activity LLR calculation. The reason for this is that each of the L_F multiuser detectors observes the same sparsity pattern through another matrix \mathbf{A} . Assuming that \mathbf{A} does not change means that the extrinsic activity information each multiuser detector generates is nearly the same. Especially, in the noise free region, each multiuser detector observes nearly the same symbol. If the matrix \mathbf{A} changes each symbol randomly, each multiuser detector observes a different receive symbol \mathbf{y} yielding different extrinsic information. Further, the multiuser interference also changes randomly by applying random sequence spreading.

To demonstrate the impact of random sequence spreading, we consider a setup with $N = 60$ nodes and a spreading sequence length of $M = 20$. The frame length is $L_F = 60$ and the repetition factor is $R = 5$. According to the investigations above, the frame BP yields zero BER at $1/R\sigma_w^2 = 12\text{dB}$. We compare the evolution of the activity LLRs L_a within the frame BP over the number of iterations carried out in a system with $N_{\text{act}} = 4$ active nodes. Fig. 4.12 (a) shows that in case random sequence spreading, the activity

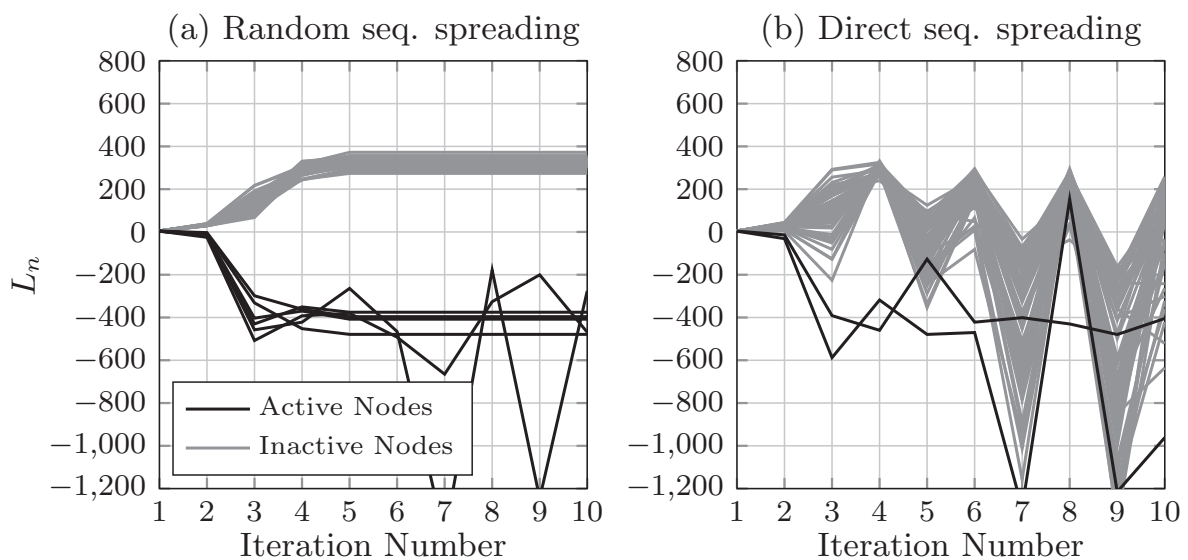


Figure 4.12: Evaluation of the activity LLRs within a frame BP over the number of iterations carried out for random sequence spreading in (a) and with direct sequence spreading in (b).

LLRs for active nodes fast turn negative, while the remaining activity LLRs turn positive. Additionally, we see that the evaluation of the activity LLRs is rather stable with increasing number of iterations. This behavior is not true with short spreading yielding to a non changing composite signature matrix. Here all activity LLRs are subject to strong variations, yielding a high uncertainty about the node activity. Consequently, we observe that the frame BP yields huge performance gains with changing signature matrices.

4.5 Chapter Summary

Within this chapter we have shown an iterative soft processing algorithm that jointly estimated the activity and the data of nodes in CS-MUD. This frame belief propagation algorithm is based on the recent advances of message passing in the field of Compressed Sensing. The algorithm shown augments state-of-the-art solutions by processing soft information from a channel decoder and from an activity estimator jointly. Therefore, the frame BP consists of three entities accounting for the estimation of the multiuser signal, the information bits and the activity states of the nodes. These entities exchange extrinsic information and do not perform any hard estimation. Hence, the information symbols from all nodes (active and inactive) are estimated. This leads to the fact that missed detection errors can not be distinguished from frame errors. However, the activity probability of the nodes can also be calculated by taking the respective activity LLRs that the frame BP calculates.

It could be shown that the frame BP enables exploiting the channel code for decreasing the number of observations in CS-MUD. The results shown applied a repetition code with repetition factor R . It was shown that increasing R allows decreasing the number of observations by decreasing the spreading sequence length M . Consequently, the system load β can be increased by choosing a low rate channel code. Further, it was shown that the algorithm requires random sequence spreading sequences as they yield random multiuser interference that changes each symbol. As shown via simulations, random sequence spreading is necessary to ensure convergence of the activity LLRs.

Chapter 5

Multuser Energy Detection

5.1 Overview

The previous two chapters focused on optimally detecting activity and data in CS-MUD. Both chapters showed that exploiting knowledge about frame activity yields performance gains in the detection. However, especially the optimal activity detection concepts presented in Chapter 3 suffered from the bias contained in the activity LLRs for frame-based transmissions. Further, the algorithms presented were optimized for finite alphabet source data which requires perfect Channel State Information (CSI) which may be an issue in a practical system with a massive number of nodes only sporadically transmitting data. Another point is the complexity while K-Best detection is a viable approach for decreasing the complexity of tree search algorithms, the frame BP shown had a tremendous complexity due to the iterative message exchange.

For addressing the detection in systems with a massive number of nodes, these points have to be taken into regard, therefore raising demand for low-complexity and robust algorithms with practical applicability. The aim of this chapter is to focus on these points and to close the gap between theory and practice by formulating low-complexity and robust algorithms that can be implemented in a system, thereby, leveraging the formulation of a practical system based on CS-MUD as presented in Chapter 6.

We therefore consider separate activity and data detection in a two stage setup. The idea followed in this chapter is to focus on activity detection algorithms for frame-based systems by looking at the received energies of

the nodes. This is facilitated by looking at the receive covariance matrix at the base-station and goes back to the concept of energy detection which is a commonly known concept with wide applicability. The main idea of energy detection is to estimate the presence of unknown signal from a noisy observation. Thus, the idea followed here is to apply this concept to CS-MUD to estimate the node activity by estimating the presence of a node.

However, the straightforward application of the energy detection concept to CS-MUD is not possible due to the under-determined multiuser system. To still enable energy detection in CS-MUD it is necessary to estimate all energies for all nodes in the system from a superimposed multiuser signal. To address this task, the heart of the energy detector for CS-MUD is a block that estimates the individual node energies from the receive covariance matrix at the base-station. Subsequently, we call this block *multiuser energy estimator*. The multiuser energy estimator estimates the support set $\mathcal{S}_{\mathbf{X}}$ based on the receive covariance matrix. This estimated support set is then forwarded to a data detector, thereby, following a two step activity and data detection.

Applying energy detection concepts for CS-MUD has several advantages. First, we have a direct estimation of the frame support $\mathcal{S}_{\mathbf{X}}$ without looking at the multiuser symbols \mathbf{X} . This renders the underlying estimation problems for the multiuser energy estimation task *simple* as we only have to estimate N energies instead of $N \times L_F$ multiuser symbols. Second, energy detection based on the receive covariance matrix averages out the noise. This yields an SNR enhancing effect depending on the length of the time duration the receive covariance matrix is estimated. This has tremendous impact already with short frames of a few hundred symbols. Further it makes activity error rate control superfluous as the activity detection is already sufficiently good at very low SNR regions where data detection is not feasible. Third, as shown in this chapter, energy detection can even be applied in systems where the instantaneous receive power is not fully known to the base-station. This enables robust activity detection in setups with imperfect power control or fast fading.

We start by reviewing the general concept and the application of energy detection in Section 5.2. Further, in Section 5.4 we consider three different algorithms tailored for the energy estimation task in AWGN and the fading channel. Starting with a novel low complexity greedy Matrix Matching Pursuit (MMP) that is motivated by the well known OMP we investigate the performance of the well known MUSIC algorithm for the multiuser energy estimation task. Finally, we also consider solving the MAP optimization problem which incorporates the particular fading environment as prior probability. The MAP problem for the AWGN channel is a finite alphabet

problem and solvable by non-linear tree search approaches such as K-Best. However, for fading channels approximations have to be made in order to enable a convex problem formulation that can be solved by state-of-the-art solvers.

Section 5.5 contains the numerical evaluation via simulations. For the AWGN channel, we will show that MAP estimation allows for reliable multiuser energy estimation with $M = \sqrt{N}$ observations only, which is a remarkable result. However, especially in fading channels, the MAP approach sacrifices optimality due to approximations made during the derivation. Surprisingly, the MUSIC algorithm performs well in fading and in AWGN channels yielding a good trade-off between robustness and optimality. The introduced MMP suffers optimality in the fading channel and can only be applied for AWGN channels. Further, it can be shown that the SNR enhancing effect outperforms state-of-the-art algorithms such as the GOMP.

The results and schemes for the AWGN channel introduced in this chapter have been published in [MBD14]. Augmenting these concepts to the fading channel is a novel contribution solely contained in this thesis.

5.2 Problem Statement and State of the Art

The goal of the algorithms introduced within this chapter is to infer the frame support $\mathcal{S}_{\mathbf{X}}$ from a frame of observations at the base-station. Further, direct sequence spreading is applied such that we can use the frame-based model (2.5) to describe the receive signal at the base-station

$$\mathbf{Y} = \mathbf{A}\mathbf{X} + \mathbf{W}. \quad (5.1)$$

Further, the channel tap which is subsumed within the composite signature matrix \mathbf{A} via $\mathbf{A} = \underline{\mathbf{A}}\mathbf{H}$ may not be known to the base-station. The reason for this assumption is to formulate reliable algorithms with practical applicability that may suffer from imperfect power control or fast fading. To still enable robust multiuser energy detection we subsume the channel coefficient into the matrix containing the multiuser signals via $\tilde{\mathbf{X}} = \mathbf{H}\mathbf{X}$. Hence, the rows of $\tilde{\mathbf{X}}$ contain the modulation symbol weighted with the node specific channel tap. Both are unknown to the base-station. In summary the estimation problem reads

$$\mathbf{Y} = \underline{\mathbf{A}}\tilde{\mathbf{X}} + \mathbf{W}. \quad (5.2)$$

The ideas presented to solve (5.2) consider the energy detection task in CS-MUD. This is a combination of well known energy detection and Compressed Sensing. The state-of-the-art, thus, briefly reviews the advances from both disciplines.

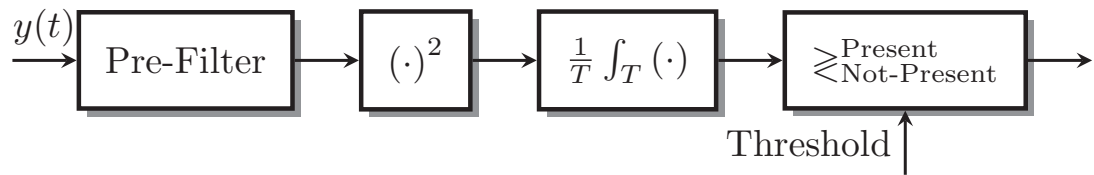


Figure 5.1: Block diagram of energy detection.

5.2.1 Energy Detection

The main idea of energy detection originates back to the task of detecting the presence of an unknown signal in a noisy environment [Urk67, DAS07]. Based on the received energy, the energy detector performs a binary hypothesis test that estimates whether the signal is present or not. The received energy over a certain time period is thereby used as input statistic of the hypothesis test. The basic principle of energy detection is relatively simple and shown in Fig. 5.1. Based on some knowledge about the signal of interest the energy detector consists of a filter that filters out the band of interest followed by a squaring device¹ that squares the input signal which is then fed into an integrator. Depending on the time the signal is integrated over the output corresponds to the received energy in that time interval². If the signal of interest is present, the received energy is composed of the energy of that particular signal plus the accumulated noise energy. If the signal is not present, the output contains the noise energy only. The goal is to define a threshold that performs an estimation whether the signal was present or not. Depending on this threshold the corresponding false alarm and missed detection probabilities of the energy detector are defined.

Due to the recent research in the field of Cognitive Radio, where spectral holes have to be identified, energy detection experienced an upswing. Here energy detection concepts were reinvented under the name *radiometry* to detect the spectral occupation of a band [SF92, HSCCK06, ZKL08]. Beyond that sub-Nyquist sampled energy detection has been investigated as a strategy to estimate the spectral occupation in Cognitive Radio, combining energy detection concepts with the idea of sub-Nyquist sampling from the field of Compressed Sensing [ME11, CE16, CE14]. This idea is picked up in Subsection 5.4.3 for MAP multiuser energy estimation.

Furthermore, energy detection was also used in the field of communications. Here concepts were used to estimate the set of active users in CDMA systems.

¹Sometimes also called square law device

²Depending on whether the signal is normalized to the time period where the integration is carried out the power is considered instead of energy. Since both only differ in a scaling factor the statistical properties do not change and the term energy detector is kept.

The concepts used there range from subspace methods via MUSIC [WC98] to Kalman filtering and random set theoretic approaches [VM13]. Especially sub-space based concepts are of major interest as the underlying estimation problem is based on the receive covariance matrix. Thus, the MUSIC approach considered in Subsection 5.4.2 is based on state-of-the-art concepts. The major difference to the state-of-the-art concepts is to consider the application of MUSIC in overloaded systems.

5.2.2 Multiple Measurement Vector Compressed Sensing

The energy detection task via the receive covariance matrix has not been directly considered in the Compressed Sensing literature. In Compressed Sensing the problem of estimating variables with a common support as (5.2) refers to the so-called Multiple Measurement Vector Compressed Sensing (MMV-CS) problem. Solving the MMV-CS model (2.5) is a commonly known problem [CREKD05]. However, instead of only estimating the frame support $\mathcal{S}_{\mathbf{X}}$ as pursued here, MMV-CS algorithms aim at estimating the whole matrix $\tilde{\mathbf{X}}$, which is a quite more complex task than the estimation of the frame support only. Among the numerous algorithms existing for MMV-CS problems we employ the GOMP subsequently as a benchmark to assess the performance of multiuser energy detection. The application of the GOMP in CS-MUD has been extensively studied in the past [SD12] where it was used to jointly detect activity and data. The GOMP algorithm is shown in Listing 5.1 and is a straightforward extension of the single measurement OMP algorithm to the MMV-CS case.

Akin to the OMP, the GOMP is an iterative and greedy algorithm that identifies active users by correlating the signature matrix with the residual, corresponding to the received signal in the first iteration. The node corresponding to the column of \mathbf{A} with the highest correlation is assumed to be active and the data of that particular node is estimated in a least-squares sense. In the next step, the residual is updated by subtracting the contribution of the nodes that have been estimated as active. The algorithm proceeds by correlating the signature matrix with the residual. Clearly, this approach is heuristic and greedy as an activity decision is never revised during the iterative algorithm. The GOMP produces an estimate for the whole matrix $\tilde{\mathbf{X}}$. Instead of processing the matrix $\tilde{\mathbf{X}}$ we only consider the estimated support set $\mathcal{S}_{\tilde{\mathbf{X}}}$ from the GOMP.

Throughout this chapter we assume genie knowledge of N_{act} at the base station. This assumption is clearly not feasible in general and requires future research. With this knowledge, the GOMP stops after $v = N_{\text{act}}$ iterations,

Algorithm 5.1 Group Orthogonal Matching Pursuit (GOMP)

$\mathbf{R}^0 = \mathbf{Y}$, $\mathcal{S}_{\hat{\mathbf{X}}}^{(0)} = \emptyset$, $v = 0$, $\hat{\mathbf{X}} = \mathbf{0}^{N \times L_F}$
repeat
 $v = v + 1$
 #Find Column with highest correlation to residual#
 $n = \arg \max_n \sum_{l=1}^{L_F} |\mathbf{A}_{(:,n)}^H \mathbf{R}_{(:,l)}|$
 #Update estimated support set#
 $\mathcal{S}_{\hat{\mathbf{X}}}^{(v)} \cup n$
 #Estimate data of active nodes#
 $\hat{\mathbf{X}}_{(\mathcal{S}_{\hat{\mathbf{X}}}^{(v)}, :)} = \mathbf{A}_{(:, \mathcal{S}_{\hat{\mathbf{X}}}^{(v)})}^\dagger \mathbf{Y}$
 #Update residual#
 $\mathbf{R}^v = \mathbf{Y} - \mathbf{A} \hat{\mathbf{X}}_{(\mathcal{S}_{\hat{\mathbf{X}}}^{(v)}, :)}$
until $v = N_{\text{act}}$
#Output#
 $\hat{\mathbf{X}} = \hat{\mathbf{X}}_{(\mathcal{S}_{\hat{\mathbf{X}}}^{(v)}, :)}$, $\mathcal{S}_{\hat{\mathbf{X}}} = \mathcal{S}_{\hat{\mathbf{X}}}^{(v)}$

making the dimensions of the partial system matrix to be $M \times N_{\text{act}}$ in the last iteration. Thus, the complexity of the matrix inversion can be upper-bounded by $\mathcal{O}(N_{\text{act}}^3)$ [GVL12]. Incorporating N_{act} iterations, we have a complexity that scales as $N_{\text{act}} \cdot \mathcal{O}(N_{\text{act}}^3)$.

5.3 Multiuser Energy Detection

To apply the energy detection concept to CS-MUD two problems need to be solved. First, compared to energy detection, where only a single signal is received CS-MUD involves the superposition of multiple signals at the base-station. Therefore, we have to estimate the energy of all N nodes from the received signal \mathbf{Y} . Subsequently, we call this stage multiuser energy estimator. Second, with $M < N$, the system is under-determined with only a limited number of observations leading to additional multiuser interference whose impact on the multiuser energy estimation has to be investigated.

Considering (5.2) clearly shows that squaring the input signal \mathbf{Y} as done in energy detection is not directly possible. Therefore, we follow the concept from [CE16] where the authors introduced a concept for sub-Nyquist power spectral density estimation. This concept uses the receive covariance matrix for estimating the power spectral density in Cognitive Radio.

To use this approach in CS-MUD, we first assume the frame length to

be $L_F \rightarrow \infty$. In this case the receive covariance matrix for frame-based transmissions (5.2) reads

$$\Phi_{YY} = E(\mathbf{y}_l \mathbf{y}_l^H) = \mathbf{A} \mathbf{P}_{XX} \mathbf{A}^H + \sigma_w^2 \mathbf{I}_M. \quad (5.3)$$

Here $\mathbf{P}_{XX} = E(\tilde{\mathbf{x}}_l \tilde{\mathbf{x}}_l^H)$ denotes the covariance matrix of the multiuser signals weighted with the node specific channel taps. Assuming uncorrelated symbols, \mathbf{P}_{XX} is a diagonal matrix whose n th diagonal element corresponds to the received power from node n denoted as ρ_n^+ and zero, if the n th node is inactive. This power activity model is analogous the augmented modulation alphabet from chapter 3. Here we write $\rho_n \in \rho_n^+ \cup \{0\}$ to summarize the power from active and inactive nodes. The variable ρ_n^+ denotes the powers from active nodes that has to be positive. Thus, the diagonal elements of \mathbf{P}_{XX} can be used to estimate the activity and the frame support of the nodes. To approach this two steps have to be taken into regard. First, frames have finite length L_F thus the expectation in (5.3) has to be approximated by the sample average. Second, having the estimated receive covariance matrix $\hat{\Phi}_{YY}$, the diagonal elements of $\hat{\mathbf{P}}_{XX}$, have to be estimated, which may be complicated as \mathbf{A} is under-determined.

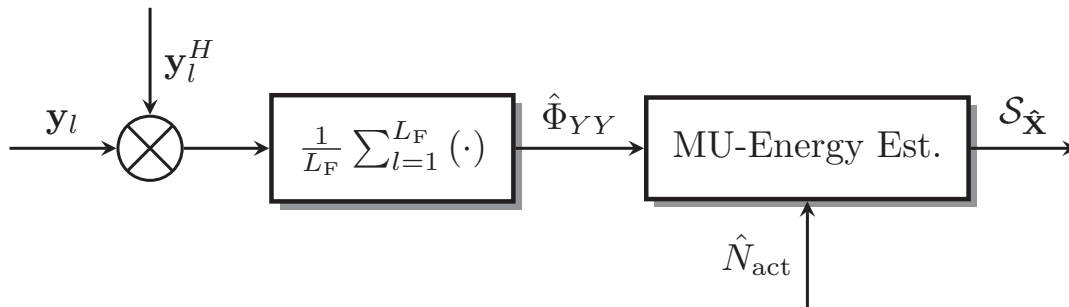


Figure 5.2: Block diagram of multiuser energy detection.

The concept for multiuser energy detection followed here is depicted in Fig. 5.2. First, the receive covariance matrix is estimated by averaging $\mathbf{y}_l \mathbf{y}_l^H$ over L_F symbols. Calculating the outer product $\mathbf{y}_l \mathbf{y}_l^H$ can be seen as a pendant to the square law device in the aforementioned energy detector and averaging over L_F outer products refers to the integration over L_F symbols. However, as stated previously, we have to estimate the individual energies for all N nodes, which is done by the multiuser energy estimator in a subsequent step. The task of this block is to take $\hat{\Phi}_{YY}$ and to estimate the frame support $\mathcal{S}_{\hat{\mathbf{x}}}$. Further this block requires an estimate for the number of active nodes \hat{N}_{act} as input. Based on \hat{N}_{act} the false alarm and missed detection rates of this approach are defined. Within this thesis our focus lies

on the design of different algorithms for the multiuser energy estimation. To achieve benchmark performance among these algorithms we assume \hat{N}_{act} to be known at the base-station. Estimating the number of active nodes via the receive covariance matrix is not generally new. Especially the distribution of the Eigenvalues of the sample covariance matrix yields a good input statistic for this estimation task. For further information the reader is referred to [CW10], where the authors review different approaches for this estimation tasks.

5.4 Concepts for Multiuser Energy Estimation

Subsequently, we consider the multiuser energy estimator whose input signal is the estimated receive covariance matrix $\hat{\Phi}_{YY}$ over a frame of L_F symbols.

$$\hat{\Phi}_{YY} = \frac{1}{L_F} \mathbf{Y}\mathbf{Y}^H = \underline{\mathbf{A}}\hat{\mathbf{P}}_{XX}\underline{\mathbf{A}}^H + \Phi_{WW}. \quad (5.4)$$

Here, the matrix $\Phi_{WW} = \frac{1}{L_F} \mathbf{W}\mathbf{W}^H$ models the sample noise covariance matrix. This matrix obeys the class of Wishart distributions and can be separated as $\Phi_{WW} = \sigma_w^2 \mathbf{I}_M + \Theta$, where $\sigma_w^2 \mathbf{I}_M$ corresponds to the mean of the covariance matrix and Θ is a random variable whose elements have zero mean and variance σ_w^4/L_F [JKB02]. It follows from the law of large numbers that in the limit, $L_F \rightarrow \infty$, Φ_{WW} converges to its mean $\sigma_w^2 \mathbf{I}_M$ while the remaining noise, modeled by Θ converges to zero. A detailed proof based on the law of large numbers is given in Appendix A.3. Here we already see that the frame length L_F has a strong de-noising effect on the estimation task as the random part of Φ_{WW} converges to zero with increasing frame length. We will see in the results that this denoising property allows for very reliable activity estimation in SNR regions, where data detection is not possible. The following subsections introduce different approaches for estimating the diagonal elements of $\hat{\mathbf{P}}_{XX}$, from $\hat{\Phi}_{YY}$.

5.4.1 Matrix Matching Pursuit

To estimate $\hat{\mathbf{P}}_{XX}$, from $\hat{\Phi}_{YY}$ we first consider a straightforward and heuristic approach. More specifically we incorporate a greedy Matching Pursuit (MP) [MZ93] algorithm that iteratively estimates the non-zero diagonal elements of $\hat{\mathbf{P}}_{XX}$. This algorithm is inspired by the OMP and can be seen as an extension thereof. We subsequently denote this algorithm as Matrix Matching Pursuit since the underlying estimation task is over matrix

dictionaries and not as at the OMP over vector dictionaries. To illustrate this idea we expand the detection model (5.4) by neglecting the noise at this point as

$$\hat{\Phi}_{YY} \approx \underline{\mathbf{A}} \hat{\mathbf{P}}_{XX} \underline{\mathbf{A}}^H = \sum_{n=1}^N \rho_n \underline{\mathbf{A}}_{(:,n)} \underline{\mathbf{A}}_{(:,n)}^H. \quad (5.5)$$

Here ρ_n denotes the n th diagonal element of the matrix $\hat{\mathbf{P}}_{XX}$. The outer product $\underline{\mathbf{A}}_{(:,n)} \underline{\mathbf{A}}_{(:,n)}^H$ corresponds to an entry of an over-complete dictionary also known as atom. Expanding $\hat{\Phi}_{YY}$ by (5.5) neglects the off-diagonal elements in the matrix $\hat{\mathbf{P}}_{XX}$, which is true for the limit $L_F \rightarrow \infty$ and an approximation for finite frame lengths.

The pseudo code of MMP is given in Listing 5.2. The MMP correlates the atoms with the sample covariance matrix $\hat{\Phi}_{YY}$ and selects the atom with the highest correlation as active. If the received power of that particular node is known, e.g., in AWGN $\hat{\rho}_n = \rho_n$ can be set, otherwise the received power can be estimated via least-squares estimation. In the next step the MMP subtracts the contribution of the selected atom from the received signal. The algorithm repeats this procedure and correlates the atoms with the updated received signal and selects the next atom in the same manner as described before. The MMP algorithm repeats this procedure until a pre-defined stopping criterion is met. This stopping criterion depends on the estimate for N_{act} . With genie knowledge we stop after $v = N_{\text{act}}$ iterations.

The main advantage of the MMP is its low complexity and simplicity. The pseudo code of this algorithm shows that it mainly consists of a correlator bank composed of N different correlators identifying the node with the highest received power. Depending on whether the received power of the node is known the estimation consists of the calculation of a single pseudo inverse of the partial system matrix $\underline{\mathbf{A}}_{(:,\mathcal{S}_{\mathbf{x}}^{(v)})}$ per iteration. The algorithm stops after $v = N_{\text{act}}$ iterations, making the dimensions of the partial system matrix to be $M \times N_{\text{act}}$ in the last iteration. Thus, the complexity of the matrix inversion can be bounded by $\mathcal{O}(N_{\text{act}}^3)$ [GVL12]. Incorporating N_{act} iterations, we have a complexity that scales as $N_{\text{act}} \cdot \mathcal{O}(N_{\text{act}}^3)$, which is the same as for the GOMP. However, in pure AWGN channels the complexity is much lower, as no matrix inversion has to be carried out.

5.4.2 Multiple Signal Classification (MUSIC)

Another and also heuristic approach to estimate the node activity is to look at the Eigenvalue decomposition of the receive covariance matrix. This approach is commonly known as MUSIC algorithm which originates from the field of direction of arrival estimation in the array processing [Sch86].

Algorithm 5.2 Matrix Matching Pursuit (MMP)

```

 $\mathbf{R}^0 = \hat{\Phi}_{YY}, \mathcal{S}_{\hat{\mathbf{x}}}^{(0)} = \emptyset, v = 0, \hat{\mathbf{P}}_{XX} = \mathbf{0}^{N \times N}$ 
repeat
   $v = v + 1$ 
  #Matrix correlation#
   $n = \arg \max_n \underline{\mathbf{A}}_{(:,n)}^H \mathbf{R}^{v-1} \underline{\mathbf{A}}_{(:,n)}$ 
  #Update estimated support set#
   $\mathcal{S}_{\hat{\mathbf{x}}}^{(v)} \cup n$ 
  if {Receivd Powers are known} then
     $\hat{\mathbf{P}}_{XX,n,n}^v = p_n$ 
  else
    #Estimate receive power of active nodes#
     $\hat{\mathbf{P}}_{XX, \mathcal{S}_{\hat{\mathbf{x}}}^{(v)}, \mathcal{S}_{\hat{\mathbf{x}}}^{(v)}}^v = \underline{\mathbf{A}}_{(:, \mathcal{S}_{\hat{\mathbf{x}}}^{(v)})}^\dagger \hat{\Phi}_{YY} \underline{\mathbf{A}}_{(:, \mathcal{S}_{\hat{\mathbf{x}}}^{(v)})}^{\dagger H}$ 
  end if
  #Update residual#
   $\mathbf{R}^v = \hat{\Phi}_{YY} - \underline{\mathbf{A}} \hat{\mathbf{P}}_{XX}^v \underline{\mathbf{A}}^H$ 
until  $v = N_{\text{act}}$ 
#Output#
 $\{\rho_n\}_1^N = \mathbf{dg} \left( \hat{\mathbf{P}}_{XX}^v \right)$ 

```

The application of MUSIC to multiuser detection has been introduced in [WC98]. There, the authors used MUSIC to estimate the set of active nodes in a CDMA system. The application refers to an activity detection in CDMA which is the same as here. While the authors rather considered non-overloaded CDMA systems, we address applying MUSIC to CS-MUD involving under-determined systems with sporadic node activity. Thus, the results presented here yield another viewpoint of the application of MUSIC.

The idea of MUSIC is to perform an Eigenvalue decomposition of the sample covariance matrix $\hat{\Phi}_{YY}$ and to separate between noise and signal subspace. We now briefly review the general ideas of MUSIC and its application to estimate the node activity in CS-MUD. The Eigenvalue decomposition of the covariance matrix yields,

$$\Phi_{YY} = \underline{\mathbf{A}} \mathbf{P}_{XX} \underline{\mathbf{A}}^H = \mathbf{U} \Lambda \mathbf{U}^H \quad (5.6)$$

where Λ is a diagonal matrix and $\mathbf{dg}(\Lambda) = [\lambda_1, \dots, \lambda_{N_{\text{act}}}, 0, \dots, 0_M]^T$ contains $N_{\text{act}} \leq M$ nonzero Eigenvalues in descending order on the main diagonal. The remaining diagonal elements are zero. Each active node leads to one non-zero eigenvalue in Λ . The matrix \mathbf{U} contains M orthonormal Eigenvectors

that span the column space of the matrix $\underline{\mathbf{A}}$ which also corresponds to the vector space of the received signal. This vector space is composed of signal and noise. Consequently, the noise covariance matrix $\Phi_{WW} = \sigma_n^2 \mathbf{I}_M$ can also be represented using the *same* eigenvectors as

$$\sigma_w^2 \mathbf{I}_M = \sigma_w^2 \mathbf{U} \mathbf{U}^H. \quad (5.7)$$

Hence, we can write for the receive covariance matrix

$$\Phi_{YY} = \sum_{i=1}^{N_{\text{act}}} \lambda_i \mathbf{u}_i \mathbf{u}_i^H + \sigma_w^2 \sum_{i=1}^M \mathbf{u}_i \mathbf{u}_i^H \quad (5.8)$$

$$= \underbrace{\sum_{i=1}^{N_{\text{act}}} (\lambda_i + \sigma_w^2) \mathbf{u}_i \mathbf{u}_i^H}_{\text{Signal space}} + \underbrace{\sigma_w^2 \sum_{i=N_{\text{act}}+1}^M \mathbf{u}_i \mathbf{u}_i^H}_{\text{Noise space}}. \quad (5.9)$$

Equation (5.9) shows that the N_{act} greatest Eigenvalues of Φ_{YY} identify the active nodes. The corresponding Eigenvectors span the so-called N_{act} dimensional signal space. The remaining $M - N_{\text{act}}$ Eigenvectors span the so-called noise space. Since all Eigenvectors are orthonormal the signal and the noise space are orthogonal vector spaces within the M dimensional vector space. In the following we summarize the noise subspace via the matrix $\bar{\mathbf{U}} \in \mathbb{C}^{M \times M - N_{\text{act}}}$. This separation allows the conclusion that the column vectors in $\underline{\mathbf{A}}$ corresponding to active nodes will likely be part of the signal space and not of the noise space. Therefore, active nodes can be estimated by finding the N_{act} column vectors of $\underline{\mathbf{A}}$ that have least ℓ_2 norm in the noise space. This is facilitated by the so called MUSIC null-spectrum defined as

$$\mathcal{S}_{\hat{\mathbf{x}}} = \{ \{n\}_1^{N_{\text{act}}} : \underset{n}{\operatorname{argmin}} \underline{\mathbf{A}}_{(:,n)}^H \bar{\mathbf{U}} \bar{\mathbf{U}}^H \underline{\mathbf{A}}_{(:,n)} \}. \quad (5.10)$$

Note that this scheme works as long as the number of active nodes N_{act} is smaller than the number of observations M , i.e., $N_{\text{act}} < M$ is a necessary condition. If this condition is violated, the $M - N_{\text{act}}$ dimensional noise subspace is empty and the algorithm fails. Further, it should be noted that the derivation assumed the noise covariance matrix Φ_{WW} to be diagonal. This is true in the limit for $L_F \rightarrow \infty$ and an approximation for finite frame lengths.

Compared to the MMP, the MUSIC algorithm does not distinguish between known and unknown receive powers. In both cases, the algorithm is carried out in the same manner. The pseudo-code of the MUSIC algorithm is summarized in listing 5.3. The MUSIC is an algorithm with wide applicability. Therefore, it is not a surprise that previous works also addressed

Algorithm 5.3 MUSIC

```

Input:  $\hat{\Phi}_{YY}, \underline{\mathbf{A}}, N_{\text{act}}$ 
#Perform eigenvalue decomposition#
 $[\mathbf{U}, \Lambda] = \text{evd}(\hat{\Phi}_{YY})$ 
#Formulate noise sub-space#
 $\bar{\mathbf{U}} = \mathbf{U}_{(:, M - N_{\text{act}} : \text{end})}$ 
#Calculate MUSIC null-spectrum#
 $\mathbf{r} = \text{dg}\left(\left(\underline{\mathbf{A}}^H \bar{\mathbf{U}} \bar{\mathbf{U}}^H \underline{\mathbf{A}}^H\right)\right)$ 
#Sort null-spectrum in ascending order#
IndexSet = sort( $\mathbf{r}$ , 'ascend')
#Output: Estimate frame support#
 $\mathcal{S}_{\hat{\mathbf{x}}} = \text{IndexSet}(1 : N_{\text{act}})$ 

```

estimating the number of unknown signals that we assumed to be known through the knowledge of N_{act} . A promising approach to estimate N_{act} is to consider the sorted distribution of the Eigenvalues. As (5.9) shows the receive covariance matrix has N_{act} Eigenvalues summarizing the active nodes and $M - N_{\text{act}}$ Eigenvalues summarizing noise only. Since the N_{act} Eigenvalues have a higher magnitude, one possibility to distinguish between active and inactive nodes is to consider the derivative of the sorted Eigenvalue distribution. This approach has been discussed in connection of estimating the number of active nodes in the CDMA context [WC98]. However, this point is left for further research.

The complexity of MUSIC is dominated by the calculation of the eigenvalue decomposition of the receive covariance matrix which has a complexity of $\mathcal{O}(M^3)$ [GVL12]. It scales therefore with the spreading sequence length and not with the number of active nodes as the MMP does. As $N_{\text{act}} \leq M$ has to hold it can be assumed that MUSIC has a higher complexity than the MMP.

5.4.3 Approximate MAP Energy Estimation

Within this section we consider the MAP problem for the multiuser energy detection task. We summarize this approach subsequently as Maximum-a-Posteriori Energy Estimator (MAP-E). The MAP-E approach addresses the impact of having a finite frame length which affects the estimated receive covariance matrix $\hat{\Phi}_{YY}$. Especially, the noise covariance matrix is not deterministic and still contains noise. To incorporate this noise in the estimation we address estimating the diagonal elements of $\hat{\mathbf{P}}_{XX}$, from the

noisy observation $\hat{\Phi}_{YY}$. We start by defining the corresponding likelihood function relating $\hat{\Phi}_{YY}$ and $\hat{\mathbf{P}}_{XX}$, and incorporate the prior power probability later on. As we will see throughout this subsection we require certain approximations to end up with a practical algorithm.

The starting point is to consider the main diagonal elements of $\hat{\mathbf{P}}_{XX}$, denoted as $\boldsymbol{\rho} := \mathbf{dg}(\hat{\mathbf{P}}_{XX})$. Describing $\hat{\mathbf{P}}_{XX}$, by its main diagonal is only valid in the limit $L_F \rightarrow \infty$. Therefore, neglecting the off-diagonal elements of $\hat{\mathbf{P}}_{XX}$, is the first approximation required for this derivation. To estimate $\boldsymbol{\rho}$ from $\hat{\Phi}_{YY}$ we first decompose the covariance matrix of the noise according into

$$\begin{aligned}\hat{\Phi}_{YY} &= \underline{\mathbf{A}}\hat{\mathbf{P}}_{XX}\underline{\mathbf{A}}^H + \Phi_{WW} \\ &= \underline{\mathbf{A}}\hat{\mathbf{P}}_{XX}\underline{\mathbf{A}}^H + \sigma_n^2\mathbf{I}_M + \Theta.\end{aligned}\quad (5.11)$$

In (5.11) $\hat{\Phi}_{YY}$ is described as a noisy observation where the noise is summarized in the matrix Θ . This matrix is determined by the statistical properties of the noise sample covariance matrix Φ_{WW} , obeying to a Wishart distribution. In the limit $L_F \rightarrow \infty$ the stochastic part of this variate summarized as Θ diminishes and the mean $\sigma_n^2\mathbf{I}_M$ remains. To model the stochastic part of the Wishart variate we employ a Gaussian approximation with proper mean and variance. According to the derivations carried out in appendix A.3 we approximate the elements of Θ via a symmetric circular Gaussian distribution with zero mean and variance σ_w^4/L_F . Accordingly, the m, m' th element of Θ is assumed to be distributed according to

$$\theta_{m,m'} \sim \mathcal{N}(0, \sigma_w^4/L_F) \quad 1 \leq m \leq M \quad 1 \leq m' \leq M. \quad (5.12)$$

Note, that this approximation keeps mean and variance of $\theta_{m,m'}$, but changes the type of the distribution to a Gaussian variate. Most importantly one should once again note the SNR enhancing effect as the variance of the remaining noise decreases linearly in L_F . The MAP estimate $\hat{\boldsymbol{\rho}}$ for the diagonal elements maximizes the a-posteriori probability $\Pr(\hat{\mathbf{P}}_{XX}|\hat{\Phi}_{YY})$ which is rewritten using the Bayes' rule to

$$\hat{\boldsymbol{\rho}} = \arg \max_{\boldsymbol{\rho} \succeq 0} p_{\hat{\Phi}_{YY}}(\hat{\Phi}_{YY}|\hat{\mathbf{P}}_{XX}) p_{\boldsymbol{\rho}}(\boldsymbol{\rho}). \quad (5.13)$$

The likelihood function $p_{\hat{\Phi}_{YY}}(\hat{\Phi}_{YY}|\hat{\mathbf{P}}_{XX})$ is determined by the statistics of the remaining noise Θ . Due to the approximations made, the likelihood function is proportional to a Gaussian variate according to

$$p_{\hat{\Phi}_{YY}}(\hat{\Phi}_{YY}|\hat{\mathbf{P}}_{XX}) \propto \exp\left[-\frac{L_F}{\sigma_w^4}\|\hat{\Phi}_{YY} - \sigma_n^2\mathbf{I}_M - \underline{\mathbf{A}}\hat{\mathbf{P}}_{XX}\underline{\mathbf{A}}^H\|_F^2\right]. \quad (5.14)$$

From now on we substitute $\bar{\Phi}_{YY} = \hat{\Phi}_{YY} - \sigma_n^2 \mathbf{I}_M$ to ease notation. Note that the optimization problem (5.13) is still dependent on the whole matrix $\hat{\mathbf{P}}_{XX}$, due to the definition of the likelihood function (5.14). With, (5.14) we rewrite (5.13) into a vector optimization problem only depending on the diagonal elements $\boldsymbol{\rho}$, thereby neglecting the off-diagonals. To do so, we introduce an equivalent real valued system description

$$\hat{\boldsymbol{\rho}} = \arg \min_{\boldsymbol{\rho} \succeq 0} \|\tilde{\Phi}_{YY} - \tilde{\mathbf{A}}_1 \tilde{\mathbf{P}} \tilde{\mathbf{A}}_2^T\|_F^2 - \frac{\sigma_w^4}{L_F} \log p_{\boldsymbol{\rho}}(\boldsymbol{\rho}), \quad (5.15)$$

where $\tilde{\Phi}_{YY} = [\text{Re}\{\bar{\Phi}_{YY}^T\}, \text{Im}\{\bar{\Phi}_{YY}^T\}]^T$ is the stacked matrix composed of real and imaginary part of $\bar{\Phi}_{YY}$. The matrices $\tilde{\mathbf{A}}_1$ and $\tilde{\mathbf{A}}_2$ are

$$\tilde{\mathbf{A}}_1 = \begin{bmatrix} \text{Re}\{\underline{\mathbf{A}}\} & -\text{Im}\{\underline{\mathbf{A}}\} \\ \text{Im}\{\underline{\mathbf{A}}\} & \text{Re}\{\underline{\mathbf{A}}\} \end{bmatrix}, \quad \tilde{\mathbf{A}}_2 = \begin{bmatrix} \text{Re}\{\underline{\mathbf{A}}\} & -\text{Im}\{\underline{\mathbf{A}}\} \end{bmatrix}. \quad (5.16)$$

The matrix $\tilde{\mathbf{P}}$ is composed of

$$\tilde{\mathbf{P}} = \begin{bmatrix} \hat{\mathbf{P}}_{XX}, & \mathbf{0}_{N,N} \\ \mathbf{0}_{N,N} & \hat{\mathbf{P}}_{XX} \end{bmatrix}. \quad (5.17)$$

We now rewrite (5.15) into a vector optimization problem by applying the $\text{vec}(\cdot)$ operator to the argument of the Frobenius norm in (5.15). This turns the Frobenius norm into an ℓ_2 vector norm. Additionally, we make use of the identity $\text{vec}(\mathbf{XYZ}) = \mathbf{Z}^T \otimes \mathbf{X} \text{vec}(\mathbf{Y})$ [PP⁺08] which allows us to reformulate (5.15) to

$$\hat{\boldsymbol{\rho}} = \arg \min_{\boldsymbol{\rho} \succeq 0} \left\| \text{vec}(\tilde{\Phi}_{YY}) - \tilde{\mathbf{A}}_2 \otimes \tilde{\mathbf{A}}_1 \text{vec}(\tilde{\mathbf{P}}) \right\|_2^2 - \frac{\sigma_w^4}{L_F} \log(p_{\boldsymbol{\rho}}(\boldsymbol{\rho})). \quad (5.18)$$

Substituting $\boldsymbol{\varphi}_{YY} = \text{vec}(\hat{\Phi}_{YY})$ and $\boldsymbol{\Upsilon} = \tilde{\mathbf{A}}_2 \otimes \tilde{\mathbf{A}}_1$ finally leads to

$$\hat{\boldsymbol{\rho}} = \arg \min_{\boldsymbol{\rho} \succeq 0} \|\boldsymbol{\varphi}_{YY} - \boldsymbol{\Upsilon} \mathbf{B} \boldsymbol{\rho}\|_2^2 - \frac{\sigma_w^4}{L_F} \log(p_{\boldsymbol{\rho}}(\boldsymbol{\rho})). \quad (5.19)$$

Here, the matrix \mathbf{B} is used to obtain the transformation $\text{vec}(\tilde{\mathbf{P}}) = \mathbf{B} \boldsymbol{\rho}$. This matrix is composed of two stacked matrices as

$$\mathbf{B} = \begin{bmatrix} \mathbf{B}_1 \\ \mathbf{0}_{2N,N} \\ \mathbf{B}_1 \end{bmatrix} \quad (5.20)$$

Where the rows $[i(2N + 1) - 2N], i = 1, \dots, N$ of \mathbf{B}_1 contains the i th row of the $N \times N$ identity matrix, while the remaining entries are zero yielding the matrix $\mathbf{B} \in \{0, 1\}^{4N^2 \times N}$. The matrix $\mathbf{\Upsilon B} \in \mathbb{R}^{2M^2 \times N}$ is of rank $\min[M^2, N]$ [CE16]. This fact plays a key role in our scheme as it shows that as long as $N \leq M^2$ holds, $\mathbf{\Upsilon B}$ is of full rank. This is a strong result as $\mathbf{\Upsilon B}$ is invertible if the spreading sequence length equals the square root of the number of nodes in the system. In the results we will see that we can achieve reliable activity detection if $M = \sqrt{N}$ holds.

Determining The Prior Power Probability

Equation (5.19) still depends on the log prior power probability $p_{\boldsymbol{\rho}}(\boldsymbol{\rho})$ which summarizes the node activity model and the distribution of the received power for active nodes. The previously introduced Rician fading channel model (2.2) determines the distribution of the received power from active nodes as [Stü11]

$$\begin{aligned} p_{\boldsymbol{\rho}^+}(\boldsymbol{\rho}^+) &= \prod_{n=1}^N p_{\rho^+}(\rho_n^+) \\ &= \prod_{n=1}^N \frac{1}{\Gamma(\omega)} \frac{\omega}{\bar{\rho}_n} \rho_n^{+(\omega-1)} \exp\left(-\frac{\omega \rho_n^+}{\bar{\rho}_n}\right) \\ \omega &= \frac{(K_{\text{rice}} + 1)^2}{2K_{\text{rice}} + 1}, \end{aligned} \quad (5.21)$$

where K_{rice} is the parameter of the Rician channel model and $\bar{\rho}_n$ is the average receive power coming from the n th node for the time the node is active. As described in Chapter 2, $\bar{\rho}_n$ is assumed to be known to the base-station. In combination with the Bernoulli activity model, the prior power probability including node activity can be found analogous to the derivation of the prior probability given in (3.6) as

$$\begin{aligned} p_{\boldsymbol{\rho}}(\boldsymbol{\rho}) &= \prod_{n=1}^N p_{\rho}(\rho_n) \\ &= (1 - p_a)^{N - \|\boldsymbol{\rho}\|_0} \cdot (p_a p_{\boldsymbol{\rho}^+}(\boldsymbol{\rho}))^{\|\boldsymbol{\rho}\|_0}. \end{aligned} \quad (5.22)$$

In (5.22) PDF of the node power still depends on the joint PDF of the received powers of active nodes $p_{\boldsymbol{\rho}^+}(\boldsymbol{\rho})$ which is weighted with the probability for node activity p_a .

Inserting (5.22) in (5.19) yields

$$\hat{\boldsymbol{\rho}} = \arg \min_{\boldsymbol{\rho} \succeq 0} \|\boldsymbol{\varphi}_{YY} - \mathbf{YB}\boldsymbol{\rho}\|_2^2 + \frac{\sigma_w^4}{L_F} \|\boldsymbol{\rho}\|_0 \log \left(\frac{1 - p_a}{p_a p_{\boldsymbol{\rho}^+}(\boldsymbol{\rho})} \right). \quad (5.23)$$

Depending on the particular fading environment, we can formulate two different MAP-E algorithms. In case of AWGN channels ($K_{\text{rice}} \rightarrow \infty$), the estimation reduces to a finite alphabet problem since the received power is known to be from the finite set $\{0, \bar{\rho}_n\}$, which allows for powerful non-linear detection schemes. If the fading environment, however, turns out to be Rician distributed with non-line-of-sight components, the energy detection problem has to be solved in a continuous valued manner. Here, non-linear detection schemes are far too complex. Therefore, we consider the two extreme cases of Rayleigh fading and AWGN only, thereby capturing the cases of a finite alphabet and a continuous valued estimation problem. This is clearly an approximation, however, the impact of the log prior linearly decreases with the frame length L_F . Therefore it can be assumed that most of the gains for MAP-E are achieved by the formulation of the likelihood function.

Support Estimation

Solving the MAP optimization problem (5.19) gives the estimate for $\hat{\boldsymbol{\rho}}$. To estimate the support set $\mathcal{S}_{\mathbf{X}}$ from $\hat{\boldsymbol{\rho}}$ an additional threshold device is required in order to decide in favor of activity or inactivity. Based on N_{act} that we assume to be fully known to the base-station, this rule is set up such that the nodes corresponding to the N_{act} greatest powers are estimated as active via

$$\mathcal{S}_{\hat{\mathbf{X}}} = \{\{n\}_1^{N_{\text{act}}} : \underset{n}{\operatorname{argmax}} \hat{\rho}_n\}. \quad (5.24)$$

Multiuser Energy Estimation in AWGN Channels

AWGN channels are modeled by setting $K_{\text{rice}} \rightarrow \infty$. In this case, the joint power prior probability can be factorized according to [Stü11]

$$\lim_{K_{\text{rice}} \rightarrow \infty} p_{\boldsymbol{\rho}^+}(\boldsymbol{\rho}^+) = \prod_{n=1}^N \delta(\rho_n^+ - \bar{\rho}_n). \quad (5.25)$$

This makes the prior probability for active nodes deterministic as it is known that the n th active node has a received power of $\bar{\rho}_n$. As a consequence, the energy detection problem can be carried out over a finite alphabet which consists of the known mean received powers of the N nodes, augmented

by zero power for inactive nodes. This means the optimization problem is carried out over the finite set $\{0, \bar{\rho}_n\}^N$. The finite alphabet energy detection problem for AWGN channels thus reads

$$\hat{\boldsymbol{\rho}} = \arg \min_{\boldsymbol{\rho} \in \{0, \bar{\rho}_n\}^N} \|\boldsymbol{\varphi}_{YY} - \mathbf{\Upsilon} \mathbf{B} \boldsymbol{\rho}\|_2^2 + \frac{\sigma_w^4}{L_F} \|\boldsymbol{\rho}\|_0 \log \left(\frac{1 - p_a}{p_a} \right) \quad (5.26)$$

This problem can efficiently be solved using the non-linear detection schemes introduced in Chapter 3, such a K-Best detection or Sphere Decoding. The complexity of this approach is determined by the application of the QR decomposition to the matrix $\mathbf{\Upsilon} \mathbf{B}$ and by the parameter K_{best} . The complexity of the QR decomposition scales cubic with the number of nodes in the system as $\mathcal{O}(N^3)$. Depending on K_{best} , the complexity of the subsequent tree-search approach scales with the size of the finite alphabet. With known transmit powers the number of nodes that is visited by a K-Best detector reads according to (3.45)

$$\sum_{n=1}^N \max [K_{\text{best}}, |2|^{N-n}] \quad (5.27)$$

We see that the application of the QR decomposition and a subsequent tree search algorithm causes a higher complexity than the previous approaches.

Multiuser Energy Estimation in Rayleigh Fading Channels

AWGN channels are only one extreme, where we only have a line-of-sight component without fading. The other extreme case with non line-of-sight components only is modeled by the Rayleigh fading channel, which is obtained by setting $K_{\text{rice}} = 0$ in (5.21). In between we experience Rician fading. For Rayleigh fading channels we can also factorize the joint prior power probability via

$$p_{\boldsymbol{\rho}^+}(\boldsymbol{\rho}^+) = \prod_{n=1}^N \frac{1}{\bar{\rho}_n} \exp \left(-\frac{\rho_n^+}{\bar{\rho}_n} \right) \quad \rho_n^+ \geq 0. \quad (5.28)$$

Inserting (5.28) into (5.23) yields after reformulation

$$\hat{\boldsymbol{\rho}} = \arg \min_{\boldsymbol{\rho} \succeq 0} \|\boldsymbol{\varphi}_{YY} - \mathbf{\Upsilon} \mathbf{B} \boldsymbol{\rho}\|_2^2 + \quad (5.29)$$

$$\frac{\sigma_w^4}{L_F} \|\boldsymbol{\rho}\|_0 \left[\log \left(\frac{1 - p_a}{p_a} \right) + \sum_{n=1}^N \log(\bar{\rho}_n) + \sum_{n=1}^N \frac{\rho_n}{\bar{\rho}_n} \right] \quad (5.30)$$

In the following, we write $\tilde{\rho}_n = \rho_n/\bar{\rho}_n$ as the normalized transmit power of the n th node. As ρ_n and $\bar{\rho}_n$ are both powers that have to be greater of equal to zero, we can also summarize

$$\sum_{n=1}^N \tilde{\rho}_n = \sum_{n=1}^N |\tilde{\rho}_n| = \|\tilde{\boldsymbol{\rho}}\|_1, \quad \tilde{\boldsymbol{\rho}} \succeq 0 \quad (5.31)$$

Still, solving (5.30) is challenging, since it is not convex due to the application of the zero-”norm”. A common approach to tackle optimization problems such as (5.30) is to replace the zero-”norm” by the ℓ_1 -norm. This step is heuristic but has shown good performance and is commonly used in optimizations [BV07]. To illustrate, the impact of replacing the zero-”norm” with the ℓ_1 -norm, is illustratively shown in Fig. 5.3 where the level-sets for the penalty term before and after convex relaxation via ℓ_1 -norm are plotted. In this example the application of the zero-”norm” yields a spike if $\rho_1 = 0$ or $\rho_2 = 0$ holds. This spike causes the levelset of the prior to be non-convex. As shown on the right hand figure, replacing the zero-”norm” with the ℓ_1 -norm replaces the prior by its convex-hull. The impact of this approximation to the result of the optimization problem can not be quantified mathematically. However, previous works have shown that the impact on the solution is minor [BV07]. With ℓ_1 relaxation of (5.30) the energy detection problem

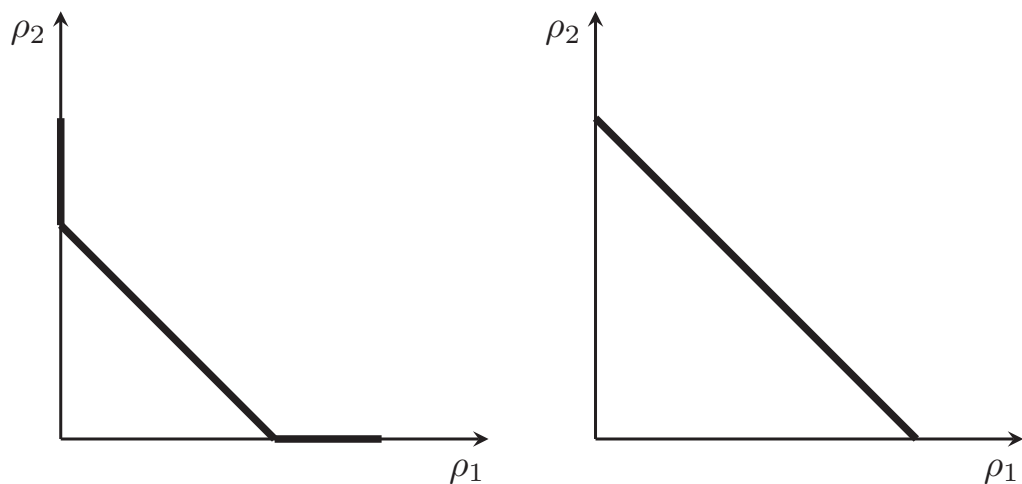


Figure 5.3: Illustration of the level-sets of the penalty term with zero-”norm” (left) and relaxed penalty term with ℓ_1 -norm (right).

for Rayleigh fading channels finally reads

$$\hat{\boldsymbol{\rho}} = \arg \min_{\boldsymbol{\rho} \succeq 0} \|\boldsymbol{\varphi}_{YY} - \mathbf{\Upsilon} \mathbf{B} \boldsymbol{\rho}\|_2^2 + \quad (5.32)$$

$$\frac{\sigma_w^4}{L_F} \|\boldsymbol{\rho}\|_1 \left[\log \left(\frac{1 - p_a}{p_a} \right) + \sum_{n=1}^N \log(\bar{\rho}_n) + \|\tilde{\boldsymbol{\rho}}\|_1 \right], \quad (5.33)$$

which is convex and can be solved by common solvers. If we w.l.o.g. assume that all nodes have the same mean transmit power $\bar{\rho}_1 = \bar{\rho}_2 = \dots = \bar{\rho}_n = 1$, we can further simplify (5.33). In this case we have

$$\hat{\boldsymbol{\rho}} = \arg \min_{\boldsymbol{\rho} \succeq 0} \|\boldsymbol{\varphi}_{YY} - \mathbf{\Upsilon} \mathbf{B} \boldsymbol{\rho}\|_2^2 + \frac{\sigma_w^4}{L_F} \|\boldsymbol{\rho}\|_1 \left[\log \left(\frac{1 - p_a}{p_a} \right) + \|\boldsymbol{\rho}\|_1 \right], \quad (5.34)$$

Within this work, we employ the CVX toolbox from [GBY08, GB08] to solve this problem.

The complexity of this approach is hard to quantify, as it depends on the particular implementation of the convex solver used. Therefore, we do not give a complexity analysis for the MAP-E with Rayleigh prior.

5.5 Performance Evaluation

Subsequently, the performance of the multiuser energy detector employing different multiuser energy estimators is investigated. In contrast to Chapter 3 and 4 we consider the activity detection task in AWGN and Rician fading channels. Beyond sole activity detection the impact on the data detection in a two stage activity and data detector is also considered. As said in the beginning, the GOMP is used as a state-of-the-art algorithm for estimating the common support. Unless stated differently, we employ a base-line parametrization to assess the performance. This base-line parametrization assumes $N = 100$ nodes transmitting 4-QAM symbols with frames of $L_F = 1000$ symbols. Moreover, MMP and MAP-E have finite alphabet and continuous versions, depending on the prior power probability one might outperform the other and there clearly exists a certain break-even point. To preserve clarity, the finite alphabet versions for the MMP and MAP-E are only applied to the pure AWGN case. Whenever fading is considered, the respective continuous versions are employed. Determining the break-even point for both algorithms is left as an open question for future research.

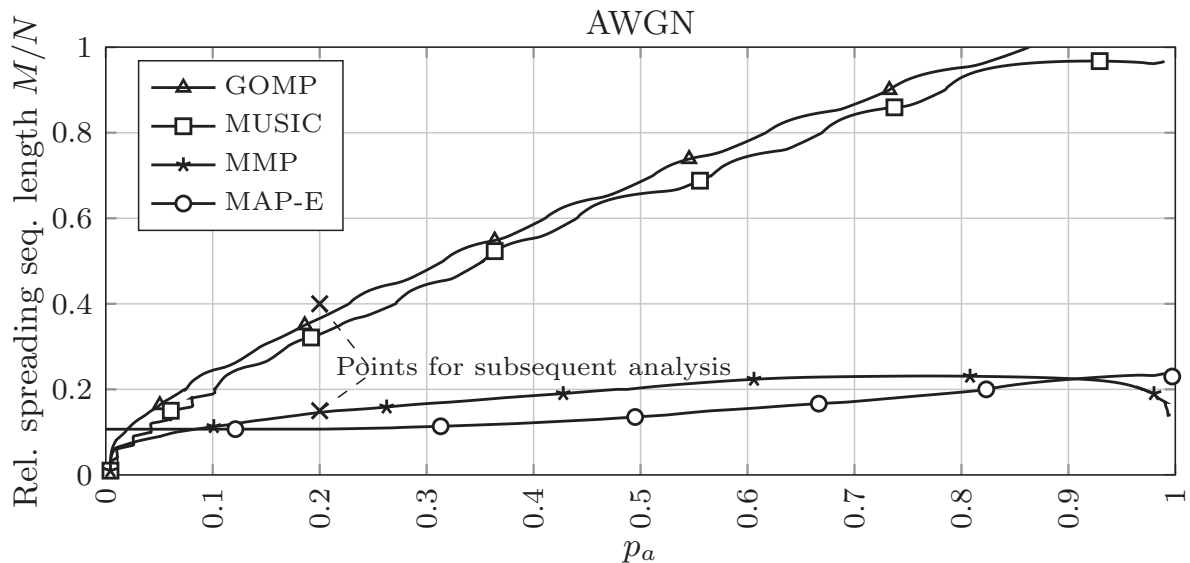


Figure 5.4: Phase transition diagram showing the region under the curve, where an activity error rate below 10^{-3} can be achieved with different multiuser energy estimation algorithms. Lower curves denote superior results.

5.5.1 Performance in AWGN Channels

Phase Transition Diagrams

To assess the capability of the different algorithms with respect to the system load and p_a , we first consider the phase transition diagram in the noise free case in Fig. 5.4 where the region of an Activity Error Rate (AER) below 10^{-3} is plotted. With AWGN channels, the instantaneous received power for all nodes is known. Therefore, it is not a surprise that the MMP and the MAP-E exhibit much better performance than the GOMP and MUSIC as MMP and MAP-E exploit the knowledge of a finite alphabet receive power. The underlying optimization problem for the MAP-E is of full rank as long as $M^2 \geq N$ holds such that N nodes require a spreading sequence length of $M = \sqrt{N}$ only. This is validated as the MAP-E performs well with a relative spreading sequence length of $M/N \approx 0.1$, corresponding to $M = 10$ which matches $M = \sqrt{N} = \sqrt{100}$. With increasing activity probability, the required spreading only increases moderately for the MAP-E. The gap between the MAP-E and the MMP is only moderate and both algorithms exhibit only slight losses from increasing p_a . The curve for the MMP decreases slightly for $p_a \rightarrow 1$, which is a side effect based on the genie knowledge for N_{act} .

Compared to that, the GOMP and MUSIC require higher spreading sequence lengths if the number of nodes increase. This behavior confirms

known results from the GOMP [Sch15]. The MUSIC algorithm shows only slight performance gains over the GOMP. Here we directly see the demand of the MUSIC for $M < N_{\text{act}}$ to ensure a non-empty noise space. Increasing p_a , also increases N_{act} and thus increasing the demand for longer spreading sequences for the MUSIC.

Performance over the SNR

To assess the performance of the algorithms in noisy environments, Fig. 5.5 plots the activity error rates achieved for two significant points from the phase transition diagram that only differ in the spreading sequence length. Fig 5.5 (a) considers a relative spreading sequence length of $M/N = 0.4$. For the GOMP and MUSIC the number of observations is too low and both fail at detecting the activity over the entire SNR range. MAP-E and the MMP enable activity detection and exhibit nearly the same performance, only differing in the error floor that the MMP has at higher SNR showing that the MAP-E approach is superior in this region.

Increasing the relative spreading to $M/N = 0.4$ as shown in Fig. 5.5 (b) removes the error floor of the MMP algorithm, making the performance of MMP and MAP-E to be the same. Further, the GOMP and MUSIC algorithm also show performance gains. Both algorithms converge to low activity error rates, but for higher SNRs. Most interestingly, the MUSIC nearly achieves the performance of the MAP-E and MMP. The SNR gap between these algorithms and the GOMP is significant.

Performance over the Frame Length

The superiority of the multiuser energy estimation algorithms over the GOMP is based on the fact that the noise averages out when the frame length L_F increases. Therefore, the advantage over the GOMP has to be seen in conjunction with the particular frame length. To highlight this effect, we consider the activity error rate over the frame length L_F for a fixed SNR of $1/\sigma_w^2 = 0\text{dB}$. Fig. 5.6 plots the activity error rates for this setup for a relative spreading of $M/N = 0.15$ (a) and $M/N = 0.4$ (b). On the left plot we see a strong decline in terms of activity error rates for the MMP and the MAP-E algorithm, which is almost log linear over the frame length. The error floor for the MMP appears at approximately a frame length of $L_F = 400$ and the MMP does not gain from higher frame lengths, showing that the error floor is not caused by noise, but rather caused by multiuser interference that can not be resolved. In contrast to that the MAP-E yields performance gains as the frame length increases. With longer spreading sequences as shown in Fig. 5.6 (b) we observe a strong decline for

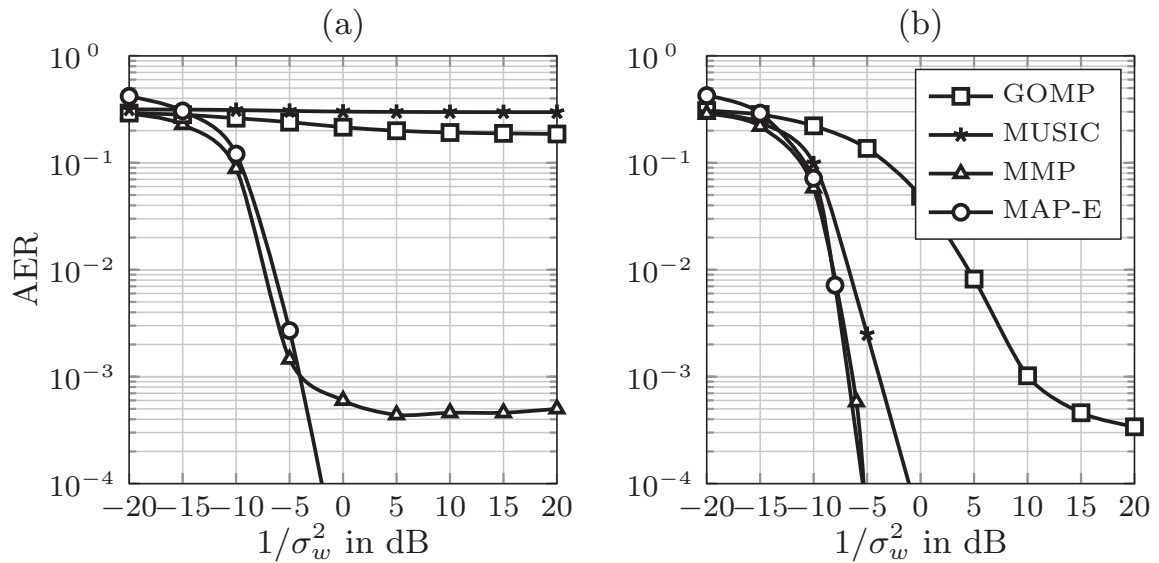


Figure 5.5: Activity Error Rates for multiuser energy estimation algorithms over the SNR in a system with $N = 100$, $L_F = 1000$, $p_a = 0.2$ and a relative spreading of $M/N = 0.15$ (left) and $M/N = 0.4$ (right).

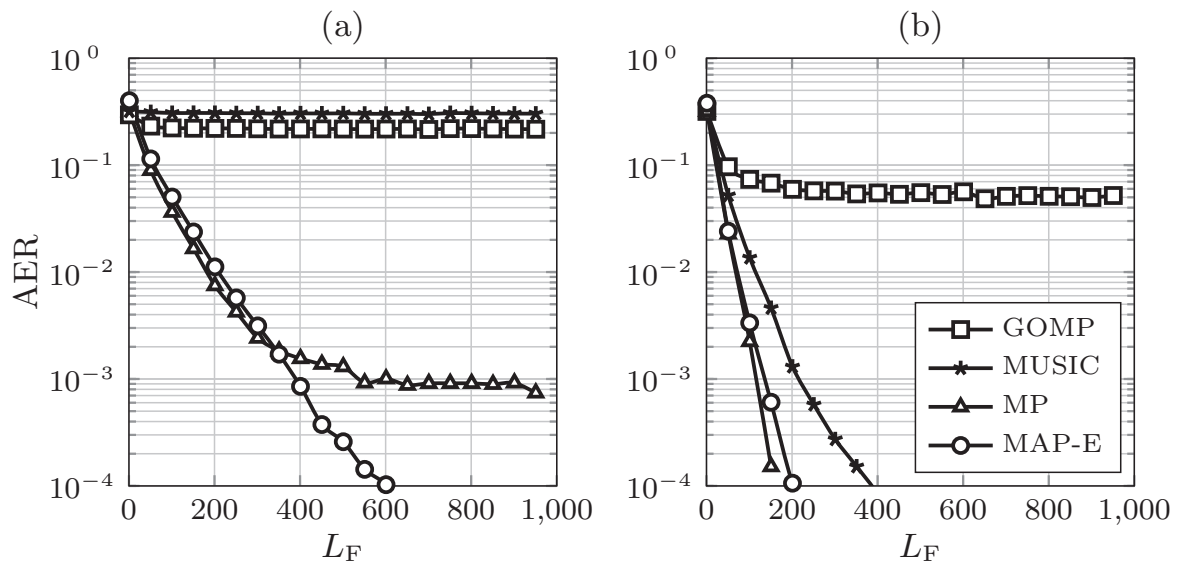


Figure 5.6: Activity Error Rates for multiuser energy estimation algorithms over the frame length L_F in a system with $p_a = 0.2$, $1/\sigma_w^2 = 0$ dB and a relative spreading of $M/N = 0.15$ (left) and $M/N = 0.4$ (right).

all multiuser energy estimation algorithms. This shows the strong denoising property of this approach, which is not exploited by the GOMP achieving only gains for short frames. Both analysis show that the denoising property of multiuser energy estimation is a clear advantage, that can already be expected with short frames of only $L_F \approx 200$ symbols.

Performance Involving Data Detection

The impact of the combination of multiuser energy detection and data detection is briefly discussed in the sequel. Therefore, the multiuser energy detector is followed by a linear least-squares data detector that estimates the data of nodes by solving the reduced multiuser system (2.21) determined by the estimate for the frame support $\mathcal{S}_{\hat{\mathbf{x}}}$. The goal is to call the optimality of $\hat{N}_{\text{act}} = N_{\text{act}}$ into question. Varying this variable by over or underestimating N_{act} impacts the false alarm and missed detection rates. To investigate this impact we set $\hat{N}_{\text{act}} = N_{\text{act}} + \Delta N_{\text{act}}$ and consider the resulting BER. Fig. 5.7 plots the BER for different estimates parametrized by ΔN_{act} at a relative spreading of $M/N = 0.4$ and an SNR of $1/\sigma_w = 10\text{dB}$. The curves

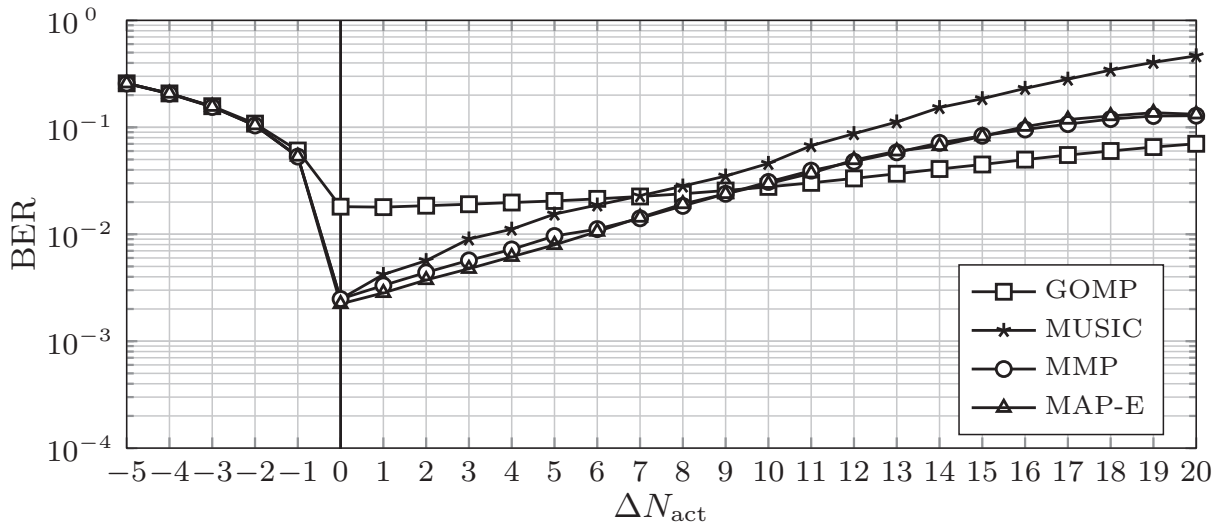


Figure 5.7: BER at the output of a least-squares data detector followed. At a SNR of $1/\sigma_w^2 = 10\text{ dB}$, $M/N = 0.4$.

in Fig. 5.7 show a clear dependence of the BER and N_{act} for all multiuser energy detectors considered. In all cases the optimal value is $\Delta N_{\text{act}} = 0$, which matches the number of active nodes. Decreasing this value yields severe losses in terms of the BER due to the fact that with $\Delta N_{\text{act}} < 0$ missed detection errors occur. Increasing ΔN_{act} leads to false alarm errors, decreasing the BER due to the false alarm SNR loss as highlighted in Section 2.4.4. However, it can remarkably be observed that this SNR loss is rather moderate for the GOMP. The reason can be found by visualizing that the activity detection performance of the GOMP is imperfect at the SNR considered. As shown in 5.5 (b), the GOMP only achieves an AER $\approx 10^{-3}$. Thus, increasing ΔN_{act} does not only increase the false alarm SNR loss it also decreases the missed detection rate. Hence, the false alarm SNR loss is

compensated by the decreased missed detection rate, which has a positive impact on the BER.

The activity detection for MMP, MUSIC and MAP-E is nearly perfect for the SNR considered. Thus, changing ΔN_{act} automatically either leads to a false alarm SNR loss or to missed detections. Applying one of these activity detection algorithms in combination with a least-squares data detector leads to an interference limited data detection. As a consequence, activity error control does not make sense in this setting. We will see that this effect has an even higher dominance in fading channels.

5.5.2 Performance in Fading Channels

Phase Transition Diagram

As stated previously, assuming perfect knowledge about the instantaneous received power is a very optimistic assumption and requires well designed power control algorithms that may not be feasible in practice. Additionally, fading may lead to sudden changes of the received power that is unknown to the receiver. To this end, we subsequently consider multiuser energy detection in Rician fading channels. For the following analysis we employ the continuous version of the MMP and the Rayleigh fading prior version of the MAP-E.

Again we start with the phase transition diagram to assess the performance in the noise free region as depicted in Fig. 5.8. Here the phase transition diagram is plotted for different fading parametrized by the Rice factor K_{rice} highlighting the impact of having a dominant direct path. The extreme case, employing sole indirect fading, i.e., via Rayleigh fading only is also shown.

At a first glance, we observe that throughout all K_{rice} considered, the GOMP and MUSIC exhibit nearly the same asymptotic performance remarkably showing that unknown fading does not change the asymptotic performance of these algorithms. In contrast to that, MMP and MAP-E severely suffer from the fading. Already with $K_{\text{rice}} = 30$, both algorithm exhibit performance losses while the MAP-E still has the best performance among all algorithms considered. Increasing the fading decreases the performance of these two concepts drastically, while for the extreme case of Rayleigh fading MAP-E and MMP fail to recover the frame support. One might think that MAP-E should exhibit superior performance especially in the Rayleigh fading channel due to the prior knowledge. However, one has to keep in mind that MAP-E is the MAP estimator for the power ρ and not for $\mathcal{S}_{\mathbf{x}}$. Here we consider the performance w.r.t. the activity error rates based on $\mathcal{S}_{\mathbf{x}}$ which subsumes the combination with a threshold device. Even though the number of active nodes is fully known to the detector, estimating

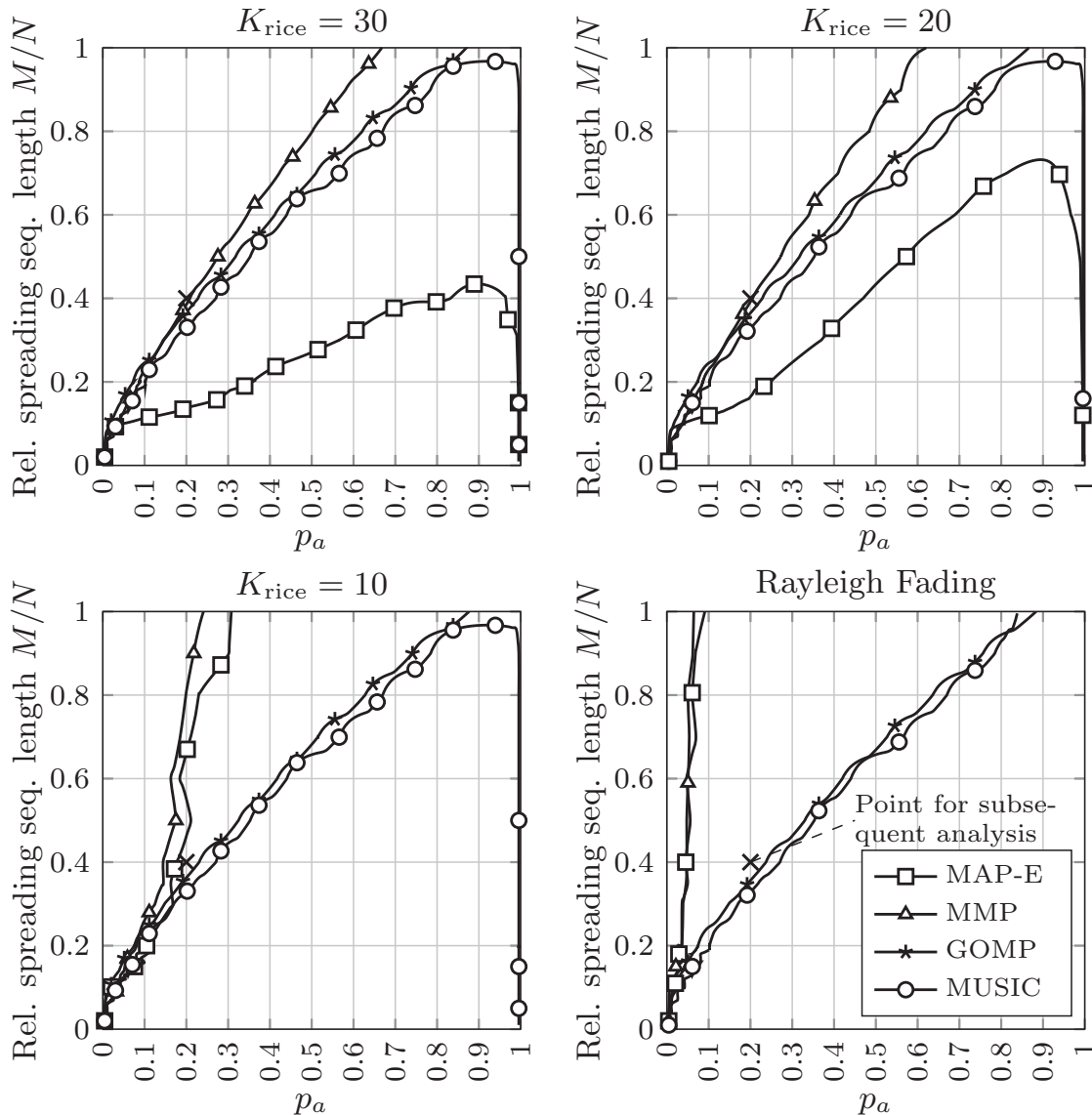


Figure 5.8: Phase transition diagrams showing the region where an activity error rate below 10^{-3} can be achieved for different multiuser energy estimation algorithms employing Rician Channels parametrized by K_{rice} .

the nodes with the N_{act} greatest powers as active might not be optimal.

Performance over the SNR

Since the phase transition diagram only captures the asymptotic performance, we consider two examples where we look at the AER over the SNR. The following analysis restricts to a system with a relative spreading of $M/N = 0.4$ and an activity probability of $p_a = 0.2$. Fig. 5.9 shows the performance of the algorithms introduced over the SNR for a Rayleigh fading channel with no line-of-sight component $K_{\text{rice}} = 0$ (a) and for a channel employing a Rice

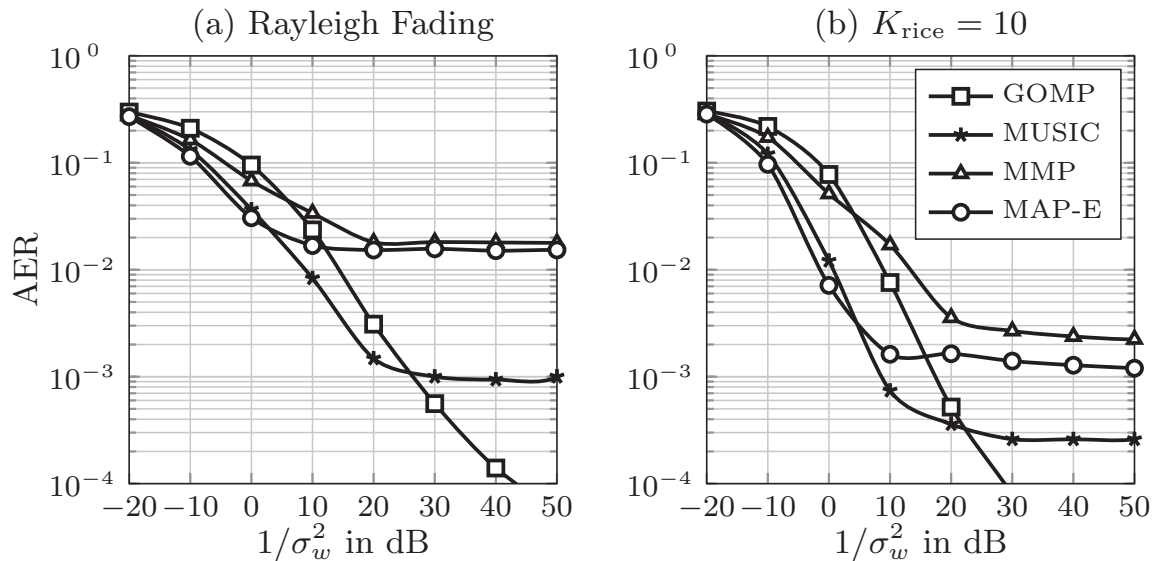


Figure 5.9: Activity error rate over the SNR for different multiuser energy estimators in a system with $N = 100$, $M = 40$, $p_a = 0.2$ yielding a relative spreading of $M/N = 0.4$ for Rayleigh fading channels $K_{\text{rice}} = 0$ on (a) and for Rician fading $K_{\text{rice}} = 10$ (b).

factor of $K_{\text{rice}} = 10$ (b). In the Rayleigh fading channel, all algorithms apart from the GOMP exhibit an error floor. Thereby the results from the phase transition diagram in Fig. 5.8 are confirmed, where only the GOMP and MUSIC are able to achieve an $\text{AER} < 10^{-3}$. The results also show that the MAP-E achieves the lowest AER in the low SNR range but shows an error floor for the mid and high SNR range. From 5.9 (a), MUSIC appears to be a good algorithm for activity detection in Rayleigh fading channels as it exhibits low activity error rates over the low and mid SNR range, while it suffers from a relatively low error floor. In terms of robustness, the GOMP outperforms all other algorithms as the resulting AER declines for increasing SNR. This robustness comes at the cost of an SNR loss of approx. 5 dB in the mid SNR range.

In channels with a dominant line-of-sight component 5.9 (b) the performance characteristics of all algorithms is nearly preserved. The error floors for MAP-E, MMP and MUSIC have decreased compared to the previous analysis. Again the MAP-E shows the best performance in the low and mid SNR range and exhibits an error floor for high SNR. However, the error floor at approx. $\text{AER} = 10^{-3}$ is much lower than in the preceding example, making MAP-E a feasible approach in this setup. The performance of MUSIC is nearly the same as for MAP-E, and only differs in the error floor that is even lower than for MUSIC. Again the GOMP shows a strongly declining AER over the entire SNR range with the drawback of an SNR loss

of approx. 10dB. Nevertheless, this SNR loss has to be seen in the context of fixed frame length of $L_F = 1000$ symbols. As shown previously in Fig 5.6 the SNR gain of MMP, MUSIC and MAP-E increase for longer frames, as the noise is averaged out. This effect does not apply to GOMP in general.

Impact of the Rice Factor

To further highlight the impact of having strong line-of-sight components, Fig. 5.10 shows the performance over the Rice factor K_{rice} at a fixed SNR of $1/\sigma_w^2 = 0\text{dB}$ in (a) and for a higher SNR of $1/\sigma_w^2 = 10\text{dB}$ in (b).

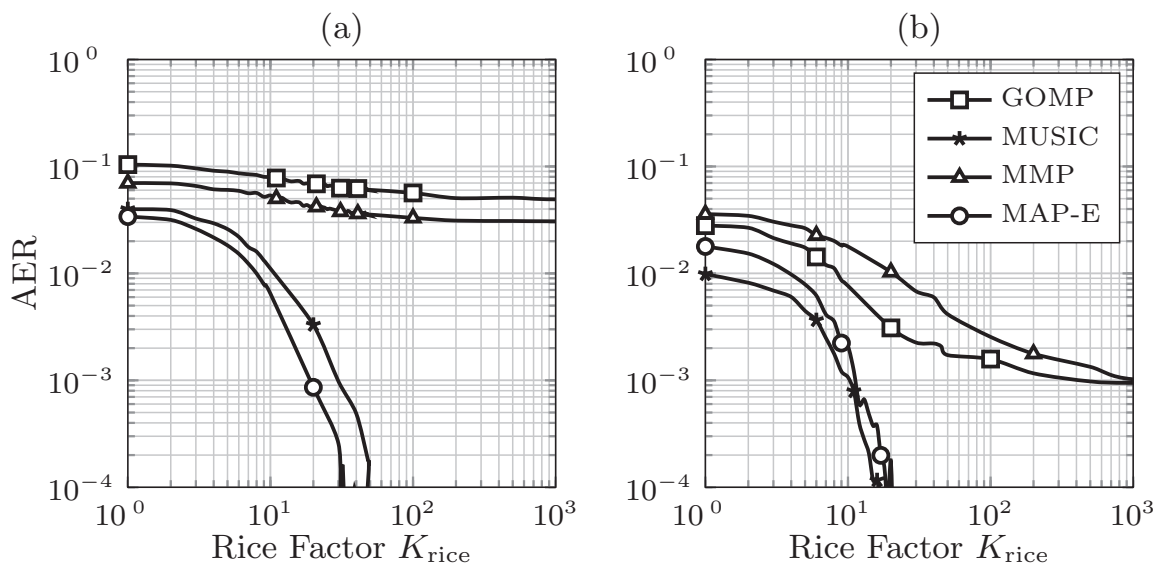


Figure 5.10: Activity error rate over the factor for the Rician fading K_{rice} for different multiuser energy estimators in a system with $N = 100$, $M = 40$, $p_a = 0.2$ yielding a relative spreading of $M/N = 0.4$ for an $1/\sigma_w^2 = 0\text{dB}$ in (a) and an SNR of $1/\sigma_w^2 = 10\text{dB}$ in (b) (b).

Fig. 5.10 (a) shows a strong decline in the AER for the MAP-E and the MUSIC algorithm for an increasing dominance of the line-of-sight component. Here we see that the MAP-E preserves its superiority in the low to mid SNR range for all fading channels considered. For the SNR considered MMP and GOMP fail to estimate the node activity for all fading channels considered. Even with a strong line-of-sight component the AER does not decrease showing that the algorithms are limited by the SNR in this setup. For higher SNR of $1/\sigma_w^2 = 10\text{dB}$, the situation changes. Here the MUSIC algorithm shows a strong gain with strong line-of-sight components. The same holds true for the MAP-E algorithm which exhibits slightly worse performance than MUSIC, but still achieves a strong decline by increasing the dominance of the line-of-sight component. This effect also holds true for the MMP and

the GOMP algorithms but is not that strong and both algorithms rather converge to a constant error rate.

Performance Involving Data Detection

In the following the BER with unknown received power through fading channels is investigated. As above, this setup assumes that the multiuser energy detector has no knowledge about the instantaneous received power from all nodes. The estimated support set $\mathcal{S}_{\hat{\mathbf{x}}}$ is forwarded to a least-squares data detector which estimates the data. Fig. 5.11(a) plots the BER for the Rayleigh fading case with no line-of-sight component summarized via $K_{\text{rice}} = 0$. Fig. 5.11 (b) plots the BER for the Rician fading case parametrized by $K_{\text{rice}} = 10$.

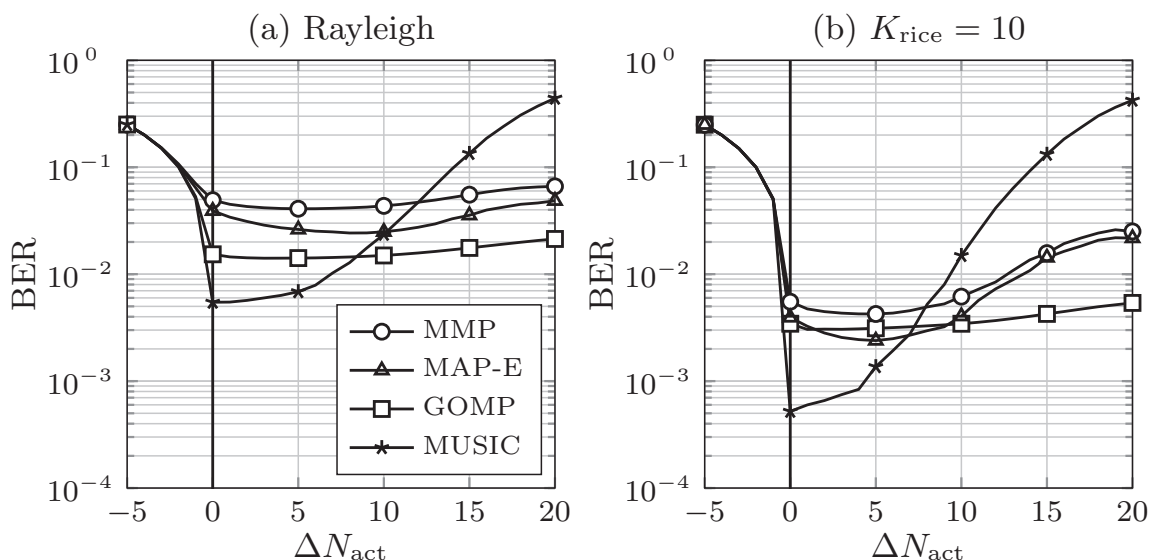


Figure 5.11: BER at the output of a least-squares data detector at a SNR of $1/\sigma_w^2 = 20\text{dB}$, $M/N = 0.4$, $N = 100$ with $K_{\text{rice}} = 0$ on (a) and $K_{\text{rice}} = 10$ on (b).

At a first glance, we also observe that the BER severely degrades for setting $\Delta N_{\text{act}} < 0$, which is obviously caused by missed detection errors as this threshold is lower than the number of active nodes. However, the behavior for setting $\Delta N_{\text{act}} > 0$ differs from the AWGN case. Here, we see that increasing ΔN_{act} indeed decreases the BER. This effect is quite strong for the MAP-E, whose optimal threshold is clearly $\Delta N_{\text{act}} > 0$. The MMP, GOMP and MUSIC also show this behavior. Here we see that the activity detection is imperfect leading to a BER limited by the activity detection. We also see how the false alarm SNR loss can be compensated. Thus, increasing the false alarm rate not only decreases the SNR in this setup, it also decreased the missed detection rate. Obviously, both effects compensate each other

making the requirements for the threshold to be $\Delta N_{\text{act}} > 0$. However, we also observe that this does not hold true for the MUSIC algorithm. Here, we see a moderate increase of the BER in the Rayleigh fading case and a strong increase in the Rician fading channel. This is due to the inherent effect of the MUSIC to degrade if ΔN_{act} is increased. The dimension of the MUSIC null-spectrum over which the activity detection is carried out has a dimension of $M - (N_{\text{act}} + \Delta N_{\text{act}})$. Reducing the dimension of this vector space also decreases the robustness of the algorithm as stated in subsection 5.4.2.

The results above show that, except for MUSIC, overestimating N_{act} does not harm in the fading case. The reason for this lies in the imperfect activity detection. Consequently, the false alarm SNR loss caused by overestimating N_{act} is compensated by the fact that the missed detection rate also decreases.

Discussion and open Questions

The results show that different fading environments require different algorithms. For the AWGN channel, the MAP-E exhibits the best asymptotic AER and the strongest decline over the SNR. Additionally, the MAP-E shows good performance gains for increasing the frame length. A good alternative is the MMP, which nearly achieves the performance of the MAP-E in AWGN channels with the drawback that the asymptotic performance is slightly worse, as shown in the phase transition diagram.

The picture changes in fading channels. Here the GOMP seems to be a good choice in terms of robustness as it exhibits the lowest asymptotic AER in the noise free region in all setups considered. This good asymptotic performance, however, comes at the cost of an SNR loss compared to other algorithms. The performance gains of the MAP-E can only be preserved in the low and mid SNR range.

In the high SNR range the MAP-E exhibits an error floor for the scenarios considered. The winner in fading channels, seems to be the MUSIC algorithm. It exhibits nearly the same asymptotic performance as the GOMP. Additionally, MUSIC preserves a considerable SNR gain over the GOMP at the cost of an error floor. The MMP algorithm neither shows a good asymptotic performance, nor does it show good performance over the SNR. Hence, the application of the MMP is restricted to the AWGN channel.

Additionally, this chapter also showed that activity error rate control can be achieved by over or underestimating N_{act} . Especially in the fading channel an acceptable false alarm SNR loss can cause a decreased missed detection rate, leading to overall lower BER performance.

An open question of this chapter is the estimation N_{act} which we assumed to be optimal. In practical systems N_{act} has to be estimated properly.

Another open point is the switching point between the continuous versions of MAP-E and MMP with their respective finite alphabet versions. This point has not been addressed in this chapter and left for further research. However, it can be assumed that at a certain K_{rice} the finite alphabet versions outperform the continuous pendants due to the prior knowledge applied.

5.6 Chapter Summary

Within this chapter we have focused on low complexity concepts for the frame support estimation in CS-MUD based on energy detection. The application of the energy detection concept to CS-MUD requires the introduction of a multiuser energy estimator that estimates the energies of the nodes from the receive covariance matrix. Here it is shown that estimation based on the receive covariance matrix averages out the noise and yields an SNR gain that is proportional to the frame length considered.

Further, we have introduced three algorithms for the energy estimation task. These are compared to one state-of-the-art approach from Compressed Sensing, the Group Orthogonal Matching Pursuit. The algorithms are tailored to work in both, fading and AWGN channels. The results show that different fading scenarios call for different algorithms. Especially, the pure AWGN channel allows for applying non-linear and finite alphabet techniques that outperform any continuous valued algorithms. However, this picture changes in the fading channel ranging from Rician fading to pure Rayleigh fading channels. Here, we could show that sub-space methods such as MUSIC yield a good trade-off between optimality and robustness as it allows for reliable activity detection in AWGN and in the Rayleigh fading channel. Further it was shown that activity error rate control is superfluous in the AWGN channel as the activity detection carried out by energy detection is perfect in SNR regions where data detection is not feasible. This changes in the fading channel and it is shown that a slightly increased false alarm rate yields performance gains in terms of the data detection. The reason is the imperfect activity detection that produces both false alarm and missed detection errors. Thus, increasing the false alarm rate also decreases the missed detection rate, which yields improved data detection despite the false alarm SNR loss.

Chapter 6

Multi-Carrier Compressed Sensing Multiuser Detection

6.1 Overview

While the previous chapters of this thesis were rather focusing on algorithmic concepts, this chapter aims at putting previous advances in a wider context to formulate a candidate system for massive M2M. We use the concepts and schemes from the preceding chapters to formulate a system that implements CS-MUD and direct random access. As the first step, we formulate key requirements that such a system should meet in order to fulfill the demands for a realistic massive M2M concept. Based on these requirements, we then introduce a system concept that uses CS-MUD techniques in combination with non-coherent receiver structures and multi-carrier concepts. In this so-called MCSM system, the bandwidth is divided into sub-carriers by a multi-carrier system. Subsequently, the nodes employ a spreading of their data-symbols and multiplex the chips to the sub-carriers. In MCSM this multiplexing is carried out such that the chip sequences of the nodes are mapped into the coherence bandwidth of the wireless channel enabling non-coherent receiver concepts, allowing for simple channel estimation and robustness against minor offsets.

The following chapter is divided into three parts. First, in Section 6.3 we identify the key requirements for MCSM and introduce the system concept in Section 6.4 with the corresponding chip to sub-carrier multiplexing. Here

we also address the impact of asynchronicity and show that MCSM allows for a certain degree of robustness. The second part of this chapter, Section 6.5 shows a possible MCSM parametrization and simulatively highlights the activity error rates and the frame error rates. The setup considered assumes a wireless channel closely aligned to industrial applications including a delay spread of $1\mu\text{s}$ and a target data-rate of approx. 12kBit/s per active node. Additionally, we apply the previously introduced multiuser energy detection concepts introduced in Chapter 5 to estimate node activity. The data detection is carried out via least-squares detection. Results show that reliable data detection can be carried out at a system load of $\beta = 3$ nodes per resource at an activity probability of $p_a = 0.1$. The third part of this chapter, Section 6.6 aims at verifying MCSM via a prototype implementation on a hardware demonstrator setup. The implementation consists of a transmitter and a receiver block which allow for over-the-air measurements of MCSM. Here we measure the phase transition diagram of MCSM in a non-line-of-sight scenario with a transmitter to receiver distance of 60 m. The results show a good match between measurement and simulations.

6.2 Relevant Publications and State of the Art

The MCSM concept is a candidate technology for implementing massive M2M in a cellular infrastructure such as networks in the 5G context or in industrial M2M applications. In the past, various technology components for M2M have been proposed in projects such as METIS and 5GNOW. METIS identified direct random access as a key technology component for approaching M2M [MP15a], which is closely aligned with this thesis. Beyond that, novel waveforms are under current discussion and can also be seen as an emerging technology component. Some advances from 5GNOW are summarized in [WJK⁺14].

While novel technology components on the one hand aim to support the applicability of M2M in 5G networks, on the other hand, various works investigate modifying existing infrastructure to support M2M. First and foremost the aggregation of M2M into LTE is still under research. Recent advances in this context were focusing on narrow-band transmissions with limited data-rate and bandwidth [Nok14, RPL⁺15]. Since 2016 the LTE standard incorporates NB-IoT which characterizes different device types for M2M. For ultra low data-rate M2M LTE Rel.13 standardizes devices with 250kBit/s in the uplink, while occupying a bandwidth of only 180kHz . These transmissions can either be multiplexed inside or next to an existing

LTE band, allowing for some degree of coexistence.

Comparing these directions to MCSM is complicated as parameters such as the data-rate depend on the underlying wireless channel and the corresponding delay spread. As MCSM allows for very different modes of operation, a fixed data-rate is hard to formulate. Within the parametrization considered, we have a base data-rate of approx. 12kBit/s per node while occupying a bandwidth of 250 kHz. These numbers cannot be directly compared to the NB-IoT parameters followed in LTE. First, LTE considers single-user uplink, while we have a multiuser uplink consisting of multiple nodes. Second, the MCSM data-rate is a base data-rate for a single MCSM system. As several systems can simultaneously be multiplexed, nodes can be active in more than one system, yielding a multiple of the base data-rate. Third, data-rate and bandwidth are only two parameters that have to be seen in a wider context involving target error rates, throughput, latency and many more.

The work presented in the following combines technology components to a novel narrow-band physical layer system. This system, was first published in [MWBD15b], where the technology components and the general idea was presented. Later in [MWBD15a] we augmented MCSM by channel coding and a method for gaining frequency diversity over the time frame. Practical measurements showing MCSM implemented on a hardware demonstrator have been published in [BMWD15] and [WMBD16] where also measurements of MCSM in an industrial environment was shown. The MCSM system has also been patented under the Patent Cooperation Treaty (PCT) under [MWBD16].

6.3 Problem Statement

Aggregating a massive number of nodes at a central aggregation point requires a refined look at the system specific requirements that have to be taken into regard. Previous chapters only considered the symbol-by-symbol or the frame-based detection model. Here, the focus is wider and we aim at putting this simple and abstract model in an all-encompassing system context, thereby, closing the gap between the previous works of this thesis and a over-the-air transmission with a hardware setup. To start, we identify key requirements that such a system has to address. The following enumeration is only a sub-set of emerging requirements that have been identified by previous research in the M2M context. For a thorough overview the reader is referred to [DSG⁺15, ZOAZ⁺14] and the referenced therein.

1. **Massive Access with low signaling:** In massive M2M one of the main requirements is to handle numerous nodes simultaneously. While

focusing on resolving the multiuser interference of the nodes, the system also has to ensure a certain degree of reliability for the data detection. Additionally, the medium access has to be kept simple with low overhead in terms of signaling.

2. **Sporadic Traffic:** Nodes in massive M2M can be assumed to be only active occasionally, yielding sporadic traffic which yields sporadic medium access. Together, with the aforementioned direct random access, the statistic properties of the sporadic M2M traffic have to be taken into account
3. **Low Pilot Overhead:** Especially, channel estimation should be kept as simple as possible as channel estimation of *many* nodes yields huge pilot overhead. In cases where nodes are inactive for a certain time channel estimation yields huge overhead as the channel has to be estimated prior to each transmission due to outdated CSI.
4. **Scalability:** To ensure flexible aggregation of a varying number of nodes, a system has to be scalable. Scalability means that a system should be able to accommodate varying number of nodes with bounded complexity.
5. **Coexistence:** In terms of optimally, exploiting the resources given a possible system should be able to coexist with other systems such as existing proprietary infrastructure. This requires a flexible time and frequency resource allocation of the M2M traffic.
6. **Low complexity nodes:** In massive M2M nodes are assumed to be *simple* devices with low processing capability and limited battery lifetime. Considering this demands, requires simple transmitter structures. Moreover, while nodes may sleep for a long period, receiving capabilities may be limited.
7. **Robustness:** Since nodes can not be assumed to transmit perfectly synchronized, timing and frequency offsets have to be taken into account into a system design.

6.4 The MCSM System Concept

To formulate a system solving these requirements, we identify three physical layer technologies that address most of the aforementioned challenges.

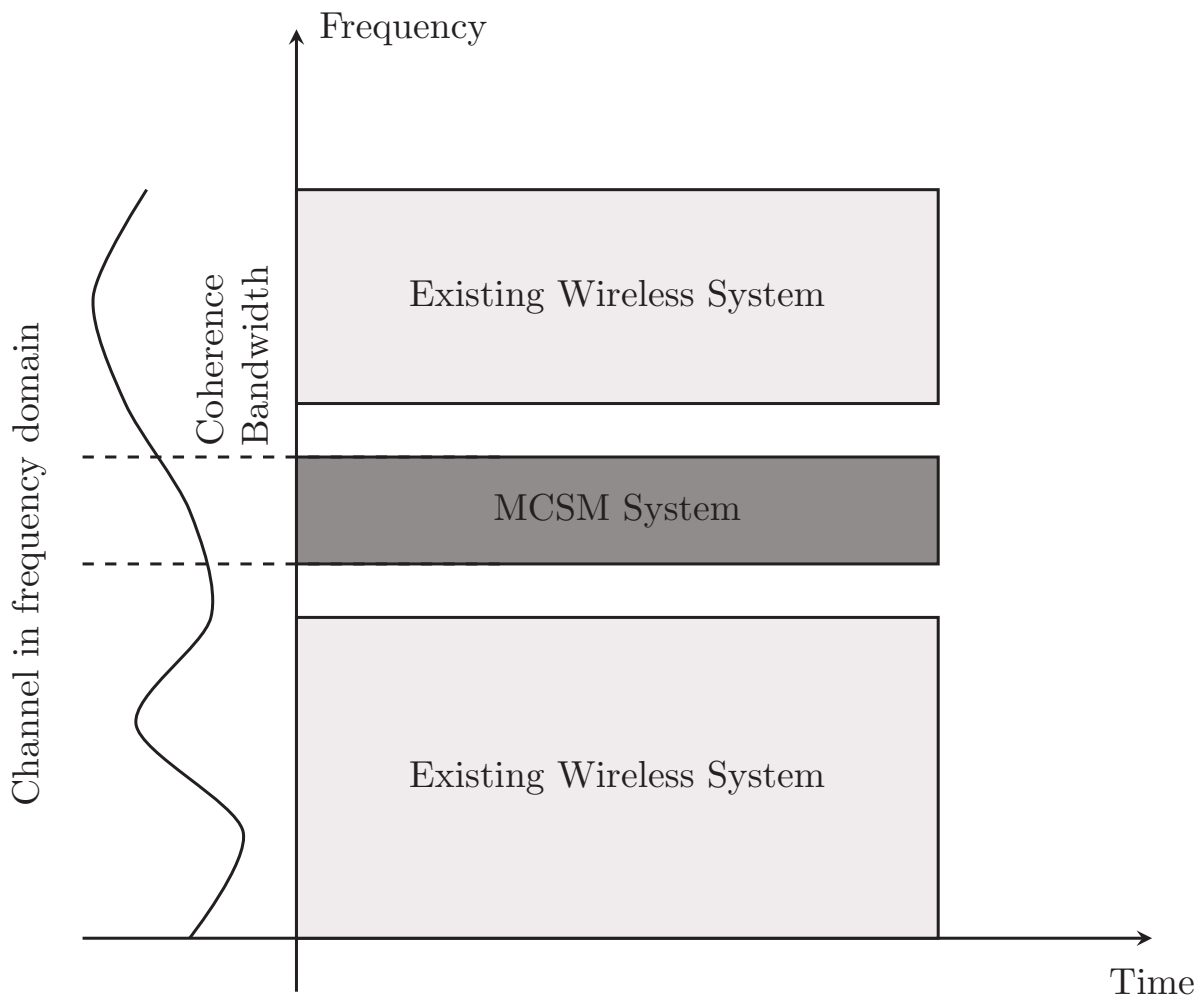


Figure 6.1: Illustration of an MCSM system, that is mapped into the coherence bandwidth of the wireless channel sharing the overall bandwidth with two other wireless systems.

6.4.1 Key Technology Components

A) Multi-Carrier Modulation

For flexible spectrum allocation multi-carrier systems with carefully designed waveforms have been identified as a potential solution [MP15b]. On the one hand, coexistence management is enabled by good spectral containment; on the other hand, spectrally efficient time-frequency scheduling can be achieved. Thus, the first technology component of MCSM is a suitable multi-carrier concept to flexibly allocate time-frequency resources for MCSM systems in one frequency band. In this thesis we restrict ourself to Orthogonal Frequency Division Multiplexing (OFDM) as a multi-carrier scheme, but general waveforms providing better spectral containment are equally applicable and are subject of ongoing research [OMM16].

Assume that the bandwidth shown in Fig. 6.1 is divided into overall L_{IFFT}

sub-carriers with a sub-carrier spacing Δf . Then a subset of L_{sc} sub-carriers is allocated to one particular MCSM system. MCSM systems are narrow-band systems serving up to N nodes per system and several systems can coexist within a certain bandwidth by simply allocating non-overlapping sub-carrier blocks. This addresses the requirement for coexistence management by blanking out sub-bands used by other communication systems. Additionally, several MCSM systems can coexist and share the bandwidth given. We restrict the following descriptions to a single MCSM system to ease notation. Thus, the most important design criterion is choosing L_{sc} to determine the bandwidth of the MCSM system. In order to ease channel estimation, the bandwidth $L_{sc}\Delta f$ has to coincide with the coherence bandwidth $B_c \approx 1/\tau_h$ of the wireless channel determined by its delay spread τ_h . If this requirement is fulfilled, we can apply non-coherent receiver structures and differential modulation at the nodes.

B) Non-Coherent Modulation

To enable non-coherent reception within the coherence bandwidth of the channel we apply a Differential Phase Shift Keying (D-PSK) at the nodes. To this end, each node modulates its symbols to a sequence of differentially modulated symbols denoted as $b_{n,l} = c_{n,l}b_{n,l-1}$ with a known starting phase as $b_{n,1} = 1$. Applying non-coherent modulation concepts inherently decreases the pilot overhead for channel estimation down to a known starting phase which corresponds to a single pilot symbol per node. Another advantage of D-PSK over QAM modulations is its inherent robustness against a Carrier Frequency Offset (CFO) between node and base-station, which suits the demands for low complexity nodes with limited processing performance. This robustness comes at the cost of a limited data-rate as higher order modulation schemes can not be applied with D-PSK.

C) Compressed Sensing Multiuser Detection

While multi-carrier modulation provides a flexible spectrum allocation, the physical channel access enabling the handling of massive access for sporadic nodes has to be designed. Therefore, we employ the CS-MUD techniques introduced previously in this thesis as medium-access strategy on top of OFDM. Following the concepts from previous chapters each node spreads its differentially modulated symbols to a chip sequence of length M . This chip sequence is then multiplexed to the L_{sc} sub-carriers allocated for the MCSM system. The particular multiplexing is a MCSM specific degree of freedom which allows adapting the system to the wireless channel. While the L_{sc} sub-carriers used coincide with the coherence bandwidth of the wireless

channel, MCSM follows a spread spectrum narrow-band transmission. The idea of narrowband spread spectrum may appear inconsistent at a first glance. However, we show that this is feasible and in our example parametrization we demonstrate that base data-rates of approx 12kBit/s can be expected. The term base data-rate reflects the fact that nodes can simultaneously be assigned to several MCSM systems such that the data-rate is a multiple of the base data-rate. This already addresses the scalability of MCSM where several MCSM systems can coexist to support more nodes or higher data-rates. The scalability is explained in more detail in the next subsection.

6.4.2 Specification of MCSM Node Processing

In the following we describe the MCSM transmit signal generation at node n as also depicted in Fig. 6.2. This node model can be seen as a MCSM specific detection model for the nodes. Again inactive nodes are modeled as transmitting with zero power, such that the detection is carried out with respect to the augmented alphabet \mathcal{A}_0 . The following lines describe the signal generation of one particular active node. First, a data stream

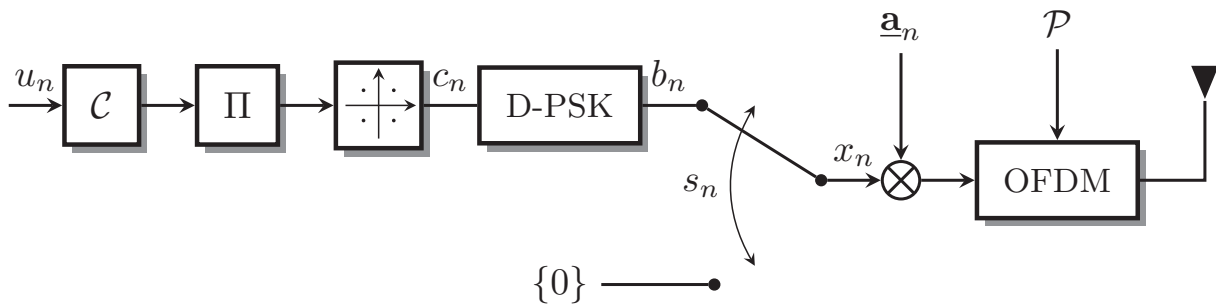


Figure 6.2: Block diagram of signal generation at MCSM node n .

of L_u payload bits, u_n , is encoded into a stream of code bits by a known channel encoder with code-rate R_c . Subsequently, the stream of code bits is interleaved and further mapped to symbols c_n , which are differentially modulated by D-PSK. The l th modulation symbol reads $b_{n,l} = c_{n,l}b_{n,l-1}$ with an arbitrary known starting phase $b_{n,1} = 1$. Here $c_{n,l}$ denotes the l th symbol corresponding to a symbol from a PSK modulation. The symbol $b_{n,l}$ denotes the differentially encoded symbol. Mapping and differential encoding are subsequently summarized by the D-PSK modulator. Analogous to the previous chapters we assume that nodes can be inactive as well by *transmitting* zeros. Thus, we again have $x_{n,l} \in b_{n,l} \cup \{0\}$ as augmented modulation symbol for node n . The next stage spreads the augmented modulation symbols to chips via an unique and node specific spreading

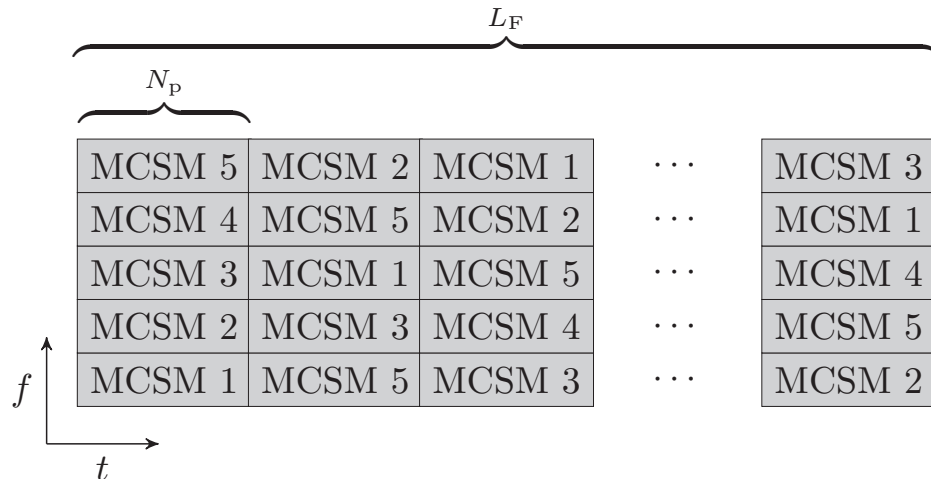


Figure 6.3: Illustration of possible scheduling. Each MCSM system changes its sub-carrier allocation each N_p symbols to gain frequency diversity.

sequence $\underline{\mathbf{a}}_n \in \mathbb{C}^M$. The last step in the MCSM signal generation is to multiplex the chips to physical resources, i.e, to the time-frequency grid. With OFDM we divide the bandwidth into L_{IFFT} sub-carriers. Here, we multiplex the chips of the spread augmented modulation symbol $\underline{\mathbf{a}}_n x_{n,l}$ to $\mathcal{P}(l) \subseteq \{1, \dots, L_{\text{IFFT}}\}$ sub-carriers of the overall L_{IFFT} sub-carriers. The number of sub-carriers used is denoted as $|\mathcal{P}(l)| = L_{\text{sc}}$. This multiplexing is carried out at the node by using a power normalized partial IDFT matrix $\mathbf{F}_{\mathcal{P}(l)}^H \in \mathbb{C}^{L_{\text{IFFT}} \times L_{\text{sc}}}$. Adding a cyclic-prefix as guard interval of length L_{CP} via the CP insertion matrix $\mathbf{T}_{\text{I}} \in \{0, 1\}^{L_{\text{IFFT}} + L_{\text{CP}} \times L_{\text{IFFT}}}$ yields the following description for the baseband signal in vector notation for node n and augmented symbol l

$$\mathbf{T}_{\text{I}} \mathbf{F}_{\mathcal{P}(l)}^H \underline{\mathbf{a}}_n x_{n,l}. \quad (6.1)$$

As shown in (6.1) the set $\mathcal{P}(l)$ determines the sub-carriers that are allocated for transmission. for the remainder of this thesis, we assume $|\mathcal{P}(l)| = M \forall l$, i.e., the spreading factor matches the number of sub-carriers allocated.

Scalability and Frequency Diversity

In narrowband systems like MCSM channels in a deep fading state may affect the performance of the end-to-end transmission. To address this impact the sub-carrier allocation $\mathcal{P}(l)$ may change over time according to a predefined pattern resulting in frequency hopping. This procedure enables frequency diversity gains by reallocating the sub-carriers every N_p OFDM symbols. Frequency hopping is especially appealing if several MCSM systems are multiplexed to a certain bandwidth addressing the scalability aspect of MCSM. When multiple MCSM system are available nodes can be assigned

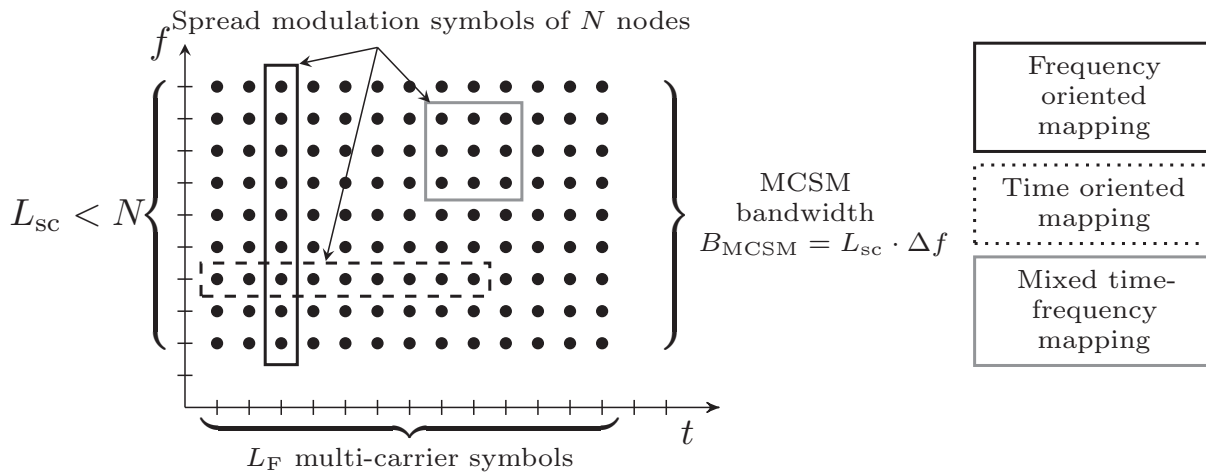


Figure 6.4: Illustration of different mappings of spreading sequence to resource grid.

to empty systems therefore offloading full systems. Additionally, one node can simultaneously transmit in several systems at the same time to meet higher data-rate requirements. With the scalability of MCSM the data-rate depends on the number of coexisting MCSM systems. In the following we restrict ourselves to the description of one MCSM system.

Figure 6.3 illustrates the sub-carrier reallocation pattern exemplary in a setup with 5 MCSM systems, where each MCSM system changes its sub-carrier allocation after N_p OFDM symbols and, thus, gains frequency diversity due to the encoding and interleaving across the time symbols. Assuming that each OFDM symbol carries one modulation symbol $b_{n,l}$ this reallocation leads to a rate loss of $1/N_p$ in each frame caused by differential modulation. The first transmit symbol carries the starting phase and no information. Complex scheduling algorithms can be avoided, by implementing a static hopping pattern repeated for each frame.

6.4.3 Resource Efficient Time-Frequency Mapping

In Chapter 2 direct random access was motivated with systems that are overloaded such fewer resources than nodes are used. In the MCSM system, the resources are summarized by the sub-carriers in frequency domain, and by multi-carrier symbols in time domain yielding a radio resource grid. Due to the mapping of chips to radio resources we can overload the systems by using a lower number of radio resources than nodes in the system. The mapping \mathcal{P} determines, whether the mapping is either time oriented, frequency oriented or a mixture of both as depicted in Fig. 6.4.

Frequency Oriented Mapping

For the frequency oriented mapping, the spread modulation symbol $\underline{\mathbf{a}}_{n,l} \forall n, l$ of length M is mapped along the frequency direction to $L_{sc} = M$ sub-carriers yielding a one-to-one mapping described by $\mathcal{P}(l)$. In this mapping, the symbol clock is along the time domain such that each OFDM symbol contains one spread transmit symbol. In this case, the multiuser interference has to be resolved by a multiuser detector along the frequency axis while the differential demodulation and the encoding works over the time axis. This requires the coherence bandwidth of the channel to be smaller than $M \cdot \Delta f$, while the coherence time must be small enough such that the differential demodulation can be carried out over two neighboring OFDM symbols.

Time Oriented Mapping

In the time oriented mapping, the spreading is carried out in the time direction such that the chip sequence is mapped along the time axis over M OFDM symbols. The modulation symbols are transmitted over the frequency direction and each sub-carrier contains one transmit symbol. In this case the multiuser detector works along the time axis, while the differential demodulation is carried out along the frequency axis. To ensure multiuser detection, the coherence time of the channel has to be greater than $M \cdot T_{\text{OFDM}}$. Additionally, the coherence bandwidth of the channel has to be greater than the sub-carrier spacing to enable differential demodulation along the frequency axis.

Mixed Mapping

Besides these two extreme cases also mixed time-frequency mapping can be carried out. A mixed time-frequency mapping might be the right choice for flexible allocation in scenarios with jointly limited coherence bandwidth and coherence time. Within this thesis we restrict ourself to a sole frequency oriented mapping with $L_{sc} = M$ coinciding with the coherence bandwidth of the wireless channel.

6.4.4 Base-Station Processing

Subsequently, we mathematically formalize the MCSM system model and state the detection model at the base-station. According to the description above, the received signal at the base-station can be described via the superposition of transmit signals of N nodes. The first processing step at the base-station is to remove the guard interval via the CP removal matrix

$\mathbf{T}_R \in \{0, 1\}^{L_{\text{IFFT}} \times (L_{\text{IFFT}} + L_{\text{CP}} - 1)}$, subsequently the time domain signal is transformed into frequency domain by $\mathbf{F}_{\mathcal{P}(l)}$. Thus, we can describe the l th received symbol \mathbf{y}_l in frequency domain in vector notation as

$$\mathbf{y}_l = \sum_{n=1}^N \mathbf{F}_{\mathcal{P}(l)} \mathbf{T}_R \mathbf{H}_n \mathbf{T}_I \mathbf{F}_{\mathcal{P}(l)}^H \mathbf{a}_n x_{n,l} + \mathbf{w}_l. \quad (6.2)$$

Here, $\mathbf{H}_n \in \mathbb{C}^{(L_{\text{IFFT}} + L_h - 1) \times L_{\text{IFFT}}}$ denotes the convolution matrix of the underlying wireless channel of node n with length L_h . To simplify notation we assume w.l.o.g. that L_h is the same for all nodes. Further, to alleviate ISI $L_{\text{CP}} = L_h$ holds. The vector \mathbf{w}_l denotes the frequency domain i.i.d. circular symmetric white Gaussian noise with zero mean and variance σ_w^2 . Note that the circulant matrix $\mathbf{T}_R \mathbf{H}_n \mathbf{T}_I = \mathbf{F}^H \mathbf{\Lambda}_n \mathbf{F}$ can be expanded via its eigenvalue decomposition, where $\mathbf{F} \in \mathbb{C}^{L_{\text{IFFT}} \times L_{\text{IFFT}}}$ denotes a L_{IFFT} -point DFT matrix and the diagonal matrix $\mathbf{\Lambda}_n \in \mathbb{C}^{L_{\text{IFFT}} \times L_{\text{IFFT}}}$ contains the L_{IFFT} channel coefficients of node n in frequency domain on its main diagonal. Subsequently, we make use of the assumption that the spreading factor coincides with the coherence bandwidth, justifying the assumption of a single tap channel in frequency domain. Mathematically, we have $\mathbf{F}_{\mathcal{P}(i)} \mathbf{T}_R \mathbf{H}_n \mathbf{T}_I \mathbf{F}_{\mathcal{P}(i)}^H \approx h_{n,l} \mathbf{I}_{L_{\text{sc}}}$, where $\mathbf{I}_{L_{\text{sc}}}$ denotes the L_{sc} dimensional identity matrix and $h_{n,l}$ describes the channel behavior within the coherence bandwidth by only one scalar channel coefficient for node n in frequency domain at transmit symbol l . This connection allows simplification to

$$\mathbf{y}_l = \sum_{n=1}^N \mathbf{a}_n \underbrace{h_{n,l} x_{n,l}}_{\tilde{x}_{n,l}} + \mathbf{w}_l = \mathbf{A} \tilde{\mathbf{x}}_l + \mathbf{w}_l, \quad (6.3)$$

where the columns of $\mathbf{A} \in \mathbb{C}^{L_{\text{sc}} \times N}$ contain the spreading sequence \mathbf{a}_n of all N nodes and $\tilde{\mathbf{x}}_l \in \mathbb{C}^N$ contains the augmented modulation symbols weighted with the node specific frequency domain channel tap. More specifically we have

$$\tilde{x}_{n,l} = \begin{cases} h_{n,l} b_{n,l} & \text{if } n\text{th node was active} \\ 0 & \text{else.} \end{cases} \quad (6.4)$$

With this definition, the symbol clock model described by (6.3) can be extended to capture frame-based transmissions of the nodes. In the following we first assume synchronous transmissions, while asynchronous transmissions are considered later on. Assuming that all nodes transmit frames containing L_F OFDM symbols allows for writing the received signal

$$\mathbf{Y} = \mathbf{A} \tilde{\mathbf{X}} + \mathbf{W}, \quad (6.5)$$

where $\mathbf{Y} \in \mathbb{C}^{L_{sc} \times L_F}$ contains the L_F received superimposed multiuser symbols. The model (6.5) assumes proper multiplexing of chips to sub-carriers at the nodes and proper de-multiplexing at the base-station. More specifically, (6.5) summarizes the detection model after multi-carrier processing.

With (6.5) we have frame-based transmission model with a physical interpretation. The chips of the nodes are transmitted on sub-carriers of a OFDM system that is specified, such that the spread sequence coincides with the coherence bandwidth of the channels. Most interestingly, the model (6.5) perfectly matches the assumptions made in the previous chapters. Especially, the fact of an unknown channel gain renders the multiuser energy detector introduced in Chapter 5 as a perfect candidate to detect the activity by estimating the frame support $\mathcal{S}_{\mathbf{X}}$ for the nodes. Beyond that, the application of Bayesian posteriori approaches or graphical models as introduced in the chapters 3 and 4 can generally be applied as well. However, these require the system to be of finite alphabet. This condition requires perfect channel state information at the receiver, which does not match the philosophy of non-coherent modulation concepts. However, the frame BP introduced in Chapter 4 can generally be extended to also track the channel state information. First advances towards message-passing-based differential demodulation including channel tracking has been introduced in the single-user setup in [Bar10]. Augmenting the frame BP towards non-coherent reception including channel tracking is out of the scope of this thesis and left for further research. Subsequently, as also depicted in Fig. 6.5, we follow a two stage activity and data detection concept based on multiuser energy detection. The superimposed received signals are processed according to an OFDM demodulator and the output stream is demultiplexed according to the sub-carrier allocations summarized by $\mathcal{P}(l)$. Then a multiuser energy detector as described in Chapter 5 estimates the node activity by estimating $\mathcal{S}_{\hat{\mathbf{X}}}$. This is forwarded to a least-squares data estimator, that resolves the multiuser interference and separates the multiuser signal into single-user streams. Finally, these streams are sorted and fed into individual demodulators followed by a decoders and CRC.

6.4.5 Robustness to Asynchronous Transmissions

Dealing with delays caused by asynchronous transmissions is one of the major challenges in M2M uplink communications. These delays may have a physical origin caused by different distances between nodes and base-station. Further, practical impairments such as imperfect clocks of low-cost nodes may also cause asynchronous transmissions. The big challenge is to resolve these delays from the multiuser signal received by the base-station. In the

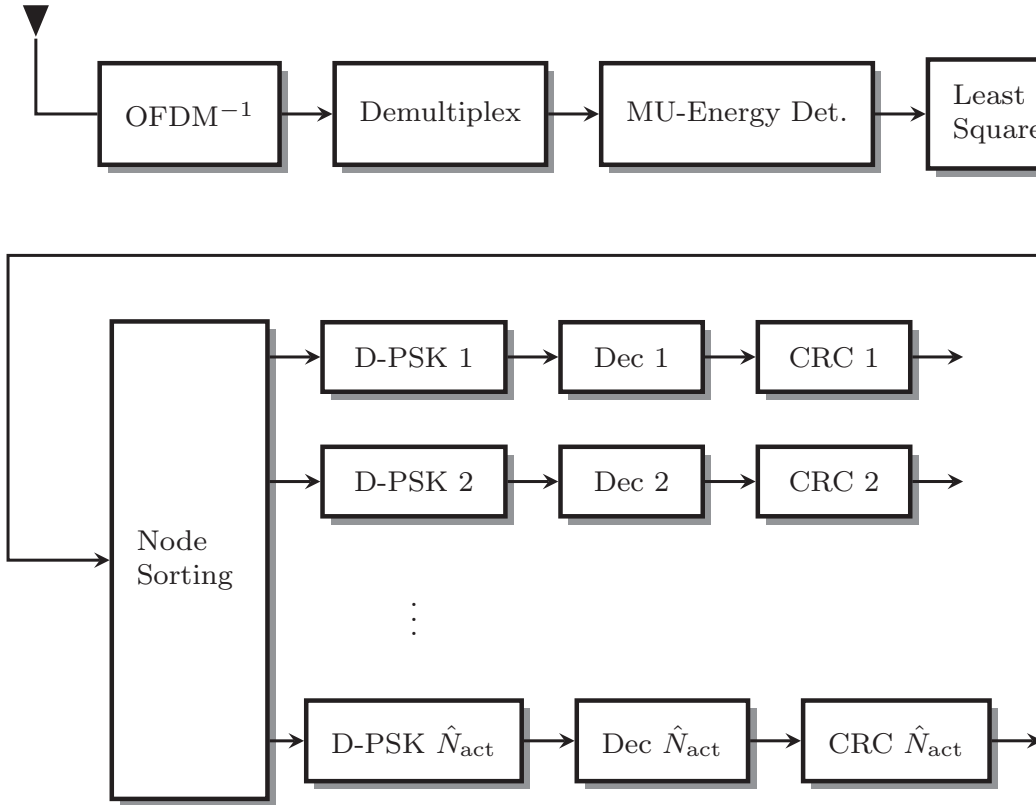


Figure 6.5: Overview of MCSM base-station processing including a multiuser energy estimator.

sole context of CS-MUD, previous works have shown a scheme of extending the detector by so-called delay hypotheses reflecting the expected delays of the nodes in the detector [SBD13]. Each delay hypotheses summarizes one specific possible delay for one specific node. The increase in terms of algorithmic complexity is high, especially if numerous delay hypothesis are covered.

In contrast to that, the application of OFDM in MCSM inherently allows some degree of asynchronicity as long as the maximum delay is restricted to the length of the cyclic-prefix in time domain, i.e., the cyclic-prefix has to match the length of the channel impulse response and the expected time shift from asynchronous transmissions. Clearly, extending the cyclic-prefix to cope with asynchronicity leads to a loss in spectral efficiency.

If the cyclic-prefix matches the maximum delay plus the length of the channel impulse response, a time shift of $\Delta\tau$ samples leads to a phase rotation over the sub-carriers, which is due to the time-shift property of the Fourier transform. Subsequently, we assume that the receiver performs a L_{IFFT} -point FFT to transform the received signal into frequency domain. Further we assume a transmission according to the system model described in (6.2) with $N_{\text{act}} = 1$ active node indexed with n . It is now assumed

that this node transmits with a delay $\Delta\tau_n$. The cyclic prefix is assumed to be longer than this delay plus the length of the channel impulse response $L_{CP} \geq L_h + \Delta\tau_n$. In this case the m th sample of the frequency domain symbol \mathbf{y}_l experiences a phase shift and can be written as

$$\tilde{y}_m = y_m \cdot \exp\left(\frac{-j2\pi m \Delta\tau_n}{L_{\text{IFFT}}}\right), \quad (6.6)$$

Note that (6.6) assumes a one-to-one mapping from chips to sub-carriers in a frequency oriented mapping. For other mappings the particular impact of phase shifts is different. Assuming our MCSM system occupies L_{sc} consecutive sub-carriers inside the spectrum, we can summarize the phase shift for node n in matrix form

$$\mathbf{D}_n = \left[\mathbf{dg} \left(e^{\frac{-j2\pi 1}{L_{\text{IFFT}}}}, e^{\frac{-j2\pi 2 \Delta\tau_n}{L_{\text{IFFT}}}}, \dots, e^{\frac{-j2\pi N_s \Delta\tau_n}{L_{\text{IFFT}}}} \right) \right]. \quad (6.7)$$

Here, $\mathbf{dg}(\cdot)$ sets up the $L_{sc} \times L_{sc}$ dimensional diagonal matrix. Consequently, we can explicitly write down the impact of the delay on the spreading sequence of node n via

$$\tilde{\mathbf{a}}_n = \mathbf{D}_n \mathbf{a}_n. \quad (6.8)$$

If more than one node is active, each node experiences its individual phase shift over the composite signature sequence. Thus, (6.8) also holds true for the general case. Subsequently, we can write the phase shift in our MCSM system model as

$$\mathbf{Y} = \tilde{\mathbf{A}} \tilde{\mathbf{X}} + \mathbf{W}, \quad (6.9)$$

where $\tilde{\mathbf{A}}$ summarizes the spreading sequences of the nodes according to (6.8). However, the time shifts $\Delta\tau_n$ are unknown at the receiver and, thus, degrade the performance as shown later.

As time shifts lead to phase shifts over sub-carriers, possible solutions are 1) to change the chips to sub-carrier multiplexing $\mathcal{P}(l)$ by multiplexing rather in time instead of frequency direction, or 2) decrease the spreading sequence lengths with the drawback that fewer nodes can be supported within one MCSM system.

6.4.6 MCSM Parametrization

The parameter space of MCSM is beyond what this thesis can show. Thus, a reasonable example parametrization is presented in the following. The goal of the parameters selected is to match with a realistic M2M setup. To start, we need a realistic specification of the underlying wireless channel. Especially, the coherence bandwidth determined by the delay spread, needs

to be specified. The specifications in LTE assume delay spreads of up to 10km by adding a cyclic-prefix of length $T_{\text{CP}} = 33.33\mu\text{s}$ to the transmit symbols. Assuming a delay spread of 10km for low data-rate, M2M communication might cover applications such as smart metering in agricultural applications or road monitoring. Clearly, applying MCSM to these scenarios is possible by making the cyclic prefix sufficiently large. Within this thesis we want to demonstrate the applicability of MCSM in an industrial application where channel impulse responses are much shorter. In [SCFCA13] the authors investigated the channel impulse responses for several industrial M2M scenarios and argued that the maximum delay spread is below $\tau_h \leq 1\mu\text{s}$ for 2.4GHz carrier frequencies. The results coincide with recent channel measurement performed in conjunction with the HiFlecs project [CWU⁺16]. There, delay spreads below $0.5\mu\text{s}$ were measured for industrial indoor scenarios. To match the results of recent research, we assume a delay spread of $\tau_h = 1\mu\text{s}$, yielding a maximum path difference of $d_{\text{max}} = 300\text{m}$ for the underlying wireless channel with exponential decaying channel impulse response and a path-loss exponent of $\epsilon = 2$. Hence, the coherence bandwidth reads $B_c = 1/\tau_h = 1\text{MHz}$. The coherence bandwidth is only a heuristic measure, therefore we set the MCSM bandwidth to be smaller than the coherence bandwidth to $B_{\text{MCSM}} = 0.25\text{MHz}$. To keep the algorithmic complexity at a reasonable level, we assume that a MCSM system serves $N = 60$ nodes with a spreading sequence length of $M = 20$ yielding a system load of $\beta = 3$ nodes per resource on average. Further, we apply frequency oriented mapping, where the spreading sequence length matches the number of sub-carriers occupied $M = L_{\text{sc}}$. This yields a sub-carrier spacing of $\Delta f = 0.25\text{MHz}/M=20 = 12.5\text{kHz}$. With this parametrization, the per node base data-rate is

$$R_b = R_c \frac{2\text{Bit/Symbol}}{\frac{1}{\Delta f} + T_{\text{CP}}} = R_c 24.7\text{kBit/s}. \quad (6.10)$$

Assuming a half-rate code of $R_c = 1/2$, we end up with a per-node base data-rate of approximately 12kBit/s assuming a D-QPSK. In this parametrization each OFDM symbol has a length of $T_{\text{OFDM}} = \frac{1}{\Delta f} + T_{\text{CP}} = 81\mu\text{s}$. Since the differential modulation is carried out in time direction, the coherence time of the channel must fall below this value.

This parametrization is clearly only one example for an MCSM system justifying that the assumption of spread multi-carrier symbols is a reasonable assumption for low data-rate M2M traffic. In a real setup, the system specific parameters have to be adapted to the underlying scenario and the system requirements. In the following we will restrict ourself to this example parametrization to discuss the impacts observed.

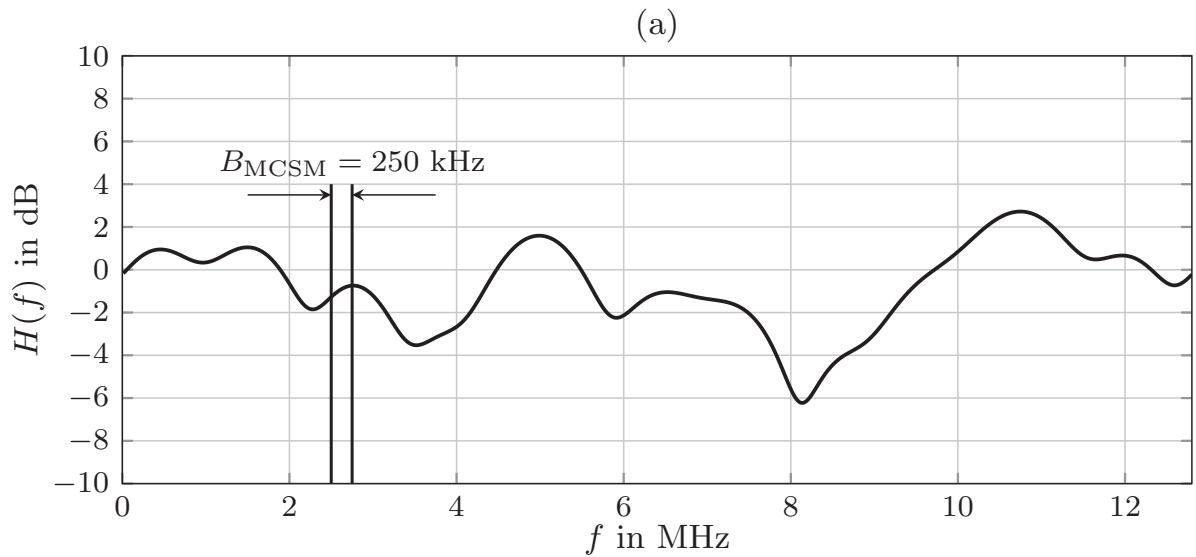


Figure 6.6: Exemplary frequency response of the channel between any MCSM node and the base-station over $L_{\text{IFFT}} = 1024$ sub-carrier.

6.5 Simulative Performance Verification

To analyze the performance of MCSM simulative, we set up a parametrization along with the previous calculative example that is used as a reasonable setup for subsequent simulations. These parameters are summarized in Table 6.1.

MCSM relies on frequency flat channels over the sub-carriers allocated. To illustratively show the frequency selectivity of the channels between the nodes in a MCSM system and the base-station, Fig. 6.6 plots the frequency response over $L_{\text{IFFT}} = 1024$ sub-carriers with the parametrization given in Table 6.1. Exemplary, Fig. 6.6 plots the occupied bandwidth by one particular MCSM system using $L_{\text{sc}} = 20$ sub-carrier resulting in $B_{\text{MCSM}} = 250$ kHz. We see that the assumption of a flat channel is viable as only slight frequency selectivity is present over the bandwidth used. However, we will also see that this remaining frequency selectivity suffices to harm the performance of the data detection.

General Parameter	
Payload Size	$L_u = 212$ bits
Number of OFDM Symbols transmitted	$N_{\text{OFDM}} = 240$ Symbols
Delay spread of channel	$\tau_h = 1\mu\text{s} \Rightarrow 300\text{m}$
Length of sampled channel imp. resp.	$L_h = 12$
Pathloss-Exponent	$\epsilon = 2$
Bandwidth of MCSM System	$B_{\text{MCSM}} = \Delta f \cdot M = 250\text{kHz}$
Channel code	Half rate conv. [31 ₈ 33 ₈]
Modulation	D-QPSK
Data-rate	$R_b = 12\text{kBit/s}$
Frequency hopping: every	$N_p = 10$ OFDM symbols
Frequency hops per frame	$N_{\text{Hop}} = 24$
CS-MUD Specific Parameter	
Number of nodes	$N = 60$
Spreading seq. length	$M = 20$
System load	$\beta = 3$ nodes per resource
Activity detection	GOMP,MMP,MUSIC,MAP-E
Data detection	Linear least-squares on $\mathcal{S}_{\hat{\mathbf{x}}}$
Multi-carrier Specific Parameter	
Chip to sub-carrier multiplexing	Frequency oriented
Number of sub-carriers for MCSM system	$L_{\text{sc}} = M$
IFFT length for OFDM symbol generation	$L_{\text{IFFT}} = 1024$
Sub-carrier spacing	$\Delta f = 12.5\text{kHz}$
OFDM symbol length	$T_{\text{OFDM}} = 81\mu\text{s}$
Cyclic-prefix length	$T_{\text{CP}} = \tau_h$
Sampling time	$T_s = 78\text{ns}$

Table 6.1: Set of Simulation parameters subsequent analysis is based on.

6.5.1 Phase Transition Diagrams

To start the analysis, we consider the activity detection capabilities of MCSM. The activity detection capability of MCSM is solely determined by the multiuser energy detection stage. To see how the concepts from Chapter 5 perform under MCSM conditions, we plot the phase transition diagram in Fig. 6.7. For comparison, the phase transition diagram in a Rician channel without MCSM with a Rice factor of $K_{\text{rice}} = 30$ is also recapped in Fig. 6.7 (b).

As done previously the phase transition diagram plots the trajectory where the activity error rate is below 10^{-3} in the noise-free region. Comparing both diagrams shows that the performance of the activity detection algorithms in MCSM is nearly the same as in one tap Rician channels with $K_{\text{rice}} = 30$. The reason for this can be found in the frequency hopping, such that the sub-carrier allocation changes each $N_p = 10$ OFDM symbols to gain frequency diversity over time. With this hopping, the channel realization changes every $N_p = 10$ symbols and since the receive covariance matrix is used to perform activity detection, the algorithms exploit frequency diversity. Increasing the frequency hopping even improves the activity detection capabilities of MCSM. This effect will be shown later in another context.

6.5.2 Performance over the SNR

To show the performance of MCSM over the SNR range, Fig. 6.8 (a) and (b) plot the activity error rates and the frame error rates over the SNR range. The corresponding false alarm and missed detection rates are shown on (c) and (d) respectively. While MUSIC and MAP-E exhibit a strong decline in terms of activity error rates over the SNR, MMP and especially the GOMP suffer a remarkable loss and yield an imperfect activity estimation even in the high SNR range. The frame error rates on the other hand are almost the same for all activity detection algorithms considered. Only the FER for the GOMP exhibits a higher error floor than the other algorithms. Here we see the impact of the imperfect activity detection capability of the GOMP. Considering the activity error rates (c)-(d) in more detail, shows that the GOMP exhibits both, false alarms and missed detections, while the other activity detection algorithms show non-measurable activity error rates.

Most interestingly, this analysis implicates that the FER is limited by two effects. For MUSIC, MMP and MAP-E the activity error rates decline at much lower SNR than the corresponding frame error rates. This shows that the gap in between is due to multiuser interference that cannot be resolved by the least-squares detector. However, multiuser interference is not the only limitation affecting the FER. Especially the error floor at high SNR is

caused by the remaining frequency selectivity in the MCSM band. Still, a FER of approx $3 \cdot 10^{-3}$ can be achieved with MMP, MUSIC and MAP-E.

It can be concluded that activity error rate control does not help to improve the FER. Especially in the low SNR range we observe a perfect activity estimation that does not limit the FER. For the high SNR region we observe limitations caused by the remaining frequency selectivity in the MCSM band.

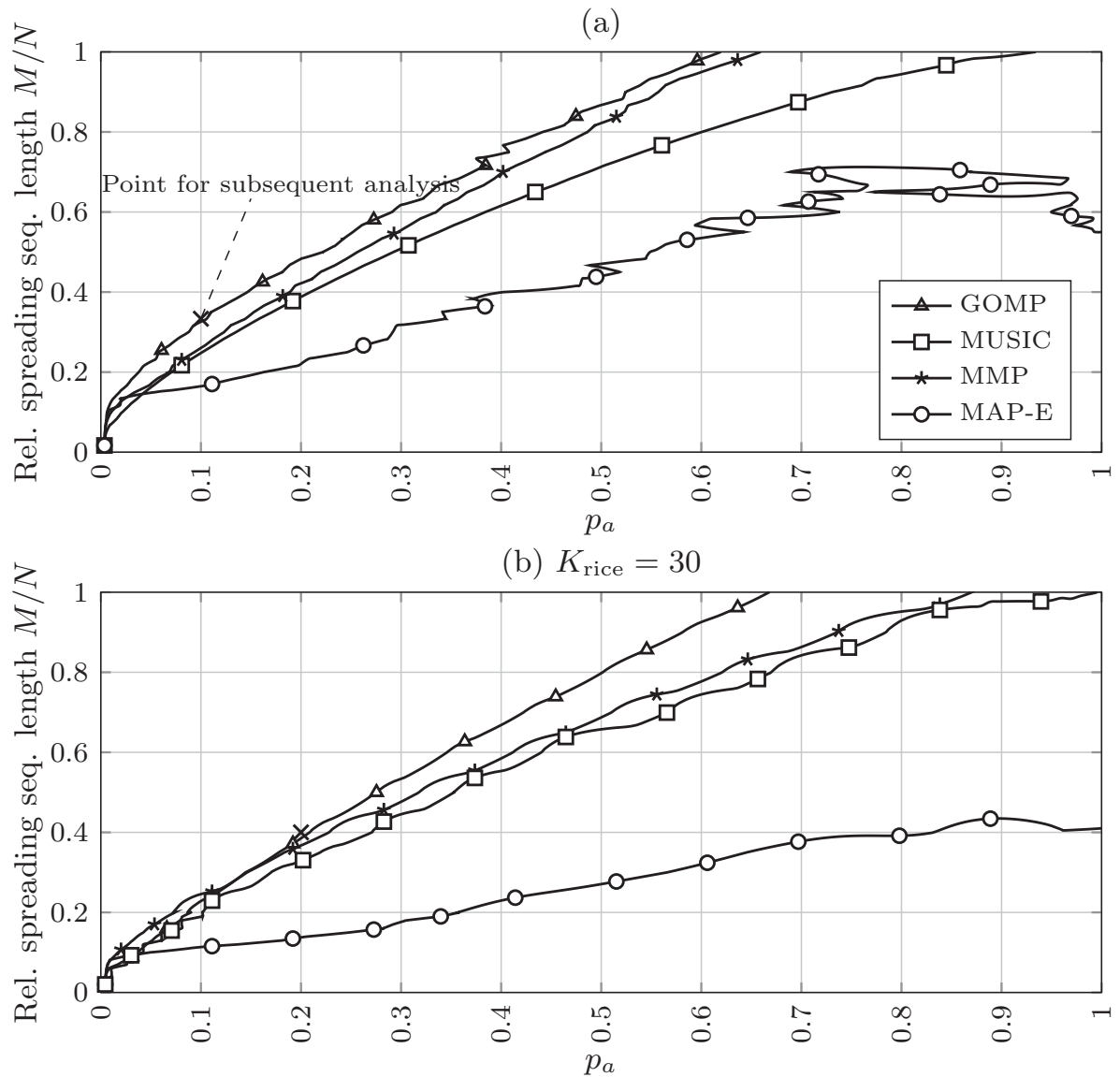


Figure 6.7: Phase transition diagram for the activity detection performance of different algorithms in MCSM in (a). For comparison, the phase transition diagram of the same algorithms in a Rice channel with $K_{\text{rice}} = 30$ is shown on (b).

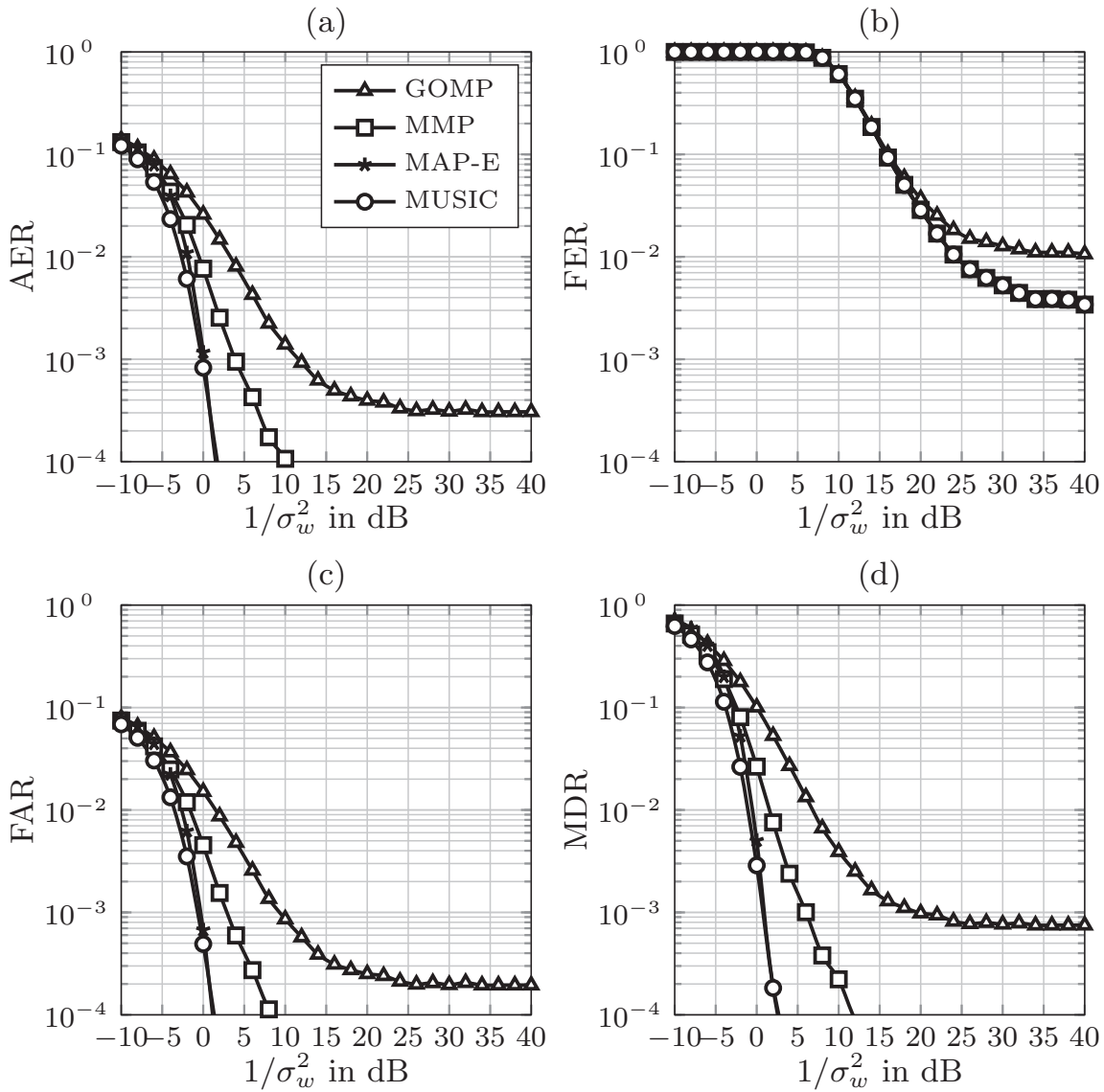


Figure 6.8: Activity Error Rate (a), Frame Error Rate (b), False Alarm (c) and Missed Detection Rates (d) for the MCSM system as given in Table 6.1

6.5.3 Time-Frequency Diversity

Gaining frequency diversity by reallocating the chip to sub-carrier multiplexing each N_p OFDM symbols improves the performance of MCSM. This reallocation was illustrated in Fig. 6.3. Additionally, highly frequency selective channels also yield higher frequency diversity than their counterparts exhibiting only low frequency selectivity, making these channels favorable for MCSM. The downside of high frequency selectivity is that the coherence bandwidth is smaller, requiring lower spreading such that the spread sequence matches the coherence bandwidth. In this case the number of nodes each MCSM system supports is lower. Another option to counteract high frequency selectivity is to decrease the base data-rate by making the OFDM symbols longer. This decreases the sub-carrier spacing and counteracts frequency selectivity. In summary, we observe that frequency selectivity, on the one hand, yields diversity while, on the other hand, it restricts the data-rate and the number of nodes in the system.

The positive effect of frequency diversity on MCSM is twofold. Most obviously, reallocating the sub-carrier set each N_p OFDM symbols enhances the data detection. In case of deep fading only a block of N_p symbols is affected and the bits contained can still be recovered due to the application of a channel code with proper interleaving. The second effect concerns the multiuser energy detection applied which estimates the received power of the nodes based on the receive covariance matrix. The application of frequency hopping decreases the randomness in the received power, thereby, increasing the detection performance. To make this clear, we consider the received signal for a single-user only. According to (6.3) we have

$$\mathbf{y}_l = \mathbf{a}_n h_{n,l} x_{n,l} + \mathbf{w}_l. \quad (6.11)$$

Carrying out multiuser energy detection means that the detector estimates the magnitude squared of the accumulated receive power over one frame by estimating $\frac{1}{L_F} \sum_{l=1}^{L_F} |h_{n,l}|^2 \cdot |x_{n,l}|^2$ which is the input statistic for the multiuser energy detector. If $|h_{n,l}|^2$ and $|x_{n,l}|^2$ do not change over l , and if we assume w.l.o.g $|x_{n,l}|^2 = 1, \forall l$ then the accumulated received power only corresponds to $|h_{n,l}|^2$, which is a sample of a random variable. However, if $h_{n,l}$ changes each N_p OFDM symbols and if we have $N_{\text{Hop}} = N_{\text{OFDM}}/N_p$ hops per transmit frame, the variance of this random variable decreases with $1/N_{\text{Hop}}$. This is a consequence of the law of large numbers. In the limit $N_{\text{Hop}} \rightarrow \infty$, the variance of the received power becomes a constant and the effective received power is deterministic, corresponding to an AWGN channel from the perspective of the multiuser energy detection. Without frequency hopping, the received power is random, corresponding to full

Rayleigh fading. Therefore, it can be assumed that the impact on the multiuser energy detection is similar to Rician fading investigated in chapter 5 and that increasing N_{Hop} has similar effects than increasing the Rice factor K_{rice} .

To show the gains achieved by frequency hopping, we consider the activity and frame error rates for different number of frequency hops N_{Hop} . Fig. 6.9 plots activity and frame error rates for a system without frequency hopping $N_{\text{Hop}} = 0$ in (a) and (b). Further, a system that performs a single frequency hop $N_{\text{Hop}} = 1$ only is shown in (c) and (d) and a system with a frequency hopping determined by $N_{\text{Hop}} = 12$ in (e) and (f). Performing a single frequency hop only yields gains for the MUSIC algorithms. The other activity detection algorithms maintain their performance. Gains can be observed by setting $N_{\text{Hop}} = 12$. Besides the GOMP all activity detection algorithms applied achieve performance gains, confirming the theory that frequency hops decrease the randomness in the accumulated received energy. Most interestingly, the GOMP still suffers from an error floor in activity detection, which matches the results from the preceding chapter. There we saw that the impact of having either Rayleigh fading or AWGN is rather minor for the GOMP. This robust behavior of the GOMP comes at the cost that multiuser energy detection concepts as MMP, MAP-E and MUSIC outperform the GOMP if frequency hopping is applied.

Considering the frame error rates on the right hand side of Fig. 6.9 confirms the observations made above. The impact of the activity detection on the data detection is minor. The only exception is the setup without frequency hopping characterized by $N_{\text{Hop}} = 0$, here the MAP-E and the MMP achieve imperfect activity detection, limiting the frame error rate. Enabling frequency hopping, only yields minor gains in terms of the frame error rate, which is due to the remaining frequency selectivity that limits the FER in the high SNR range. To address the huge gap between the activity and frame error rate, more sophisticated data detection schemes beyond least-squares detection are required, which is out of the scope of this thesis but are subject to current research.

Increasing the number of hops only yields minor gains for the activity detection. The reader may compare the results from Fig. 6.9 to the activity error rates for the base-line parametrization characterized by $N_{\text{Hop}} = 24$, shown in Fig. 6.8. Beyond that one has to keep in mind that increasing N_{Hop} leads to a small loss in data-rate due to the fact that the first modulation symbol in a block corresponds to the known starting phase. This has to be compensated by making the frames longer, decreasing the data-rate of MCSM.

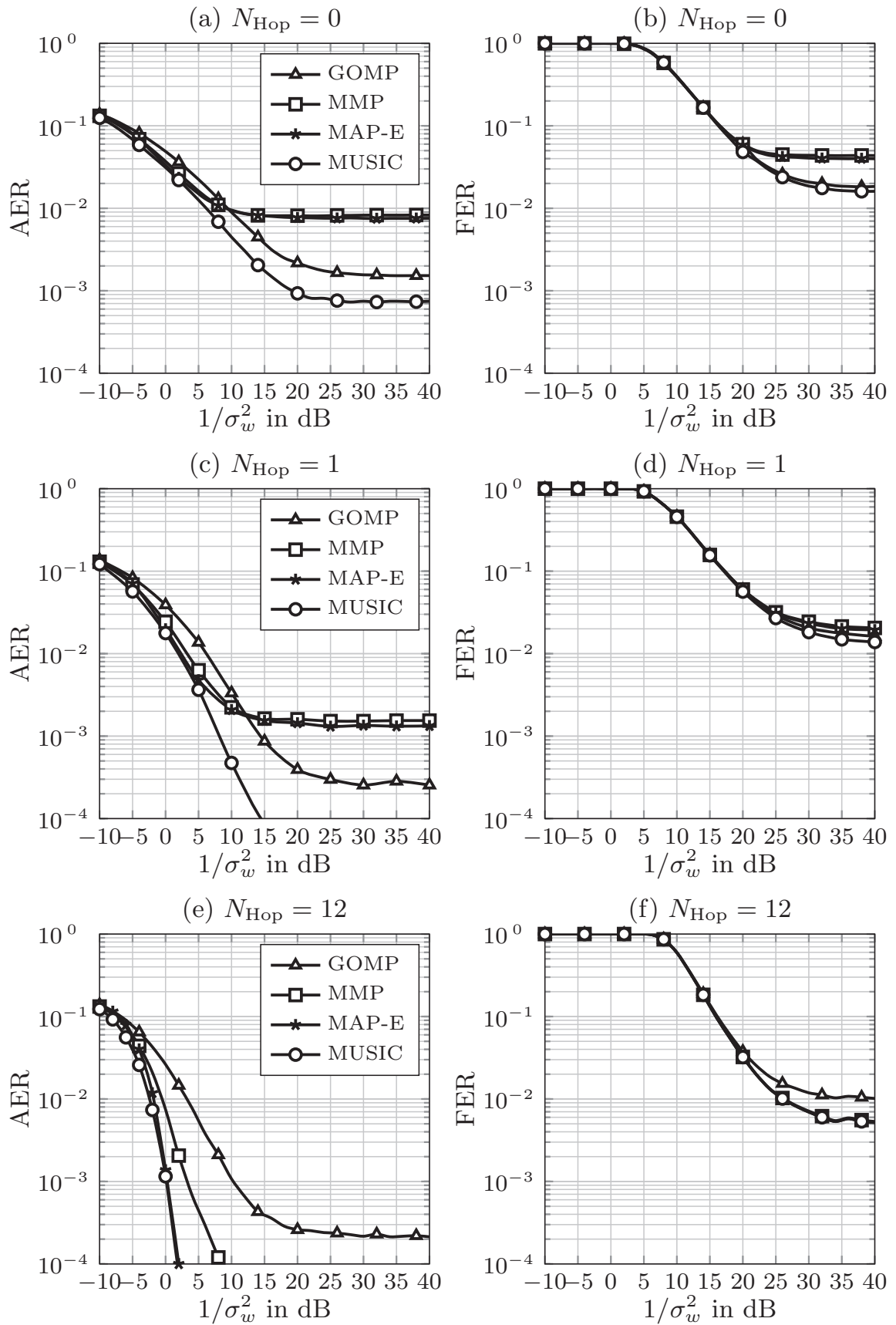


Figure 6.9: Activity error and frame error rates for different numbers of frequency hops N_{Hop} .

6.5.4 The Data-Rate Bandwidth Trade-Off

Clearly, the anticipated data-rate of $R_b = 12\text{kBit/s}$ is a design parameter to match the delay spread of the channel $\tau_h = 1\mu\text{s}$. The upper results have shown that the base-line parametrization allows for good performance of the activity detection, while the data detection via least squares is still imperfect. Increasing or decreasing the data-rate by making the time symbol shorter or longer is generally a viable approach and affects the performance of MCSM. In consequence the sub-carrier spacing changes resulting in increased or decreased bandwidth occupation for the MCSM system. Increasing the bandwidth of the MCSM system increases the frequency selectivity within the system, violating the assumption of a single tap channel. Hence, distortions that are not equalized occur at the detector.

To analyze this impact, Fig. 6.10 plots the activity error rate in (a) and frame error rates in (b) for different data-rates achieved by varying the OFDM symbol duration T_{OFDM} . The activity error rates are plotted at an SNR of 0dB while the data detection is considered at 30dB.

The corresponding channel frequency response over $L_{\text{IFFT}} = 1024$ sub-carriers with B_{MCSM} is illustratively shown for $R_b = 0.1\text{kBit/s}$ in (c) and $R_b = 40\text{kBit/s}$ in (d). The corresponding bandwidth for one MCSM system reads $B_{\text{MCSM}} = 2\text{kHz}$ for $R_b = 0.1\text{kBit/s}$ and $B_{\text{MCSM}} = 833\text{kHz}$ for $R_b = 40\text{kBit/s}$, respectively. Most interestingly, the impact on the activity detection is only minor due to the correlation property of the receiver concepts used and due to the frequency hopping applied. Here, the frequency hopping yields the discussed averaging effect. This effect is not true for the data detection, where each symbol is estimated individually. For the data detection we first observe that very low data-rates lead to very low frame error rates. Here we have very low frequency selectivity within the MCSM band such that the least-squares data detector is able to perfectly estimate the data of the nodes. Increasing the data-rate also increases the frequency selectivity and we see that a graceful degradation in the FER. Even though there is an increase in the FER for higher data-rates, we still achieve FERs of $2 \cdot 10^{-2}$ for a data-rate of $R_b = 40\text{kBit/s}$, which may still be sufficient for some applications.

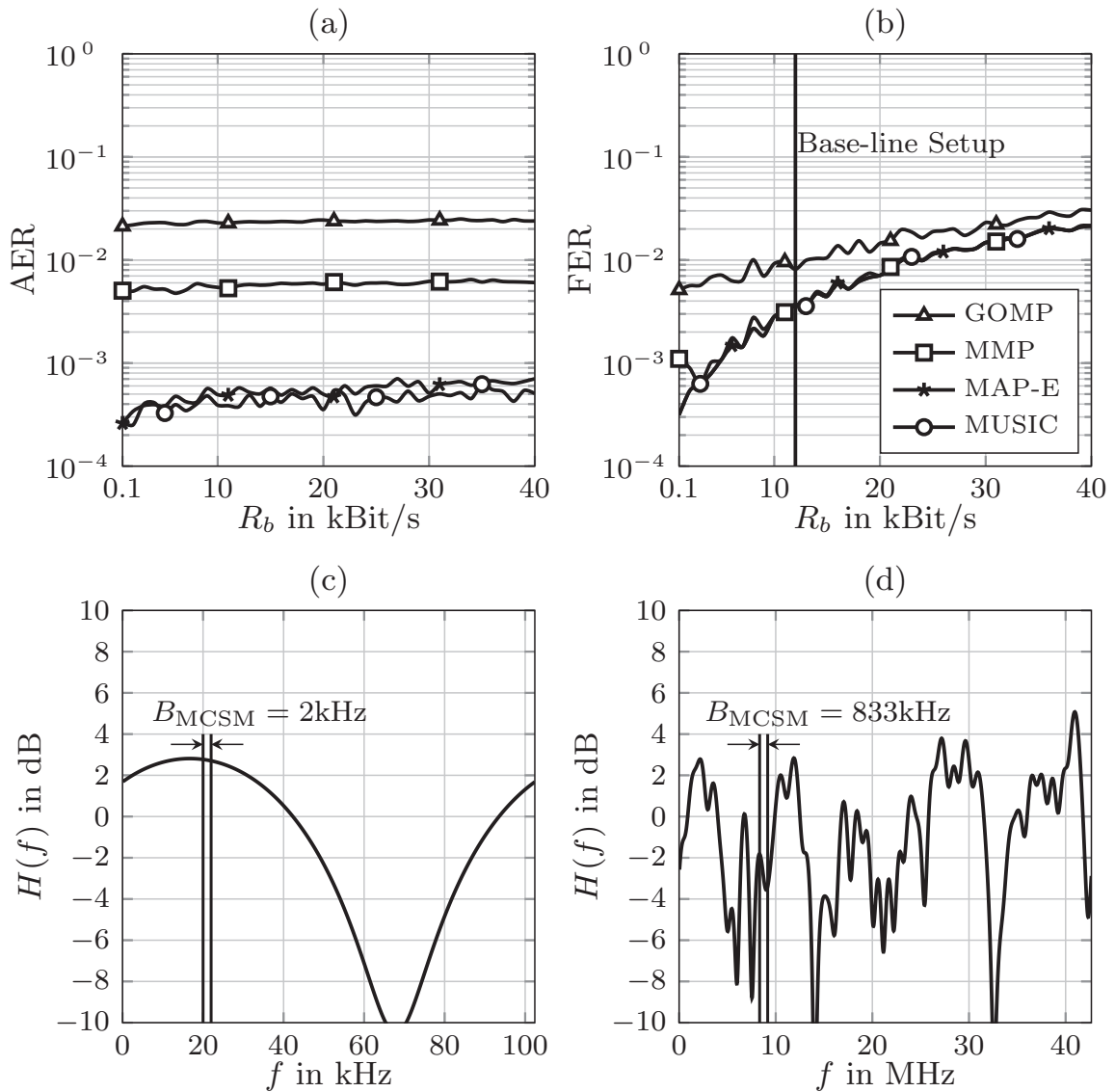


Figure 6.10: Activity error rate vs. data-rate in (a) at $1/\sigma_w^2 = 0$ dB and frame error rate vs. data-rate in (b) at $1/\sigma_w^2 = 30$ dB. Illustrative frequency response of the wireless channel for $R_b = 0.1$ kBit/s (c) and $R_b = 40$ kBit/s in (d).

6.5.5 Asynchronous Transmissions

Within a M2M system, synchronicity is one of the major requirements, determining the performance of the system. Besides delays occurring on the wireless link caused by different node to base-station distances, also delays due to imperfect clocks may occur. Especially, when nodes are cheap and have long sleeping periods, synchronizing to a central base-station clock is fundamentally necessary. Therefore, it can be assumed that there exist some type of downlink channel providing control signals to enable a coarse timing alignment of nodes within the system. However, small timing offsets due to

propagation delay, or other practical constraints will remain, and the base-station can expect that the nodes do not transmit in a perfectly synchronized fashion. As shown, increasing the length of the cyclic-prefix allows coping with asynchronicity to some degree. However, as shown previously, the downside of this approach is that the sub-carriers are affected by a phase shift according to eq. (6.6) which is not compensated at the receiver and thus yields additional interference. Especially, when frequency oriented mapping is employed, this random phase shift directly affects the spreading sequence of the nodes. Fig. 6.11 plots the activity error rate on (a) and the frame error rate on (b) versus the maximum delay expected in the network $\Delta\tau_{\max}$. Here, each active node has a random delay uniformly chosen from the interval $\Delta\tau_n \sim [0, \Delta\tau_{\max}]$. Again the activity detection is considered at an SNR of

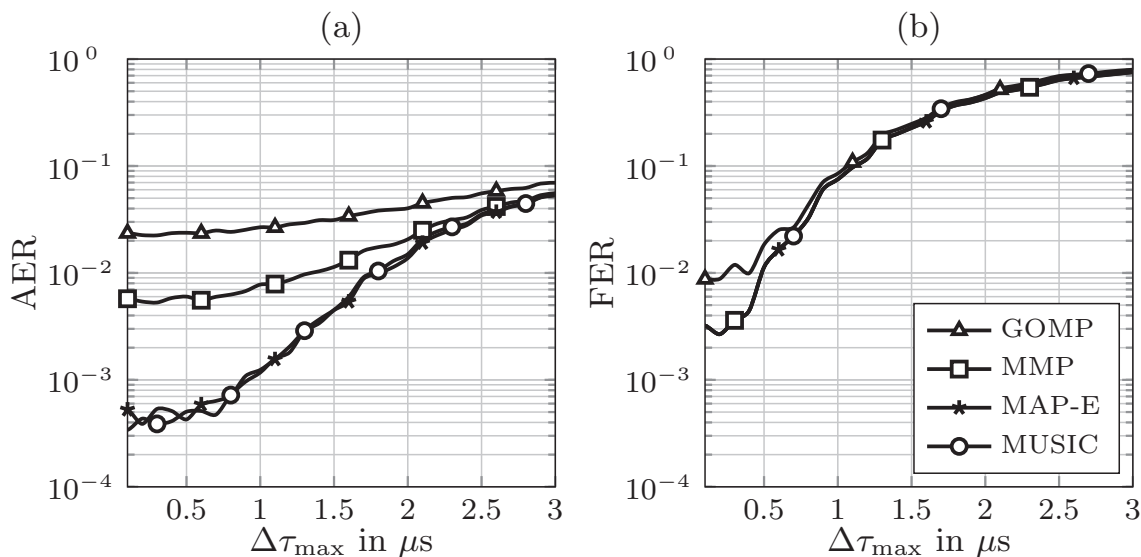


Figure 6.11: Simulation of activity error rate on (a) and frame error rate on (b) versus the maximum asynchronicity $\Delta\tau_{\max}$.

$1/\sigma_w^2 = 0$ dB while the data detection is considered at $1/\sigma_w^2 = 30$ dB. The impact on the activity and on the data detection shows that small delays of $\Delta\tau_{\max} \leq 0.5\mu\text{s}$ do not considerably affect the performance of MCSM. However, while the asynchronicity increases, the performance gracefully degrades. Especially, the frame error rate shows a considerable increase caused by the phase shifts that the least-squares data detector can not resolve. Unfortunately, the frequency hopping cannot improve this situation. The random phase shift is the same for all sub-carrier allocations.

Possible approaches to still maintain the performance of MCSM under highly asynchronous transmissions would be to estimate the node delay at the detector and to resolve the interference caused. This requires pilot symbols and increased the complexity of the detector.

Another, more elegant approach which suits to the MCSM system is to change the multiplexing of chips to sub-carriers from multiplexing along the frequency axis to a mapping along the time axis, also shown in Fig. 6.4. In this case, the phase shift over the sub-carriers is summarized by the effective channel tap that each node experiences. This can only be done, if the time variations of the channel summarized by the coherence time is sufficiently low. Thus, in a static scenario with a non or only slowly varying channel, multiplexing of chips along the time axis allows to fully overcome the impact of asynchronicity as long as the cyclic prefix is sufficiently long.

6.6 Verification via Lyrtech Hardware Platform

6.6.1 Lyrtech Hardware Demonstration Platform

Within this subsection we verify the theoretical results of MCSM practically via a hardware demonstrator platform for over-the-air transmissions. To this end we use two hardware demonstrator platforms from Lyrtech. Each of these contains a Windows PC running MATLAB for baseband signal generation and processing. An ethernet line connects both platforms to measure error rates. This setup is illustratively depicted in Fig. 6.12.

Both platforms are equipped with an 8 channel 14 bit analog/digital converter with up to 500MSPS. The maximum sampling rate is 104MHz, which is decreased to 26MHz for our measurements due to memory limitations. Hence, a sample timing of $T_s = 1/26\text{MHz} = 38.462\text{ns}$ results. Both transceivers are equipped with 4 RF frontends providing transmit powers of 26dBm in the 2.4GHz ISM band. The RF frontend is implemented as a non-DC coupled high pass, where all frequencies larger than 100Hz up to a maximum bandwidth of 20MHz pass. The typical CFO is specified with 100ppm of the carrier frequency used. In our setup we use a carrier frequency of $f_{\text{lo}} = 2.4\text{GHz}$, yielding an offset of $f_{\text{CFO}} \approx \pm 2.4\text{kHz}$ per transceiver. During operation with both Lyrtech platforms twice the Carrier Frequency Offset (CFO) can be experienced due to the utilization of two transceiver chains, yielding an $f_{\text{CFO}} \approx 5\text{kHz}$ that we expect during our measurements.

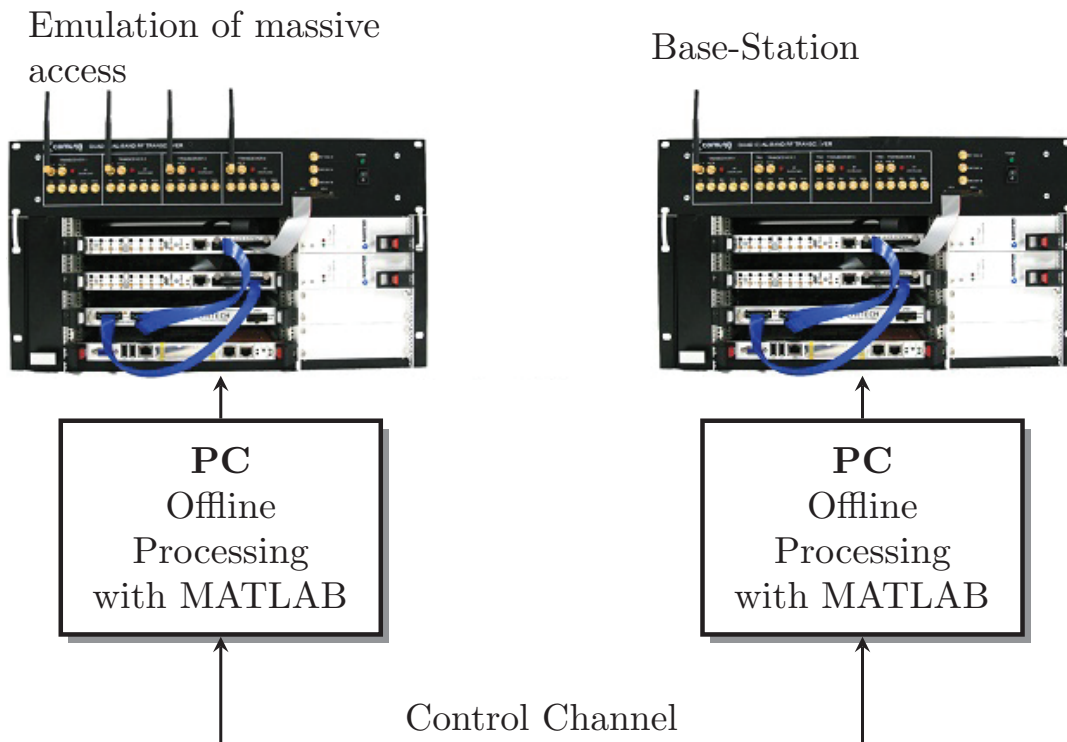


Figure 6.12: Hardware in the loop setup including the Lyrtech platform.

6.6.2 Description of the Testbed

Virtual Massive Access

The practical evaluation of massive access faces the challenge of realizing a massive number of nodes with a common transmitter chain. As mentioned previously the transmitter consists of four RF transceivers equipped with a single antenna each. To still model massive access of nodes over four antennas, we randomly assign the active nodes to the four transmit antennas yielding something we call *virtual* massive access. In virtual massive access the active nodes are randomly assigned to the four possible transmit antennas, if more than one active node is assigned to the same antenna, the baseband transmit signals of these are added, while the transmit signals of other active nodes are superimposed on the wireless channel. With virtual random access we have four physically different uplink channels that the active nodes share. The base-station has no knowledge about the mapping of nodes to antennas.

Frame Structure and Timing

The overall frame structure of the MCSM system for our practical evaluation is shown in Fig. 6.13. Here we multiplex a single MCSM system. At this point, one should keep in mind that multiple MCSM systems can be

multiplexed to the bandwidth available as indicated by the gray MCSM systems in Fig 6.13. However, for simplicity we only demonstrate a single MCSM system in the following. The overall bandwidth is $B = 26\text{MHz}$ at a carrier frequency of $f_{10} = 2.484\text{GHz}$. In this implementation we target LTE like parameters to also motivate the LTE compatibility of MCSM. To this end, the bandwidth is divided into $L_{\text{IFFT}} = 2048$ sub-carrier, leading to a core symbol duration of $T_{\text{OFDM}} = L_{\text{IFFT}}/26\text{MHz} = 78.77\mu\text{s}$ with a sub-carrier spacing of $\Delta f = 1/T_{\text{OFDM}} = 12.695\text{kHz}$. With $L_{\text{sc}} = 20$ sub-carrier, we have a bandwidth for MCSM of $B_{\text{MCSM}} = 253\text{kHz}$. The cyclic-prefix has a length of 144 samples, leading to a length of $T_{\text{CP}} = 5.538\mu\text{s}$. These

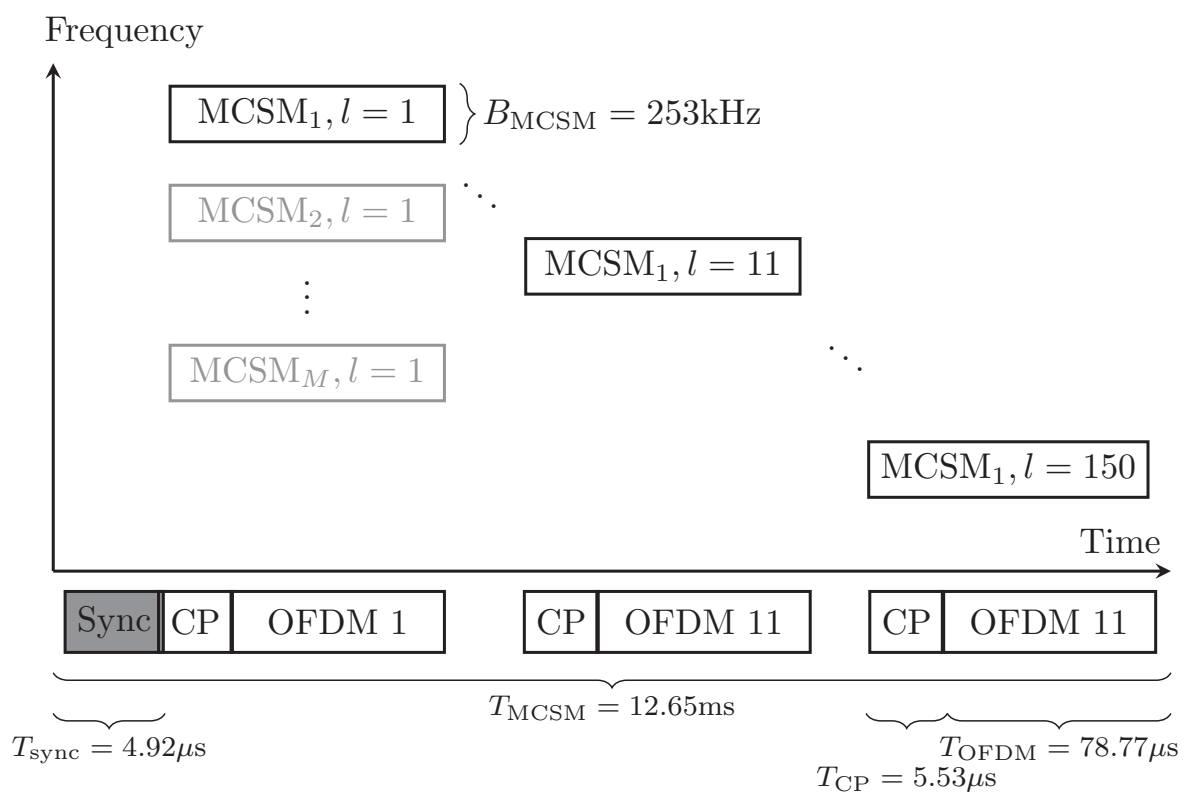


Figure 6.13: MCSM Frame design and symbol timing.

parameters are also shown in Table 6.2, where we also show the corresponding parameters used in LTE. Unless stated differently, the MCSM system itself is parametrized according to the base-line parametrization given in the simulation which is summarized in Table 6.1. The only differences between simulation and hardware setup is that we use a payload size of $L_u = 150$ bits for the practical evaluation. This payload in combination with the frame design yields a base data-rate of 20 kBit/s. The smaller payload size is caused by the storage capability of the Lyrtech platforms. With a spreading sequence length of $M = 20$ and a one-to-one multiplexing along the frequency axis, the MCSM system occupies $L_{\text{sc}} = 20$ sub-carriers,

Parameter	Var	MCSM	LTE
Carrier frequency	f_{lo}	2.484 GHz	see 3GPP LTE [R ⁺ 13]
Sampling Time	T_s	38.462 ns	32.552 ns
IFFT length	L_{IFFT}	2048	2048
OFDM Symbol time	T_{OFDM}	$78.77\mu\text{s}$	$66.6666\mu\text{s}$
CP length	L_{CP}	144	144/160 or 512
CP Symbol time	T_{CP}	$5.538\mu\text{s}$	$4.6875\mu\text{s}$
Sub-carrier spacing	Δf	12.69 kHz	15 kHz
Base Data-Rate	R_b	12 kBit/s	see 3GPP LTE [R ⁺ 13]

Table 6.2: System parameters: MCSM compared to LTE

yielding a bandwidth of $B_{\text{MCSM}} = M\Delta f = 253\text{kHz}$. The MCSM transmit frame consist of $L_{\text{F}} = 150$ OFDM symbols, giving a total frame length of $T_{\text{MCSM}} = 12.65\text{ms}$, which is slightly longer than the corresponding LTE frame. Additionally, a random frequency hopping is implemented, where the MCSM system randomly reallocates its sub-carriers each $N_{\text{p}} = 10$ OFDM symbols to exploit frequency diversity. To find the start of an MCSM frame an LTE like synchronization sequence of 128 samples or $T_{\text{sync}} = 4.92\mu\text{s}$ is added to the frame. To compensate CFO, a downlink control channel is implemented at the base-station, sending a single tone at a baseband frequency of 500kHz. Prior to transmission, the transmitter receives this tone and estimates the offset to the known frequency. Having the offset estimated, the transmit signal is pre-compensated by the corresponding CFO. To avoid collisions of the MCSM system and the downlink control channel, we avoid the sub-carriers corresponding to the tone.

6.6.3 Measurement Setup

The setup for the measurements is depicted in Fig. 6.14. It corresponds to a non-line-of-sight measurement in an office building with a transmitter receiver distance of approx. 60m. The floor and ceiling consist of concrete, while the walls within the building mainly consists of lightweight constructions made of fiber boards. The rooms containing receiver and transmitter were both closed by a wooden door during the time measurements are taken.

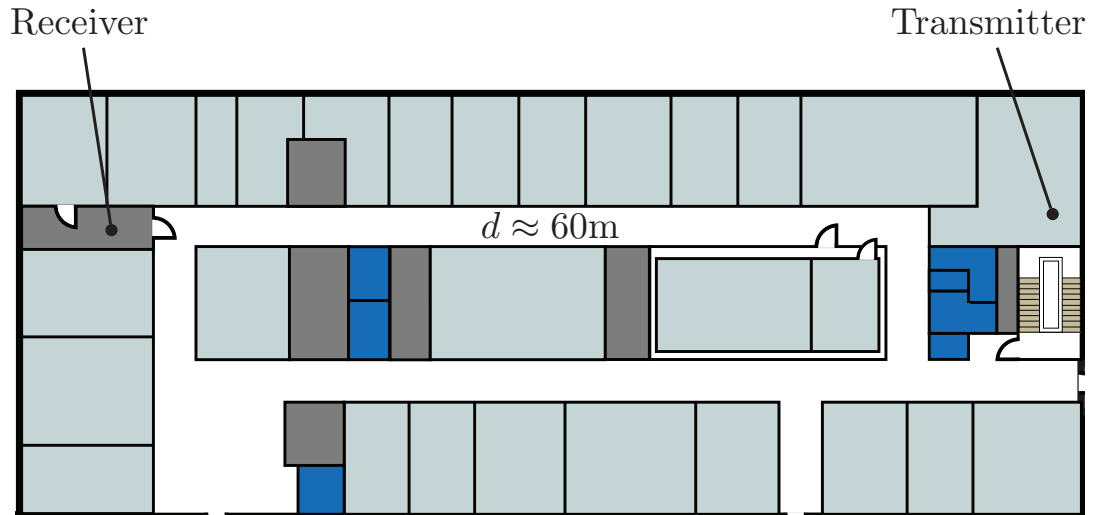


Figure 6.14: Floorplan of the measurement setup.

6.6.4 Results and Discussion

First, we show the estimated frequency domain response of the wireless channel between the four transmit antennas and the receive antenna in Fig. 6.15. To measure this impulse response, we assigned pilot symbols on all sub-carriers of one OFDM symbol. We transformed the measured impulse response back into the time domain and took only the first 4 taps, while the remaining taps only contain noise. The corresponding frequency domain impulse response shows that the channels are only slightly frequency selective over the band considered. By looking at the dominant taps in the time domain we measured a delay spread of approximately $\tau_h \approx 80\text{ns}$, corresponding to a distance between shortest and longest path of approximately 24m, which is clearly not much but matches the observation of only moderately frequency selective channels. Especially from the MCSM perspective the bandwidth occupied by $L_{sc} = 20$ can be considered as frequency flat. To compare the measurements with the simulations about MCSM, we show the measurements results in the following and compare them to a simulation. In the simulation we take the same parameters as in the measurement, summarized in Table 6.2.

The low frequency flat channel is problematic since gaining diversity over time is not possible anymore. Especially, if the channel is in a bad condition, frequency hopping does not yield the desired effect. As we have seen in the previous section, the multiuser energy detection suffers in this case which also impacts the data detection.

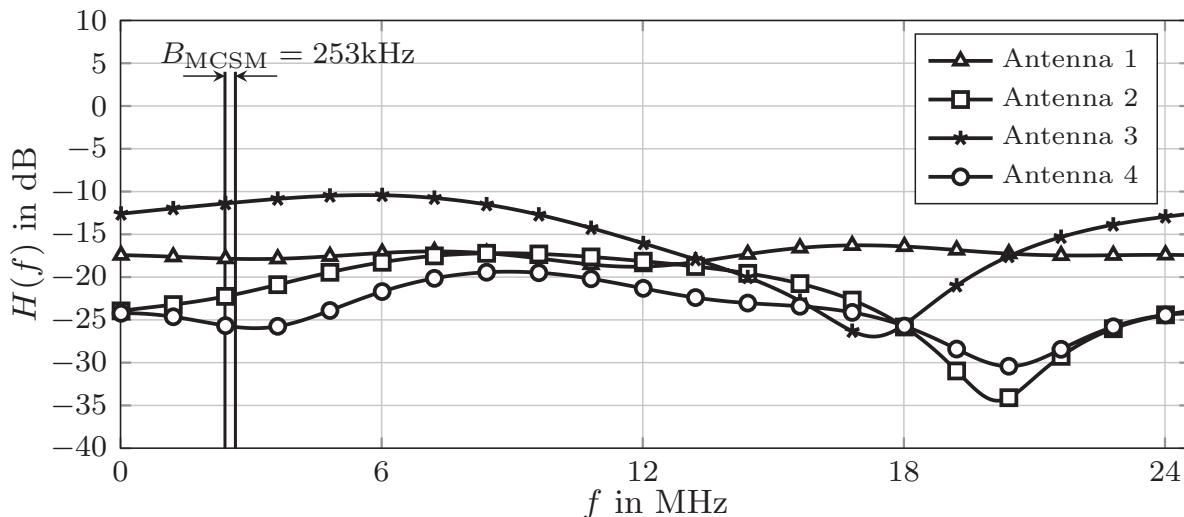


Figure 6.15: Measured frequency response of the channels between transmitter and receiver. The channel impulse response is restricted to 4 taps in time domain.

Measured Phase Transition Diagram

To start we consider the measured phase transition diagram, reflecting the asymptotic performance of the multiuser energy detector. Since the measurements are taken in a real setup, noise free curves cannot be achieved anymore. However, we set the transmit power to the maximum possible level allowing for high SNR measurements. The measured phase transition diagrams are shown in Fig. 6.16. For verification, the phase transition diagram obtained by simulation is also shown. Most interestingly, we observe only a small mismatch between the simulations and the measurements, which is most likely caused by impairments that are not modeled in the simulations, such as RF impairments or a mismatch of the channel modeling. Here, we also see the lack of frequency diversity leading to decreased performance of the activity detection. This becomes obvious by comparing Fig. 6.16 with the simulated phase transition diagram in the beginning of this chapter in Fig. 6.7 where the delay spread was assumed to be 1000m. There the performance of the activity detection is better which is caused by the higher frequency diversity achieved.

The MUSIC algorithm seems to be the most reliable approach for carrying out activity detection. Here, the measurements conform to the previous simulative results. MMP and MAP-E suffer losses which is caused by the unknown receive power, confirming the results from Chapter 5,

For the sake of completeness, the reader may compare the measured phase transition diagram with the phase transition diagrams from Chapter 5, where the algorithms were tested in Rician channel environments in Fig. 5.8.

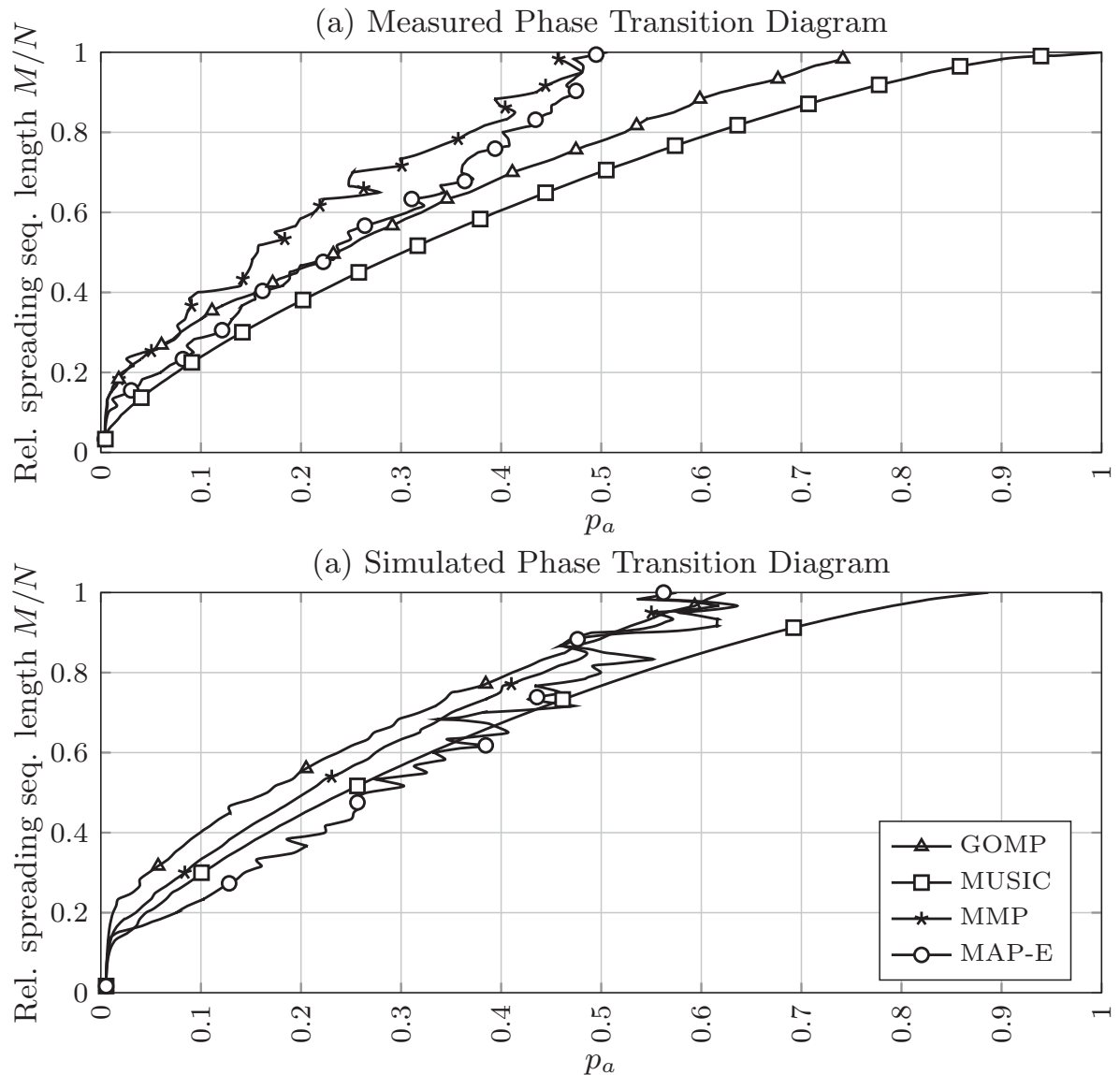


Figure 6.16: Measured (a) and simulated (b) phase transition diagram for MCSM showing the region where the activity error rate is below 10^{-3} .

We can observe remarkable similarities between the measurements and the simulations in a Rician channel with Rice factor $K_{\text{rice}} = 10$. This again confirms our theory that frequency hopping and increased Rice factor have similar effects on the performance of the activity detection. However, it should be noted that this effect is only an observation without proof.

Measured Performance over the SNR

For further analysis we consider the performance over the output power, which is proportional to the SNR. Based on the fact that active nodes randomly share the four transmit antennas, a thorough SNR definition is

hard to formulate. Active nodes share the transmit power of the RF frontend they are assigned to. Therefore, our SNR measurement is carried out over the transmit power per frontend, which is 26dBm at maximum. Fig. 6.17 plots the measured activity error rates in (a) and the measured frame error rates in (b) over the transmit power per frontend in a system a spreading sequence length of $M = 20$. Below that, in (c) and (d) the corresponding simulated error rates are plotted over the inverse noise variance. Due to the lack of a thorough SNR definition, the x-axis of both plots is comparable up to a constant offset. In the measurements, we observe a decline in activity and frame error rate for increasing output power, showing that the practical verification of M-CSM is feasible. Most interestingly, the MUSIC algorithm again exhibits the best performance which matches the previous observations and also the simulative verification. We also observe an error floor for MMP, MAP-E and GOMP, which can only be confirmed via simulations for the GOMP algorithm. This mismatch between simulation and practical evaluation may be due to impairments that are not covered by the simulation. In terms of frame error rate, the hardware setup confirms the theoretical results. Most interestingly, the SNR gap between activity and frame error rate, which is about 20dB in the simulation is confirmed by the hardware measurement. The average gap between both error rates is in the same range.

In Fig. 6.18 we see the same measurement carried out for a setup with a smaller spreading sequence length of only $M = 15$. Again, the hardware measurements are compared to the simulations. As expected the decreased spreading sequence length leads to worse performance in terms of activity and frame error rates. For the activity detection this results in error floors for the MMP, MAP-E and for the GOMP which are confirmed by the simulations. The same holds true for the corresponding frame error rates, which exhibit nearly the same SNR gap in measurements and simulations, showcasing that M-CSM's biggest potential lies in the design of a sophisticated multiuser detector.

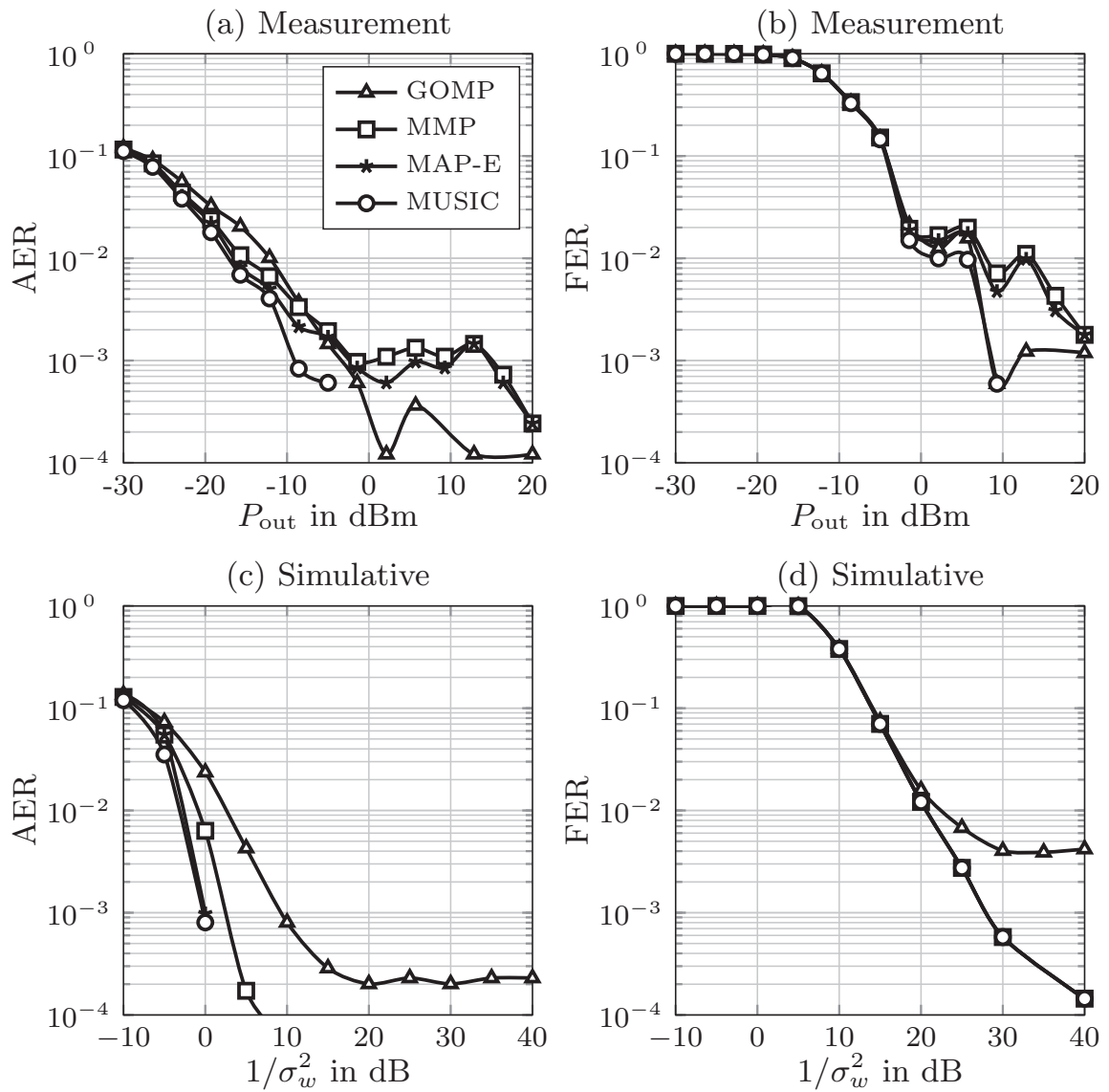


Figure 6.17: Comparison of measurement and Simulation for MCSM. Activity error rates in the left and frame error rate in the right hand side for a MCSM system with a spreading sequence length of $M = 20$.

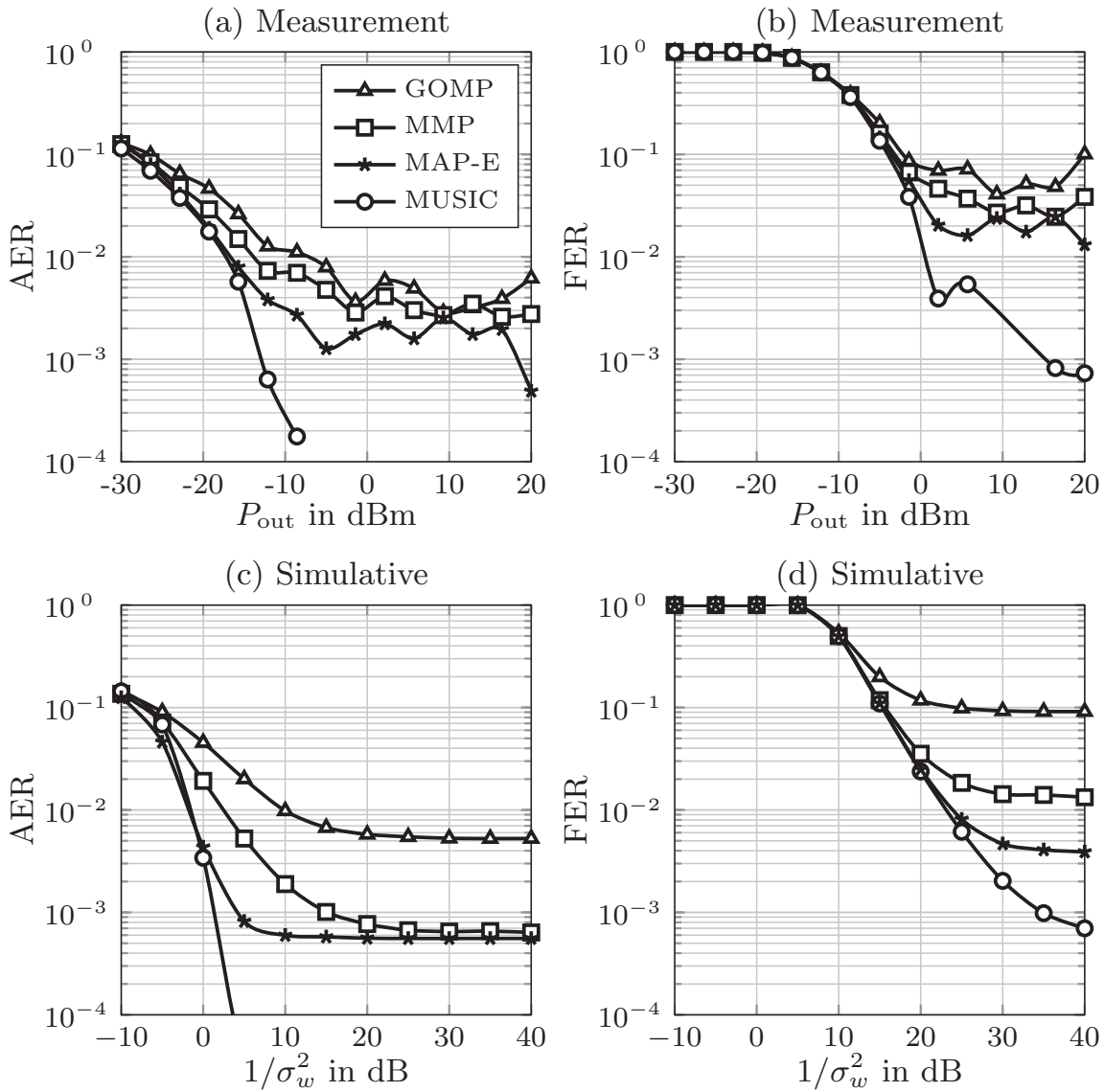


Figure 6.18: Comparison of measurement and Simulation for MCSM. Activity error rates in the left and frame error rate in the right hand side for a MCSM system with a spreading sequence length of $M = 15$.

6.7 Chapter Summary

Based on the results of the previous chapters, this chapter presented a practical system based on CS-MUD. Here CS-MUD was shown to be only one technology component required to meet the demands for massive M2M. We identified three key technology components that work together in a system called MCSM. More specifically, besides CS-MUD, MCSM is composed of a multi-carrier concept, non-coherent receiver and differential modulation. Due to the application of a multi-carrier scheme, the M2M uplink transmissions can be freely multiplexed within the time-frequency grid. We have shown that different multiplexing forms have certain advantages and disadvantages regarding the robustness to channel variations or frequency selectivity. Further it has been shown that MCSM offers a wide range of parameters to adapt the system to certain propagation environments. Within this chapter we have focused on a parametrization yielding a baseline data-rate of 12kBit/s per active node.

The feasibility of the MCSM system was demonstrated via simulations and via practical measurements carried out in a non-line-of-sight setup. In the simulations we showed that frequency hopping allows for gaining frequency diversity which increases the performance of the activity and data detection. Additionally, it was shown that the data detection in MCSM is limited by the multiuser interference and not by the activity detection. Further the impact of having asynchronous transmissions was investigated. With our setup we could cope with time delays of up to $1\mu\text{s}$. In the practical measurements we could confirm the results obtained by simulations. The parametrization pursued in this thesis demonstrated MCSM in an industrial like propagation environment involving a delay spread of the wireless channel of $1\mu\text{s}$. Beyond industrial applications MCSM offers applicability in M2M systems with large cells characterized by a large delay spread. The flexible system design of MCSM makes it a candidate technology for various M2M applications within the 5G context and beyond.

Chapter 7

Summary

The era of sole human-oriented traffic disappears, thereby raising novel challenges on the design of future communication systems such as 5G and beyond. Among the demands, the aggregation of M2M is and remains one of the most challenging ones. Ranging from sporadic and short messages to high data-rate ultra-reliable communication, M2M can be seen as a diverse traffic source, whose aggregation requires carefully designed physical layer concepts. Especially, efficient aggregation of a massive amount of M2M devices with low overhead in terms of the medium access is a challenging task. To this end, the aim of this thesis is to address the physical layer aspects of the aggregation of sporadic M2M with a focus on low overhead.

In **Chapter 2**, first an overview of sporadic M2M was given. The resulting system model encompasses the description of nodes that sporadically access the wireless channel to transmit small data packages to a central aggregation point. The medium access was closely aligned to CDMA and nodes spread their data to chips prior to transmission. The main difference to the classical application of CDMA is that the length of the spreading codes is much shorter than the number of nodes in the system, yielding overloaded systems. Further it was shown that the base-station has to perform a joint activity and data detection. Hence, activity errors affect the performance of the communication. The corresponding error measures known as false alarm and missed detection were presented and it was shown that the system impact of both is fundamentally different. While false alarm errors result in a SNR loss at the data detection, missed detection errors lead to a loss of data.

Motivated by this observation, the aspect of sole activity detection with a subsequent data detection was presented in **Chapter 3**. Here the focus was to tackle the activity detection problem from a communication's point of view

via soft information processing to control false alarm and missed detection rates. The basis for this chapter was the formulation of the activity LLR and corresponding decision rules. The eye opener was the fact that the typically optimal MAP decision rule yields undesirable activity error rates. Especially, the missed detection rate was shown to be very high when pursuing MAP estimation. Subsequently, two additional decision rules were introduced to enable controlling the activity error rates. First, the Bayes-Risk detection rule was shown to be a generalized MAP decision rule with an adjustable parameter Ω , determining the preference of the detector towards activity or inactivity. Preferring one direction automatically decreases one of the activity error rates while increasing the other rate. The Bayes-Risk decision rule allows overcoming the shortcomings of the MAP rule. However, the connection between Ω and resulting activity error rates has to be determined numerically. To enable full activity error rate control Chapter 3 introduced an adaptive threshold Neyman Person detector. This approach minimizes one activity error rate while bounding the other rate to a constant value. The results exemplary show that adaptive threshold Neyman-Pearson detection achieves a constant missed detection rate while simultaneously minimizing the false alarm rate.

Additionally, Chapter 2 addressed the implementation of upper decision rules. More specifically, the efficient calculation of the activity LLRs via Sphere Decoding was addressed. Here it was shown that the calculation of an activity LLR can be cast as a non-convex, penalized and underdetermined set of equations with a finite alphabet constraint. It was shown that this problem can implicitly be regularized by exploiting the penalty term. Results show that Sphere Decoding allows for optimal calculation of the activity LLRs at the cost of random complexity with exponential bound. Thus, K-Best detection is used as a sub-optimal approach which nearly achieves the performance of Sphere Decoding.

The joint activity and data detection was addressed in **Chapter 3** via an all-encompassing detector involving knowledge about frame activity and channel coding. More specifically a message passing detector was formulated that accounts for a full soft estimation in frame based transmissions. This detector was shown to consist of three building blocks, a multiuser detector, a decoder and a frame activity estimator called SPE. The multiuser detector is based on recent advances from the field of message passing in Compressed Sensing and estimates the augmented symbols from the nodes. Combining several multiuser detectors to a bank lead to frame Belief Propagation. Here messages are exchanged between a bank of decoders, a bank of SPEs and a bank of multiuser detectors. After some iterations this frame belief propagation algorithm yields the soft information for the information bits

and for the node activity states. The simulations have shown that the utilization of a low rate channel code allows to further decrease the spreading sequence length by decreasing the code-rate. Simulations were carried out using a repetition code, therefore it might be the case that more sophisticated channel codes even further decrease the spreading sequence length required.

Chapter 2 and Chapter 3 addressed the optimal activity and the optimal joint activity and data detection. Results were promising and it was shown that knowledge about frame activity boosts the detection performance. **Chapter 4** goes away from optimal algorithms to low complexity algorithms for detecting frame activity. The idea followed there was to use the concept of energy detection for estimating node activity in CS-MUD. Here we showed that the individual receive energy for each node can be estimated from the estimated receive covariance matrix at the base-station. This concept leaves the assumption of having AWGN channels between the node and the base-station to fading channels ranging from Rician to full Rayleigh fading. The main advantage of using the receive covariance matrix is the SNR enhancing effect caused by the averaging carried out. The results showed that the algorithms developed in this chapter exhibit tremendous SNR gains for already for short frames. Further, three algorithms were introduced. First, a simple and heuristic matrix matching pursuit motivated by the well known OMP was presented. Here energies are estimated by correlating the receive covariance matrix with the columns of a dictionary to identify active nodes. This algorithm was shown to be simple but sacrifices performance, especially in the fading channel where receive powers are unknown. Its application is restricted to the AWGN channel. Second, the well known MUSIC algorithm, based on the Eigenvalue decomposition of the receive covariance matrix was considered. Its application turned out to be quite powerful as MUSIC is able to estimate the activity in Rayleigh and Rician fading channels with good reliability. Finally, the MAP optimization problem for the powers denoted as MAP-E based on the receive covariance matrix was considered. Here it was shown that the particular fading can be subsumed into the prior power probability contained in the MAP. Depending on AWGN or Rayleigh fading channel, two versions of the MAP-E were formulated. In case of AWGN the optimization problem is over a finite alphabet allowing for non-linear algorithms such as Sphere Decoding. The results showed that the MAP-E algorithm achieves reliable activity detection with $M = \sqrt{N}$ observations only. Unfortunately, this is not true for the Rayleigh fading channel. Here the MAP-E showed performance losses and was even outperformed by MUSIC.

The last chapter of this thesis, **Chapter 5** aimed at putting the advances of the preceding chapters into a practical system concept. The main focus was to identify certain key challenges that a practical system for M2M

has to address. Based on these requirements, the resulting MCSM system was defined. MCSM was shown to consist of three key technologies that hand in hand allow for the aggregation of sporadic M2M. First, a multi-carrier scheme was used to flexibly allocate time and frequency resources. The MCSM system concept summarizes narrow-band systems that are simultaneously multiplexed to the bandwidth given. The assumption of narrowband systems lead to the second key technology component, being non-coherent receiver concepts driven by differential modulation. Due to the application of differential modulation the pilot overhead could be decreased down to a known starting phase. The third technology component was CS-MUD which is used on top of OFDM. Here the nodes multiplex their chips to the sub-carriers prior to transmission. This multiplexing was shown to be one of the MCSM specific design parameters that allow adapting the system to various channel conditions. In MCSM the activity detection schemes from Chapter 4 were used in combination with a least-squares data detector. The verification of the MCSM system was shown via an example parametrization simulatively and via a hardware demonstration platform. The concept shown can be seen as a candidate system for aggregating sporadic M2M uplink traffic in various scenarios. Depending on the propagation environment, the channel conditions and the requirements, MCSM allows adapting its parameters to match the requirements. This powerful property renders MCSM to be a candidate technology not only for 5G systems but also for M2M system in various other setups such as industrial applications.

Open Questions and Future Work

- The complexity of the frame BP was shown to be very high. Here recent research has shown that the complexity of the multiuser detector can be decreased by using second order approximations of the messages. The resulting algorithm is known as AMP and has been published in [DMM09]. Applying these approximations may help to further decrease the performance.
- Further, the frame BP could be augmented to work within the MCSM system. This requires involving a differential demodulator within the frame BP. The connecting point would be the variable for the augmented symbol x_n , whose prior probability summarized by f_n would change. Therefore, the messages from the augmented symbol x_n to the likelihood factor g_m change. Here, the simple numeric calculation of mean and variance may not be possible anymore as x_n is continuous-valued. The sole task of differential demodulation via belief propagation has been considered in [Bar10]. However, merging the results with the frame BP is still an open challenge.
- For multiuser energy estimation shown in Chapter 5 it was assumed that the base-station has instantaneous knowledge about the number of active nodes N_{act} . Here, future work can address the question of how this information is obtained. As stated within the corresponding chapter, existing works consider the Eigenvalue distribution of the covariance matrix [CW10].
- The MCSM system concept offers a wide field for possible future work. Within this thesis we applied a least-squares data-detector, which is clearly not the best one can do. Thus, improved multiuser detection in MCSM is one possible direction of future research.
- The second point addresses the multi-carrier scheme applied. Here we used OFDM which comes at the cost of a cyclic-prefix. Further, it is well known that OFDM suffers performance in case of offsets such as Doppler impact. One idea would be to change the multi-carrier scheme to a generalized waveform accommodating these effects. The other side of the medal is that with non-orthogonal waveforms, more sophisticated multiuser detectors are required. A promising approach here is again to use message passing to detect the data of the nodes.

Appendix A

Appendix

A.1 Proof of the Bayes-Risk

The Bayes-Risk detector minimizes the Risk of an erroneous decision, where we can assign the weights C_{FA} for false alarm and C_{MD} for missed detection. We hereby implicitly set the risks for correct decisions to zero. The risk can be formulated via

$$\begin{aligned} \mathcal{R} = & C_{\text{FA}} \Pr(x_n = 0) \int_{Z_A} p_{\mathbf{y}}(\mathbf{y}|x_n = 0) d\mathbf{y} + \\ & C_{\text{MD}} \Pr(x_n \in \mathcal{A}) \int_{Z_I} p_{\mathbf{y}}(\mathbf{y}|x_n \in \mathcal{A}) d\mathbf{y} \end{aligned} \quad (\text{A.1})$$

Where $Z_I \cup Z_A = Z$ are disjunct regions of the observation space Z which allows for reformulation of (A.1) according to

$$\begin{aligned} \mathcal{R} = & C_{\text{FA}} \Pr(x_n = 0) \int_{Z \setminus Z_I} p_{\mathbf{y}}(\mathbf{y}|x_n = 0) d\mathbf{y} + \\ & C_{\text{MD}} \Pr(x_n \in \mathcal{A}) \int_{Z_I} p_{\mathbf{y}}(\mathbf{y}|x_n \in \mathcal{A}) d\mathbf{y}. \end{aligned} \quad (\text{A.2})$$

With

$$\int_Z p_{\mathbf{y}}(\mathbf{y}|x_n) d\mathbf{y} = 1 \quad \forall x_n, \quad (\text{A.3})$$

we can rewrite

$$\int_{Z \setminus Z_I} p_{\mathbf{y}}(\mathbf{y}|x_n = 0) d\mathbf{y} = 1 - \int_{Z_I} p_{\mathbf{y}}(\mathbf{y}|x_n = 0) d\mathbf{y} \quad \forall x_n. \quad (\text{A.4})$$

Which allows to reformulate (A.2) to obtain

$$\begin{aligned} \mathcal{R} = & C_{\text{FA}} \Pr(x_n = 0) \left[1 - \int_{Z_I} p_{\mathbf{y}}(\mathbf{y}|x_n = 0) d\mathbf{y} \right] + \\ & C_{\text{MD}} \Pr(x_n \in \mathcal{A}) \int_{Z_I} p_{\mathbf{y}}(\mathbf{y}|x_n \in \mathcal{A}) d\mathbf{y}. \end{aligned} \quad (\text{A.5})$$

Rearranging (A.5), yields

$$\begin{aligned} \mathcal{R} = & C_{\text{FA}} \Pr(x_n = 0) + \\ & \int_{Z_I} \underbrace{C_{\text{MD}} \Pr(x_n \in \mathcal{A}) p_{\mathbf{y}}(\mathbf{y}|x_n \in \mathcal{A})}_{I_1} d\mathbf{y} - \\ & \int_{Z_I} \underbrace{C_{\text{FA}} \Pr(x_n = 0) p_{\mathbf{y}}(\mathbf{y}|x_n = 0)}_{I_2} d\mathbf{y}. \end{aligned} \quad (\text{A.6})$$

Equivalently, we can rewrite the integration in (A.5) with respect to Z_A and obtain for the risk

$$\begin{aligned} \mathcal{R} = & C_{\text{MD}} \Pr(x_k \in \mathcal{A}) + \\ & \int_{Z_A} \underbrace{C_{\text{FA}} \Pr(x_n = 0) p_{\mathbf{y}}(\mathbf{y}|x_n = 0)}_{I_2} d\mathbf{y} - \\ & \int_{Z_A} \underbrace{C_{\text{MD}} \Pr(x_n \in \mathcal{A}) p_{\mathbf{y}}(\mathbf{y}|x_n \in \mathcal{A})}_{I_1} d\mathbf{y}. \end{aligned} \quad (\text{A.7})$$

With (A.6) and (A.8) the regions Z_A and Z_I are the free parameters that allow to minimize the risk. We see that the functionals below the integrals I_1 and I_2 are all positive and show up in both expressions. The risk can be minimized by estimating H_I if $I_2 > I_1$ and H_A if $I_1 > I_2$. This strategy results in a likelihood ratio test between the two hypothesis inactive and active. Note that the hypothesis for activity is a composite hypothesis which has to be evaluated over all possible sub-hypothesis yielding.

$$\begin{aligned} \mathcal{R} = & C_{\text{MD}} \Pr(x_k \in \mathcal{A}) + \\ & \int_{Z_A} \underbrace{C_{\text{FA}} \Pr(x_n = 0) p_{\mathbf{y}}(\mathbf{y}|x_n = 0)}_{I_2} d\mathbf{y} - \\ & \int_{Z_A} \underbrace{C_{\text{MD}} \sum_{x_n \in \mathcal{A}} \Pr(x_n \in \mathcal{A}) p_{\mathbf{y}}(\mathbf{y}|x_n \in \mathcal{A})}_{I_1} d\mathbf{y}. \end{aligned} \quad (\text{A.8})$$

Deciding in favor of I_1 or I_2 results in the LRT (3.20).

A.2 Proof of the Neyman Pearson Problem

The point of (3.28) is to provide estimates for the false alarm and missed detection probabilities. We first rewrite the missed detection and false alarm probabilities in terms of activity LLRs L_n for node n . The decision regions Z_A and Z_I are fully determined by the activity LLRs as $Z_I := \{L_n : L_n \geq t\}$ and $Z_A := \{L_n : L_n < t\}$. This allows us to write missed detection and false alarm probability for node n as

$$\Pr_{\text{MD}}(t) = \Pr(x_n \in \mathcal{A}) \int_{\{L_n : L_n \geq t\}} p_{L_n}(L_n | x_n \in \mathcal{A}) dL_n \quad (\text{A.9a})$$

$$\Pr_{\text{FA}}(t) = \Pr(x_n = 0) \int_{\{L_n : L_n < t\}} p_{L_n}(L_n | x_n = 0) dL_n. \quad (\text{A.9b})$$

In the following we only focus on false alarm probabilities as the proof for the missed detection probability is nearly the same. The proof outlined here is based on the assumption that the error due to the approximation of the activity LLRs with the max-log approximation is negligible. The posteriori probability obtained from the activity LLRs $\Pr(x_n = 0 | L_n)$ is a sample of a random variable with support $L_n \in \mathbb{R}$. This is due to the fact that the activity LLRs are random variables. In the following we show that set specific averages of this random variable converges to (A.9b). We therefore rewrite (A.9b) with the application of Bayes' rule as

$$\Pr_{\text{FA}}(t) = \int_{\{L_n : L_n < t\}} \Pr(x_n = 0 | L_n) p_{L_n}(L_n) dL_n. \quad (\text{A.10})$$

We see that (A.10) is the mean of the random variable $\Pr(x_n = 0 | L_n)$ over the interval $L_n < t$. We now assume that $|\mathcal{L}_A| = \infty$. $\Pr(x_n = 0 | L_n) = \frac{1}{1 + \exp(-L_n)}$ allows us to sample this random variable, where each calculated activity LLR generates one sample. Averaging these samples gives the average missed detection probability $\tilde{\Pr}_{\text{FA}}$ and we have

$$\begin{aligned} \tilde{\Pr}_{\text{FA}}(\mathcal{L}, t) &= \lim_{|\mathcal{L}_A| \rightarrow \infty} \frac{\sum_{n \in \mathcal{L}_A} \Pr(x_n = 0 | L_k)}{|\mathcal{L}_A|} \rightarrow \\ &\int_{\{L_n : L_n < t\}} \Pr(x_n = 0 | L) p_{L_n}(L_n) dL_n. \end{aligned} \quad (\text{A.11})$$

Thus, the sample mean $\tilde{\Pr}_{\text{FA}}(\mathcal{L}, t)$ converges to the true mean $\Pr_{\text{FA}}(t)$ as the size of the set $|\mathcal{L}_A|$ is sufficiently large. \square

A.2.1 Convergence

In the following we define the approximation error as $\Delta = |\tilde{\text{Pr}}_{\text{FA}}(\mathcal{L}, t) - \text{Pr}_{\text{FA}}(t)|$. The Chebyshev inequality [PP02] allows to bound the error Δ via

$$\Pr\{\Delta \geq \epsilon\} \leq \frac{\sigma_{\tilde{\text{Pr}}_{\text{FA}}}^2}{\epsilon^2}, \quad (\text{A.12})$$

with $\sigma_{\tilde{\text{Pr}}_{\text{FA}}}^2$ being the variance of the estimate $\tilde{\text{Pr}}_{\text{FA}}(\mathcal{L}, t)$. In the following we consider the variance of $\tilde{\text{Pr}}_{\text{FA}}(\mathcal{L}, t)$ for which we assume the activity LLRs to be i.i.d. In this case, the variance can be calculated via

$$\begin{aligned} \sigma_{\tilde{\text{Pr}}_{\text{FA}}}^2 &= \text{var} \left[\frac{\sum_{n \in \mathcal{L}_A} \Pr(x_n = 0 | L_n)}{|\mathcal{L}_A|} \right] \\ &= \frac{1}{|\mathcal{L}_A|} \text{var}(\Pr(x_n = 0 | L_k)). \end{aligned} \quad (\text{A.13})$$

To obtain $\text{var}(\Pr(x_n = 0 | L_n))$, we use a first-order Taylor expansion and obtain $\frac{d}{dL_n} \frac{1}{1 + \exp(-L_n)} = \frac{\exp(L_n)}{(1 + \exp(L_n))^2}$. The variance can now be approximated as [PP02]

$$\text{var}(\Pr(x_n = 0 | L_n)) \approx \left[\frac{\exp(\bar{L}_n)}{(1 + \exp(\bar{L}_n))^2} \right]^2 \sigma_{L_n}^2, \quad (\text{A.14})$$

where $\sigma_{L_n}^2$ denotes the variance and \bar{L}_n denotes the mean of the activity LLR, respectively. Assuming the approximation (A.14) to be tight yields after inserting it into (A.13), together with (A.12)

$$\Pr\{\Delta \geq \epsilon\} \leq \left[\frac{\exp(\bar{L}_n)}{(1 + \exp(\bar{L}_n))^2} \right]^2 \frac{\sigma_{L_n}^2}{|\mathcal{L}_A| \epsilon^2}. \quad (\text{A.15})$$

Considering (A.15) shows that the approximation error depends on several parameters. First, we see that making $|\mathcal{L}_A|$ large decreases the approximation error down to arbitrary small values. This reveals that the cardinality of the sets $|\mathcal{L}_A|$ and $|\mathcal{L}_I|$ is crucial for the performance of the Neyman-Pearson detection. Another side effect is that the mean of the activity LLR \bar{L}_n . If \bar{L}_n is large, the approximation error is negligible as the first factor of (A.15) converges to zero. This also shows that activity LLRs with mean value close to zero lead to high approximation errors. Note that this is not a rigorous proof of convergence, however the results perfectly match the observations.

A.3 Mean and Variance of Θ

We start by writing the matrix Θ as a composition of column vectors θ_l

$$\Theta = \frac{1}{L_F} \sum_{l=1}^{L_F} \theta_l \theta_l^H - \sigma_w^2 \mathbf{I}_M \quad (\text{A.16})$$

where $\frac{1}{L_F} \sum_{l=1}^{L_F} \theta_l \theta_l^H$ corresponds to a complex circular Wishart matrix $\mathcal{W}\left(\frac{\sigma_w^2}{L_F^2} \mathbf{I}_M, L_F\right)$. Here, $\frac{\sigma_w^2}{L_F^2} \mathbf{I}_M$ denotes the covariance matrix of one column vector θ_l and L_F denotes the degrees of freedom which corresponds to the number of Gaussian column vectors in (A.16). The mean of the Wishart matrix is $\sigma_n^2 \mathbf{I}_m$ and the variance of the i, j th element is $L_F \left(\frac{\sigma_n^4}{L_F^2}\right) = \sigma_n^4 / L_F$.

We start by considering the i th main diagonal element of θ which is composed as

$$\theta_{ii} = \frac{1}{L_F} \frac{\sigma_w^2}{2} \sum_{l=1}^{L_F} \theta_i \theta_i^* - \sigma_w^2, \quad (\text{A.17})$$

where θ_i is complex circular normal distributed with zero mean and variance $\sigma_{w,i}^2 = 1$ in real and imaginary part, respectively. Noting that $\theta_i \theta_i^*$ is Chi squared distributed with 2 degrees of freedom allows to express the mean of (A.17) mean (\cdot) as

$$\begin{aligned} \text{mean}(\theta_{i,i}) &= \frac{1}{L_F} \frac{\sigma_w^2}{2} L_F \text{mean}(\theta_i \theta_i^*) - \sigma_w^2 \\ &= \frac{1}{L_F} \frac{\sigma_w^2}{2} 2L_F - \sigma_w^2 = 0. \end{aligned} \quad (\text{A.18})$$

For the variance $\text{var}(\cdot)$ we have the same argumentation and obtain

$$\begin{aligned} \text{var}(\theta_{ii}) &= \frac{1}{L_F^2} \frac{\sigma_w^4}{4} L_F \text{var}(\theta_i \theta_i^*) \\ &= \frac{1}{L_F} \frac{\sigma_w^4}{4} 4 = \frac{\sigma_w^4}{L_F}. \end{aligned} \quad (\text{A.19})$$

We can nearly apply the same argumentation for the off-diagonal elements. Consider the i, j th off-diagonal element

$$w_{ii} = \frac{1}{L_F} \frac{\sigma_w^2}{2} \sum_{l=1}^{L_F} \theta_i \theta_j^*, \quad (\text{A.20})$$

its mean is given by

$$\text{mean}(\theta_{i,j}) = \frac{1}{L_F} \frac{\sigma_n^2}{2} L_F \text{mean}(\theta_i) \cdot \text{mean}(\theta_j^*) = 0 \quad (\text{A.21})$$

For the variance we end up with

$$\begin{aligned} \text{var}(\theta_{i,j}) &= \frac{1}{L_F^2} \frac{\sigma_w^4}{4} L_F \text{var}(\theta_i) \text{var}(\theta_j^*) \\ &= \frac{1}{L_F} \frac{\sigma_w^4}{4} 2 \cdot 2 = \frac{\sigma_w^4}{L_F}. \end{aligned} \quad (\text{A.22})$$

In summary, all elements of Θ are of zero mean and have variance σ_w^4/L_F .

Acronyms

AER Activity Error Rate.

AMP Approximate Message Passing.

ARQ Automatic Repeat Request.

AWGN Additive White Gaussian Noise.

bcSIC Block Correlation Successive Interference Cancellation.

BER Bit Error Rate.

BICM Bit Interleaved Coded Modulation.

BP Belief Propagation.

BPSK Binary Phase Shift Keying.

CDMA Code Division Multiple Access.

CFO Carrier Frequency Offset.

CRC Cyclic Redundancy Check.

CS Compressed Sensing.

CS-MUD Compressed Sensing Multiuser Detection.

CSI Channel State Information.

D-PSK Differential Phase Shift Keying.

D-QPSK Differential Quadrature Phase Shift Keying.

DCT Discrete Cosine Transform.

EC-GSM-IoT Extended Coverage GSM For IoT.

eNB Evolved Node B.

FER Frame Error Rate.

GOMP Group Orthogonal Matching Pursuit.

GSM Global Telephony Standard.

i.i.d. Identically Independently Distributed.

ISI Inter-Symbol-Interference.

LDPC Low Density Parity Check Code.

LLR Log-Likelihood Ratio.

LRT Likelihood Ratio Test.

LTE 3GPP Long Term Evolution.

M2M Machine-to-Machine Communication.

MAP Maximum-a-Posteriori.

MAP-E Maximum-a-Posteriori Energy Estimator.

MCSM Multicarrier Compressed Sensing Multiuser Detection.

METIS Mobile And Wireless Communications Enablers For The Twenty-twenty
Information Society.

MIMO Multiple Input Multiple Output.

MLD Maximum Likelihood Detection.

mM2M Massive Machine-to-Machine Communication.

MMP Matrix Matching Pursuit.

MMSE Minimum Mean Square Error.

MMV-CS Multiple Measurement Vector Compressed Sensing.

MP Matching Pursuit.

MSE Mean Square Error.

MUD Multi-User Detector.

MUSIC Multiple Signal Classification.

NB-IoT Narrowband Internet Of Things.

OFDM Orthogonal Frequency Division Multiplexing.

OLS Orthogonal Least Squares.

OMP Orthogonal Matching Pursuit.

PAPR Peak To Average Power Ratio.

PCT Patent Cooperation Treaty.

PDF Probability Density Function.

PED Partial Euclidian Distance.

-
- PMF** Probability Mass Function.
- PN** Pseudo Noise.
- PRACH** Physical Random Access Channel.
- PSK** Phase Shift Keying.
- PUSCH** Physical Uplink Shared Channel.
- QAM** Quadrature Amplitude Modulation.
- RIP** Restricted Isometric Property.
- ROC** Receiver Operating Characteristics.
- SCMA** Sparse Code Medium Access.
- SER** Symbol Error Rate.
- SIC** Successive Interference Cancellation.
- SOTA** State Of The Art.
- SPE** Sparsity Pattern Equalizer.
- Sphere Decoding** Sphere Decoding.
- SQRD** Sorted QR Decomposition.
- SVD** Singular Value Decomposition.
- UE** User Equipment.

List of Symbols

Functions and Operators

$\phi(\cdot)$	Decision Rule
$\delta(\cdot)$	Delta distribution
Δ	Distance increment
\exp	Exponential function
$\mathbf{1}_{\mathcal{A}}$	Indicator function w.r.t. set \mathcal{A}
\log_{10}	Log to base 10
\log	Log to base e
$\nu_{g \rightarrow x}(\cdot)$	Message from g to x
$\ \cdot\ _F$	Matrix Frobenius norm
$\ \cdot\ _p$	p -vector norm
$D_n(\cdot)$	Partial Euclidean distance at layer n
Pr_{FA}	Probability for false alarm
Pr_{MD}	Probability for missed detection
$\text{Pr}(\cdot)$	Event Probability
$\text{Im}(\cdot)$	Imaginary part
$\text{Re}(\cdot)$	Real part
$\mathbf{dg}(\cdot)$	Sets up diagonal matrix or gives back diagonal elements
$\text{evd}(\cdot)$	Eigenvalue decomposition
$p_n(\cdot)$	n th factor of Channel Decoder
$g_m(\cdot)$	m th factor of likelihood function
$f_n(\cdot)$	n th of prior probability
$h_n(\cdot)$	n th factor of Sparsity pattern equalizer
$f_p(\cdot)$	Functional for penalizing underdet. system
$p_x(x)$	Probability Density Function of the variable x

$\text{vec}()$ Stacks the columns of a matrix as vector

General and Calligraphic Symbols

\mathcal{A}_0 Augmented Mod. Alphabet including zero

\in Element of

\cup Union of sets

\mathcal{L} Set of activity LLRs

$\mathcal{O}(\cdot)$ Landau Symbol

\mathcal{A} Modulation Alphabet

σ_w Variance of AWGN

$\mathcal{N}(\mu, \sigma^2)$. . . Normal distribution with mean and variance

\mathbf{A}^\dagger Left side Moore Penrose inverse of \mathbf{A}

$\mathbb{X}_{n,\nu}$ Set of vectors with n th element set to ν

\cap Intersection of sets

\otimes Kronecker product

\mathcal{P} Sub-carrier allocation for MCSM

Greek Symbols

α Penalty term for under-determined system

κ Success probability of Bernoulli variable

τ_h Delay spread of wireless channel

η Threshold for Neyman-Pearson detector

Ω Ratio of costs for false alarm and missed detection

ϵ Path-loss exponent

Σ Variable to regularize underdetermined system

Θ Remaining noise contained in the est. receive covariance matrix

$\Delta\tau_{\max}$ Maximum timing offset

$\Delta\tau$ Time offset

δ Parameter to regularize under-determined system

Λ Eigenvalue matrix

λ Eigenvalue

Υ System matrix for energy detection

γ Normalization constant for a pdf

β System load

$\mu_{q \rightarrow m}$ Mean value from node q m

ω	Parameter for Nakagami M-fading
Φ_{WW}	Noise covariance matrix
$\boldsymbol{\rho}$	Vector with received powers
\mathbf{P}_{XX}	Covariance Matrix of data symbols weighted with channel tap
Φ_{YY}	Receive covariance matrix
$\boldsymbol{\varphi}_{YY}$	Vectorized receive covariance matrix
$\zeta_{m \rightarrow n}$	Variance from node m to node n

Roman Symbols

x	Symbol
B_{MCSM}	Bandwidth occupied by a single MCSM system
R_c	Code rate
\mathbf{A}	Composite signature matrix
\mathbf{H}	Convolution matrix of the wireless channel
C_{FA}	Costs for false alarm
C_{MD}	Costs for missed detection
\mathbf{F}	DFT matrix
R_b	Data rate
t	Decision threshold
b	Differentially encoded symbol
d_{max}	Distance between longest and shortest path
\mathbf{T}_I	Matrix for inserting the guard interval
\mathbf{T}_R	Matrix for removing the guard interval
H_A	Hypothesis for activity
H_I	Hypothesis for inactivity
\mathbf{I}_N	$N \times N$ identity matrix
u	Information bit
K_{best}	Parameter for K-Best detection
T_{CP}	Time duration for cyclic prefix
L_{CP}	Length of cyclic prefix in samples
L_F	Frame Length
L	Activity LLR
\mathbf{x}	Multiuser vector
L_c	Number of Code Bits

L_u	Number of Info Bits
ΔN_{act}	Offset for the number of active nodes
N_{act}	Number of active nodes
N	Number of Nodes
M	Number of observations at base-station
N_p	Number of OFDM symbols after which the sub-carriers are reallocated
N_{Hop}	Number of frequency hops performed per MCSM frame
\mathbf{D}	Matrix summarizing the phase shifts caused by timing offsets
p_a	Activity probability
\mathbf{P}	diagonal matrix with received powers
\mathbf{Q}	Unitary matrix from QR-Decomposition
\mathbf{N}	Stochastic part of noise covariance matrix
\mathbf{y}	Receive signal vector
\mathbf{R}	Upper triangular from QR-Decomposition
d	Sphere radius for Sphere Decoder
\mathbf{A}	Matrix with spreading sequence
\mathcal{S}_x	Support set
c	Code symbol
T_{MCSM}	Time to transmit one symbol in MCSM
T_{OFDM}	Time for a single OFDM symbol
Z_A	Region in observation space where activity is decided
$\mathbf{0}_N$	$N \times 1$ zero vector
Z_I	Region in observation space where inactivity is decided
s	Node activity state
Δf	Sub-carrier spacing
L_{sc}	Number of used sub-carriers
\mathbf{h}	Channel vector
B_c	Number of used sub-carriers
\mathbf{U}	Unitary Eigenvector matrix
\mathcal{S}_x	Frame support set
m	Index for receive vector
q	Context dependent index
l	Symbol index

n	Node index
v	Context dependent index
K_{rice}	Parameter for Rician fading channel
L_{IFFT}	Number of sub-carriers for MCSM
L_{u}	Number of information bits
\mathbf{B}	Permutation matrix
\mathbf{N}	Remaining noise in receive covariance matrix
R	Repetition factor for repetition code
$\bar{\rho}_n$	Average receive power of n th node
$\tilde{\rho}_n$	Normalized received power of n th node
ρ_n	Receive power of n th node
$\tilde{\mathbf{X}}$	Multuser signal weighted with channel tap
$v_{q \rightarrow m}$	Variance from node q to node m
$z_{m \rightarrow n}$	Mean value from node m to node n

Bibliography

- [3GP16] 3GPP, “Narrowband-Internet of Things”, *Part of LTE Release 13*, 2016. 3
- [Bar10] A. Barbieri, “Blind per-state detection of DPSK over correlated fading channels”, *IEEE Transactions on Vehicular Technology*, volume 59, no. 5, pp. 2320–2327, 2010. 144, 175
- [BBW⁺05] A. Burg, M. Borgmann, M. Wenk, M. Zellweger, W. Fichtner, and H. Bölcskei, “VLSI implementation of MIMO detection using the sphere decoding algorithm”, *IEEE Journal of Solid-State Circuits*, volume 40, no. 7, pp. 1566–1577, 2005. 32, 60
- [BDDW08] R. Baraniuk, M. Davenport, R. DeVore, and M. Wakin, “A simple proof of the restricted isometry property for random matrices”, *Constructive Approximation*, volume 28, no. 3, pp. 253–263, 2008. 21
- [BMWD15] C. Bockelmann, F. Monsees, M. Woltering, and A. Dekorsy, “Hardware-In-the-Loop Measurements of the Multi-Carrier Compressed Sensing Multi-User Detection (MCSM) System”, *Jahreskolloquium Kommunikation in der Automation (KommA) 2015*, Magdeburg, Germany, Nov 2015. 8, 135
- [Boc15] C. Bockelmann, “Iterative Soft Interference Cancellation for Sparse BPSK Signals”, *IEEE Communications Letters*, volume 19, no. 5, pp. 855 – 858, May 2015. 74
- [BPN⁺16] C. Bockelmann, N. Pratas, H. Nikopour, K. Au, T. Svensson, C. Stefanovic, P. Popovski, and A. Dekorsy, “Massive machine-type communications in 5G: physical and MAC-layer solutions”, *IEEE Communications Magazine*, volume 54, no. 9, pp. 59–65, 2016. 16, 17
- [BSB10] D. Baron, S. Sarvotham, and R. G. Baraniuk, “Bayesian compressive sensing via belief propagation”, *IEEE Transactions on Signal Processing*, volume 58, no. 1, pp. 269–280, 2010. 73
- [BSD13] C. Bockelmann, H. F. Schepker, and A. Dekorsy, “Compressive sensing based multi-user detection for machine-to-machine communication”, *Transactions on Emerging Telecommunications Technologies*, volume 24, no. 4, pp. 389–400, 2013. 5, 18, 22

- [BV07] S. Boyd and L. Vandenberghe, *Convex Optimization*, Cambridge University Press, 2007. 35, 44, 120
- [CDD09] A. Cohen, W. Dahmen, and R. DeVore, “Compressed sensing and best k-term approximation”, *Journal of the American mathematical society*, volume 22, no. 1, pp. 211–231, 2009. 20
- [CE14] D. Cohen and Y. C. Eldar, “Sub-nyquist sampling for power spectrum sensing in cognitive radios: A unified approach”, *IEEE Transactions on Signal Processing*, volume 62, no. 15, pp. 3897–3910, 2014. 106
- [CE16] D. Cohen and Y. C. Eldar, “Sub-Nyquist Cyclostationary Detection for Cognitive Radio”, *arXiv preprint arXiv:1604.02659*, 2016. 106, 108, 117
- [Cho10] J. Choi, *Optimal Combining and Detection*, Cambridge University Press, 2010. 49
- [Cis16] “Cisco Visual Networking Index: Global Mobile Data Traffic Forecast Update, 2015-2020 White Paper”, *Technical report*, Cisco, 02 2016. 1
- [CK⁺01] J. Cvitanic, I. Karatzas, et al., “Generalized Neyman-Pearson lemma via convex duality”, *Bernoulli*, volume 7, no. 1, pp. 79–97, 2001. 54
- [CREKD05] S. F. Cotter, B. D. Rao, K. Engan, and K. Kreutz-Delgado, “Sparse solutions to linear inverse problems with multiple measurement vectors”, *IEEE Transactions on Signal Processing*, volume 53, no. 7, pp. 2477–2488, 2005. 107
- [CRT06] E. J. Candes, J. K. Romberg, and T. Tao, “Stable signal recovery from incomplete and inaccurate measurements”, *Communications on pure and applied mathematics*, volume 59, no. 8, pp. 1207–1223, 2006. 20
- [CT05] E. J. Candes and T. Tao, “Decoding by linear programming”, *IEEE transactions on information theory*, volume 51, no. 12, pp. 4203–4215, 2005. 20, 21
- [CW10] M. Chiani and M. Z. Win, “Estimating the number of signals observed by multiple sensors”, *2010 2nd International Workshop on Cognitive Information Processing*, pp. 156–161, IEEE, 2010. 110, 175
- [CWU⁺16] R. Croonenbroeck, A. Wulf, L. Underberg, W. Endemann, and R. Kays, “Parallel Sequence Spread Spectrum: Bit Error Performance under Industrial Channel Conditions”, *International Conference on OFDM and Frequency Domain Techniques (ICOF 2016)*, volume 19, 2016. 147
- [DAS07] F. F. Digham, M.-S. Alouini, and M. K. Simon, “On the energy detection of unknown signals over fading channels”, *IEEE Transactions on Communications*, volume 55, no. 1, pp. 21–24, 2007. 106

- [DCB00] O. Damen, A. Chkeif, and J.-C. Belfiore, “Lattice code decoder for space-time codes”, *Communications Letters, IEEE*, volume 4, no. 5, pp. 161–163, 2000. 58
- [DK17] A. Dekorsy and K.-D. Kammeyer, *Nachrichtenübertragung*, Vieweg Teubner, Stuttgart, Germany, 5th edition, Mar. 2017. 22
- [DM09] S. C. Draper and S. Malekpour, “Compressed sensing over finite fields”, *Proceedings of the 2009 IEEE International Symposium on Information Theory*, pp. 669–673, IEEE Press, 2009. 22
- [DMM09] D. L. Donoho, A. Maleki, and A. Montanari, “Message-passing algorithms for compressed sensing”, *Proceedings of the National Academy of Sciences*, volume 106, no. 45, pp. 18914–18919, 2009. 73, 80, 81, 88, 175
- [DMM10a] D. L. Donoho, A. Maleki, and A. Montanari, “Message passing algorithms for compressed sensing: I. motivation and construction”, *IEEE Workshop on Information Theory (ITW)*, pp. 1–5, IEEE, 2010. 73, 74
- [DMM10b] D. L. Donoho, A. Maleki, and A. Montanari, “Message Passing Algorithms for Compressed Sensing: II. Analysis and Validation”, *IEEE Inform. Theory Workshop*, 2010. 73
- [DSG⁺15] Z. Dawy, W. Saad, A. Ghosh, J. G. Andrews, and E. Yaacoub, “Towards Massive Machine Type Cellular Communications”, *arXiv preprint arXiv:1512.03452*, 2015. 135
- [DT09] D. Donoho and J. Tanner, “Observed universality of phase transitions in high-dimensional geometry, with implications for modern data analysis and signal processing”, *Philosophical Transactions of the Royal Society of London A: Mathematical, Physical and Engineering Sciences*, volume 367, no. 1906, pp. 4273–4293, 2009. 97
- [EK12] Y. C. Eldar and G. Kutyniok, *Compressed sensing: theory and applications*, Cambridge University Press, 2012. 20, 21
- [FP85] U. Fincke and M. Pohst, “Improved methods for calculating vectors of short length in a lattice, including a complexity analysis”, *Mathematics of computation*, volume 44, no. 170, pp. 463–471, 1985. 57
- [Gal62] R. G. Gallager, “Low-density parity-check codes”, *IRE Transactions on Information Theory*, volume 8, no. 1, pp. 21–28, 1962. 73
- [Gal13] R. G. Gallager, *Stochastic processes: theory for applications*, Cambridge University Press, 2013. 54
- [GB08] M. Grant and S. Boyd, “Graph implementations for nonsmooth convex programs”, V. Blondel, S. Boyd, and H. Kimura (Editors), *Recent Advances in Learning and Control*, Lecture Notes in Control and Information Sciences, pp. 95–110, Springer-Verlag Limited, 2008, http://stanford.edu/~boyd/graph_dcp.html. 121

- [GBY08] M. Grant, S. Boyd, and Y. Ye, “CVX: Matlab software for disciplined convex programming”, 2008. 121
- [GVL12] G. H. Golub and C. F. Van Loan, *Matrix computations*, volume 3, JHU Press, 2012. 108, 111, 114
- [HMJ⁺15] G. Hannak, M. Mayer, A. Jung, G. Matz, and N. Goertz, “Joint channel estimation and activity detection for multiuser communication systems”, *2015 IEEE International Conference on Communication Workshop (ICCW)*, pp. 2086–2091, IEEE, 2015. 73
- [HMMG16] G. Hannak, M. Mayer, G. Matz, and N. Goertz, “Bayesian QAM demodulation and activity detection for multiuser communication systems”, *IEEE International Conference on Communications (ICC)*, pp. 596–601, IEEE, 2016. 23, 73
- [HOP96] J. Hagenauer, E. Offer, and L. Papke, “Iterative decoding of binary block and convolutional codes”, *IEEE Transactions on Information Theory*, volume 42, no. 2, pp. 429–445, 1996. 74
- [HSCK06] N. Han, S. Shon, J. H. Chung, and J. M. Kim, “Spectral correlation based signal detection method for spectrum sensing in IEEE 802.22 WRAN systems”, *2006 8th International Conference Advanced Communication Technology*, volume 3, pp. 6–pp, IEEE, 2006. 106
- [HV02] B. Hassibi and B. Vikalo, “On the expected complexity of integer least-squares problems”, *IEEE International Conference on Acoustics, Speech, and Signal Processing (ICASSP)*, volume 2, pp. II–1497, IEEE, 2002. 57
- [IHB⁺16] M. Ivanov, C. Häger, F. Brännström, A. G. i Amat, A. Alvarado, and E. Agrell, “On the information loss of the max-log approximation in BICM systems”, *IEEE Transactions on Information Theory*, volume 62, no. 6, pp. 3011–3025, 2016. 35
- [JBD15] Y. Ji, C. Bockelmann, and A. Dekorsy, “Compressed Sensing Based Multi-User Detection with Modified Sphere Detection in Machine-to-Machine Communications”, *10th International ITG Conference on Systems, Communications and Coding (SCC 2015)*, Hamburg, Germany, Feb 2015. 13, 17
- [JKB02] N. L. Johnson, S. Kotz, and N. Balakrishnan, *Continuous multivariate distributions, volume 1, models and applications*, volume 59, New York: John Wiley & Sons, 2002. 110
- [JO05] J. Jalden and B. Ottersten, “Parallel Implementation of a Soft Output Sphere Decoder”, *Asilomar Conference on Signals, Systems and Computers*, pp. 1013–1016, Asilomar, CA, USA, November 2005. 58
- [KF98] F. R. Kschischang and B. J. Frey, “Iterative decoding of compound codes by probability propagation in graphical models”, *IEEE Journal*

- on Selected Areas in Communications*, volume 16, no. 2, pp. 219–230, 1998. 73
- [KFL01] F. R. Kschischang, B. J. Frey, and H.-A. Loeliger, “Factor graphs and the sum-product algorithm”, *IEEE Transactions on Information Theory*, volume 47, no. 2, pp. 498–519, 2001. 73, 77, 79, 86, 90, 91
- [KMB⁺13] B. Knoop, F. Monsees, C. Bockelmann, D. Wübben, S. Paul, and A. Dekorsy, “Sparsity-Aware Successive Interference Cancellation with Practical Constraints”, *17th International ITG Workshop on Smart Antennas (WSA 2013)*, Stuttgart, Germany, Mar 2013. 7
- [KMB⁺14] B. Knoop, F. Monsees, C. Bockelmann, D. Peters-Drolshagen, S. Paul, and A. Dekorsy, “Compressed Sensing K-Best Detection for Sparse Multi-User Communications”, *22nd European Signal Processing Conference 2014 (EUSIPCO)*, Lissabon, Portugal, Sep 2014. 7, 33
- [Kot33] V. A. Kotelnikov, “On the carrying capacity of the ether and wire in telecommunications”, *Material for the First All-Union Conference on Questions of Communication*, Izd. Red. Upr. Svyazi RKKA, Moscow, volume 1, 1933. 19
- [LCL11] S.-Y. Lien, K.-C. Chen, and Y. Lin, “Toward ubiquitous massive accesses in 3GPP machine-to-machine communications”, *IEEE Communications Magazine*, volume 49, no. 4, pp. 66–74, 2011. 1
- [Liv11] G. Liva, “Graph-based analysis and optimization of contention resolution diversity slotted ALOHA”, *IEEE Transactions on Communications*, volume 59, no. 2, pp. 477–487, 2011. 17
- [LR05] E. L. Lehmann and J. P. Romano, *Testing statistical hypotheses*, Springer Texts in Statistics, Springer, New York, 3rd edition, 2005. 54
- [MBD13a] F. Monsees, C. Bockelmann, and A. Dekorsy, “Compressed sensing Bayes-risk detection for frame based multi-user systems”, *2013 IEEE 24th Annual International Symposium on Personal, Indoor, and Mobile Radio Communications (PIMRC)*, pp. 218–222, IEEE, 2013. 7
- [MBD13b] F. Monsees, C. Bockelmann, and A. Dekorsy, “Compressed sensing Bayes-risk detection for frame based multi-user systems”, *IEEE 24th International Symposium on Personal Indoor and Mobile Radio Communications (PIMRC)*, pp. 218–222, IEEE, 2013. 33
- [MBD13c] F. Monsees, C. Bockelmann, and A. Dekorsy, “Compressed Sensing Soft Activity Processing for Sparse Multi-User Systems”, *9th IEEE Broadband Wireless Access Workshop co-located with IEEE Globecom 2013*, Atlanta, USA, Dec 2013. 7, 33
- [MBD13d] F. Monsees, C. Bockelmann, and A. Dekorsy, “Joint Activity and Data Detection for Machine to Machine Communication via Bayes

- Risk Optimization”, *IEEE International Workshop on Signal Processing Advances in Wireless Communications (SPAWC)*, Darmstadt, Germany, Jun 2013. 7
- [MBD14] F. Monsees, C. Bockelmann, and A. Dekorsy, “Reliable activity detection for massive machine to machine communication via multiple measurement vector compressed sensing”, *2014 IEEE Globecom Workshops (GC Wkshps)*, pp. 1057–1062, IEEE, 2014. 8, 105
- [MBD15] F. Monsees, C. Bockelmann, and A. Dekorsy, “Compressed Sensing Neyman-Pearson Based Activity Detection for Sparse Multiuser Communications”, *10th International ITG Conference on Systems, Communications and Coding (SCC 2015)*, Feb 2015. 7, 33, 50
- [MBWD12] F. Monsees, C. Bockelmann, D. Wübben, and A. Dekorsy, “Sparsity Aware Multiuser Detection for Machine to Machine Communication”, *Second International Workshop on Machine-to-Machine Communication at IEEE Globecom 2012*, Anaheim, USA, Dec 2012. 7, 33
- [MBWD13] F. Monsees, C. Bockelmann, D. Wübben, and A. Dekorsy, “Compressed Sensing Bayes Risk Minimization for Under-determined Systems via Sphere Detection”, *2013 IEEE 77th Vehicular Technology Conference (VTC2013-Spring)*, Dresden, Germany, Jun 2013. 7, 33
- [ME11] M. Mishali and Y. C. Eldar, “Wideband spectrum sensing at sub-Nyquist rates [applications corner]”, *IEEE Signal Processing Magazine*, volume 28, no. 4, pp. 102–135, 2011. 106
- [MG15] M. Mayer and N. Goertz, “Improving Approximate Message Passing Recovery of Sparse Binary Vectors by Post Processing”, *SCC 2015; 10th International ITG Conference on Systems, Communications and Coding; Proceedings of*, pp. 1–6, VDE, 2015. 73
- [MP15a] METIS-Project, “D2.4: Proposed solutions for new radio access, ICT-317669-METIS/D2.4”, February 2015. 134
- [MP15b] METIS-Project, “D6.6: Final Report on the METIS System Concept and Technology Roadmap, ICT-317669-METIS/D6.6”, April 2015. 137
- [MSP13] G. C. Madueno, Č. Stefanović, and P. Popovski, “How many smart meters can be deployed in a GSM cell?”, *2013 IEEE International Conference on Communications Workshops (ICC)*, pp. 1263–1268, IEEE, 2013. 3
- [MWBD15a] F. Monsees, M. Woltering, C. Bockelmann, and A. Dekorsy, “Compressive Sensing Multi-User Detection for Multi-Carrier Systems in Sporadic Machine Type Communication”, *IEEE 81th Vehicular Technology Conference (VTC2015-Spring)*, volume 81, Glasgow, Great Britain, May 2015. 8, 135

- [MWBD15b] F. Monsees, M. Woltering, C. Bockelmann, and A. Dekorsy, “A Potential Solution for MTC: Multi-Carrier Compressive Sensing Multi-User Detection”, *The Asilomar Conference on Signals, Systems, and Computers*, Asilomar Hotel and Conference Grounds, USA, Nov 2015. 8, 135
- [MWBD16] F. Monsees, M. Woltering, C. Bockelmann, and A. Dekorsy, “Patent: Mehrträger Compressed Sensing Multi-User System, Filed under PCT /EP2016/060064”, 05 2016. 8, 135
- [MZ93] S. G. Mallat and Z. Zhang, “Matching pursuits with time-frequency dictionaries”, *IEEE Transactions on Signal Processing*, volume 41, no. 12, pp. 3397–3415, 1993. 110
- [NB13] H. Nikopour and H. Baligh, “Sparse code multiple access”, *2013 IEEE 24th Annual International Symposium on Personal, Indoor, and Mobile Radio Communications (PIMRC)*, pp. 332–336, IEEE, 2013. 17
- [Nok14] Nokia, “Nokia LTE M2M: Optimizing LTE for the Internet of Things”, *White Paper*, 2014. 134
- [NP33] J. Neyman and E. S. Pearson, “On the Problem of the Most Efficient Tests of Statistical Hypotheses”, *Philosophical Transactions of the Royal Society of London. Series A, Containing Papers of a Mathematical or Physical Character*, volume 231, pp. 289–337, 1933. 49
- [OMM16] A. Osseiran, J. F. Monserrat, and P. Marsch (Editors), *5G Mobile and Wireless Communications Technology*;, Cambridge University Press, Cambridge, 02 2016, ISBN 9781316417744. 2, 4, 17, 137
- [PLWL04] L. Ping, L. Liu, K. Wu, and W. K. Leung, “On interleave-division multiple-access”, *IEEE International Conference on Communications*, volume 5, pp. 2869–2873, IEEE, 2004. 96
- [Poh81] M. Pohst, “On the computation of lattice vectors of minimal length, successive minima and reduced bases with applications”, *ACM Sigsum Bulletin*, volume 15, no. 1, pp. 37–44, 1981. 57
- [PP02] A. Papoulis and S. U. Pillai, *Probability, random variables, and stochastic processes*, Tata McGraw-Hill Education, 2002. 180
- [PP⁺08] K. B. Petersen, M. S. Pedersen, et al., “The matrix cookbook”, *Technical University of Denmark*, volume 7, p. 15, 2008. 116
- [R⁺13] M. Rumney et al., *LTE and the evolution to 4G wireless: Design and measurement challenges*, John Wiley & Sons, 2013. 163
- [Ran11] S. Rangan, “Generalized approximate message passing for estimation with random linear mixing”, *IEEE International Symposium on Information Theory Proceedings (ISIT)*, pp. 2168–2172, IEEE, 2011. 73

- [Rob75] L. G. Roberts, "ALOHA packet system with and without slots and capture", *ACM SIGCOMM Computer Communication Review*, volume 5, no. 2, pp. 28–42, 1975. 17
- [RPL⁺15] R. Ratasuk, A. Prasad, Z. Li, A. Ghosh, and M. A. Uusitalo, "Recent advancements in M2M communications in 4G networks and evolution towards 5G", *18th International Conference on Intelligence in Next Generation Networks (ICIN)*, pp. 52–57, IEEE, 2015. 134
- [SBB07] C. Studer, A. Burg, and H. Bölcskei, "Soft-output sphere decoding: Algorithms and VLSI implementation", *IEEE Journal on Selected Areas in Communications*, April 2007. 58
- [SBD13] H. F. Schepker, C. Bockelmann, and A. Dekorsy, "Coping with CDMA asynchronicity in compressive sensing multi-user detection", *Vehicular Technology Conference (VTC Spring), 2013 IEEE 77th*, pp. 1–5, IEEE, 2013. 145
- [SCFCA13] P. Stenumgaard, J. Chilo, J. Ferrer-Coll, and P. Angskog, "Challenges and conditions for wireless machine-to-machine communications in industrial environments", *IEEE Communications Magazine*, volume 51, no. 6, pp. 187–192, 2013. 147
- [Sch86] R. Schmidt, "Multiple emitter location and signal parameter estimation", *IEEE Transactions on Antennas and Propagation*, volume 34, no. 3, pp. 276–280, 1986. 111
- [Sch10] P. Schniter, "Turbo reconstruction of structured sparse signals", *44th Annual Conference on Information Sciences and Systems (CISS)*, pp. 1–6, IEEE, 2010. 72, 80
- [Sch15] H. F. Schepker, *Compressive Sensing Multi-User Detection Approaches for Sporadic Communication*, Ph.D. thesis, University of Bremen, 2015. 18, 19, 74, 98, 123
- [SD11] H. Schepker and A. Dekorsy, "Sparse Multi-User Detection for CDMA Transmission using Greedy Algorithms", *8th International Symposium on Wireless Communication Systems (ISWCS 11)*, Aachen, Germany, Nov 2011. 5, 22
- [SD12] H. Schepker and A. Dekorsy, "Compressive Sensing Multi-User Detection with Block-Wise Orthogonal Least Squares", *2012 IEEE 75th Vehicular Technology Conference: VTC2012-Spring*, Yokohama, Japan, May 2012. 5, 107
- [SE94] C.-P. Schnorr and M. Euchner, "Lattice basis reduction: improved practical algorithms and solving subset sum problems", *Mathematical programming*, volume 66, no. 1-3, pp. 181–199, 1994. 32, 60
- [SF92] A. Sonnenschein and P. M. Fishman, "Radiometric detection of spread-spectrum signals in noise of uncertain power", *IEEE Transactions on Aerospace and Electronic Systems*, volume 28, no. 3, pp. 654–660, 1992. 106

- [SF14] S. Sparrer and R. F. Fischer, “Adapting compressed sensing algorithms to discrete sparse signals”, *18th International ITG Workshop on Smart Antennas (WSA)*, pp. 1–8, VDE, 2014. 23
- [Sha01] C. E. Shannon, “A mathematical theory of communication”, *ACM SIGMOBILE Mobile Computing and Communications Review*, volume 5, no. 1, pp. 3–55, 2001. 19
- [Stu09] C. Studer, *Iterative MIMO Decoding: Algorithms and VLSI Implementation Aspects*, Ph.D. thesis, ETH Zurich, 2009. 60
- [Stü11] G. L. Stüber, *Principles of mobile communication*, Springer Science & Business Media, 2011. 117, 118
- [Tib96] R. Tibshirani, “Regression shrinkage and selection via the lasso”, *Journal of the Royal Statistical Society. Series B (Methodological)*, pp. 267–288, 1996. 57
- [TS313] “Study on provision of low-cost Machine-Type Communications (MTC) UEs based on LTE”, *Technical Report TS 36.888*, 3rd Generation Partnership Project (3GPP), 06 2013. 2, 3
- [Urk67] H. Urkowitz, “Energy detection of unknown deterministic signals”, *Proceedings of the IEEE*, volume 55, no. 4, pp. 523–531, 1967. 106
- [VB99] E. Viterbo and J. Boutros, “A universal lattice code decoder for fading channels”, *IEEE Transactions on Information Theory*, volume 45, no. 5, pp. 1639–1642, 1999. 57
- [Ver98] S. Verdú, *Multiuser detection*, Cambridge University Press, 1998. 15
- [VHK04] H. Vikalo, B. Hassibi, and T. Kailath, “Iterative decoding for MIMO channels via modified sphere decoding”, *Wireless Communications, IEEE Transactions on*, volume 3, no. 6, pp. 2299–2311, 2004. 58
- [VM13] M. A. Vázquez and J. Míguez, “User activity tracking in DS-CDMA systems”, *IEEE Transactions on Vehicular Technology*, volume 62, no. 7, pp. 3188–3203, 2013. 33, 107
- [VT04] H. L. Van Trees, *Detection, estimation, and modulation theory*, John Wiley & Sons, 2004. 42, 43
- [WBR⁺01] D. Wübben, R. Böhnke, J. Rinas, V. Kühn, and K.-D. Kammeyer, “Efficient algorithm for decoding layered space-time codes”, *Electronics letters*, volume 37, no. 22, p. 1, 2001. 61
- [WC98] W.-C. Wu and K.-C. Chen, “Identification of active users in synchronous CDMA multiuser detection”, *IEEE Journal on Selected Areas in Communications*, volume 16, no. 9, pp. 1723–1735, 1998. 33, 107, 112, 114
- [Whi15] E. T. Whittaker, “On the functions which are represented by the expansions of the interpolation-theory”, *Proceedings of the Royal Society of Edinburgh*, volume 35, pp. 181–194, 1915. 19

- [WJK⁺14] G. Wunder, P. Jung, M. Kasparick, T. Wild, F. Schaich, Y. Chen, S. Ten Brink, I. Gaspar, N. Michailow, A. Festag, et al., “5GNOW: non-orthogonal, asynchronous waveforms for future mobile applications”, *IEEE Communications Magazine*, volume 52, no. 2, pp. 97–105, 2014. 134
- [WMBD16] M. Woltering, F. Monsees, C. Bockelmann, and A. Dekorsy, “Multi-Carrier Compressed Sensing Multi-User Detection System: A Practical Verification”, *19th International Conference on OFDM and Frequency Domain Techniques (ICOF 2016)*, Essen, Germany, Aug 2016. 8, 135
- [Wym07] H. Wymeersch, *Iterative receiver design*, volume 234, Cambridge University Press Cambridge, 2007. 74
- [ZG11] H. Zhu and G. B. Giannakis, “Exploiting sparse user activity in multiuser detection”, *IEEE Transactions on Communications*, volume 59, no. 2, pp. 454–465, 2011. 22, 33
- [ZKL08] Y. Zeng, C. L. Koh, and Y.-C. Liang, “Maximum eigenvalue detection: Theory and application”, *2008 IEEE International Conference on Communications*, pp. 4160–4164, IEEE, 2008. 106
- [ZOAZ⁺14] K. Zheng, S. Ou, J. Alonso-Zarate, M. Dohler, F. Liu, and H. Zhu, “Challenges of massive access in highly dense LTE-advanced networks with machine-to-machine communications”, *IEEE Wireless Communications*, volume 21, no. 3, pp. 12–18, 2014. 135